

---

# Measuring Topological Invariants and Chiral Meissner Currents with Ultracold Bosonic Atoms

Marcos Exequiel Atala

---



Dissertation an der Fakultät für Physik  
der Ludwig-Maximilians-Universität München

vorgelegt von  
Marcos Exequiel Atala  
aus Córdoba, Argentinien

München, 2014

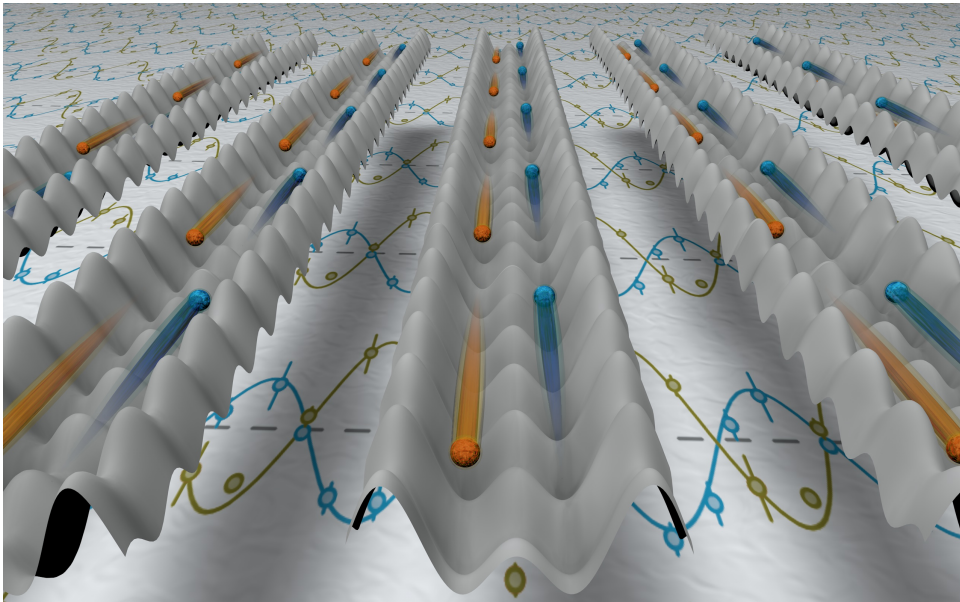


---

# Measuring Topological Invariants and Chiral Meissner Currents with Ultracold Bosonic Atoms

Marcos Exequiel Atala

---



Dissertation an der Fakultät für Physik  
der Ludwig-Maximilians-Universität München

vorgelegt von  
Marcos Exequiel Atala  
aus Córdoba, Argentinien

München, September 2014

Tag der mündlichen Prüfung: 20.11.2014

Erstgutachter: Prof. I. Bloch

Zweitgutachter: Prof. U. Schollwöck

# Zusammenfassung

Topologische Invarianten sind von zentraler Bedeutung für die Interpretation vieler Phänomene kondensierter Materie. In dieser Arbeit wird die erste Messung einer solchen Invarianten vorgestellt. Dazu wird ein neu entwickeltes Messprotokoll mit ultrakalten bosonischen Atomen in einem eindimensionalen optischen Gitter verwendet. Außerdem wird die Messung chiraler Meissner-Ströme in einer Leitergeometrie in einem künstlichen Magnetfeld sowie die Präparation sogenannter "Resonating Valence Bond"-Zustände (RVB) in vier Gitterplätze umfassenden Plaketten präsentiert. Das Hauptmerkmal des experimentellen Aufbaus ist ein Paar orthogonaler Übergitter-Potentiale, die es ermöglichen eine Vielzahl verschiedener Systeme zu simulieren. Die Modulation des Übergitters mit einem weiteren Paar interferierender Strahlen ermöglicht zu dem die Realisierung eines künstlichen Magnetfelds.

Die Zak-Phase ist eine Invariante, welche die topologischen Eigenschaften eines Energiebandes charakterisiert. Sie ist definiert als die Berry-Phase eines Teilchens bei adiabatischem Durchlaufen eines Pfades im Quasiimpulsraum durch die Brillouinzone. Ein einfaches Beispiel für ein System mit zwei verschiedenen topologischen Klassen ist eine eindimensionale Kette mit alternierender Tunnelkopplungsstärke. Im Experiment können diese Klassen durch Messung der Differenz zwischen ihren Zak-Phasen  $\Delta\Phi_{\text{Zak}} \approx \pi$  unter Verwendung von Bloch-Oszillationen und Ramsey-Interferometrie in Übergittern unterschieden werden.

Der zweite Teil dieser Arbeit befasst sich mit der Messung chiraler Meissner-Ströme von Bosonen in einer Leitergeometrie mit magnetischem Fluss, welche eines der einfachsten Modelle zur Beobachtung von Orbitaleffekten ist. Obwohl die Atome ladungsneutral sind und daher keine Lorentzkraft auf sie wirkt, kann durch eine externe Modulation im Übergitter ein künstliches Magnetfeld erzeugt werden. Die dadurch hervorgerufenen Wahrscheinlichkeitsströme auf beiden Seiten der Leiter wurden separat mit einer Projektionsmethode gemessen. Beim Ändern der Tunnelkopplung entlang der Leitersprossen wurde, in Analogie zu einem Typ-II Supraleiter, ein Übergang zwischen einer Meissner-artigen Phase mit gesättigtem maximalen chiralen Strom und einer Vortex-Phase mit abnehmendem Strom beobachtet. Dieses System mit ultrakalten Atomen kann auch als Analogon zur Spin-Bahn-Kopplung betrachtet werden.

RVB-Zustände gelten als fundamental für das Verständnis von Hochtemperatursupraleitern. Der dritte Teil der Arbeit widmet sich mit der Realisierung eines Minimalbeispiels solcher Zustände auf einer Plakette bei halber Füllung. In diesem System wurden die zwei RVB-Zustände mit s- und d-Wellen-Symmetrie sowie Superpositionen der beiden Zustände präpariert.

Die in dieser Arbeit vorgestellten Experimente stellen einen neuen Ansatz dar, die topologischen Eigenschaften von Bloch-Bändern in optischen Gittern zu untersuchen; sie öffnen die Türen zur Erforschung von wechselwirkenden Teilchen in niedrigdimensionalen Systemen in einem homogenen Magnetfeld sowie der Eigenschaften des Grundzustandes des Heisenberg-Modells.

# Abstract

The determination of topological invariants is of fundamental importance to interpret many condensed-matter phenomena. This thesis reports on the implementation of a newly developed protocol to measure these invariants for the first time, using ultracold bosonic atoms in one-dimensional optical lattices. In addition, it deals with the measurement of chiral Meissner currents in a ladder-like lattice geometry exposed to an artificial magnetic field, and presents results on the preparation of Resonating Valence Bond (RVB) states on plaquettes. The key feature of the experimental setup is a pair of orthogonal superlattice potentials that permit a rich variety of systems to be simulated, and that when combined with a pair of interfering beams which periodically modulate the lattice allow the realization of artificial magnetic fields.

The Zak phase is an invariant that characterizes the topological properties of an energy band, and is defined as the Berry phase that a particle acquires as it adiabatically moves in the quasimomentum space across the Brillouin zone. A dimerized lattice – a one-dimensional chain with alternating couplings – is a simple example of a system that possesses two different topological classes. Using a combination of Bloch oscillations and Ramsey interferometry in superlattices we measured the difference of the Zak phase  $\approx \pi$  for the two possible polyacetylene phases, which directly indicates that they belong to different topological classes.

The second part of this thesis deals with the measurement of chiral Meissner currents in bosonic ladders with magnetic flux, one of the simplest models to observe orbital effects. Although charge neutrality prevents atoms from experiencing the Lorentz force when they are exposed to a magnetic field, employing lattice modulation techniques we implemented an artificial magnetic field on a ladder created with optical lattices. By using a projection technique, we were able to measure the probability currents on each side of the ladder. When changing the coupling strengths along the rungs of the ladder, we found, in analogy to type-II superconductors, a transition between a Meissner-like phase with saturated maximum chiral current and a vortex phase with decreasing currents. Additionally, the flux ladder realizes spin-orbit coupling with ultracold atoms.

It is believed that RVB states are fundamental for the understanding of high- $T_c$  superconductivity. The third part of this work describes our measurements on the preparation

of minimum instances of RVB states with bosonic atoms in isolated four-site plaquettes at half filling. These small systems possess two RVB states with  $s$ - and  $d$ -wave symmetry. Using atom manipulation techniques we prepared these two states, as well as a quantum resonance between them.

The experiments in this thesis establish a new general approach for probing the topological structure of Bloch bands in optical lattices. Moreover, they open up the pathway to exploring interacting particles in low dimensions exposed to uniform magnetic fields and to studying ground state properties of the Heisenberg Hamiltonian.

# Contents

<b>Zusammenfassung</b>	<b>v</b>
<b>Abstract</b>	<b>vii</b>
<b>1 Introduction</b>	<b>1</b>
<b>2 Ultracold Bosons in optical lattices – Experimental setup</b>	<b>11</b>
2.1 Experimental setup . . . . .	11
2.1.1 Description of the machine and the cooling and trapping schemes	11
2.1.2 Atom-light interaction: optical potentials . . . . .	12
2.1.3 Dipole Trap potential . . . . .	14
2.1.4 Lattice potentials . . . . .	16
2.1.5 Running-wave beams for lattice shaking . . . . .	18
2.2 Single particle in periodic potentials . . . . .	18
2.2.1 Quantum mechanics of a single particle in a periodic potential . .	18
2.2.2 Wannier functions . . . . .	21
2.3 Ultracold atoms in periodic potentials . . . . .	22
2.3.1 Bose-Einstein condensates of non-interacting particles . . . . .	22
2.3.2 Bose-Einstein condensates with weak interactions . . . . .	24
2.3.3 The Bose-Hubbard model . . . . .	26
2.3.4 Superfluid and Mott insulator states . . . . .	28
<b>3 Theory of Zak phase and its relation to topological invariants</b>	<b>31</b>
3.1 Geometric phases in quantum mechanics . . . . .	31
3.2 Geometric phases in condensed matter: topological invariants . . . . .	35
3.2.1 Geometric phases in periodic systems - the Zak phase . . . . .	35
3.2.2 Gauge dependence of the Zak phase . . . . .	37
3.2.3 The Chern number of Bloch bands . . . . .	38
3.3 The SSH and Rice-Mele models and their Zak phases . . . . .	39
3.3.1 The SSH and Rice-Mele models . . . . .	39
3.3.2 The Zak phase in the SSH and Rice-Mele models . . . . .	41

3.3.3	Chiral symmetry . . . . .	44
3.3.4	Zak phase and edge states in finite systems . . . . .	46
3.4	Theory of bulk polarization in solids and its relation to the Zak phase . .	50
3.4.1	Bulk polarization – definition and subtleties . . . . .	50
3.4.2	Zak phase and its relation to bulk polarization change . . . . .	51
3.4.3	Polarization change in the Rice-Mele model . . . . .	54
<b>4</b>	<b>Measurement of the Zak phase in a dimerized system</b>	<b>57</b>
4.1	Theoretical proposals for measuring the Zak phase . . . . .	57
4.1.1	Zak phase on a single band: theoretical proposal and limitations .	57
4.1.2	Proposal for measuring the Zak phase difference between the two dimerizations of the SSH model . . . . .	59
4.2	Experimental measurement of the Zak phase . . . . .	61
4.2.1	Experimental setup to realize the dimerized system . . . . .	61
4.2.2	Experimental sequence . . . . .	62
4.2.3	Edge states and trapping effects . . . . .	66
4.3	Experimental measurement of fractional Zak phases . . . . .	67
4.3.1	Experimental sequence and results . . . . .	67
4.3.2	Extracting the phase difference $\varphi_{\text{Zak}} - \varphi_{\text{Zak}}(\Delta)$ . . . . .	68
4.3.3	Symmetries and generalizations of the measurement scheme . . .	71
4.4	Conclusion . . . . .	72
<b>5</b>	<b>Analog of the Meissner effect in flux ladders</b>	<b>75</b>
5.1	Introduction to the Meissner effect . . . . .	75
5.2	Meissner-like effect in a ladder . . . . .	78
5.2.1	Ladder in a magnetic field . . . . .	78
5.2.2	Currents in ladders . . . . .	81
5.2.3	Meissner-like effect in the ladder . . . . .	83
5.2.4	Momentum distribution . . . . .	87
5.3	Spin-orbit coupling mapping . . . . .	89
<b>6</b>	<b>Measurements of chiral Meissner currents in the flux ladder</b>	<b>93</b>
6.1	Experimental realization of the flux ladder . . . . .	93
6.1.1	Experimental setup . . . . .	93
6.2	Experimental sequence and projection into isolated double wells . . . . .	96
6.2.1	Experimental sequence . . . . .	96
6.2.2	Relation between currents and oscillations in isolated double wells	99
6.3	Measurements of chiral Meissner currents . . . . .	101
6.3.1	Rabi oscillations in double wells . . . . .	101
6.3.2	Results of the measurements of the chiral Meissner currents . . . .	103

6.3.3	Calibration of laser-assisted tunneling . . . . .	107
6.3.4	Interaction energy . . . . .	110
6.4	Measurements of the momentum distribution after free expansion . . . . .	111
6.5	Conclusion . . . . .	115
<b>7</b>	<b>Resonating valence bond states in plaquettes</b>	<b>117</b>
7.1	Introduction to resonating valence bond states . . . . .	117
7.1.1	Quantum resonances in chemistry . . . . .	117
7.1.2	RVB states in condensed matter . . . . .	118
7.2	Spin Hamiltonian with ultracold atoms in optical plaquettes . . . . .	121
7.3	Experimental realization of the spin Hamiltonian in a plaquette . . . . .	124
7.3.1	Loading in plaquettes at half filling . . . . .	124
7.3.2	Preparation of the initial state . . . . .	124
7.4	Measurements of the resonating valence bond states . . . . .	125
7.4.1	Observation of the valence bond resonance . . . . .	125
7.4.2	Preparation of the $s$ -wave RVB state . . . . .	127
7.4.3	Preparation of the $d$ -wave RVB state . . . . .	129
7.4.4	Decoherences in the singlet subspace . . . . .	131
7.4.5	Population evolution during the dynamics . . . . .	131
7.5	Conclusions . . . . .	132
<b>8</b>	<b>Conclusions and Outlook</b>	<b>135</b>
<b>A</b>	<b>Time of flight expansion and absorption imaging</b>	<b>139</b>
A.1	Time of flight expansion: . . . . .	139
A.2	Absorption Imaging: . . . . .	140
<b>B</b>	<b>Detection of population fractions on the plaquette</b>	<b>143</b>
B.1	Dumping sequence: . . . . .	143
B.2	Band mapping sequence: . . . . .	144
B.3	Dumping and band mapping in two directions: . . . . .	145
<b>C</b>	<b>Oscillations in double wells: calibration of the hopping terms</b>	<b>147</b>
<b>D</b>	<b>Eigenstates of the Rice-Mele model and the choice of the unit cell</b>	<b>149</b>
D.1	Boundary conditions for $\alpha_k$ and $\beta_k$ : . . . . .	149
D.2	Solutions of the Rice-Mele Hamiltonian for the choice of the unit cell indicated in section 3.3.4: . . . . .	150

---

<b>E</b>	<b>Theory of Bloch oscillations and the phases acquired during the evolution</b>	<b>153</b>
E.1	Bloch oscillations in lattices . . . . .	153
E.2	Phase evolution during the Bloch oscillations . . . . .	154
<b>F</b>	<b>Ramsey interferometry</b>	<b>159</b>
F.1	Ramsey interferometry . . . . .	159
<b>G</b>	<b>Sequence for the preparation of initial states in plaquettes</b>	<b>163</b>
G.1	Filtering sequences . . . . .	163
<b>H</b>	<b>Singlet and triplet states: oscillations and detection</b>	<b>165</b>
H.1	Detection of singlet and triplet fractions . . . . .	165
H.2	Singlet-triplet oscillations in isolated double wells . . . . .	167
	<b>References</b>	<b>171</b>
	<b>Acknowledgements</b>	<b>193</b>

# Chapter 1

## Introduction

Ultracold atoms have proven to be a very useful and versatile tool for simulating condensed matter systems due to the high degree of control they offer over all relevant parameters together with the very low number of imperfections in the system. In contrast to condensed matter, in cold atom experiments the Hamiltonian is well known and can be controlled and dynamically modified with almost no limitations. Moreover, these systems offer a large variety of tools to probe quantum states, like absorption and phase contrast imaging [1], spectroscopic techniques [2, 3] and also the newly developed in-situ high-resolution-fluorescence imaging [4, 5] that allows for single-site resolved detection and manipulation of atoms in an optical lattice.

A fundamental achievement in the field was the first creation of a Bose-Einstein condensate (BEC) in dilute atomic gases in 1995 [6, 7], where all atoms occupy the same quantum state. Since then, the field has undergone a remarkable development. Subsequent experiments successfully studied fundamental properties of superfluidity through the creation of vortices [8–10], wave-matter interference of condensates to probe their macroscopic phases [11], as well as confirmation of Bogoliubov’s theory for weakly interacting particles [12, 13]. Important advances followed in 1999, when the first quantum degenerate gas of fermionic atoms was realized [14]. Entering the strongly correlated regime, where mean field theory is not valid and the interatomic interactions play a crucial role, was achieved through the use of Feshbach resonances [15, 16], which permit to freely tune the scattering length to enhance or fully suppress interactions by varying an external magnetic field. This allowed to study the crossover between BEC and BCS (Barden-Cooper-Schrieffer) phases [17, 18].

Entering the strongly interacting regime for bosons using Feshbach resonances is very challenging due to strong collisional losses. In this case, one solution came about with the advent of optical lattices, which are created by the interference of laser beams to produce a standing wave. Atoms in optical lattices play the role of the electrons in a solid crystal, interacting with the optical lattices in a similar way as the electrons

interact with the ions. Optical lattices decrease the kinetic energy scales, and at the same time they strongly confine the wavefunctions which leads to an enhancement of the interactions. This makes it feasible to enter a regime in which interactions set the dominant scale. In a seminal paper, D. Jaksch and coworkers [19] proposed a method to realize the Bose-Hubbard model [20] – a well known model in condensed matter which describes the behavior of interacting bosons in a crystalline solid – using bosonic atoms in optical lattices. Some of the first experiments which explored the physics of this model in one-dimension were the study of Bloch oscillations [21] and Wannier stark ladders [22].

A breakthrough in the field was the observation of the quantum phase transition from a superfluid to a Mott insulating state of bosons in an optical lattice in 2002 by M. Greiner and collaborators [23], a transition that was predicted for the Bose-Hubbard model by Fisher and coworkers in 1989 [20]. Following this work, Mott insulators for one- and two-dimensional systems were also created [24, 25]. Furthermore, a Tonks-Girardeau gas [26, 27] and a band insulator for fermions were realized [28]. These results marked the path towards the strongly interacting regime using optical lattices.

Recent developments in the field have enabled the Bose-Hubbard model to be extended to a variety of different lattice configurations. These geometries include cubic lattices [23], superlattices [29, 30] as well as triangular [31], hexagonal [32] and kagome lattices [33].

Even though ultracold atoms in optical lattices offer an ideal platform for the simulation of condensed matter systems, there is a limiting factor that prevents the direct realization of a large variety of phenomena: unlike electrons, atoms are electrically neutral. When placed in an external magnetic field, they do not experience the Lorentz force that would otherwise be present for electrons in a real material. This prevents for example the direct realization of the quantum Hall effect. In order to overcome this limitation, there have been several theoretical proposals that allow the Hamiltonian of a charged particle exposed to an external magnetic field to be artificially recreated. One idea, which has already been experimentally realized, exploits the analogy between the magnetic Lorentz force and the Coriolis force present in a rotating BEC [9, 34, 35]. However, the angular velocity necessary to enter into the physically interesting regime of strong fields is too large to be experimentally realized. Other proposals involve the use of Raman lasers to imprint Berry phases on moving particles [36–38]. In the context of optical lattices, the key point to simulate magnetic fields is to be able to engineer complex tunneling elements between different lattice sites in such a way that the corresponding Peierls phases give rise to a non-zero magnetic flux. Along these lines, there have been proposals using spin-dependent tilted lattices, where the tunneling along the tilted direction is provided by Raman-assisted tunneling [39–41]. However, that method involves the use of near-resonant light which induces heating on the atomic

cloud and leads to atom losses and decoherence in the system. Other ideas make use of time-periodic modulation in tilted lattices to induce laser-assisted tunneling, which in contrast to Raman-assisted tunneling does not involve near-resonant light, avoiding undesired heating [42, 43]. Recently, using this and similar techniques, it has been possible to experimentally realize artificial gauge fields in optical lattices with a large flux that is almost impossible to produce for real materials [44–49].

Thanks to the progress in the field of ultracold atoms, the simulation of condensed matter phenomena is becoming more and more common, and perhaps soon it will help to solve problems that so far have been puzzling the scientific community. One particular problem, which is linked to the phenomenon of high- $T_c$  superconductivity [50], is the ground state solution of the antiferromagnetic Heisenberg Hamiltonian in two or more dimensions, which so far due to its complexity has been out of reach even for numerical simulations. This motivates the use of ultracold atoms to reproduce spin Hamiltonians and use novel techniques to prepare and study its ground state. Heisenberg Hamiltonians are readily available in cold atoms, however one big experimental challenge is to produce a Fermi gas at low enough temperature to enable the preparation of its ground state.

With the advent of new experimental methods to engineer artificial magnetic fields, and moreover experimentally simulate systems with band structures that have rich topological properties, a whole new branch of physics opportunities was opened, mainly due to the experimental possibilities which are not available in condensed matter systems. This thesis reports on the first experimental measurement of topological invariants in one-dimensional systems using a newly developed interferometric protocol for Bloch bands [51]. It also presents results on the measurement of chiral currents in a ladder system exposed to an artificial magnetic field, which exhibit some analogies with the Meissner effect in a type-II superconductor [52]. Furthermore, it describes the experimental creation and manipulation of minimum instances of resonating valence bond states in four-site plaquettes, which possess  $s$ - or  $d$ -wave symmetry [53].

### **Zak phases in a dimerized system**

If a quantum system described by a Hamiltonian that depends on an external parameter is adiabatically evolved such that it describes a closed path in parameter space, then the system returns to the original quantum state except for a phase. That phase has a dynamical component which is due to the intrinsic time-evolution governed by the Schrödinger equation, and a geometrical phase – the so-called Berry phase – which is determined only by the geometry of the path and does not depend on how the path is traversed [54]. This concept also applies to spatially periodic systems, where the states are labeled by the quasimomentum and the parameter space is given by the Brillouin

zone. The topological character of a Bloch band is defined by certain invariants that can be expressed in terms of the Berry phase acquired by a particle during the motion through the band. Non-trivial topological structures give rise to fundamental physical phenomena, as for example the integer quantum Hall effect [55] and topologically protected surface edge states in topological insulators [56, 57]. The most well-known topological invariant is the first Chern number, which is related to the Berry phase for a contour enclosing the Brillouin zone and determines the quantized value of the Hall conductivity of a filled two-dimensional band [55].

The measurement of topological invariants has so far only been realized in condensed matter systems, exploiting the relation between the Chern number and the Hall conductivity for a filled band introduced by Thouless-Kohmoto-Nightingale-De Nijs [55]. Cold atom systems offer a very clean playground for realizing Bloch bands, however, it is very challenging to realize transport measurements to extract the topological invariants as is typically done in condensed matter systems. For cold atoms one would need, for example, to connect a pair of reservoirs to the system in order to inject and retrieve the particles. Recently there have been some proposals of how to measure topological invariants using time-of-flight images [58, 59] or by measuring an anomalous velocity in the classical dynamics of lattices exposed to an external force [60, 61]. In this thesis, we present a novel method that enabled us to experimentally extract the Zak phase in a one-dimensional system [62]. The Zak phase is the Berry phase acquired during the adiabatic motion of a particle across the Brillouin zone, which can be viewed as an invariant that characterizes the topological properties of the band [63, 64].

In our experiment we implemented a protocol to measure the Zak phase on a one-dimensional chain with alternating coupling  $J$  and  $J'$  created by a superlattice potential. This dimerized system models a polyacetylene chain [65], and possesses two topologically distinct phases, characterized by the difference in their Zak phases equal to  $\pi$  [63]. In order to extract the phase difference we implemented a newly developed interferometric protocol, which combines Bloch oscillations and Ramsey interferometry [51]. The idea behind the protocol is to create a superposition state of two spin components that have opposite magnetic moments and to drive Bloch oscillations in the dimerized lattice, such that the two components explore the Bloch band in opposite directions. Then after half of a Bloch period, when the two components encounter each other again, one can extract their phase difference using Ramsey interferometry. As the two components explore the band in opposite directions, the difference of the phases they pick up is equal to the Zak phase of the band. In the experiment this interferometric idea was implemented in an extended protocol that involved the two lowest bands and a sudden change of dimerization, i.e. exchange of  $J$  and  $J'$ . These changes allowed to directly extract the phase difference between the two topological classes, which directly reflects their different topological character.

There is a strong interest in realizing topological bands with ultracold atoms, motivated by the possibility of measuring topological quantities for more general systems. An extension to higher dimensions of the protocol used here allows the measurement of other topologically relevant quantities [66], for example the  $\pi$  Berry flux concentrated around a Dirac cone [67, 68] or the Chern number of a band [60].

### **Chiral Meissner currents in a ladder-like lattice with magnetic flux**

When a superconductor is exposed to a weak external magnetic field, a current appears on its surface that fully screens the field in the core of the material. This is known as the Meissner effect and it is the hallmark feature of a superconductor subjected to a magnetic field [69, 70]. In the case of a type-II superconductor, for a field smaller than the critical value  $H_{c1}$  the surface currents fully screen the field, and the superconductor behaves as a perfect diamagnet. However, above the critical value the superconductor is unable to fully screen the applied field and an Abrikosov vortex lattice phase is formed in the system. Locally studying this phase transition, as well as the effect of interparticle interactions, is quite challenging in condensed matter, which motivates the simulation of systems that present similar features with ultracold atoms.

In order to measure an analogue of the Meissner effect, we implemented an optical lattice to realize an array of isolated bosonic ladders exposed to an artificially engineered magnetic field created by laser-assisted tunneling [39, 41, 42, 71]. In the experiment we prepared the ground state of the flux ladder and measured the probability current on either leg of the ladder by using a projection technique that instantaneously isolates pairs of sites. The subsequent evolution of the populations on the sites allows the extraction of the direction and strength of the average probability current on each leg. This idea is similar to suddenly blocking the flow of a stream. By monitoring the current strength as a function of the ratio of the transverse rung coupling to the coupling along the legs of the ladder, we find evidence for a "Meissner phase" with maximal chiral currents that are determined by the applied magnetic field. Below a critical coupling strength we find a decreasing current, in agreement with the transition to the vortex phase. The characteristic momentum distribution of the atoms in these two phases was studied in a second series of measurements, where the two phases could also be well distinguished. The flux ladder allows for not only the realization of a low-dimensional Meissner-like effect, but it can also be mapped into a spin-orbit coupled system, where the legs of the ladder play the role of pseudo spins.

### **Resonating valence bond states in four-site plaquettes**

For certain materials superconductivity occurs at particularly high temperatures, and

they are for this reason denominated high- $T_c$  superconductors. The standard theory to explain normal superconductivity, which describes the phenomenon as a result of the pairing of fermions forming the so-called Cooper pairs that behave as Bosons [70], cannot explain high- $T_c$  superconductivity [72]. It is believed that on these materials superconductivity occurs on planes where spin one-half electrons at half-filling are in a Mott insulating regime where they cannot tunnel, and the physics is dominated by the spin degrees of freedom described by an antiferromagnetic Heisenberg Hamiltonian [50]. In 1987, Anderson suggested that the mechanism leading to superconductivity could originate from the formation of a special state, called Resonating Valence Bond (RVB) state, that contains singlet pairs which become mobile and superconducting under doping. RVB states had previously been introduced in the context of chemical bonds by Pauling [73], and by Anderson [74] in condensed matter as candidates for ground state solutions of the antiferromagnetic Heisenberg Hamiltonian in frustrated triangular lattices.

In the experiment small instances of RVB states were created. An ultracold gas of bosonic atoms was loaded into a two-dimensional superlattice potential which creates an array of isolated four-site plaquettes. When populated with two internal states of the atoms, and when choosing appropriate lattice depths to enter the Mott regime at half-filling, the system is described by the Heisenberg Hamiltonian. In the total singlet subspace of the plaquette system, the Hilbert space is spanned by two RVB states, one with  $s$ -wave and the other with  $d$ -wave symmetry. In order to prepare these states, first a special filtering technique was employed to be able to extract the signal just from the plaquettes at half-filling, avoiding inconveniences produced by imperfect initial atom loading. Singlet Triplet Oscillations (STO) [75] and spin changing collisions [76] were then used to generate singlet states along the vertical bonds of the ladder, which were the initial states for the experiments. Different protocols that involved adiabatic paths or sudden changes of the vertical to horizontal coupling ratio in the ladder enabled us to prepare the two RVB states as well as to create a resonance between them. To probe these states STO and subsequent merging and band mapping techniques were used, with the results being in good agreement with the theoretical predictions.

A key motivation for the preparation of RVB states on plaquettes is that for fermionic atoms, one expects that the adiabatic connection of such isolated plaquettes could potentially lead to the creation of a macroscopic RVB state on the two-dimensional lattice, and furthermore be used to investigate the properties of the ground state of the Heisenberg Hamiltonian under doping [77–79].

---

## Outline

- In chapter 2 a brief overview of ultracold atoms in optical lattices is given, where the principle of Bose-Einstein condensation is introduced as well as the Bose-Hubbard model used to describe atoms in a lattice. The experimental realization of the optical lattices together with a short overview of the experimental setup is also provided.
- Chapter 3 provides the theoretical background of geometric phases in quantum mechanics and directly applies this theory to a periodic system. Here, the concept of Zak phases is first introduced and is linked to topological invariants on Bloch bands. Additionally, the relation between the Zak phase and the polarization change in solids is discussed.
- Chapter 4 starts with a description of the two main tools used to measure the Zak phase in optical lattices: Ramsey interferometry and Bloch oscillations. The implementation of a dimerized lattice that models polyacetylene or conjugated diatomic polymers is then explained. Then the protocol to measure the Zak phase difference between the two phases of a dimerized system is given and the main results of the experiment are presented. In the outlook strategies to use our protocol or extensions of it to two-dimensional systems are discussed.
- Chapter 5 deals with the phenomenon of the Meissner effect in superconductors and relates it to an analogous effect predicted in a ladder system exposed to a large magnetic field. This last system is described and modeled in detail and it is shown that it possesses two phases: a Meissner-like phase and a vortex phase. The currents along the legs of the ladder are defined and calculated, and it is demonstrated that they behave differently in the two phases. The chapter proceeds with the description of the momentum distribution of the atomic cloud after time-of-flight expansion, which provides another experimental observable that reveals the distinction between the two phases. Finally, a mapping from the ladder Hamiltonian to a system with spin-orbit coupling is given.
- In chapter 6 we report on the realization of a ladder with flux using artificially engineered magnetic fields and optical lattices. There the lattice shaking technique used to emulate magnetic fields on neutral atoms is discussed, and a projection method to determine the chiral currents along the legs of the ladder is described. The behavior of these currents is studied as a function of the leg to rung coupling strength ratio. The last part deals with the measurement of the momentum distribution of the cloud after free expansion.

- In chapter 7 the concept of a quantum resonance in the context of chemical structures is discussed, and in connection to that the definition of Resonating Valence Bond states (RVB) in condensed matter is reviewed. Here, the experimental results on the creation of minimum instances of RVB states on four-site plaquettes are presented, which consists of three parts: the measurement of a valence bond resonance and the creation of a RVB state with *s*-wave and with *d*-wave symmetry.

# Publications

This thesis is based on the following publications, which resulted from research conducted during the author's PhD.

- ***Observation of chiral currents with ultracold atoms in bosonic ladders***  
 Marcos Atala, Monika Aidelsburger, Michael Lohse, Julio T. Barreiro, Belén Paredes, Immanuel Bloch  
 Nature Physics **10**, 588-593 (2014).
- ***Direct measurement of the Zak phase in topological Bloch bands***  
 Marcos Atala\*, Monika Aidelsburger\*, Julio T. Barreiro, Dmitry Abanin, Takuya Kitagawa, Eugene Demler and Immanuel Bloch  
 Nature Physics **9**, 795-800 (2013).  
 \*These two authors contributed equally to this work.
- ***Experimental Realization of Plaquette Resonating Valence-Bond States with Ultracold Atoms in Optical Superlattices***  
 Sylvain Nascimbène, Yu-Ao Chen, Marcos Atala, Monika Aidelsburger, Stefan Trotzky, Belén Paredes, and Immanuel Bloch  
 Phys. Rev. Lett. **108**, 205301 (2012).

The following references have also been published during the course of this thesis:

- ***Revealing the Topology of Hofstadter Bands with Ultracold Atoms***  
 Monika Aidelsburger, Michael Lohse, Christian Schweizer, Marcos Atala, Julio T. Barreiro, Sylvain Nascimbène, Nigel Cooper, Immanuel Bloch and Nathan Goldman  
 arXiv: 1407.4205 (2014).
- ***Realization of the Hofstadter Hamiltonian with Ultracold Atoms in Optical Lattices***  
 Monika Aidelsburger, Marcos Atala, Michael Lohse, Julio T. Barreiro, Belén Paredes, and Immanuel Bloch  
 Phys. Rev. Lett. **111**, 185301 (2013).
- ***Experimental Realization of Strong Effective Magnetic Fields in an Optical Lattice***  
 Monika Aidelsburger, Marcos Atala, Sylvain Nascimbène, Stefan Trotzky, Yu-Ao Chen, and Immanuel Bloch  
 Phys. Rev. Lett. **107**, 255301 (2011).

- *Controlling Correlated Tunneling and Superexchange Interactions with ac-Driven Optical Lattices*

Yu-Ao Chen, Sylvain Nascimbène, Monika Aidelsburger, Marcos Atala, Stefan Trotzky, and Immanuel Bloch

Phys. Rev. Lett. **107**, 210405 (2011).

## Chapter 2

# Ultracold Bosons in optical lattices – Experimental setup

In our experiments a Bose-Einstein condensate of  $^{87}\text{Rb}$  atoms in optical lattices is used to realize different quantum models. In this chapter we give a brief description of the experimental setup employed to cool and trap the atoms and to create the optical lattices. Then, the basics of the theory of Bose-Einstein condensates is discussed, as well as the solutions to the Schrödinger equation for periodic potentials, where the theory of Bloch bands is reviewed. Towards the end of the chapter, interacting BECs in optical lattices are considered and the Bose-Hubbard model with its superfluid and Mott insulator phases are described.

### 2.1 Experimental setup

#### 2.1.1 Description of the machine and the cooling and trapping schemes

Our experimental machine was built around ten years ago in Munich by previous students, and it has been moved to Mainz and back to Munich during that time, without ever breaking the vacuum. The setup and the experimental sequence used to prepare an atomic condensate have been described in detail in several previous PhD and Diplom/Master thesis [80–87], and therefore we give here only a brief summary of them.

The experimental apparatus consists of two sections, one for the magneto optical trap (MOT) and a second one containing the glass cell for BEC production and experiments. These two sections are connected by a differential pumping tube and the whole apparatus was designed in this way in order to have a large optical access in the glass cell section. The MOT section consists of a vacuum chamber with a pressure of  $10^{-9}$  mbar, to which an oven is attached which releases the Rb atoms. The idea of the MOT is to capture atoms from the background gas and cool them down to  $\approx 20 \mu\text{K}$  by using six red

detuned circularly polarized laser beams, and simultaneously confining them using a magnetic trap created by a pair of coils in an anti-Helmholtz configuration [88–92]. The MOT sequence lasts nearly 15 s, and produces  $10^9$  atoms in the  $|^2S_{1/2}, F = 1, m_F = -1\rangle$  state of the  $^{87}\text{Rb}$  atoms.

Connected to the MOT chamber there is a magnetic transport system that brings the atoms to the glass cell. The transport setup consists of an L-shaped array of coils that are sequentially turned on and off in such a way that the minimum of the magnetic potential moves smoothly without strongly changing the volume of the trap to avoid losses. The transport takes in total around 4 s, and the atom losses are on the order of 10 – 20%.

At the end of the transport the atoms are transferred to a quadrupole trap (QT) inside the glass cell, where the pressure is  $\approx 10^{-11}$  mbar. Once in the QT, a blue detuned plug beam [6] is switched on and the first evaporative cooling process takes place [91]. In that process, called radio frequency evaporative cooling [1], radio frequency radiation that resonantly transfers atoms at the edge of the trap to untrapped hyperfine states is sent to remove the hottest atoms from the cloud. This causes a reduction in the temperature of the cloud as the remaining atoms thermalize. This process takes in total 8.5 s, and the function of the plug beam is to prevent the atoms to go to the center of the QT where the magnetic field is zero, avoiding in that way atom losses due to Majorana spin flips [93].

After the radio frequency evaporation the atoms are loaded into a dipole trap (DT) consisting of two red detuned laser beams with  $\lambda = 1064$  nm and a power of 4.5 W on each of them. During the loading, the QT field is ramped down to almost zero, and once the atoms are in the DT the plug beam is removed. To obtain a BEC, first gravity and QT potentials are used to tilt the trap and induce forced evaporation [94, 95], and then a further evaporation is performed by slowly decreasing the intensity of the dipole trap beams for 8.5 s [96, 97]. At the end of this process we end up with a pure BEC in the trap, at a temperature of  $\sim 20$  nK and containing about  $5 \times 10^5$  atoms. Finally the lattice beams are turned on according to the specific experiment to be realized. The entire cycle, starting from the MOT until the BEC production lasts 43 s. At the end of the experiment the atomic cloud is released from the trap and is imaged with a resonant beam (see appendix A).

### 2.1.2 Atom-light interaction: optical potentials

When neutral atoms are exposed to a light field two processes take place: a dissipative process where the atoms absorb photons and then release them by spontaneous scattering, and a conservative process where the light interacts with the induced dipole moment of the atom. While the latter one is the basic tool for creating trapping potentials, the former is unwanted due to the additional heating that it induces on the cloud

in the trap. The basic mechanism behind the optical trap relies on the induced dipole moment on the atoms due to the oscillating field [98–100]. This dipole moment can be written as

$$\mathbf{d} = \alpha(\omega)\mathbf{E}, \quad (2.1)$$

where  $\alpha$  is the complex polarizability of the atom,  $\mathbf{E}$  is the electric field and  $\omega$  its frequency. The effective dipole potential of the induced dipole moment is determined by time-averaging the potential energy  $\mathbf{d} \cdot \mathbf{E}$ , which results in

$$U_{dip} = -\text{Re}(\alpha(\omega))|\mathbf{E}|^2. \quad (2.2)$$

This is proportional to the intensity of the light field  $I = 1/2\epsilon_0 c |\mathbf{E}|^2$ . An explicit expression of the atomic polarizability can be obtained by modeling the atom as a two level system interacting with a classical radiation field [92, 99]. From that semi-classical model the following dipole potential is obtained

$$U_{dip}(\mathbf{r}) = \frac{3\pi c^2}{2\omega_0^3} \left( \frac{\Gamma}{\omega_0 - \omega} + \frac{\Gamma}{\omega_0 + \omega} \right) I(\mathbf{r}) \approx \frac{3\pi c^2}{2\omega_0^3} \frac{\Gamma}{\Delta} I(\mathbf{r}), \quad (2.3)$$

where  $\Gamma$  is the decay constant between the two states,  $\hbar\omega_0$  is the energy difference between the atomic levels and  $\Delta = \omega - \omega_0$  is the detuning of the light field. The right term is obtained by applying the rotating wave approximation, which is valid for a detuning much smaller than the transition frequency. This effect is called AC-Stark shift. By engineering spatially varying intensities in the light field one can create trapping potentials [101, 102]. Additionally, by choosing a positive or negative detuning one can make the potentials repulsive or attractive respectively.

The lowest energy levels for  $^{87}\text{Rb}$  are shown in Fig. 2.1. The transition lines  $D1 : ^2S_{1/2} \rightarrow ^2P_{1/2}$  and  $D2 : ^2S_{1/2} \rightarrow ^2P_{3/2}$  with transition frequencies  $\lambda_{D1} = 795 \text{ nm}$  and  $\lambda_{D2} = 780 \text{ nm}$  respectively are the most relevant for the optical potentials. The nuclear spin of this atomic species is  $3/2$ , which leads to a hyperfine splitting of the atomic ground state of about  $6.8 \text{ GHz}$  and a splitting of the excited state of a few hundred MHz. To consider all these atomic levels one has to use an extended model instead of the simple two-level system mentioned above. When the detuning is large compared to the hyperfine splitting one can derive an expression for the dipole potential that includes both lines [98, 99]

$$U_{dip}(\mathbf{r}) = \frac{\pi c^2}{2\omega_0^3} \left( \frac{\Gamma_{D2}(2 + \mathcal{P}g_F m_F)}{\Delta_{D2}} + \frac{\Gamma_{D1}(1 - \mathcal{P}g_F m_F)}{\Delta_{D1}} \right) I(\mathbf{r}). \quad (2.4)$$

Here  $\Delta_{D1/D2}$  are the detunings respect to the lines  $D1$  and  $D2$ ,  $g_F$  and  $m_F$  are the Landé factors and the magnetic number, and  $\mathcal{P}$  is a number that depends on the polarization

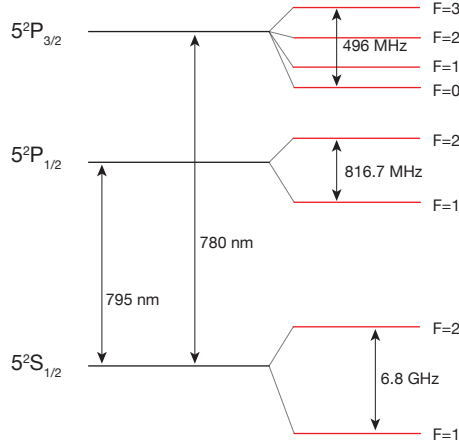


Figure 2.1: Energy levels of  $^{87}\text{Rb}$  [103]. The ground state is  $5^2S_{1/2}$ , and the  $D$  lines are  $D1 : ^2S_{1/2} \rightarrow ^2P_{1/2}$  and  $D2 : ^2S_{1/2} \rightarrow ^2P_{3/2}$  with transition frequencies  $\lambda_{D1} = 795 \text{ nm}$  and  $\lambda_{D2} = 780 \text{ nm}$ , respectively. The hyperfine lines with the corresponding energy differences are also illustrated.

of the field, which is equal to  $\pm 1$  for  $\sigma^\pm$  polarization and 0 for linearly polarized light. In our experiment only linearly polarized light is employed to create the optical traps.

The dissipative process mentioned at the beginning of the section originates from the imaginary part of the polarizability, which allows the atoms to absorb energy from the radiation field and reemit it as dipole radiation. This process can also be calculated using the two-level model discussed above, which for the case of large detuning yields [99]

$$\Gamma_{sc} \approx \frac{3\pi c^2}{2\hbar\omega_0^3} \left(\frac{\Gamma}{\Delta}\right)^2 I(\mathbf{r}). \quad (2.5)$$

Here again the rotating wave approximation has been applied. The energy acquired by the atoms due to spontaneous emission is typically very large compared to the trapping potential, therefore, in the experiments one has to decrease  $\Gamma_{sc}$  as much as possible in order to avoid undesired heating and subsequent atom losses. A comparison between the dipole potential given in Eq. 2.3 and  $\Gamma_{sc}$  shows that by increasing  $\Delta$  and  $I(\mathbf{r})$  one can decrease  $\Gamma_{sc}$  while still having a large amplitude  $U_{dip}$ .

### 2.1.3 Dipole Trap potential

According to Eq. 2.3, a beam with a spatially varying amplitude that is red detuned with respect to the atomic resonance ( $\Delta < 0$ ) can be used to trap atoms at the point of maximum intensity. A common optical trap is created by a Gaussian beam, which has an intensity profile given by

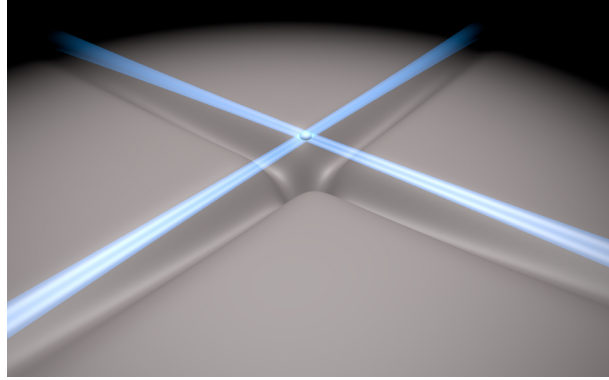


Figure 2.2: Crossed dipole trap. Two red detuned Gaussian beams cross at their focuses, where the atoms are located. The surface below illustrates the total dipole trap potential, with the potential minimum at the crossing point.

$$I(\mathbf{r}) = I_0 \left( \frac{w_b}{w(z)} \right)^2 e^{-\frac{2r^2}{w(z)^2}}, \quad (2.6)$$

where the beam propagates along the  $z$ -direction and  $r$  is the distance from that axis to the point  $\mathbf{r}$ . The quantity  $w_b$  is the beam waist, i.e. radius of the beam at its focus,  $I_0$  is the beam intensity at the point ( $r = 0, z = 0$ ) and

$$w(z) = w_b \sqrt{1 + \left( \frac{z}{z_R} \right)^2}, \quad z_R = \frac{\pi w_b^2}{\lambda}, \quad (2.7)$$

is the radius of the beam as a function of  $z$ . As it can be inferred from the equations above, the Gaussian beam has a maximum intensity at the point ( $r = 0, z = 0$ ) making them very suitable for optical traps.

In our experiment we use a crossed dipole trap potential created by two perpendicular Gaussian beams propagating along the  $x$ - and  $y$ -directions that cross at their focus position, as illustrated in Fig. 2.2. The wavelength of the beams is  $\lambda_{DT} = 1064 \text{ nm}$  and their waists are approximately  $160 \mu\text{m}$ , while the power in each arm is  $4.5 \text{ W}$ . The frequency of the laser beams is shifted by  $160 \text{ MHz}$  with respect to each other such that the atoms cannot follow the interference term and it averages out.

By approximating the potential at the bottom of the trap by a harmonic potential, one can define the trapping frequencies along the three axis as

$$V_{dip} \approx \frac{1}{2} m (\omega_x^2 + \omega_y^2 + \omega_z^2), \quad (2.8)$$

where  $m$  is the mass of the atoms. These frequencies depend on the beam parameters and power, and are important when the lattices are present because the number of

occupied lattice sites depends on them. As a general rule, the larger the frequencies the smaller the number of occupied sites. However, it also depends on other factors like the interaction energy. The calibrated values of the trap in our experiment are  $\omega_x \approx \omega_y \approx 2\pi * 25$  Hz and  $\omega_z \approx 2\pi * 35$  Hz, for a power of 0.4 W on each beam.

### 2.1.4 Lattice potentials

In all our experiments optical lattices are employed to reproduce the periodic potentials that the electrons experience in a solid crystal due to the ions. In order to create a lattice, two counter-propagating Gaussian beams with the same frequency are used, which interfere and create a one-dimensional periodic potential. The way this is realized in practice is by sending a forward beam towards the atoms, and retro-reflecting it with a mirror such that the retro beam travels back towards the atoms and both beams share the same path (see Fig. 2.3). The total potential seen by the atoms is

$$V_{latt}(\mathbf{r}) = V_0 e^{-\frac{2r^2}{w_b^2}} \cdot \sin^2(kz), \quad (2.9)$$

where  $V_0$  is the potential depth of the optical lattice,  $w_b$  is the beam waist,  $k = 2\pi/\lambda$  and  $\lambda$  is the wavelength of the lattice beam. Here the beams propagate along the  $z$  axis. For a red detuned beam, the atoms are attracted towards the zones of maximum intensity, while for a blue detuned one the opposite holds. The spacing between the different lattice sites is  $d = \lambda/2$ . Note that for red-detuned lasers the atoms are also confined in the transverse to the lattice directions due to the Gaussian shape of the beam.

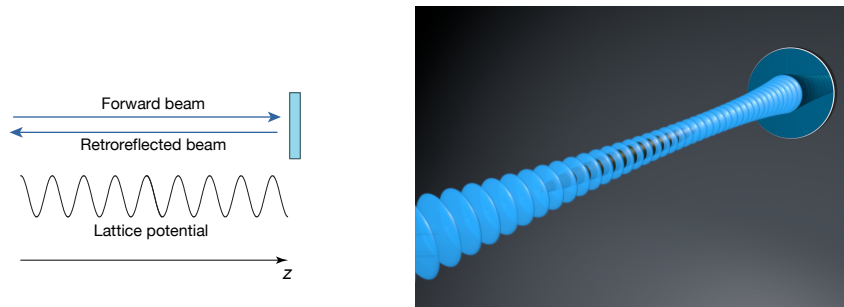


Figure 2.3: Lattice potential formed by the interference of two superimposed beams propagating in opposite directions. In our experiment we realize the lattice by retroreflecting a laser beam from a mirror as illustrated on the right. The atoms (black oval) are on the beam path and they experience the lattice potential.

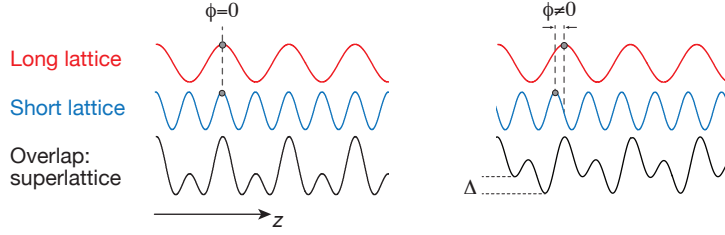


Figure 2.4: Superlattice potential created by the superposition of two single lattices of wavelengths  $\lambda_s$  and  $\lambda_l = 2\lambda_s$ . When the phase difference  $\phi = 0$  (left), the superlattice potential creates an array of double wells. The inter- and intra-well tunneling can be independently controlled by changing the amplitude of the short and long lattices. For  $\phi \neq 0$  (right) an energy offset is introduced in each double well.

An extension to three dimensions is also possible by employing three non-interfering mutually perpendicular lattices that cross at a single point. In that case, the total potential is the sum of the three individual potentials, resulting in a three-dimensional optical lattice (as with the dipole trap, the interference terms between the beams are averaged out by choosing a frequency difference of some tens of MHz between the beams).

In our setup we also use a special lattice configuration called superlattice. It consists of a superposition of a short and a long lattice with wavelengths  $\lambda_s$  and  $\lambda_l = 2\lambda_s$  respectively, which together give rise to the periodic potential

$$V_{dip}(\mathbf{r}) = V_l e^{-\frac{2r^2}{w_l^2}} \sin^2(k_l z + \phi/2) + V_s e^{-\frac{2r^2}{w_s^2}} \sin^2(2k_l z + \pi/2). \quad (2.10)$$

In this expression  $V_{l/s}$  are the strengths of the lattices,  $\phi$  indicates their relative phase and equal beam waist is assumed for both beams. Figure 2.4 displays some examples of different superlattice potentials that can be achieved by changing the relative amplitude of the lattices and the phase  $\phi$ . In general one can create arrays of symmetric/tilted double wells or one-dimensional lattices with staggered energy offset (see chapter 3). In the experiment two perpendicular superlattices are installed, which combined allow to create isolated four-site potentials (so-called plaquettes), or even a two-dimensional potential with energy staggering in both directions.

The wavelengths used in our experiment are  $\lambda_s = 767$  nm and  $\lambda_l = 1534$  nm, and the beam waists are  $\approx 140$   $\mu$ m. For the long lattice a fiber laser is used, whose frequency is stabilized with respect to a 767 nm Ti:Sa laser used to create the short lattice. In order to do this, the 1534 nm light is frequency doubled with a PPLN crystal in a single pass configuration and then it is offset locked to the Ti:Sa laser. By controlling the offset lock frequency one can slightly change the relation  $\lambda_l/\lambda_s = 2$  and with that control the relative phase  $\phi$  at the atom position, while still having a homogeneous lattice over the entire cloud (for details see [82]).

### 2.1.5 Running-wave beams for lattice shaking

In chapter 6 we will present an optical lattice system with an artificially engineered magnetic field. In order to simulate the field, a running-wave potential is used to modulate an underlying lattice structure and induce laser-assisted tunneling [42, 104]. This modulation modifies the tunneling terms between consecutive lattice sites making them complex such that an effective Hamiltonian that recreates the physics of a charged particle in a magnetic field is realized. In this section the details of the running-wave potential that was used to induce the magnetic field are described.

Consider two orthogonal beams propagating along the  $x$  and  $y$  direction with wavelengths  $\lambda_{rx} \approx \lambda_{ry} \approx 1534$  nm, that cross and interfere creating an optical lattice of the form

$$V_K(\mathbf{r}) = V_K^0 \cos^2(\mathbf{q} \cdot \mathbf{r}/2), \quad (2.11)$$

where  $\mathbf{q} = \mathbf{k}_x - \mathbf{k}_y$ , with  $\mathbf{k}_i = \hat{e}_i 2\pi/\lambda_{ri}$  the wavevectors of the beams, and  $V_K^0$  the lattice strength (see Fig. 2.5). If the wavelengths are chosen to be slightly different such that there is a frequency difference  $\omega = \omega_x - \omega_y$  between the two beams, then the total optical potential becomes

$$V_K(\mathbf{r}) = V_K^0 \cos^2(\mathbf{q} \cdot \mathbf{r}/2 + \omega t/2). \quad (2.12)$$

This is a running-wave potential, i.e. a lattice whose phase evolves linearly in time, which modulates the local potential on each lattice site as a function of time. The choice  $\lambda_{rx} \approx \lambda_{ry} \approx \lambda_l = 1534$  nm ensures that for a lattice spacing of  $\lambda_s/2$  the time-dependent modulation on each lattice site repeats every four sites in the  $x$  and  $y$  directions. It will be shown in chapter 6 that this ensures a magnetic flux of  $\pi/2$  per plaquette.

## 2.2 Single particle in periodic potentials

### 2.2.1 Quantum mechanics of a single particle in a periodic potential

In this section the solutions of the Schrödinger equation for a single particle moving on an infinitely long periodic potential are briefly discussed. Such a system underlies the basis of all the experiments presented in this thesis. For a detailed description we refer to the literature [105, 106].

Consider a single particle in a static three-dimensional periodic potential. Since the corresponding Hamiltonian does not have crossing terms that couple the different directions, one can solve the system independently for each direction. For a one-dimensional periodic system the Hamiltonian reads

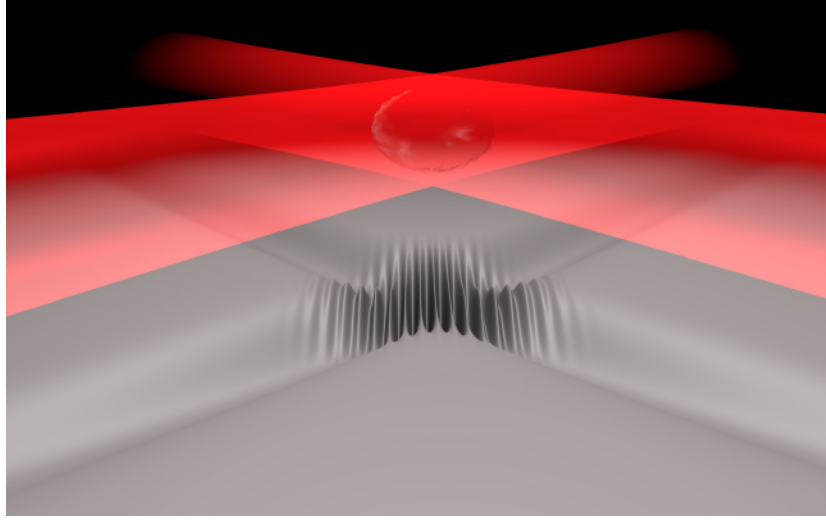


Figure 2.5: Lattice potential formed by the interference of two beams propagating in orthogonal directions. Both beams have a polarization perpendicular to the plane that they form, and interfere creating a lattice potential depicted in the figure by the surface. By introducing a small frequency difference between the two beams the standing wave forming the lattice becomes a running wave which can be used to periodically modulate the system.

$$\hat{H} = \frac{\hat{p}^2}{2m} + V_{lat}(x), \quad (2.13)$$

where  $\hat{p} = -i\hbar \partial_x$  is the momentum operator and  $V_{lat}(x)$  is the periodic potential with periodicity  $d$ , i.e.  $V_{lat}(x + d) = V_{lat}(x)$ . Due to the translational symmetry of  $\hat{H}$ , the Bloch theorem tells us that the eigenstates of the system can be written as

$$\psi_{n,k}(x) = e^{ikx} u_{n,k}(x), \quad (2.14)$$

where quantum number  $k$  is the so-called quasimomentum, which is contained in the first Brillouin zone, i.e.  $k \in (-\pi/d, \pi/d)$ , and  $n$  is a second quantum number denominated band index. The cell-periodic wavefunction  $u_{n,k}(x)$  satisfies

$$u_{n,k}(x + d) = u_{n,k}(x). \quad (2.15)$$

By inserting the ansatz given in Eq. 2.14 into the Schrödinger equation, one obtains the following eigenvalue equation for  $u_{n,k}(x)$

$$\hat{H}u_{n,k}(x) = \varepsilon_k^n u_{n,k}(x), \quad \text{with} \quad \hat{H} = \frac{(\hat{p} + \hbar k)^2}{2m} + V_{lat}(x), \quad (2.16)$$

where  $\varepsilon_k^n$  are the eigenenergies. For a non-vanishing potential  $V_{lat}(x)$  this equation gives as a result an energy spectrum which is separated in regions denominated energy bands,

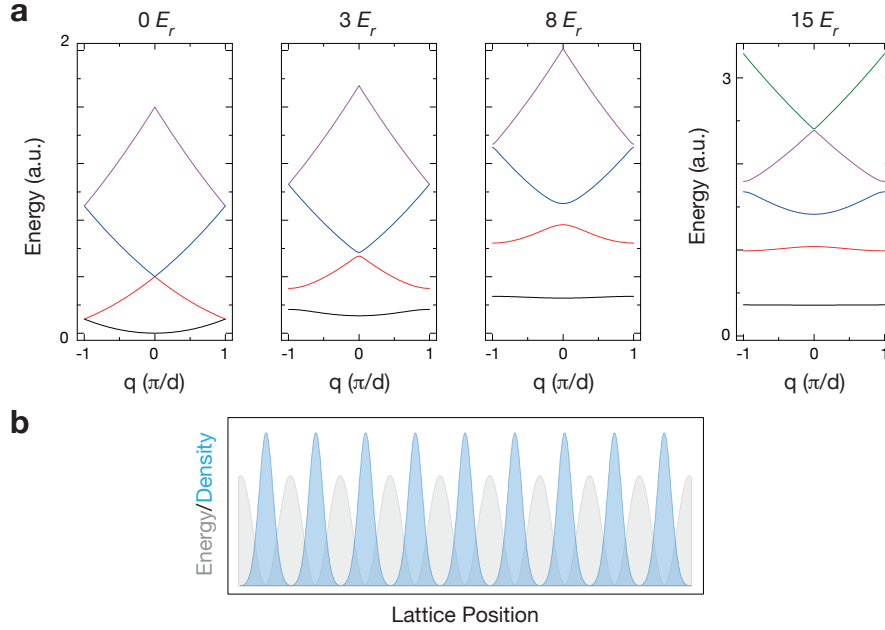


Figure 2.6: Energy bands and Bloch function density for a simple periodic potential. **(a)** Energy bands for different lattice depths  $V_0$ . For  $V_0 = 0 E_r$  the bands touch with each other and the energy corresponds to a free particle energy spectrum. As  $V_0$  is increased a gap opens at the edges of the Brillouin zone and the bands start to separate. For very large depths the lowest bands become flatter, converging towards harmonic oscillator levels. **(b)** Wavefunction density for the Bloch state  $\psi_{n=1,k=0}(x)$  for a lattice depth of  $8 E_r$ . The gray shaded area indicates the depth of the potential and the light blue shaded area the density.

and that are labeled by the band index  $n$ . The properties of these bands depend on the particular structure of the periodic potential.

Figure 2.6a shows the energy bands for the simplest case of a periodic potential of the form  $V_{lat}(x) = V_0 \cos^2(\pi x/d)$  for different lattice depths  $V_0$ . When  $V_0$  is zero the particle is in free space and the energy spectrum corresponds to a single parabola ( $\hbar k^2/2m$ ). As the depth is increased an energy gap opens up at the band edges, i.e.  $k = \pm\pi/d$ , and the energy spectrum is split into bands. The energy is continuous as a function of the quasimomentum  $k$  and each of these bands are isolated. The bandwidth of the lowest lying bands decreases exponentially with the lattice depth. In the limit of very high lattice depths each single well becomes more and more isolated and one can approximate the periodic potential as an harmonic potential on each well, resulting in an energy separation between the bands equal to  $\hbar\omega_h$ , where  $\omega_h$  is the harmonic frequency of the site. Figure 2.6b shows the density distribution  $|\psi_{n=1,k=0}(x)|^2$  of the Bloch function for the lowest band. Due to the periodic structure,  $\psi_{n=1,k=0}(x)$  extends over the entire system and its modulus also possesses the same periodicity.

A natural unit for the energy of a particle in the lattice is the recoil energy. It corresponds

to the kinetic energy that the particle acquires due to the recoil motion after emitting a photon of light. For a given lattice wavelength  $\lambda$  and mass  $m$ , the recoil energy is

$$E_r = \frac{h^2}{2m\lambda^2}. \quad (2.17)$$

This energy unit is also convenient for expressing the strength of a lattice, as it is the characteristic energy scale set by the periodicity.

In our experiments, periodic potentials are realized through the use of the already-mentioned optical lattices. While they in principle allow for the creation of a perfect periodic potential, due to the harmonic confinement given by the Gaussian mode of the beams, the potential is not an homogeneous and infinitely extended lattice, and therefore one has to include this information to obtain more quantitative results. Another point to consider is that the analysis presented here is only valid for non-interacting particles, which is not the case for  $^{87}\text{Rb}$  atoms. However, under some conditions explained later in the chapter one can make the interactions negligible.

### 2.2.2 Wannier functions

The Bloch functions are the eigenstates of a particle in a periodic potential, however, they are not convenient for the description of the system in terms of local operators on the different lattice sites. In that case a more appropriate basis set is formed by the Wannier functions, introduced by G. H. Wannier [107, 108]. They are an orthogonal set of functions that are localized on the different lattice sites. While they are not uniquely defined, the most common definition is [105]

$$w_{x_j}^n(x) = \frac{1}{\sqrt{N}} \sum_k e^{-ik \cdot x_j} \psi_{n,k}(x), \quad (2.18)$$

where  $x_j = jd$  with  $j$  integer are the lattice sites of the Bravais lattice where the Wannier functions are located,  $n$  is the band index,  $N$  is the length of the system and the sum runs over the  $N$  quasimomentum states  $k = 2\pi j / (Nd)$ ,  $j \in [1, N]$  uniformly distributed over the first Brillouin zone. Commonly one only refers to the Wannier functions of the first Bloch band, and leaves out the band index  $n$ .

The inverse relation is also valid, and one can write the Bloch functions as a superposition of Wannier states

$$\psi_{n,k}(x) = \frac{1}{\sqrt{N}} \sum_{x_j} e^{ik \cdot x_j} w_{x_j}^n(x). \quad (2.19)$$

These expressions are valid for the three independent directions, and the Wannier function on a single lattice site in the three dimensional system can be simply written as the product of the Wannier functions along the three directions.

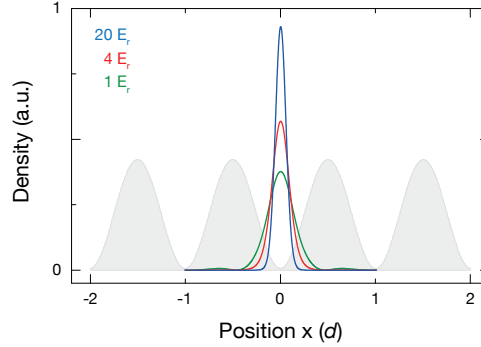


Figure 2.7: Wannier function density  $|w_{x_j}^1(x)|^2$  for the lowest band and for different lattice depths. The grey shaded area represents the periodic potential. As the depth is increased the Wannier functions become more localized on a single lattice site. The tunneling between consecutive sites depends on the overlap integral of the Wannier functions of the sites. Therefore, for large lattice depths the tunneling probability decreases.

The spatial extension of the Wannier function depends on the lattice depth. In Figure 2.7 one can see that as the depth is increased the Wannier function becomes more and more localized on a single lattice site. The tunneling between two consecutive lattice sites depends on the overlap of the respective Wannier functions (see section 2.3.3). Therefore, for larger depths the tunneling between lattice sites is strongly suppressed.

For periodic potentials with an internal structure, the Wannier functions as defined above are localized on the unit cell. In the case of the one-dimensional superlattice potential introduced in Fig. 2.4, the unit cell contains two different sites and the Wannier function extends over both sites simultaneously. In order to define a Wannier-like function that is localized on each single lattice site an extension of the definition is needed [109–112].

## 2.3 Ultracold atoms in periodic potentials

### 2.3.1 Bose-Einstein condensates of non-interacting particles

The theoretical prediction of Bose-Einstein condensates (BEC) dates from 1927 [113], when A. Einstein, following the work of N. Bose on the statistics of photons [114], predicted that below a critical temperature  $T_c$  a gas of non-interacting massive bosons would condense to the lowest single particle energy state. The first BEC for a dilute gas of cold atoms was realized in the groups of W. Ketterle and E. A. Cornell in 1995 using Sodium and Rubidium atoms, respectively [6, 7].

Statistical mechanics tells us that a thermalized system of non-interacting bosons has a mean occupation number of

$$P_n = \frac{1}{e^{(\varepsilon_n - \mu)/k_B T} - 1} \quad (2.20)$$

particles per single-particle eigenstate  $\varepsilon_n$ , where  $\mu$  and  $T$  are the chemical potential and temperature of the system, and  $k_B$  is the Boltzmann constant. The chemical potential is determined from the condition that the sum of the occupation numbers is equal to the total number of particles  $N$ , and it always lies below the minimum energy state  $\varepsilon_0$  of the system, such that  $P_n$  is always positive.

The principle of Bose-Einstein condensation can be understood from Eq. 2.20, and relies on the fact that  $\mu < \varepsilon_0$ . An intuitive explanation is as follows. First, let us split the number of particles  $N$  in two parts:

$$N = N_0 + N_{th}, \quad (2.21)$$

with  $N_0$  and  $N_{th}$  the number particles in the ground and the excited states, respectively. For a given temperature, the number of particles in the excited states increases with  $\mu$ , but it is bounded as  $\mu$  cannot exceed  $\varepsilon_0$ . If that bound is larger than the total number of particles  $N$ , then Eq. 2.21 can be satisfied for  $\mu < \varepsilon_0$  and the occupation  $N_0$  is not macroscopic, i.e.  $N_0/N \ll 1$ . However, if the bound is smaller than  $N$ , then  $\mu$  has to get closer to  $\varepsilon_0$ . Since  $N_0$  diverges as  $\mu \rightarrow \varepsilon_0$ , then the occupation number of the ground state will be macroscopic. The possibility of having a BEC depends strongly on the system, particularly its dimensionality and size, because it determines the single-particle density of states which ultimately indicates the relation between the chemical potential and  $N_{th}$ .

In our experiments a three-dimensional optical potential is used to create the trap where the atoms are located. In that case a BEC is possible, and when the interactions are neglected the transition temperature can be approximated by [1, 93, 115, 116]

$$k_B T_c \approx 0.94 \hbar \omega_T N^{1/3}, \quad (2.22)$$

where  $\omega_T = (\omega_x \omega_y \omega_z)^{1/3}$  is the geometrical mean of the trapping frequencies along the three directions. The fraction of atoms in the condensed state for this trap is

$$\frac{N_0(T)}{N} = 1 - \left( \frac{T}{T_c} \right)^3. \quad (2.23)$$

In the limit of zero temperature all the atoms occupy the lowest energy state. For the typical experimental parameters only a very small fraction of atoms populates the excited states and it can be safely neglected.

When all the atoms are condensed in the lowest energy state the many-body wavefunction is

$$\psi_{mb}(\mathbf{r}_1, \mathbf{r}_2, \dots, \mathbf{r}_N) = \prod_{i=1}^N \psi_0(\mathbf{r}_i), \quad (2.24)$$

where  $\psi_0(\mathbf{r}_i)$  is the ground state single-particle wavefunction. An alternative description can be made by introducing the macroscopic wavefunction or order parameter [117]

$$\psi(\mathbf{r}) = \sqrt{N} \psi_0(\mathbf{r}), \quad (2.25)$$

which is proportional to the ground state wavefunction, and is normalized to the total number of particles. The particle density is given by  $n(\mathbf{r}) = |\psi(\mathbf{r})|^2$ . Therefore, for non-interacting particles, by solving the single-particle Schrödinger equation of the system one can obtain the spatial density distribution.

### 2.3.2 Bose-Einstein condensates with weak interactions

In a real system atom-atom interactions due to van der Waals forces are also present, and at low densities they are dominated by binary collisions [118]. In the framework of quantum-mechanical scattering theory, for a given interatomic scattering potential  $V(r)$ , with  $\mathbf{r}$  denoting the relative distance between the two particles involved in the collision, one can use the following ansatz for the asymptotic wavefunction after the elastic scattering process [119]

$$\psi(r) \propto e^{ikz} + f(\theta) \frac{e^{ikr}}{r}, \quad (2.26)$$

which consists of an incoming plane wave and an outgoing spherical wave, whose amplitude is  $f(\theta)$ , and  $\theta$  is the scattering angle with respect to the direction of the incoming wave. Here  $k$  is the momentum of the incident wave and for simplicity we have assumed a spherically symmetric scattering potential  $V(r)$ , which is a very good approximation. It can be shown that  $f(\theta)$  admits the following decomposition in terms of its angular momentum components

$$f(\theta) = \sum_{\ell=0}^{\infty} (2\ell + 1) \left( \frac{e^{i2\delta_\ell} - 1}{2ik} \right) P_\ell(\cos(\theta)), \quad (2.27)$$

where  $\delta_\ell$  is the phase shift that is acquired by the angular momentum component  $\ell$  and  $P_\ell$  are the Legendre polynomials. The total cross section is

$$\sigma = \frac{4\pi}{k^2} \sum_{\ell=0}^{\infty} (2\ell + 1) \sin^2(\delta_\ell). \quad (2.28)$$

The phase shifts  $\delta_\ell$  are proportional to  $k^{2\ell+1}$ , and therefore for collisions with a small relative momentum only the component  $\ell = 0$  contributes to the cross section. This situation holds for cold atoms, due to the low temperature of the system. In that case

one can prove that  $f(\theta) = -a_s$ , where  $a_s$  is called the  $s$ -wave scattering length, and the total cross section simplifies to

$$\sigma \approx 4\pi a_s^2, \quad (2.29)$$

which is equal to the cross section of a hard sphere with radius  $a_s$ . For indistinguishable bosonic particles the cross section is modified due to the spatially symmetric wavefunction, and takes the value  $\sigma \approx 8\pi a_s^2$ . Therefore, the interaction is fully characterized by the scattering length  $a_s$ . Its experimental value for the state used in our experiment ( $|F = 1, m_F = -1\rangle$ ) is  $a_s = 103 \pm 5 a_0$ , where  $a_0 = 0.05292$  nm is the Bohr radius [120].

The interatomic potentials are very complex and can only be calculated for a very few systems. However, due to the low momentum of the interacting particles, their de Broglie wavelength is very large and the details of the particular potential are not important. Then, the interatomic potential can be replaced by the effective contact interaction

$$V(\mathbf{r}) = \frac{4\pi\hbar^2 a_s}{m} \delta^3(\mathbf{r}) = g \cdot \delta^3(\mathbf{r}), \quad (2.30)$$

where  $m$  is the mass of the atoms and  $\mathbf{r}$  their relative position. Here  $g = 4\pi\hbar^2 a_s / m$  is called the coupling constant. The diluteness of the sample is characterized by the ratio  $|a_s|^3 n$ , where  $n$  is the density of atoms. Typically that value is on the order of  $10^{-3}$ .

The Hamiltonian of  $N$  interacting bosons confined by an external potential  $V_e(\mathbf{r})$  and with an interatomic interaction potential  $V(\mathbf{r})$  is

$$\begin{aligned} \hat{H} &= \int d\mathbf{r} \hat{\psi}^\dagger(\mathbf{r}) \left( -\frac{\hbar^2}{2m} \nabla^2 + V_e(\mathbf{r}) \right) \hat{\psi}(\mathbf{r}) \\ &+ \frac{1}{2} \int d\mathbf{r} d\mathbf{r}' \hat{\psi}^\dagger(\mathbf{r}) \hat{\psi}^\dagger(\mathbf{r}') V(\mathbf{r} - \mathbf{r}') \hat{\psi}(\mathbf{r}) \hat{\psi}(\mathbf{r}'), \end{aligned} \quad (2.31)$$

where  $\hat{\psi}^\dagger(\mathbf{r})$  is the bosonic field operator that creates a particle at position  $\mathbf{r}$ . By replacing  $V(\mathbf{r})$  by the interatomic potential given in Eq. 2.30 one obtains for the interaction component

$$g \int d\mathbf{r} \hat{\psi}^\dagger(\mathbf{r}) \hat{\psi}^\dagger(\mathbf{r}) \hat{\psi}(\mathbf{r}) \hat{\psi}(\mathbf{r}). \quad (2.32)$$

Due to the high diluteness of the system, one can solve the problem using a mean field approximation. This was done by Bogoliubov in 1947 [121]. In that description the bosonic field operator is decomposed into two parts

$$\hat{\psi}(\mathbf{r}, t) = \psi(\mathbf{r}, t) + \delta\hat{\psi}(\mathbf{r}, t), \quad (2.33)$$

where  $\psi(\mathbf{r}, t) = \langle \hat{\psi}(\mathbf{r}, t) \rangle$  is the condensate contribution to the field operator and the second component is called the fluctuating field operator and corresponds to the non-condensed part. Neglecting the last term, one obtains the following modified Schrödinger equation for  $\psi(\mathbf{r}, t)$

$$i\hbar \frac{\partial}{\partial t} \psi(\mathbf{r}, t) = \left( -\frac{\hbar^2 \nabla^2}{2m} + V_e(\mathbf{r}) + g|\psi(\mathbf{r}, t)|^2 \right) \psi(\mathbf{r}, t). \quad (2.34)$$

This non-linear equation is known as the Gross-Pitaevskii equation [122, 123]. Here, the original interacting term has been replaced by the local wavefunction density  $|\psi(\mathbf{r}, t)|^2$ .

Due to the interaction term, the ground state solution of Eq. 2.34 is not the same as the ground state of the non-interacting Hamiltonian, but it also has an overlap with the excited states. This effect is called quantum depletion and is negligible for the experiments presented in this thesis.

### 2.3.3 The Bose-Hubbard model

A gas of ultracold bosonic atoms with weak interactions placed in an optical lattice is well described by the Bose-Hubbard model, which is a widely used model in solid state physics [19, 20]. The starting point to derive the Hamiltonian of this model is Eq. 2.31 with  $V_e(\mathbf{r}) = V_{lat}(\mathbf{r}) = V_0 e^{-2r^2/w_b^2} \cdot \sin^2(kz)$ :

$$\begin{aligned} \hat{H} &= \int d\mathbf{r} \hat{\psi}^\dagger(\mathbf{r}) \left( -\frac{\hbar^2}{2m} \nabla^2 + V_{lat}(\mathbf{r}) \right) \hat{\psi}(\mathbf{r}) \\ &+ \frac{1}{2} \int d\mathbf{r} d\mathbf{r}' \hat{\psi}^\dagger(\mathbf{r}) \hat{\psi}^\dagger(\mathbf{r}') V(\mathbf{r} - \mathbf{r}') \hat{\psi}(\mathbf{r}) \hat{\psi}(\mathbf{r}'). \end{aligned} \quad (2.35)$$

The bosonic field operator can be expanded in the site-localized Wannier base

$$\hat{\psi}^\dagger(\mathbf{r}) = \sum_i \hat{a}_i^\dagger w_{\mathbf{r}_i}(\mathbf{r}), \quad (2.36)$$

where  $\mathbf{r}_i$  are the sites of the Bravais lattice and  $\hat{a}_i^\dagger$  are the bosonic creation operators for a particle on the site  $i$ , which obey the canonical commutation relation  $[\hat{a}_i, \hat{a}_j^\dagger] = \delta_{ij}$ , and  $w_{\mathbf{r}_i}(\mathbf{r})$  are the Wannier functions of the lowest Bloch band on the site  $\mathbf{r}_i$ . This expansion assumes that all the contributions from the higher bands are being neglected, something that is only valid if the energies involved in the dynamics of the system are much smaller than the energy gap to the second band. For very low lattice depths ( $V_0 < 5 E_r$ ) the tunneling processes to the second and third lattice sites are non-negligible [124] and one should also consider the Wannier functions corresponding to higher Bloch bands.

In the tight-binding approximation the Wannier functions overlap at different sites just enough to correct the picture of isolated particles, but without fully losing the

picture of localized states. The standard approach is to only consider the overlap between nearest-neighbor sites. Under this approximation, one obtains the Bose-Hubbard Hamiltonian by inserting expression 2.36 into Eq. 2.35:

$$\hat{H} = -J \sum_{\langle i,j \rangle} \hat{a}_i^\dagger \hat{a}_j + \sum_i \frac{1}{2} U \hat{n}_i (\hat{n}_i - 1), \quad (2.37)$$

where  $\hat{n}_i = \hat{a}_i^\dagger \hat{a}_i$  is the number operator on the  $i$ th site and the first sum runs over neighboring lattice sites. The first term is the kinetic energy, describing the hopping between neighboring lattice sites whose amplitude is given by

$$J = - \int d\mathbf{r}^3 w_{\mathbf{r}_i}^*(\mathbf{r}) \left( -\frac{\hbar^2 \nabla^2}{2m} + V_{lat}(\mathbf{r}) \right) w_{\mathbf{r}_j}(\mathbf{r}). \quad (2.38)$$

Due to the discrete translation symmetry of the system, the value of  $J$  is independent of the pair of neighboring lattice sites  $\langle i, j \rangle$ . However, for more general lattice geometries it can depend on the particular sites considered.

The second term is the on-site interaction energy. Its amplitude  $U$  corresponds to the repulsion energy between two atoms on a single lattice site, and is given by

$$U = \frac{4\pi\hbar^2 a_s}{m} \int d\mathbf{r}^3 |w_{\mathbf{r}_i}(\mathbf{r})|^4. \quad (2.39)$$

Note that for the geometry considered here, the Wannier functions are the same for every site, and therefore the interaction energy does not depend on the site  $\mathbf{r}_i$ .

For a three-dimensional system the total Wannier function is equal to the product of the independent Wannier functions along the three directions

$$w_{\mathbf{r}_i}(\mathbf{r}) = w_{x_i}(x) w_{y_i}(y) w_{z_i}(z), \quad (2.40)$$

and the total interaction energy can be written as

$$U = \frac{4\pi\hbar^2 a_s}{m} \int d\mathbf{r}^3 |w_{x_i}(x)|^4 |w_{y_i}(y)|^4 |w_{z_i}(z)|^4. \quad (2.41)$$

By decreasing the lattice strength along one or two directions, or by fully removing the lattice and leaving only the remaining harmonic confinement one can decrease the value of the total interaction energy as this increases the extent of the Wannier function. For the experiments presented in this thesis it was often necessary to have negligible interactions. In order to achieve that we followed the latter approach. Another possibility to suppress interactions is to decrease the scattering length  $a_s$ . This can be done by using Feshbach resonances [16], where  $a_s$  can be almost arbitrarily controlled by an external magnetic field. However, for  $^{87}\text{Rb}$  this is not simple, because its resonances are very narrow and at very high magnetic fields, requiring an exceptional relative stability of the field [125].

The single-particle eigenenergies of the Bose-Hubbard model are given by

$$\varepsilon_k = -2J \cos(kd), \quad (2.42)$$

resulting in a bandwidth of  $4J$ . Here  $k \in (-\pi/d, \pi/d)$  is the quasimomentum of the states. For a finite size system,  $k$  is discretized according to  $k = n2\pi/(dM)$ , where  $M$  is the total number of lattice sites.

The lattice potential created by interfering Gaussian beams also contains a weak three-dimensional harmonic confinement, which was not taken into account for the derivation of Eq. 2.37. When it is included, an extra term appears in the Bose-Hubbard Hamiltonian that is important for the experiment as it influences the spatial extent of the system:

$$\hat{H} = -J \sum_{\langle i,j \rangle} \hat{a}_i^\dagger \hat{a}_j + \sum_i \frac{1}{2} U \hat{n}_i (\hat{n}_i - 1) + \sum_i (\varepsilon_i - \mu) \hat{n}_i. \quad (2.43)$$

Here  $\varepsilon_i = V_{trap}(\mathbf{r}_i)$  is the energy offset given by the harmonic trap, and  $\mu$  is the chemical potential which fixes the total number of atoms in the system.

### 2.3.4 Superfluid and Mott insulator states

The Bose-Hubbard Hamiltonian without external confinement given in Eq. 2.37 is a system where two competing energy scales are present, given by  $U$  and  $J$ . These two parameters determine the kinetic and interaction energies, and therefore they affect the properties of the ground state. In this section we will briefly describe the eigenstate solutions of the Hamiltonian in the two extrema  $J/U \ll 1$  and  $J/U \gg 1$  for a system size of  $M$  lattice sites, and for  $N$  atoms.

#### Superfluid state

In the limit  $J/U \gg 1$  the interaction term can be neglected and the ground state of the system corresponds to all the atoms occupying the Bloch state for quasimomentum  $k = 0$  (Bose-Einstein condensation in the  $k = 0$  state), as it minimizes the interaction energy:

$$|\psi\rangle = \frac{1}{\sqrt{N!}} \left( \hat{a}_{k=0}^\dagger \right)^N |0\rangle, \quad (2.44)$$

where  $|0\rangle$  is the vacuum state and the Bloch creation operator for  $k = 0$  is given by

$$\hat{a}_{k=0}^\dagger = \frac{1}{\sqrt{M}} \sum_i^M \hat{a}_i^\dagger. \quad (2.45)$$

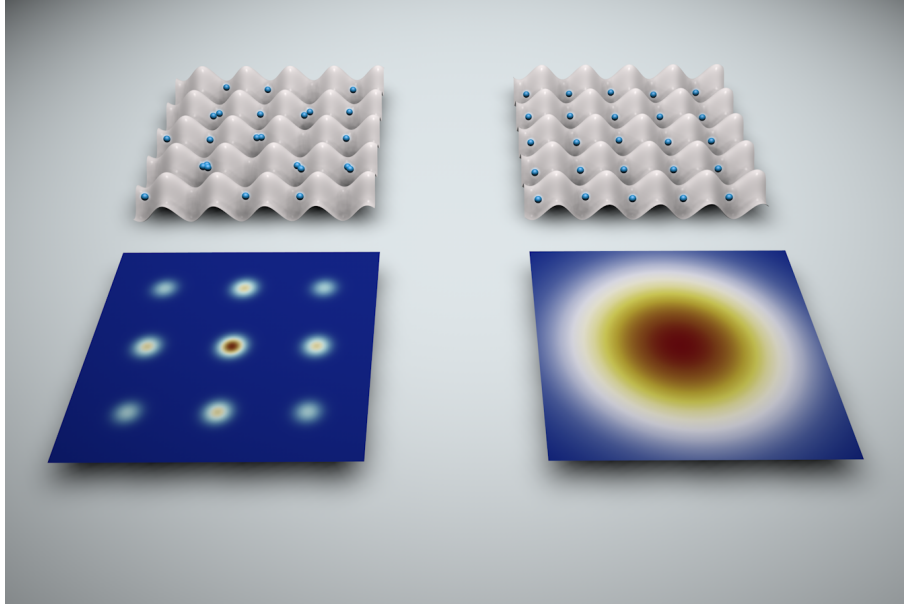


Figure 2.8: Representation of superfluid and Mott insulator states on a two-dimensional lattice. In the superfluid state (left back) the occupation number on each lattice site is randomly distributed and has a mean value of  $\bar{n} = N/M$ , where  $N$  and  $M$  are the number of atoms and lattice sites, respectively. The coherence through the system is large, resulting in a momentum distribution with characteristic momentum peaks (left front) determined by the lattice periodicity. For the Mott insulator state (right back) the occupation number on each site is equal to  $\bar{n}$  on each site. The coherences are lost and the resulting momentum distribution shows no coherences (right front). The momentum distributions have been independently normalized to the maximum value.

In this state the particles are delocalized over the entire lattice and have the same phase. For large atom number, the state  $|\psi\rangle$  is indistinguishable from the product of site-localized coherent (Glauber) states [126]

$$|\psi\rangle = \prod_i^M \exp\left(\sqrt{\frac{N}{M}} \hat{a}_i^\dagger\right) |0\rangle_i = \prod_i^M |\alpha_i\rangle. \quad (2.46)$$

The coherent states  $|\alpha_i\rangle$  are eigenstates of the operator  $\hat{a}_i$  with complex eigenvalue  $\alpha_i$ . The number of particles on each lattice sites has a Poissonian distribution and an average occupation number of  $\bar{n} \approx N/M$  particles per site (see Fig. 2.8). This eigenstate is known as superfluid state.

### Mott insulator state

In the limit of dominating interactions  $J/U \ll 1$ , the system minimizes the interaction energy by decreasing the particle number fluctuations per site. Then, the particles are

localized on the lattice sites, and the ground state can be written as a product of local Fock states

$$|\psi\rangle = \left( \prod_i^M (\hat{a}_i^\dagger)^{\tilde{n}} \right)^N, \quad (2.47)$$

where  $\tilde{n} = N/M$  is the mean occupation number, which in this case is considered to be an integer. The number of particles per lattice site is fixed and equal to  $\tilde{n}$ , and it has zero variance.

As the occupation per lattice site is fixed, the conjugate variable, i.e. the phase on each lattice site, is random. Therefore, when the atomic cloud in the Mott state is released from the trap no interference occurs (see Fig. 2.8), contrarily to the superfluid state where strong interference peaks are expected (see also appendix A).

The quantum phase transition from the superfluid to the Mott insulator state depends on the filling fraction and dimensions of the system. For a filling of  $\tilde{n} = 1$ , mean field theory predicts that the transition point occurs at  $U/J = 5.8 \cdot z$ , where  $z$  is the number of nearest neighbors of the site [20, 127, 128]. Beyond mean-field theory, Quantum Monte Carlo simulations predict the transition point at  $U/J = 4.79 \cdot z$  for a three-dimensional optical lattice [129].

## Chapter 3

# Theory of Zak phase and its relation to topological invariants

In this chapter, we review the concept of geometric phases in quantum mechanics (Berry phases) and their relation to topological quantities. In particular, we discuss geometric phases in periodic systems and give the definition of the Zak phase – the Berry phase gained during the adiabatic motion of a particle across the Brillouin zone. In connection to our experiments, we study the solutions of a dimerized system which consists of a linear chain with alternating coupling strengths. This system models polyacetylene, and when an on-site energy staggering along the chain is introduced, it models conjugated diatomic polymers. At the end of the chapter we examine the relation between the Zak phase and the theory of bulk polarization.

### 3.1 Geometric phases in quantum mechanics

A type of evolution of a physical system which is often of interest in physics is one in which the state of the system returns to its original state after the evolution. We call this a cyclic evolution. Any vector quantity that is transported around a closed loop may acquire an angle with respect to its original orientation after completing the cycle. This rotation angle is of geometrical origin, and is known as a geometrical phase. The Foucault pendulum, originally conceived to demonstrate the rotation of the Earth, is perhaps the most familiar classical system for which one can observe a geometric phase. The pendulum, fixed at a point on the Earth, constantly oscillates on its plane of oscillation (see Fig. 3.1a). As the Earth rotates, the center of mass position of the pendulum is transported in space, describing a closed trajectory which is defined by the latitude at which it is located on the Earth. After one day the pendulum is back to the original point in space it started. However, its plane of oscillation has rotated by one half of the solid angle subtended at the Earth's centre by the described spatial trajectory (see

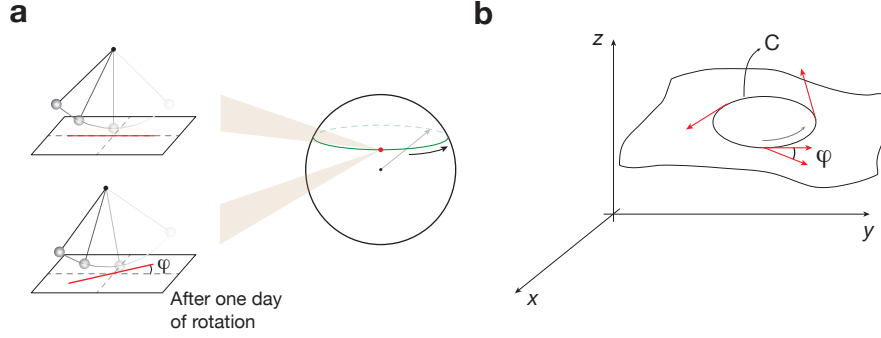


Figure 3.1: Geometric phases. **(a)** Geometric phase in the Foucault pendulum. After one day of the Earth's rotation, the pendulum is transported around a closed path defined by the latitude line at which it was initially located. When the pendulum returns, it has been rotated by the angle  $\varphi$  given by half of the solid angle enclosed by the path. **(b)** Geometric phases on general surfaces. Consider a vector that is parallel transported around a closed path on a surface. After completing the path the vector returns to the starting point, but rotated by an angle  $\varphi$  with respect to its original orientation. This angle is known as the geometric phase, and depends on the path and surface on which the transport takes place.

Fig. 3.1a). This angle is the geometric phase corresponding to the closed path around which the transport took place. The concept of a geometric phase can be generalized to any vectorial quantity, which when transported around a closed path on a surface, returns rotated by a geometric phase after it completes the path (see Fig. 3.1b). The way in which the vector is transported is called parallel transport, and roughly speaking it means that as the vector is moved along the curve it stays parallel with respect to itself and its magnitude stays constant (a proper definition involves the concept of "connection", which is a common geometrical quantity that indicates how to transport vectors [130–132]).

In quantum mechanics the concept of geometric phases was introduced by M. Berry in 1984, when he considered the problem of the adiabatic transport of a quantum system around a closed loop in parameter space [54]. In order to explain his work, consider a Hamiltonian that depends on some parameters  $\mathbf{R} = (X, Y, \dots)$ , and whose  $\mathbf{R}$ -dependent eigenstates and eigenvalues are denoted by  $|n(\mathbf{R})\rangle$  and  $E_n(\mathbf{R})$ , respectively. If initially the state of the system is  $|n(\mathbf{R}_0)\rangle$ , and the parameter  $\mathbf{R}$  is adiabatically moved around a closed path  $C$  in parameter space, then the state will evolve according to the Schrödinger equation

$$\hat{H}(\mathbf{R}(t)) |\psi(t)\rangle = i\hbar \frac{d|\psi(t)\rangle}{dt}, \quad (3.1)$$

where  $\mathbf{R}(t)$  parametrizes the path and  $\mathbf{R}(t = 0) = \mathbf{R}_0$ . According to the adiabatic theorem, if the eigenstate  $|n(\mathbf{R})\rangle$  is not degenerate along the entire path, then the system will always stay in that eigenstate [133–135]. Therefore, as the Hamiltonian is moved in

parameter space, the wavefunction up to some phase will be  $|\psi(t)\rangle = |n(\mathbf{R}(t))\rangle$ .

At  $t = t_f$  the full path  $C$  is completed and  $\mathbf{R}(t_f) = \mathbf{R}_0$ . Then the system has returned to its original state  $|n(\mathbf{R}_0)\rangle$  but differs by a phase given by

$$\exp\left\{\frac{-i}{\hbar} \int_0^{t_f} dt' E_n(\mathbf{R}(t'))\right\} \exp\{i\gamma_n(C)\}. \quad (3.2)$$

The first term is the dynamical phase factor, which is due to the time evolution of the eigenstates determined by their energy. The second term is the geometric phase, which is commonly referred to as the Berry phase. One can prove that this phase is geometric in nature because it does not depend on the rate at which the path is travelled, it is independent of the particular Hamiltonian  $H(\mathbf{R})$  chosen to produce the motion along the path and because it is not conditioned to the particular way in which the eigenstates  $|n(\mathbf{R})\rangle$  are defined, i.e. it is not important what phases are chosen in the definition of  $|n(\mathbf{R})\rangle$ .

The Berry phase  $\gamma_n$  for the closed path  $C$  can be expressed as

$$\gamma_n(C) = \oint_C \mathcal{A}_n \cdot d\mathbf{R}, \quad (3.3)$$

where the quantity  $\mathcal{A}_n = i \langle n(\mathbf{R}) | \nabla_{\mathbf{R}} | n(\mathbf{R}) \rangle$  is named the Berry connection.

A gauge transformation of the form  $|n(\mathbf{R})\rangle \rightarrow e^{i\alpha(\mathbf{R})} |n(\mathbf{R})\rangle$  modifies the Berry connection by adding a new term:

$$\mathcal{A}_n \rightarrow \mathcal{A}_n + \nabla_{\mathbf{R}} \alpha(\mathbf{R}). \quad (3.4)$$

Even though the last expression shows a gauge dependence of the Berry connection, the geometric phase is gauge independent. This can be better seen by using Stoke's theorem and rewriting Eq. 3.3 as follows

$$\gamma_n(C) = \int_S \boldsymbol{\Omega}_n \cdot d\mathbf{S}, \quad (3.5)$$

where  $\boldsymbol{\Omega}_n = \nabla_{\mathbf{R}} \times \mathcal{A}_n$  is called the Berry curvature and  $S$  is any surface whose boundary is  $C$ . This shows that  $\gamma_n(C)$  is gauge independent because  $\nabla_{\mathbf{R}} \times \nabla_{\mathbf{R}} \alpha(\mathbf{R}) = 0$ . Note that all the expressions above have been written assuming a three-dimensional parameter space. However, they can be all generalized for any dimensionality of  $\mathbf{R}$ .

The Berry curvature can also be expressed as follows

$$\boldsymbol{\Omega}_n = -\text{Im} \sum_{n' \neq n} \frac{\langle n | \nabla \hat{H} | n' \rangle \times \langle n' | \nabla \hat{H} | n \rangle}{(E_n - E_{n'})^2}, \quad (3.6)$$

where for clarity reasons we have dropped the argument  $\mathbf{R}$  [54]. This expression, which is also gauge independent, will be used later in the chapter when calculating Berry phases.

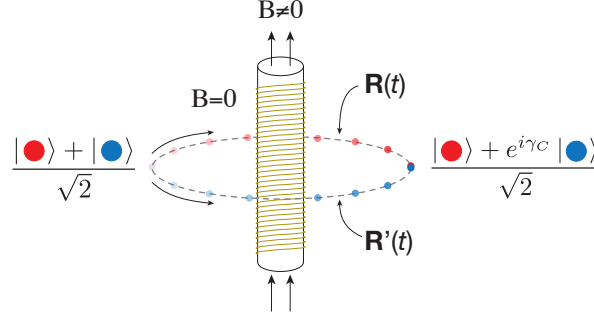


Figure 3.2: Schematic of the Aharonov-Bohm effect. A charged particle is initially located on the left side and is coherently split into two components (blue and red balls). Each component travels on independent paths, denoted by  $\mathbf{R}(t)$  and  $\mathbf{R}'(t)$ , which together enclose the coil. The coil produces a magnetic field  $\mathbf{B} \neq 0$  inside of it and  $\mathbf{B} = 0$  outside. At the end of the trajectories the components are recombined and there is a phase difference  $\gamma_C$  which is the geometric phase associated with the total flux enclosed by the combined path  $\mathbf{R}(t) + \mathbf{R}'(t)$ .

The geometrical phase could seem unimportant as it is simply a phase factor that multiplies the state. Due to that, it did not receive proper attention for many years. However, this phase has physical consequences that can be seen experimentally using interferometric techniques. One way, for example, is to coherently split the wavefunction of the system in two parts, and send one part through the path  $\mathbf{R}(t)$  and the other through  $\mathbf{R}'(t)$ , where  $\mathbf{R}(0) = \mathbf{R}'(0)$  and  $\mathbf{R}(t_f) = \mathbf{R}'(t_f)$ . The difference between the adiabatic phases picked up by the two components is equal to the total geometric phase associated with the closed loop enclosed by the paths  $\mathbf{R}(t)$  and  $\mathbf{R}'(t)$ . A typical example of this is the Aharonov-Bohm effect [136] (see Fig. 3.2), which has already been observed in several experiments [137, 138]. There, a coherently-split wavefunction of a charged particle is sent through two paths surrounding a solenoid and forming a closed loop, where the solenoid contains a magnetic field inside and a negligible one outside. Despite the fact that the two trajectories are in a field-free region, when the two parts meet on the right side they have a phase difference associated with the total magnetic flux contained in the loop, which is a geometric phase.

To conclude this section and gain a more practical interpretation of the Berry phase, we will consider the example of a single spin-1/2 particle in an external magnetic field. The Hamiltonian of the system reads

$$\hat{H}_s = \mathbf{B}\sigma, \quad (3.7)$$

where  $\mathbf{B}$  is the magnetic field and  $\sigma$  denote the Pauli matrices (units have been omitted). The eigenstates of the system are  $|\pm\mathbf{B}\rangle$ , defined by

$$\mathbf{B}\sigma|+\mathbf{B}\rangle = B|+\mathbf{B}\rangle \quad \text{and} \quad \mathbf{B}\sigma|-\mathbf{B}\rangle = -B|-\mathbf{B}\rangle, \quad (3.8)$$

with  $B = |\mathbf{B}|$ .

Now consider the parameter space defined by the three components of the magnetic field, and take a closed curve  $C$  in that space such that along the curve  $\mathbf{B} \neq 0$  (the point  $\mathbf{B} = 0$  has to be avoided because there the system becomes degenerate). A general expression of the Berry phase for the curve  $C$  will be calculated. The Berry connection for the state  $|-\mathbf{B}\rangle$  is

$$\mathcal{A}(\mathbf{B}) = i\langle -\mathbf{B} | \nabla_{\mathbf{B}} | -\mathbf{B} \rangle. \quad (3.9)$$

Using Eq. 3.5 and the fact that  $\Omega(\mathbf{B}) = \nabla_{\mathbf{B}} \times \mathcal{A}(\mathbf{B})$ , we arrive at

$$\gamma_-(C) = \int_S \Omega(\mathbf{B}) \cdot d\mathbf{S}, \quad (3.10)$$

where  $S$  is any surface whose boundary is the loop  $C$ . To calculate  $\Omega(\mathbf{B})$  one could use the gauge dependent expression for the Berry connection given in 3.9, or directly the gauge independent Berry curvature from Eq. 3.6. Using the latter, one obtains the following Berry curvature

$$\Omega(\mathbf{B}) = -\frac{\mathbf{B}}{B} \frac{1}{2B^2}. \quad (3.11)$$

This result is very particular, because it shows that  $\Omega(\mathbf{B})$  in  $\mathbf{B}$ -space takes the same form as the field generated by a point-like charge at the origin in real space. Therefore, the Berry phase of the closed loop  $C$  is the flux of the monopole field at the origin through the surface  $S$ , which corresponds to half of the solid angle subtended by the curve (similar to the case of the Foucault pendulum discussed at the beginning of the chapter).

Geometric phases have already been predicted and observed for several systems, ranging from molecular physics [139–141], to NMR and spins [142–144] and light polarization [145–148]. After the work of Berry, the concept of geometric phase was extended to the case of non-adiabatic transport [149, 150], and an even more general geometrical interpretation of the concept was recognized by Simon [151].

## 3.2 Geometric phases in condensed matter: topological invariants

### 3.2.1 Geometric phases in periodic systems - the Zak phase

The general form of a single-particle spatially periodic Hamiltonian can be written as

$$\hat{H} = \frac{\hat{p}^2}{2m} + V(\mathbf{r}), \quad (3.12)$$

where  $V(\mathbf{r} + \mathbf{d}) = V(\mathbf{r})$  is the periodic potential and  $\mathbf{d} = (n_x d_x, n_y d_y, n_z d_z)$  is any Bravais lattice vector, with  $n_\mu$  an integer and  $\mu \in (x, y, z)$ . It was already discussed in chapter 2 that the eigenstates of  $\hat{H}$  are the Bloch waves  $\psi_{n\mathbf{k}}(\mathbf{r})$ , which satisfy the boundary condition

$$\psi_{n,\mathbf{k}}(\mathbf{r} + \mathbf{d}) = e^{i\mathbf{k}\cdot\mathbf{d}}\psi_{n,\mathbf{k}}(\mathbf{r}), \quad (3.13)$$

where  $n$  is the Bloch band index and  $k_\mu \in (-\pi/d_\mu, \pi/d_\mu)$  is the quasimomentum. It was also shown that the Bloch waves can be written as  $\psi_{n,\mathbf{k}}(\mathbf{r}) = e^{i\mathbf{k}\mathbf{r}}u_{n,\mathbf{k}}(\mathbf{r})$ , where the cell-periodic wavefunction  $u_{n,\mathbf{k}}(\mathbf{r})$  satisfies

$$u_{n,\mathbf{k}}(\mathbf{r} + \mathbf{d}) = u_{n,\mathbf{k}}(\mathbf{r}) \quad \text{and} \quad \hat{H}(\mathbf{k})u_{n,\mathbf{k}}(\mathbf{r}) = \varepsilon_{n,\mathbf{k}} u_{n,\mathbf{k}}(\mathbf{r}), \quad (3.14)$$

with

$$\hat{H}(\mathbf{k}) = \frac{(\hat{\mathbf{p}} + \hbar\mathbf{k})^2}{2m} + V(\mathbf{r}). \quad (3.15)$$

The Hamiltonian given above depends on the parameter  $\mathbf{k}$ , and therefore one can use the  $\mathbf{k}$ -space as a parameter space for the Berry phase formulation given in the previous section and calculate geometric phases corresponding to closed loops in  $\mathbf{k}$ -space. This space, which is determined by the Brillouin zone, is periodic in the sense that any pair of points connected by a reciprocal lattice vector are the same, i.e.  $k_\mu$  and  $k_\mu + 2\pi/d_\mu$  refer to the same quasimomentum. For example, for a one-dimensional system the space has a circular shape, and for the case of a two-dimensional system it has a toroidal shape.

In terms of the Bloch states the Berry connection and curvature are expressed as

$$\mathcal{A}_n(\mathbf{k}) = i \langle u_{n,\mathbf{k}} | \nabla_{\mathbf{k}} | u_{n,\mathbf{k}} \rangle \quad \text{and} \quad \Omega_{n,\mathbf{k}} = i \nabla_{\mathbf{k}} \times \langle u_{n,\mathbf{k}} | \nabla_{\mathbf{k}} | u_{n,\mathbf{k}} \rangle. \quad (3.16)$$

The Berry phase that is acquired for a straight path across the Brillouin zone connecting the points  $\mathbf{k}_0$  and  $\mathbf{k}_1 = \mathbf{k}_0 + \mathbf{G}$  with  $\mathbf{G}$  a reciprocal lattice vector, is known as the Zak phase [62]:

$$\varphi_{Zak,n} = i \int_{\mathbf{k}_0}^{\mathbf{k}_1} \langle u_{n,\mathbf{k}} | \nabla_{\mathbf{k}} | u_{n,\mathbf{k}} \rangle \cdot d\mathbf{k}. \quad (3.17)$$

Note that this phase can only be defined due to the toroidal topology of the system, otherwise it would not be possible to complete a straight closed path. It also has an important role in the topology of the Bloch bands, as it will be discussed later in this chapter.

The Zak phase characterizes the topological properties of the Bloch bands, and is related for example to the formation of Wannier stark ladders [108], as well as to the polarization change in solids (see section 3.4). In general, non-trivial Zak phases underlie the existence of protected edge states (see 3.3.4 and [63, 64]), fermion number fractionalization [65, 152, 153] and irrationally charged domain walls between topologically distinct one-dimensional solids [154, 155].

### 3.2.2 Gauge dependence of the Zak phase

In his paper on the geometric phases in periodic systems [62] J. Zak showed that the Zak phase is a gauge independent quantity in the sense that it is not affected by the choice of the phase factors in the definition of  $|u_{n,k}\rangle$ . For the demonstration, he considered the transformed set of states  $|u'_{n,k}\rangle = e^{i\phi(k)} |u_{n,k}\rangle$  and calculated the new Zak phase

$$\begin{aligned}
\varphi'_{Zak,n} &= i \int_{-G/2}^{G/2} \langle u'_{n,k} | \nabla_k | u'_{n,k} \rangle \cdot dk \\
&= i \int_{-G/2}^{G/2} e^{-i\phi(k)} \langle u_{n,k} | \nabla_k (e^{i\phi(k)} | u_{n,k} \rangle) \cdot dk \\
&= i \int_{-G/2}^{G/2} \langle u_{n,k} | \nabla_k | u_{n,k} \rangle \cdot dk + i \int_{-G/2}^{G/2} (i \nabla_k \phi(k)) \langle u_{n,k} | u_{n,k} \rangle \cdot dk \\
&= \varphi_{Zak,n} + \phi(-G/2) - \phi(G/2).
\end{aligned} \tag{3.18}$$

Here  $G = 2\pi/d$ , where  $d$  is the periodicity of the system. Due to the periodicity of  $k$ -space, the points  $-G/2$  and  $G/2$  are the same, and the phase  $\phi(k)$  must satisfy  $\phi(-G/2) - \phi(G/2) = 2\pi m$ , with  $m$  an integer. Therefore, up to a phase  $2\pi m$ ,  $\varphi'_{Zak,n} = \varphi_{Zak,n}$ , proving that the Zak phase is gauge invariant. This proof holds for a one-dimensional system, and it can be readily extended to higher dimensions.

On the other hand, the Zak phase as defined in Eq. 3.17 is a gauge-dependent quantity in the sense that it depends on the choice of the unit cell, i.e. the choice of the origin of the coordinate system. The demonstration for a one-dimensional system is as follows (the extension for higher dimensions is straightforward). From the Bloch theorem we know that the Bloch functions satisfy  $\psi_{n,k}(x) = e^{-ikx} u_{n,k}(x)$ . Therefore, if the origin of coordinates is shifted by  $x_0$ , then the cell-periodic wavefunction transforms as

$$\begin{aligned}
\psi'_{n,k}(x) &= e^{-ikx} u'_{n,k}(x) = \psi_{n,k}(x + x_0) = e^{-ik(x+x_0)} u_{n,k}(x + x_0) \\
&\rightarrow u'_{n,k}(x) = e^{-ikx_0} u_{n,k}(x + x_0).
\end{aligned} \tag{3.19}$$

By substituting this into Eq. 3.17, one obtains for the Zak phase

$$\varphi'_{Zak,n} = i \int_{-G/2}^{G/2} \langle u'_{n,k} | \partial_k | u'_{n,k} \rangle \cdot dk = i \int_{-G/2}^{G/2} \langle u_{n,k} | \partial_k | u_{n,k} \rangle \cdot dk + Gx_0. \tag{3.20}$$

This general result shows that the value of the Zak phase depends on the origin of the coordinate system.

### 3.2.3 The Chern number of Bloch bands

Consider an  $\mathbf{R}$ -dependent Hamiltonian, such as the one described in section 3.1, and assume that the  $n$ -th eigenstate is non-degenerate for all  $\mathbf{R}$  in a closed surface  $S$ . The Chern number is defined as the integral of the Berry curvature over this surface:

$$C_n = -\frac{1}{2\pi} \oint_S \Omega_n(\mathbf{R}) d\mathbf{S}. \quad (3.21)$$

It can be shown that this quantity is an integer, and that its value is robust against small changes of either the Hamiltonian or the surface. The Chern number is a topological invariant and in order to change its value one has to modify the Hamiltonian such that the energy becomes degenerate at some point on the surface [56, 60, 156, 157].

In periodic systems, the explicit form of the Chern number of the  $n$ -th Bloch band is

$$C_n = -\frac{1}{2\pi} \iint dk_x dk_y \left( \frac{\partial \mathcal{A}_{y,n}}{\partial k_x} - \frac{\partial \mathcal{A}_{x,n}}{\partial k_y} \right), \quad (3.22)$$

where the integration surface  $S$  is the entire Brillouin zone.

A hallmark manifestation of the Chern number is in the integer quantum Hall effect (IQHE) [158], as explained by Thouless, Kohmoto, Nightingale and den Nijs in their seminal paper from 1982 [55]. They found that when a lattice filled with fermions is exposed to a commensurate magnetic field, i.e. one with rational flux per unit cell so that the Bloch theorem still applies, the Hall conductivity can be expressed as

$$\sigma_{x,y} = \frac{e^2}{h} \sum_n C_n, \quad (3.23)$$

where the sum runs over the occupied bands and the Fermi energy lies in a gap.

It is important to note that the Chern number cannot be directly calculated by integrating the Berry connection along the boundaries of the Brillouin zone. This is because the Berry connection is a single valued vector field and therefore, given the torus topology of the Brillouin zone, the line integral vanishes. This does not mean that the Chern number is zero, but rather that the Stokes' theorem cannot be applied to go from the surface integral to the Berry phase line integral. The reason is that the Berry connection could have vortex points on which the phase is not well defined and depends on the direction from which one approaches the point. Therefore, a non-zero Chern number indicates that the energy eigenstate  $|u_{n,\mathbf{k}}\rangle$  cannot be defined smoothly over the entire Brillouin zone, i.e. there is no way of defining the phase of  $|u_{n,\mathbf{k}}\rangle$  such that it is smooth everywhere. In that sense, the Chern number indicates the number of vortices in the phase of  $|u_{n,\mathbf{k}}\rangle$  in the Brillouin zone.

### 3.3 The SSH and Rice-Mele models and their Zak phases

#### 3.3.1 The SSH and Rice-Mele models

A polyacetylene molecule, formed by the repetition of the unit ( $\text{C}_2\text{H}_2$ ), consists of a one-dimensional array of carbon atoms with alternating single and double bonds between them (see Fig. 3.3a). Su, Schrieffer and Heeger (SSH), when studying solitons in this molecule [65], described the system with the Hamiltonian

$$\hat{H}_{SSH} = - \sum_n \left( J \hat{a}_n^\dagger \hat{b}_n + J' \hat{a}_n^\dagger \hat{b}_{n-1} + \text{h.c.} \right), \quad (3.24)$$

where  $J, J'$  denote modulated tunneling amplitudes within the unit cell and  $\hat{a}_n^\dagger (\hat{b}_n^\dagger)$  are the particle creation operators for an atom on the sublattice  $a_n (b_n)$  in the  $n$ th lattice cell (see Fig 3.3a). As it will be shown in section 3.3.2, this system is known to possess two different topological classes:  $D1$ , which corresponds to  $J > J'$ , and  $D2$  for  $J < J'$ .

An extension of this system was studied by Rice and Mele, where they modeled linearly conjugated diatomic polymers as a one-dimensional array of atoms with alternating single and double bonds between them and with an energy staggering along the array [155]:

$$\hat{H}_{RM} = - \sum_n \left( J \hat{a}_n^\dagger \hat{b}_n + J' \hat{a}_n^\dagger \hat{b}_{n-1} + \text{h.c.} \right) + \Delta \sum_n \left( \hat{a}_n^\dagger \hat{a}_n - \hat{b}_n^\dagger \hat{b}_n \right). \quad (3.25)$$

Here  $2\Delta$  is the energy offset between neighboring lattice sites (see Fig. 3.3b). Note that when  $\Delta = 0$ , one recovers the SSH Hamiltonian.

From the symmetry of the Hamiltonian, which possesses two types of lattice sites denoted by  $a_n$  and  $b_n$ , we write the ansatz for the eigenstates of  $\hat{H}_{RM}$  as a superposition of two Bloch waves of the form

$$\psi_k(x) = e^{ikx} u_k(x) = \sum_n \alpha_k e^{ikx_n} w_a(x - x_n) + \beta_k e^{ik(x_n + d/2)} w_b(x - x_n - d/2), \quad (3.26)$$

where  $x_n = nd$  with  $n$  an integer and  $d$  the size of the unit cell, and  $w_{a,b}(x)$  are the Wannier functions for  $a_n$  and  $b_n$  sites, respectively [108]. Here  $k \in (-G/2, G/2)$  is the quasimomentum, where  $G = 2\pi/d$  is the reciprocal lattice vector. In this notation, the cell-periodic wavefunction  $u_k$  can be viewed as a two-component spinor  $\mathbf{u}_k = (\alpha_k, \beta_k)$ .

Solving the Schrödinger equation for the proposed wavefunction leads to the following eigenvalue equation for  $\alpha_k$  and  $\beta_k$ :

$$\begin{bmatrix} \Delta & -\rho_k \\ -\rho_k^* & -\Delta \end{bmatrix} \begin{pmatrix} \alpha_k \\ \beta_k \end{pmatrix} = \tilde{\epsilon}_k \begin{pmatrix} \alpha_k \\ \beta_k \end{pmatrix}, \quad (3.27)$$

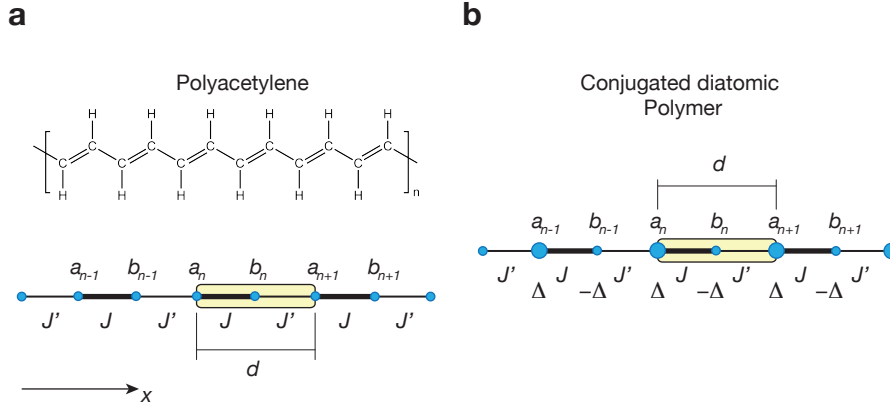


Figure 3.3: SSH and Rice-Mele dimerized models. **(a)** Polyacetylene molecule, where each line represents a single/double bond. This configuration can be modeled by the SSH Hamiltonian as shown in the figure. **(b)** Representation of the conjugate diatomic polymer system, described by the Rice-Mele Hamiltonian. The yellow boxes in (a) and (b) denote the unit cell of size  $d$ .

where

$$\rho_k = J e^{ikd/2} + J' e^{-ikd/2} = |\varepsilon_k| e^{i\theta_k}, \quad (3.28)$$

$$|\varepsilon_k| = \sqrt{J^2 + J'^2 + 2JJ' \cos(kd)}. \quad (3.29)$$

These equations can be also expressed in terms of the Hamiltonian

$$\hat{H}(k) = \mathbf{B}(k) \sigma, \quad \hat{H}(k) \mathbf{u}_k = \tilde{\varepsilon}_k \mathbf{u}_k, \quad (3.30)$$

with the "magnetic field"  $\mathbf{B}(k) = ((J + J') \cos(kd/2), -(J - J') \sin(kd/2), \Delta)$ . The solution of this equation yields two energy bands

$$\tilde{\varepsilon}_k = \pm |\mathbf{B}(k)| = \pm \sqrt{\Delta^2 + \varepsilon_k^2}. \quad (3.31)$$

Figure 3.4 displays the energy bands for two different sets of parameters. For  $\Delta = 0$ , the band gap at the band edges ( $k = \pm G/2$ ) is given by  $2|J - J'|$ , therefore for  $J = J'$  the gap closes. This can be understood when considering that for  $J = J'$  there is only one kind of lattice site, and the periodicity of the system is  $d/2$  instead of  $d$ , resulting in a single energy band in a doubled Brillouin zone, i.e. with  $k \in (-G, G)$  instead of  $k \in (-G/2, G/2)$ .

The eigenstates  $\mathbf{u}_k = (\alpha_k, \beta_k)$  can be calculated from Eq. 3.27, and must satisfy the conditions  $\alpha_{k+G} = \alpha_k$  and  $\beta_{k+G} = -\beta_k$  (see appendix D). The solutions for the lower and upper bands can be chosen as follows:

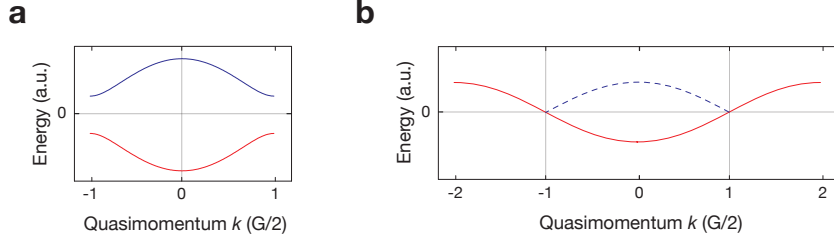


Figure 3.4: Energy bands. **(a)** Lower and upper energy bands for the Rice-Mele Hamiltonian. **(b)** Energy bands for  $\Delta = 0$  and  $J = J'$ . In this case there is a single energy band and the quasimomentum extends from  $-G$  to  $G$ .

$$\begin{aligned} \mathbf{u}_{-,k} &= \begin{pmatrix} \alpha_{-,k} \\ \beta_{-,k} \end{pmatrix} = \begin{pmatrix} \sin \frac{\gamma_k}{2} \\ \cos \frac{\gamma_k}{2} e^{-i\theta_k} \end{pmatrix}, \\ \mathbf{u}_{+,k} &= \begin{pmatrix} \alpha_{+,k} \\ \beta_{+,k} \end{pmatrix} = \begin{pmatrix} -\cos \frac{\gamma_k}{2} \\ \sin \frac{\gamma_k}{2} e^{-i\theta_k} \end{pmatrix}, \end{aligned} \quad (3.32)$$

where  $\gamma_k$  and  $\theta_k$  are given by

$$\begin{aligned} \gamma_k &= \arctan \frac{\varepsilon_k}{\Delta}, \\ \theta_k &= \arctan \frac{(J - J') \sin(kd/2)}{(J + J') \cos(kd/2)}. \end{aligned} \quad (3.33)$$

Here the expression for  $\theta_k$  was obtained from Eq. 3.28. Figure 3.5 displays  $\gamma_k$  and  $\theta_k$  for different parameters. There one can see that for  $\Delta = 0$  both Bloch wave components have the same weight for every  $k$ .

In the case of the SSH model, i.e.  $\Delta = 0$ , the eigenstates of the system satisfy the symmetry relation  $\theta_k^{D1} = -\theta_k^{D2}$  when the dimerization is changed from  $D1$  to  $D2$  (see Fig. 3.5b). Using this relation at  $k = \pm G/2$  one can see that  $\alpha_{-, \pm G/2}^{D1} = -\alpha_{+, \pm G/2}^{D2}$  and  $\beta_{-, \pm G/2}^{D1} = -\beta_{+, \pm G/2}^{D2}$ , which means that at the edges of the Brillouin zone

$$\mathbf{u}_{-, \pm G/2}^{D1} = -\mathbf{u}_{+, \pm G/2}^{D2}. \quad (3.34)$$

In the next chapter it will be shown how this relation was used in the experiment to extract the difference between the Zak phases for the two dimerized configurations.

### 3.3.2 The Zak phase in the SSH and Rice-Mele models

Using Eq. 3.17 one can calculate the Zak phase for the Rice-Mele model. In terms of  $\mathbf{u}_k = (\alpha_k, \beta_k)$  it takes the form

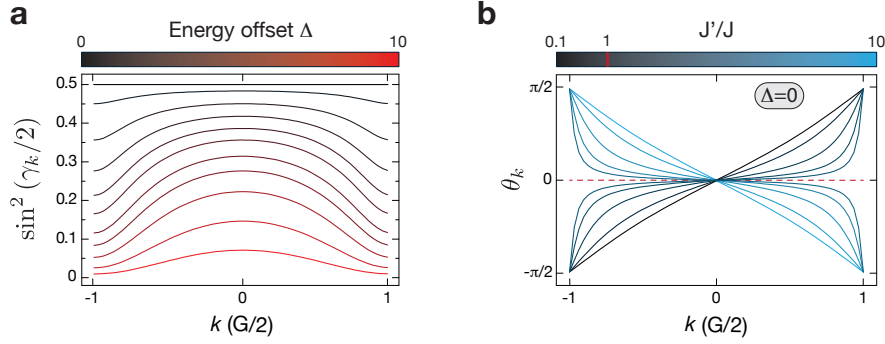


Figure 3.5: Eigenvector angles plotted for different parameters. **(a)** Population fraction  $\sin(\gamma_k/2)^2$  of the Bloch wave corresponding to the  $a_n$  sites for  $J = 1$ ,  $J' = 2$  and different values of  $\Delta$ . At  $\Delta = 0$  the fraction is one half, and it tends to zero as  $\Delta$  is increased. **(b)** Angle  $\theta_k$  for  $\Delta = 0$  as a function of  $J'/J$ . In the case  $J' = J$  the periodicity of the system is changed and the solution is not valid (see Fig. 3.4b).

$$\varphi_{Zak} = i \int_{-G/2}^{G/2} (\alpha_k^* \partial_k \alpha_k + \beta_k^* \partial_k \beta_k) dk. \quad (3.35)$$

By inserting the expressions for the eigenvectors (Eq. 3.32) one obtains the Zak phase for the lower and upper bands

$$\begin{aligned} \varphi_{Zak,-}(\Delta) &= \int_{-G/2}^{G/2} \cos^2 \frac{\gamma_k}{2} \partial_k \theta_k dk, \\ \varphi_{Zak,+}(\Delta) &= \int_{-G/2}^{G/2} \sin^2 \frac{\gamma_k}{2} \partial_k \theta_k dk. \end{aligned} \quad (3.36)$$

For the SSH Hamiltonian, where  $\Delta = 0$ , the expressions for the Zak phase take the form

$$\begin{aligned} \varphi_{Zak,-}(\Delta = 0) &= \frac{1}{2} \int_{-G/2}^{G/2} \partial_k \theta_k dk = \frac{1}{2} (\theta_{G/2} - \theta_{-G/2}), \\ \varphi_{Zak,+}(\Delta = 0) &= \frac{1}{2} \int_{-G/2}^{G/2} \partial_k \theta_k dk = \frac{1}{2} (\theta_{G/2} - \theta_{-G/2}). \end{aligned} \quad (3.37)$$

Therefore the Zak phase is the same for the upper and lower band. This can also be understood in terms of the spinors  $\mathbf{u}_k$  (see Fig. 3.6a,b). As the two states in the upper and lower bands are orthogonal, they point in opposite directions and therefore exhibit the same winding when the quasimomentum is varied adiabatically. The Zak phases for the upper and lower band are thus identical  $\varphi_{Zak}^{D1} = \pi/2$ . However, when the dimerization is changed from configuration  $D1$  to  $D2$  the corresponding geometric phase changes to  $\varphi_{Zak}^{D2} = -\pi/2$ , because of the opposite winding of the state with quasimomentum  $k$ . In

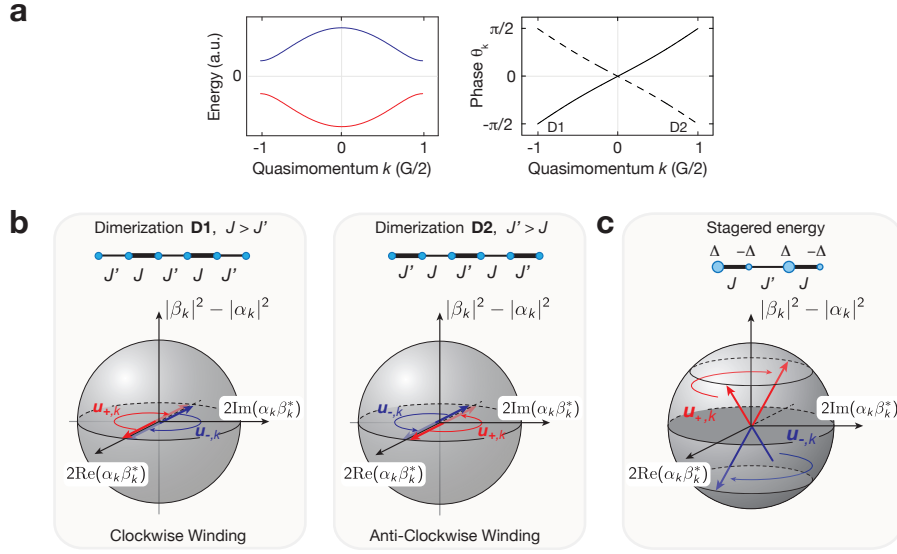


Figure 3.6: Energy Bands and topology of the SSH and Rice-Mele models. **(a)** Exemplary curves for the lower and upper energy bands (red and blue lines) and phase  $\theta_k$  for dimerization D1 and D2 (solid and dashed line) as a function of quasimomentum  $k$ . **(b)** Pseudo-spin representation of the eigenstates  $\mathbf{u}_{\mp, k}$  of the upper and lower energy bands for the two dimerization configurations D1 and D2. The pseudo-spin vectors  $\mathbf{u}_{\mp, k}$  point in opposite directions and exhibit the same sense of rotation (winding) with quasimomentum  $k$ . In the phase D1 (D2)  $\mathbf{u}_{\mp, k}$  evolve (anti-)clockwise and therefore exhibit opposite winding. **(c)** Pseudo-spin representation of the eigenstates  $\mathbf{u}_{\mp, k}$  of the upper and lower energy bands when the on-site energy staggering  $\Delta$  is present. In that case the pseudo-spin vectors move away from the equatorial plane and the value of the Zak phase is fractional in units of  $\pi$ .

the next sections it will be shown that the distinct topological character of the phases D1 and D2 is reflected in the difference of their Zak phases, for which  $\delta\varphi_{Zak} = \pi$ .

When the on-site energies are tuned to be different ( $\Delta \neq 0$ ), the system models a linearly conjugated diatomic polymer. In this case the energy offset displaces the pseudo-spin Bloch vectors away from the equatorial plane (see Fig. 3.6c) and the Zak phase is fractional in units of  $\pi$  and depends on the offset  $\Delta$  and the band index. Figure 3.7 displays the Zak phase for the upper and lower bands for different values of  $\Delta$  and for the two dimerizations. When  $J/J' > 1$  (D1) the phase lies within the  $(0, \pi)$  range, with  $\varphi_{Zak,+}(\Delta) \rightarrow \pi$  when  $\Delta \rightarrow +\infty$ , and  $\varphi_{Zak,-}(\Delta) \rightarrow 0$  when  $\Delta \rightarrow -\infty$ . On the other hand, for  $J/J' < 1$  (D2) the Zak phase belongs to  $(-\pi, 0)$  and the signs of  $\varphi_{Zak,\pm}(\Delta)$  are inverted.

In section 3.2.2 it was shown that the Zak phase is a gauge-dependent quantity which depends on the choice of the unit cell, i.e. the origin of the coordinate system. Therefore, the values presented above are for one particular unit cell, and are not universal. In the remaining part of this section it will be shown that even though the Zak phase

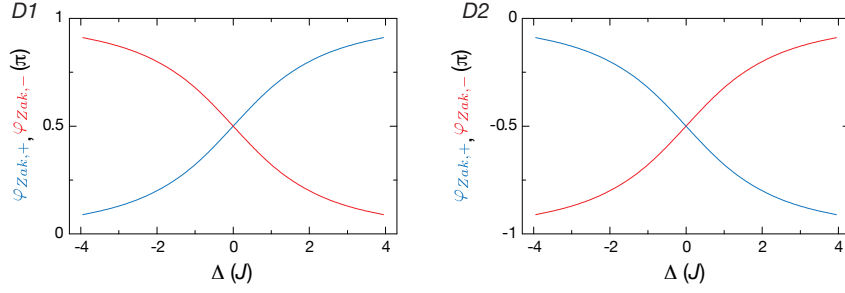


Figure 3.7: Zak phase for the Rice-Mele Hamiltonian as a function of the energy staggering for the upper (blue) and lower (red) bands. For the dimerization  $D1$  the Zak phase in the lower (upper) band decreases (increases) with  $\Delta$  and tends to zero ( $\pi$ ) when  $\Delta$  tends to infinity. For the dimerization  $D2$  the same happens, but with reversed sign. For this calculation the hopping terms used were  $J/J' = 3/1$  for  $D1$  and  $J/J' = 1/3$  for  $D2$ .

on each band depends on the chosen unit cell, the Zak phase difference between two independent Zak phases is independent of it [57, 159]. It means that the difference between two Zak phases calculated for the same system but for different parameters and/or bands is independent of the choice of the unit cell used for the calculation of both phases. The demonstration is quite simple and follows from Eq. 3.20. Assume that for a chosen unit cell the difference of the Zak phases for two sets of parameters is  $\delta\varphi_{Zak} = \varphi_{Zak}(\Delta_1, J_1, J'_1) - \varphi_{Zak}(\Delta_2, J_2, J'_2)$ . When the unit cell is changed by shifting the coordinate system by  $x_0$ , the difference is transformed according to

$$\begin{aligned} \varphi'_{Zak}(\Delta_1, J_1, J'_1) - \varphi'_{Zak}(\Delta_2, J_2, J'_2) &= \varphi_{Zak}(\Delta_1, J_1, J'_1) + Gx_0 - \varphi_{Zak}(\Delta_2, J_2, J'_2) - Gx_0 \\ &= \delta\varphi_{Zak}, \end{aligned} \quad (3.38)$$

which proves that the Zak phase difference is a well defined quantity. In particular, it proves that for the SSH model the Zak phase difference between the phases  $D1$  and  $D2$  is gauge-independent and equal to  $\pi$ . This is a very important result, because it reflects the distinct topological character of the two phases and has many consequences for the physics of the SSH model. For example, it is linked to the existence of protected edge states (see section 3.3.4) and to the change in the polarization when the system is externally modified (see section 3.4). One of the main objectives of the experiment described in the next chapter was to measure the Zak phase difference between the two phases of the SSH model using ultracold atoms in optical lattices [51].

### 3.3.3 Chiral symmetry

The SSH Hamiltonian possesses two kinds of lattice sites, denoted by  $a_n$  and  $b_n$ . Using this, one can define a chiral operator as the difference between the projectors on both

kind of lattice sites, i.e.

$$\Sigma_z = \sum_n |b_n\rangle \langle b_n| - \sum_n |a_n\rangle \langle a_n|. \quad (3.39)$$

An explicit form of this operator is

$$\Sigma_z = \sigma_z \oplus \sigma_z \oplus \dots \oplus \sigma_z, \quad (3.40)$$

where  $\sigma_z$  is the z-Pauli matrix. Due to this structure it is easy to verify that

$$\begin{aligned} \Sigma_z^\dagger \Sigma_z &= \mathbb{I}, \\ \Sigma_z^2 &= \mathbb{I}. \end{aligned} \quad (3.41)$$

Because of the absence of on-site energy terms in  $\hat{H}_{SSH}$  one can see that the chiral operator anticommutes with  $\hat{H}_{SSH}$

$$\Sigma_z \hat{H}_{SSH} \Sigma_z = -\hat{H}_{SSH}. \quad (3.42)$$

The action of the chiral operator on a state  $|\psi\rangle = \sum_n c_n |a_n\rangle + \sum_n c'_n |b_n\rangle$  is to simply flip the sign of the  $c_n$  terms, i.e.  $\Sigma_z |\psi\rangle = -\sum_n c_n |a_n\rangle + \sum_n c'_n |b_n\rangle$ . A direct consequence of the chiral symmetry is that the spectrum of  $\hat{H}_{SSH}$  is symmetric. Any eigenstate  $|\psi_n\rangle$  with energy  $\varepsilon_n$  has a conjugate state  $\Sigma_z |\psi_n\rangle$  with eigenenergy  $-\varepsilon_n$ :

$$\begin{aligned} \hat{H}_{SSH} |\psi_n\rangle &= \varepsilon_n |\psi_n\rangle, \\ \hat{H}_{SSH} \Sigma_z |\psi_n\rangle &= -\Sigma_z \hat{H}_{SSH} |\psi_n\rangle = -\Sigma_z \varepsilon_n |\psi_n\rangle = -\varepsilon_n \Sigma_z |\psi_n\rangle. \end{aligned} \quad (3.43)$$

It means that for each eigenstate of  $\hat{H}_{SSH}$  with non-zero energy, by flipping the sign of the wavefunction on the  $a_n$  sites one obtains another eigenstate with opposite energy. This is consistent with the solutions shown in Eqs. 3.32, where for  $\Delta = 0$  one directly sees that  $\mathbf{u}_{+,k}$  is obtained from  $\mathbf{u}_{-,k}$  by flipping the sign of  $\alpha_k$ .

Another conclusion one can draw is that since for  $\varepsilon_n \neq 0$  the two eigenstates  $|\psi_n\rangle$  and  $\Sigma_z |\psi_n\rangle$  have different energies, they are orthogonal, and therefore the state  $|\psi_n\rangle$  has the same projection on the sublattices  $a_n$  and  $b_n$ :

$$\langle \psi_n | \Sigma_z | \psi_n \rangle = 0 \rightarrow \langle \psi_n | \left( \sum_n |b_n\rangle \langle b_n| \right) | \psi_n \rangle = \langle \psi_n | \left( \sum_n |a_n\rangle \langle a_n| \right) | \psi_n \rangle. \quad (3.44)$$

Moreover, if the state  $|\psi_n\rangle$  has zero energy then the state  $\Sigma_z |\psi_n\rangle$  will also have zero energy. From this it follows that

$$\hat{H}_{SSH} |\psi_n\rangle + \hat{H}_{SSH}\Sigma_z |\psi_n\rangle = 0 = \hat{H}_{SSH} \left( \sum_n |b_n\rangle \langle b_n| \right) |\psi_n\rangle. \quad (3.45)$$

and similarly

$$\hat{H}_{SSH} |\psi_n\rangle - \hat{H}_{SSH}\Sigma_z |\psi_n\rangle = 0 = \hat{H}_{SSH} \left( \sum_n |a_n\rangle \langle a_n| \right) |\psi_n\rangle. \quad (3.46)$$

Therefore one can always write each pair of zero energy states such that each of the states has nonzero projection on only one type of sublattice. In the next section it will be shown that zero energy eigenstates appear for finite size SSH systems, and that those states are localized at the edges of the chain.

Note also that these results hold for any system without position-dependent on-site energy, and are not limited to infinitely-long systems. For a finite size system the Hamiltonian possesses the same structure, and therefore it still anticommutes with the chiral operator. Furthermore, the commutation also holds for Hamiltonians similar to  $\hat{H}_{SSH}$ , but with spatially-dependent hopping terms, i.e. not only for alternating couplings  $\cdots J \cdots J' \cdots J \cdots$  but also for general couplings  $\cdots J_m \cdots J_{m+1} \cdots J_{m+2} \cdots$ . We stress here that the Rice-Mele Hamiltonian does not possess chiral symmetry due to the on-site energy terms.

### 3.3.4 Zak phase and edge states in finite systems

Consider the SSH Hamiltonian for a finite size system with  $2N$  sites ( $N$  unit cells). The energy spectrum of that system is displayed in Fig. 3.8. There it can be seen that the spectrum is symmetric in the sense that for each eigenstate with energy  $\varepsilon_n$ , a second one with opposite energy exists. As explained above, this is expected due to the chiral symmetry of the SSH Hamiltonian. Additionally, the figure shows that depending on the dimerization, there are either zero ( $D2$ ) or two states ( $D1$ ) with zero energy. The fact that the number of zero-energy states is even is also consistent with the chiral symmetry of the Hamiltonian. Moreover, these two zero-energy states are localized at the edges of the system and decay exponentially in the bulk.

The presence of the edge states is related to the value of the Zak phase of the system [63]. In order to see this, it is better to calculate the Zak phase for a particular choice of the unit cell, which is illustrated in Fig. 3.8. For this unit cell the Bloch function expansion takes the form

$$\psi_k(x) = e^{ikx} u_k(x) = \sum_n \alpha_k e^{ikx_n} w_a(x - x_n) + \beta_k e^{ikx_n} w_b(x - x_n - d/2), \quad (3.47)$$

and the  $k$ -dependent Hamiltonian is

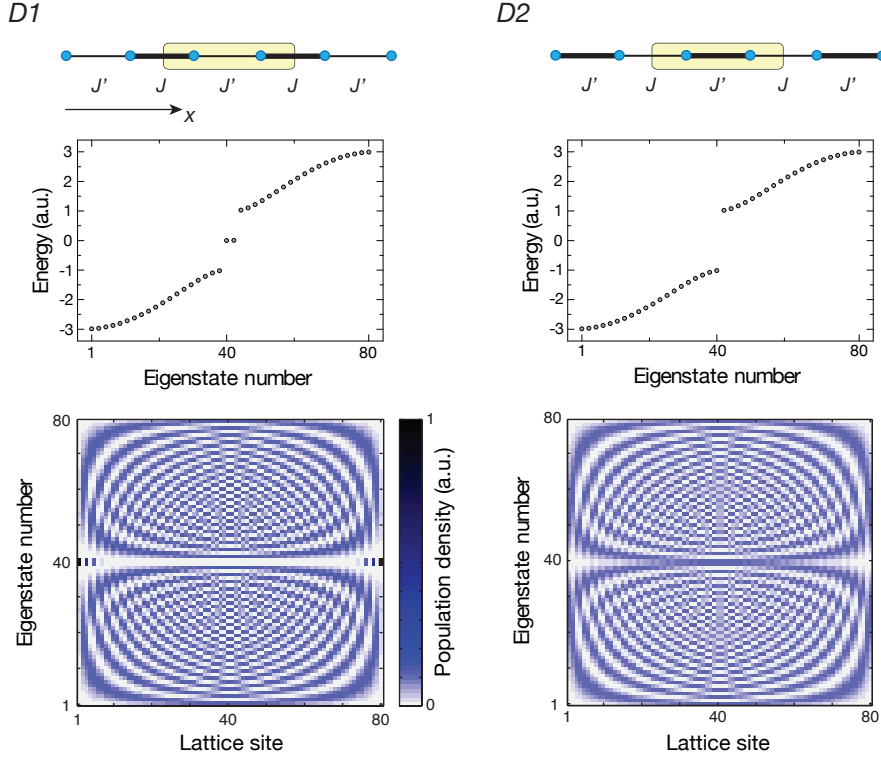


Figure 3.8: Energy and density plots for the different eigenstates for the dimerizations  $D1$  (left) and  $D2$  (right) for a finite size system. In the  $D1$  configuration one can see two eigenvalues with zero energy that correspond to the edge states. The density plots of these states show that they are localized at the edges of the system and that they decay very fast towards the bulk. For the configuration  $D2$  there are no states with zero energy and no localized states. These results were numerically calculated for a system size of 80 lattice sites and for the couplings  $J = 1$  and  $J' = 2$ .

$$\hat{H}(k) = \mathbf{B}(k)\sigma, \quad \hat{H}(k)\mathbf{u}_k = \tilde{\varepsilon}_k\mathbf{u}_k, \quad (3.48)$$

with  $\mathbf{B}(k) = (\varepsilon_k \cos(\theta_k), \varepsilon_k \sin(\theta_k), \Delta)$  (see appendix D for the details). Here  $\varepsilon_k$  and  $\tilde{\varepsilon}_k$  are the same as given in Eqs. 3.31 and 3.28, because the energy spectrum is gauge independent.

The expressions for the eigenvectors  $\mathbf{u}_k$  are the same as in Eq. 3.32, with the difference that due to the new choice of the unit cell the angle  $\theta_k$  goes from  $-\pi$  to  $\pi$  instead of  $-\pi/2$  to  $\pi/2$  as  $k$  travels across the Brillouin zone.

For each  $k$ , the internal structure of  $\mathbf{u}_{\pm k}$  depends on the vector  $\mathbf{B}(k)$ , and therefore it is interesting to study its behavior. We will focus now on the case  $\Delta = 0$ . Figure 3.9 shows the endpoints of  $\mathbf{B}(k)$  for the two dimerizations. The trajectory forms a circle in the  $xy$  plane. When  $J > J'$  ( $D1$ ) the origin of the coordinate system is contained in the circle and the winding of the vector  $\mathbf{B}(k)$  around the origin is one. On the other hand,

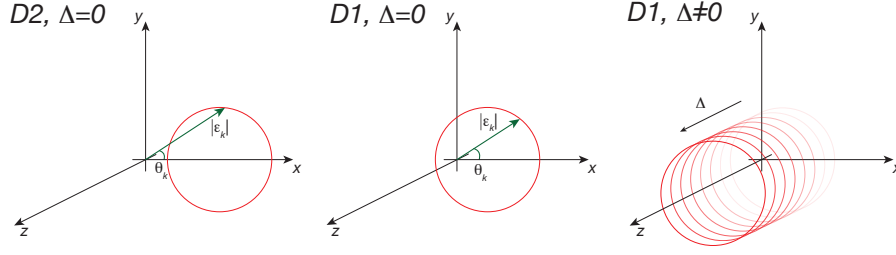


Figure 3.9: Trajectories of the vector  $\mathbf{B}(k)$  for the dimerizations  $D2, \Delta = 0$  (left),  $D1, \Delta = 0$  (center) and  $D1, \Delta \neq 0$  (right). The green arrow illustrates the vector  $\mathbf{B}(k)$ , where its length and angle are  $|\varepsilon_k|$  and  $\theta_k$ . The Zak phase is given by the winding of  $\mathbf{B}(k)$  as  $k$  varies across the Brillouin zone. For  $D1$  ( $D2$ ) the winding is one (zero) because the origin is (not) contained in the trajectory. In the special case of  $\Delta \neq 0$ , the trajectory is displaced from the  $xy$  plane, and the winding number is not well defined. In that case the Zak phase can take fractional values.

when  $J < J'$  ( $D2$ ) the origin is not contained in the circle and the winding number is zero.

The Zak phase for this particular gauge can be calculated through Eq. 3.36, for  $\Delta = 0$ :

$$\varphi_{Zak} = \frac{1}{2} \int_{-G/2}^{G/2} \partial_k \theta_k dk. \quad (3.49)$$

Since the angle of  $\mathbf{B}(k)$  is also  $\theta_k$ , this tells us that the Zak phase is  $\pi$  times the value of the winding number. Then

$$\varphi_{Zak} = \begin{cases} \pi & J > J', \\ 0 & J < J'. \end{cases} \quad (3.50)$$

This shows that to change the value of the Zak phase one has to induce a topological transition. There are two ways of doing it. The first one is by crossing the  $J = J'$  point, which closes the energy gap between the upper and lower bands. The second possibility is to break the chiral symmetry of the system by putting  $\Delta \neq 0$  (see Fig. 3.9). The latter procedure displaces the trajectory along the  $z$  direction and the gap is not closed when crossing the point  $J = J'$ .

This solution is valid for an infinite system. The eigenstates of the finite size system can be built as a linear combination of the states  $\mathbf{u}_{+,k}$ ,  $\mathbf{u}_{-,k}$ ,  $\mathbf{u}_{+,-k}$ , and  $\mathbf{u}_{-,-k}$ . In this case one finds that the solutions are of the form

$$\mathbf{v}_{\pm,k} = \frac{1}{\sqrt{2}}(\mathbf{u}_{\pm,k} - \mathbf{u}_{\pm,-k}). \quad (3.51)$$

These states must also satisfy the boundary conditions, which require that the wavefunction vanishes at the sites  $n = 0$  and  $n = 2N + 1$ . One can prove [63] that these boundary conditions can only be satisfied if

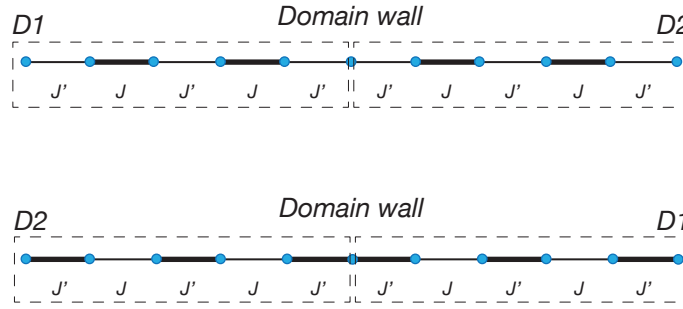


Figure 3.10: Domain walls at the interface of two chains with different dimerization. There are two ways of connecting two systems with opposite dimerizations: the  $D1$ - $D2$  configuration (top) and the  $D2$ - $D1$  one (bottom). At the interface between the chains there is a single isolated site (top) or three connected sites (bottom), and in both cases a domain wall forms.

$$\sin(k(2N + 1) - \theta_k) = 0. \quad (3.52)$$

This restriction on  $k$  links the existence of edge states with the value of the Zak phase. When  $N$  is large, it has  $N$  solutions for  $\varphi_{Zak} = 0$  and  $N - 1$  for  $\varphi_{Zak} = \pi$ . Therefore, for the dimerization  $D1$  the system has only  $2N - 2$  solutions in the bulk (two times  $N - 1$  because one has to consider the states in the lower and upper bands). The two missing solutions are edge states, which are localized at the edges of the system.

Edges states not only appear at the ends of the finite size system, but they also appear at the interface between two chains with different topology, i.e. different Zak phase. This can be understood for example in the limit  $J'/J = 0$ . In that case, each chain consists of an array of dimers, and when putting two chains with different dimerization next to each other two things can happen at the interface: either there is a lattice site that is completely isolated ( $J' = 0$ ), or there are three sites (trimer) that are connected by hopping  $J$  (see Fig. 3.10). In the first case the isolated state has zero energy and its wavefunction is clearly localized on only that site. In the second case, the odd superposition of the two end sites of the trimer is a localized state with zero energy, and it only populates one type of sublattice site. These localized states at the interfaces form domain walls and separate the regions with different dimerization. On the other hand, each of the isolated dimers in the bulk of the system has eigenstates with wavefunctions localized simultaneously on both sites, and therefore these states have non-zero energy.

When one relaxes the condition  $J'/J = 0$ , the edge states spread out with an exponentially decaying tail towards the bulk. Interestingly, when two domain walls are close enough such that their tails overlap with each other, the two edge states hybridize, forming bonding and anti-bonding states with negative and positive energies. In this situation, when the band is populated with fermions at half filling only the negative energy state is populated, and therefore the charge of the particle populating that state is

delocalized between the two sites. This phenomena is known as charge fractionalization, and it is a distinctive feature of topological insulators [65, 152, 153, 160–164].

### 3.4 Theory of bulk polarization in solids and its relation to the Zak phase

#### 3.4.1 Bulk polarization – definition and subtleties

In classical electromagnetism the polarization of a material is defined as a vector quantity that describes the dipole moment per unit volume of the medium [100, 165]. Dielectric media are characterized by a macroscopic polarization which is essential for any phenomenological description of their properties. Even though it is such a fundamental concept, its microscopic definition in the bulk was only recently given [60, 159, 166–169].

The standard picture is based on the Clausius-Mossotti model [170, 171], which considers the dielectric divided into a set of independent polarizable units, and defines the macroscopic polarization as the sum of the polarizations of all the units divided by the cell volume. That picture is unfortunately not applicable to every system, and in particular for those materials for which the electronic wavefunction is not strongly localized near the atomic position in the lattice [172, 173]. The problem behind the definition for the bulk is that the boundary conditions are not given, and since the wavefunction is typically periodic, then any particular condition leads to a different value of the polarization. For example, consider the linear atomic chain shown in Fig. 3.11a. If the electronic wavefunctions are strongly localized near the atoms, then one can divide the chain into units, each of them containing a single atom, and the macroscopic polarization can be defined as the sum of the polarizations of each unit divided by the cell volume. However, if the wavefunctions are totally delocalized (Fig. 3.11b), then the polarization is not well defined, because it strongly depends on how the units are chosen, i.e. by displacing the units one can obtain different polarizations. This proves that the Clausius-Mossotti model is not general enough and it fails.

One could take different approaches to define the bulk polarization that are not based on small units, but on the density distribution of the electronic wavefunction. For example, one could define it as

$$\mathbf{P} = \frac{1}{V} \int \mathbf{r}\rho(\mathbf{r}) \cdot d\mathbf{r}, \quad (3.53)$$

where  $\rho$  is the wavefunction density and the integral is performed over the volume  $V$  of the sample. Such an approach also fails, as the integration also involves the edges (surface) of the sample and not only the bulk, and disentangling the two contributions is not trivial.

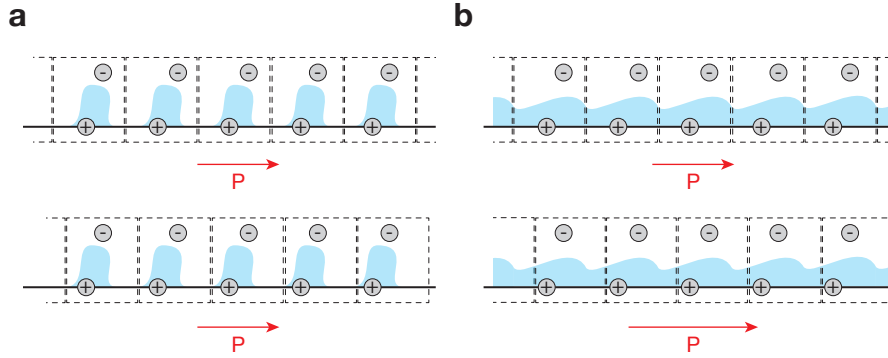


Figure 3.11: Bulk polarization in a linear chain, where the circles with the plus signs represent the atomic charge at the lattice positions and the ones with the minus sign the electronic charge distributed in the wavefunction. The red arrows represent the polarization of the units. **(a)** For a localized wavefunction one can split the sample into small unit cells (dashed boxes) and define the total polarization as the sum of the individual polarizations. In that case a small displacement of the units does not change the polarization. **(b)** If the wavefunction is totally delocalized, then for every choice of the units one can obtain a different value for the polarization, as illustrated by the two examples displayed in the figure.

As a conclusion, there is no proper definition of bulk polarization for a crystalline solid with periodic and delocalized electronic charge distribution. Aside from this definition issue, there is a proper way of defining the polarization change in the bulk when the system is adiabatically modified from one state to a different one. In the next section we will prove that statement, and furthermore we will present the results obtained by King-Smith and Vanderbilt [159], which show that the polarization change is proportional to the difference between the Zak phases of the final and initial states.

### 3.4.2 Zak phase and its relation to bulk polarization change

Consider a system that is adiabatically brought from an initial to a final state by the modification of an external parameter such as the strength of an electric field. During this process, the wavefunction is modified and a charge flow appears. If the system is totally isolated, i.e. the charge cannot leave the material, then the change in polarization will be related to the charge redistribution. This can be seen as follows [60, 159]. The polarization density is related to the charge distribution by the Maxwell equations

$$\nabla \cdot \mathbf{P}(\mathbf{r}) = -\rho(\mathbf{r}). \quad (3.54)$$

When combining this with the continuity equation

$$\frac{\partial \rho(\mathbf{r})}{\partial t} + \nabla \cdot \mathbf{j} = 0, \quad (3.55)$$

one obtains that the change in polarization density is

$$\Delta \mathbf{P}_i = \int_{\lambda_0}^{\lambda_1} d\lambda j_i, \quad (3.56)$$

where  $i$  indicates the vector component of the polarization and  $\lambda$  parametrizes the adiabatic transformation. This expression is correct up to a divergence-free part, which is usually given by the magnetization current [174].

It is important to remark that this result proves that the polarization in the bulk is an intrinsic quantity which is not related to the surface effects. Its value depends only on what happens in the bulk. This approach of defining the polarization change is actually closer to experiments, where quantities like piezoelectricity or permittivity are measured which depend on the polarization change and not on its particular value [172, 173, 175–179]. Furthermore, this explains why one cannot define the polarization as a quantity that only depends on the density of the electronic wavefunction: the currents are linked to the phase of the wavefunction, and that information was missing in the previous formulations.

In 1993 King-Smith and Vanderbilt developed a formulation of the polarization change where they proved that it is related to the Zak phase [159]. Here we will sketch a proof of it for a one-dimensional system, based on the review of Xiao *et al.* [60]. These results can easily be extended to higher dimensions.

In their theory they considered a time-dependent, spatially periodic Hamiltonian which changes very slowly in time. They assumed that the Hamiltonian was also periodic in time

$$\hat{H}(t+T) = \hat{H}(t), \quad (3.57)$$

where  $T$  is the periodicity, and as  $t$  is changed the Hamiltonian always remains spatially periodic with constant periodicity  $d$ . Under these conditions, the instantaneous eigenstates of  $\hat{H}$  are Bloch waves:  $|\psi_n(k, t)\rangle = e^{ikx} |u_n(k, t)\rangle$ , where  $n$  is the band index. Applying basic perturbation theory, they obtained that if the system is initially in the state  $|u_n(k, t)\rangle$  then after some time  $t$  it will be

$$|\psi(t)\rangle = |u_n\rangle - i\hbar \sum_{n' \neq n} \frac{|u_{n'}\rangle \langle u_{n'} | \partial_t |u_n\rangle}{\varepsilon_n - \varepsilon_{n'}}. \quad (3.58)$$

Here  $\varepsilon_n$  are the eigenenergies of the Bloch states and for simplicity we have omitted the explicit  $k$ - and  $t$ - dependences. Using this expression they obtained that the expectation value of the velocity operator takes the form

$$v_n(k) = \langle \psi(t) | \frac{\partial \hat{H}(k, t)}{\partial (\hbar k)} | \psi(t) \rangle = \frac{\partial \varepsilon_n(k)}{\hbar \partial k} - i \left[ \left\langle \frac{\partial u_n}{\partial k} \left| \frac{\partial u_n}{\partial t} \right\rangle - \left\langle \frac{\partial u_n}{\partial t} \left| \frac{\partial u_n}{\partial k} \right\rangle \right]. \quad (3.59)$$

The last term is the Berry curvature  $\Omega_n$  defined in Eq. 3.6, written for the two-dimensional parameter space  $(k, t)$ . Therefore one can write

$$v_n(k) = \frac{\partial \varepsilon_n(k)}{\hbar \partial k} - \Omega_{k,t}^n. \quad (3.60)$$

The total current is then obtained by integrating this expression over all the occupied states. In the case of a filled band the integration is over the entire Brillouin zone, and due to the periodicity of  $k$ -space the integral of the first term vanishes. Hence

$$j = -e \sum_n \int \frac{dk}{2\pi} \Omega_{k,t}^n, \quad (3.61)$$

where the sum runs over all the filled bands. This result was first obtained by Thouless *et al.* in their formulation of the quantum Hall effect [55, 180], and found many applications within the context of particle transport. Combining this with Eq. 3.56 one arrives at

$$\Delta P = \int_{\lambda_0}^{\lambda_1} d\lambda j = -e \sum_n \int_0^T dt \int \frac{dk}{2\pi} \Omega_{k,t}^n. \quad (3.62)$$

In this expression we have assumed that  $\lambda = \lambda(t)$  parametrizes the change of the Hamiltonian. Note also that it is written for a one-dimensional system, and therefore there is only one component for the polarization density.

One should also remark that due to the periodicity in  $t$  and  $k$ , the integral given above is over a torus manifold, and as discussed in 3.2.3 its value is the Chern number which is quantized in units of  $2\pi$ . Therefore, after each cycle  $t = 0 \rightarrow t = T$  there is a quantized change in the polarization. In terms of particle transport, it tells us that for every cycle there is a fixed number of transported particles, which depends on the number of occupied bands and the Chern number in the  $(k, t)$ -torus. This is a very well studied phenomena in the field of charge pumping [180–185].

To conclude, we now give a second expression for the polarization change in terms of the Zak phase of the initial and final states. For a two-dimensional parameter space, the Berry curvature takes the form

$$\Omega_{k,t}^n = \partial_k \mathcal{A}_t^n - \partial_t \mathcal{A}_k^n. \quad (3.63)$$

The term  $\mathcal{A}_t^n$  can be chosen to be periodic in  $k$ , therefore the integral of  $\partial_k \mathcal{A}_t^n$  over the Brillouin zone vanishes. Then, the change in polarization gives

$$\Delta P = e \sum_n \int \frac{dk}{2\pi} \mathcal{A}_k^n \Big|_{t=0}^{t=T}. \quad (3.64)$$

For a single filled band, it says that the polarization change is proportional to the difference of the Zak phases between the initial and final states. One should note that this

last expression does not consider the history of the path, but only the initial and final states. Due to this, the polarization change obtained using the formula above does not track how many times the system has cycled, and therefore its value is determined up to a term of the form  $me/2$ , with  $m$  integer.

### 3.4.3 Polarization change in the Rice-Mele model

To conclude this chapter we will show how the Zak phase difference between the dimerizations  $D1$  and  $D2$  in the SSH model is related to a polarization change. The SSH Hamiltonian can be written as

$$\hat{H}(k) = \mathbf{B}(k)\sigma, \quad (3.65)$$

with  $\mathbf{B}(k) = (\varepsilon_k \cos(\theta_k), \varepsilon_k \sin(\theta_k), \Delta)$ . Using the generic spherical angles  $\theta_0$  and  $\phi_0$  one can rewrite the field as  $\mathbf{B}(k) = B(\sin(\theta_0)\cos(\phi_0), \sin(\theta_0)\sin(\phi_0), \cos(\theta_0))$ , where  $\theta_0$  and  $\phi_0$  depend on the quasimomentum  $k$ , the hopping parameters  $J$  and  $J'$  and the energy staggering  $\Delta$ . The eigenvectors of the system written in terms of these angles are

$$\begin{aligned} |u_+\rangle &= \begin{pmatrix} \cos \frac{\theta_0}{2} \\ \sin \frac{\theta_0}{2} e^{i\phi_0} \end{pmatrix}, \\ |u_-\rangle &= \begin{pmatrix} \sin \frac{\theta_0}{2} \\ -\cos \frac{\theta_0}{2} e^{i\phi_0} \end{pmatrix}. \end{aligned} \quad (3.66)$$

Next we consider a process that modifies the Hamiltonian, and that is defined by the functions  $\Delta(\lambda)$  and  $J - J' = \delta(\lambda)$ , where  $\lambda$  is used to parametrize the adiabatic transformation. According to Eq. 3.62, the polarization change is given by the integral of the Berry curvature along the Brillouin zone and along the path. The Berry connection for the lower band is

$$\begin{aligned} \mathcal{A}_k &= \langle u_- | \partial_k | u_- \rangle = \cos^2(\theta_0/2) \partial_k \phi_0, \\ \mathcal{A}_\lambda &= \langle u_- | \partial_\lambda | u_- \rangle = \cos^2(\theta_0/2) \partial_\lambda \phi_0. \end{aligned} \quad (3.67)$$

From this, the Berry curvature takes the form

$$\Omega_{k,\lambda} = -\frac{1}{2} \sin(\theta_0) (\partial_\lambda \theta_0) (\partial_k \phi_0). \quad (3.68)$$

Upon integration the polarization-density change is obtained

$$\Delta P = -\frac{e}{2\pi} \int_{\lambda_0}^{\lambda_1} d\lambda \int_0^G dk \Omega_{k,\lambda} = \frac{e}{4\pi} \int_{\lambda_0}^{\lambda_1} d\lambda \int_0^G dk \sin(\theta_0) (\partial_k \phi_0) (\partial_\lambda \theta_0). \quad (3.69)$$

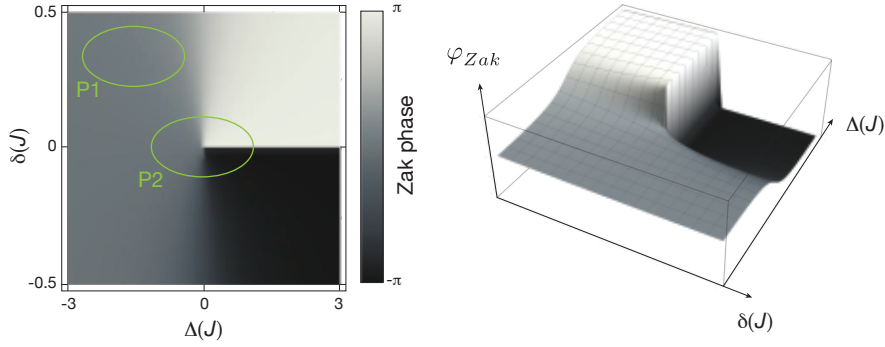


Figure 3.12: Polarization in the Rice-Mele Hamiltonian. The left graph displays the value of the Zak phase as a function of the dimerization strength  $\delta = J - J'$  and the energy staggering  $\Delta$ . In this plot we have subtracted an offset equal to  $\pi$  from the Zak phase so that it lies in the range  $(-\pi, \pi)$ . At  $\delta = 0, \Delta = 0$  there is a singularity, and the change in polarization density is equal to  $e/2$  if the closed path encloses it (P2) and zero if it does not (P1). On the right side of the figure we show the Zak phase in a 3D plot, where one can appreciate the singularity at  $\delta = 0, \Delta = 0$ .

The explicit expressions for  $\theta_0(k, \lambda)$  and  $\phi_0(k, \lambda)$  are obtained from Eqs. 3.66 and D.6:

$$\begin{aligned}\theta_0(k, \lambda) &= \gamma_k, \\ \phi_0(k, \lambda) &= -\theta_k.\end{aligned}\tag{3.70}$$

Here the dependence on  $\lambda$  is implicit. Substituting this into Eq. 3.69 one arrives at

$$\begin{aligned}\Delta P &= -\frac{e}{4\pi} \int_{\lambda_0}^{\lambda_1} d\lambda \int_0^G dk \sin(\gamma_k) (\partial_k \theta_k) (\partial_\lambda \gamma_k) \\ &= -\frac{e}{2\pi} \int_0^G dk \cos^2(\gamma_k/2) \partial_k \theta_k \Big|_{\lambda_0}^{\lambda_1}.\end{aligned}\tag{3.71}$$

Comparing this with the expression for the Zak phase (Eq. 3.36) one confirms that the Polarization is indeed the difference of the Zak phase between the initial and final states.

Figure 3.12 displays the value of the Zak phase as a function of  $J - J' = \delta$  and  $\Delta$ . One can observe that at  $\delta = 0, \Delta = 0$  there is a singularity, which is due to the change in the periodicity of the system, i.e. the size of the unit cell changes to  $d/2$  and the upper and lower bands touch each other. Thus, the polarization change depends on how many times the path  $(\delta(\lambda), \Delta(\lambda))$  encloses the singularity. For example, for the paths shown in the figure, one can have a change in the polarization density of 0 or  $e/2$ .



## Chapter 4

# Measurement of the Zak phase in a dimerized system

The direct measurement of geometric phases which allow to identify topological properties of Bloch bands has been a long standing challenge, which has been for the first time successfully addressed in this experiment using ultracold atoms in an optical lattice. In this chapter we present the experimental setup and sequence used to measure the Zak phase in a dimerized system using a combination of Bloch oscillations and Ramsey interferometry. At the end of the chapter we discuss alternative variants of the method as well as an extension to two-dimensional systems.

### 4.1 Theoretical proposals for measuring the Zak phase

#### 4.1.1 Zak phase on a single band: theoretical proposal and limitations

The Zak phase of a single band can be extracted using a combination of Bloch oscillations (see appendix E) and Ramsey interferometry (see appendix F). The theoretical proposal is shown in Fig. 4.1 and consists of two steps:

**Step 1:** Start with an atom in the state  $|\downarrow, k = 0\rangle$  and bring it into a coherent superposition state  $(|\uparrow, k = 0\rangle + |\downarrow, k = 0\rangle)/\sqrt{2}$  using a MW  $\pi/2$ -pulse. Here  $\sigma = \uparrow, \downarrow$  denotes two spin states of the atom with opposite magnetic moment. Then apply a magnetic field gradient to drive Bloch oscillations in opposite directions for the two spin components. The atomic wavepacket thus evolves into the coherent superposition state  $(|\uparrow, k\rangle + e^{i\delta\varphi} |\downarrow, -k\rangle)/\sqrt{2}$ . When both spin components reach the band edge, the differential phase between the two states is given by

$$\delta\varphi = \varphi_{\uparrow, \text{dyn}} + \varphi_{\uparrow, \text{Zeeman}} + \varphi_{\uparrow, \text{geom}} - \varphi_{\downarrow, \text{dyn}} - \varphi_{\downarrow, \text{Zeeman}} - \varphi_{\downarrow, \text{geom}} = \varphi_{\text{Zak}} + \delta\varphi_{\text{Zeeman}}, \quad (4.1)$$

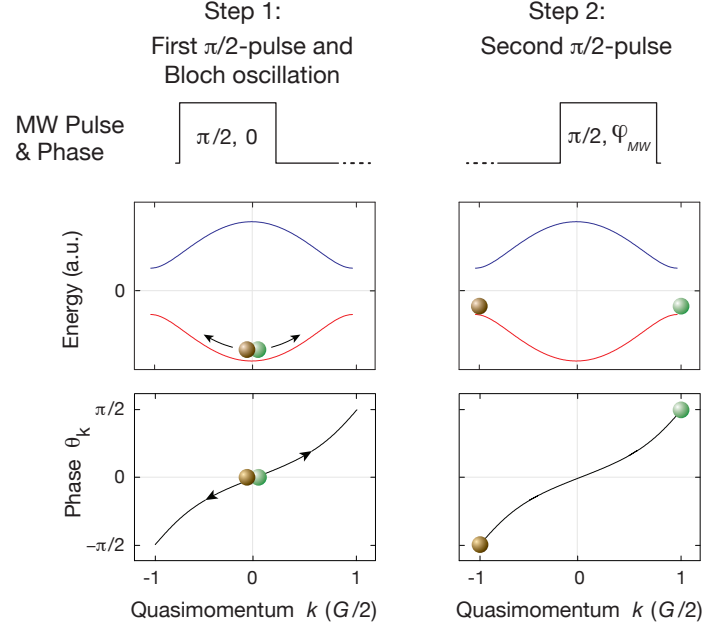


Figure 4.1: Experimental proposal for measuring the Zak phase on a single band, illustrated for the case of the SSH Hamiltonian. Energy band, MW pulses and state evolution of a single atom in a superposition of two spin-states with opposite magnetic moment (brown and green balls) during the two-step echo sequence described in the text. The winding of the state vector with  $k$  is given by  $\theta_k$ .

where  $\varphi_{\sigma,dyn}$  is the dynamical phase acquired by the  $\sigma$  component when undergoing a Bloch oscillation between  $k = 0$  and the edge of the band,  $\varphi_{\sigma,Zeeman}$  are the Zeeman phases and  $\varphi_{\sigma,geom}$  are the corresponding geometrical phases for the explored part of the band. Note that for time-reversal invariant Hamiltonians (as is the case here), the band structure is symmetric with respect to  $k = 0$ , and therefore the dynamical phase acquired during the adiabatic evolution is equal for the two spin states and it cancels in the phase difference.

**Step 2:** The sequence is completed by applying a second  $\pi/2$ -pulse with a phase  $\varphi_{MW}$  to interfere the two spin components and read out their relative phase  $\delta\varphi$  through the resulting Ramsey fringe.

The phase  $\varphi_{Zak}$  is a gauge dependent quantity which is changed to  $\varphi'_{Zak} = \varphi_{Zak} + G \cdot a$  after a shift by  $a$  of the origin of coordinates (see section 3.2.2). However, such a shift also affects the value of the Zeeman phase according to  $\varphi'_{Zeeman} = \varphi_{Zeeman} - G \cdot a$ , and therefore the experimental quantity  $\delta\varphi$  is gauge invariant as expected. Note that the particular value of  $a$  such that  $\varphi'_{Zeeman} = 0$  defines a coordinate system for which the

relative phase  $\delta\varphi$  is equal to the Zak phase.

A disadvantage of this protocol is that the phase  $\delta\varphi$  depends on the magnetic field offset due to the Zeeman phase. Therefore, if it is not well controlled (i.e. if the offset is not the same for different experimental runs), then the protocol cannot be applied experimentally. For example, for  $^{87}\text{Rb}$  the two internal states ( $F = 1, m_F = -1$ ) and ( $F = 2, m_F = -1$ ) have a linear Zeeman energy difference of 1.4 kHz/ mG, which means that for a phase noise smaller than  $\pi/10$  over 1ms one needs a stability of the magnetic field offset of at least 0.1 mG. In our experimental setup the magnetic field stability does not fulfill these stability requirements, and therefore we did not use this protocol.

This proposal is not limited to the Rice-Mele system, but it can be applied to any Hamiltonian with time-reversal symmetry. Furthermore, even for the case of systems without that symmetry, a small modification of the proposal allows the Zak phase to be extracted (see section 4.3.3).

#### 4.1.2 Proposal for measuring the Zak phase difference between the two dimerizations of the SSH model

The theoretical proposal presented in the previous section allows the measurement of the Zak phase on a single band for a particular coordinate system which depends on the magnetic field offset. For a dimerized finite size system, and for a particular choice of the unit cell, the value of the Zak phase tells us whether the  $D1$  and  $D2$  phases possess edge states, and therefore it indicates if they are topologically trivial or not. For our experimental system, where there are no hard walls, the gauge-invariant phase difference  $\delta\varphi_{\text{Zak}} = \varphi_{\text{Zak}}^{D1} - \varphi_{\text{Zak}}^{D2} = \pi$  is the quantity that indicates that the SSH model contains trivial and nontrivial topological phases. In this section we present a protocol which allows the measurement of  $\delta\varphi_{\text{Zak}}$  and is robust against magnetic field fluctuations. The three-steps proposal is displayed in Fig. 4.2 and is described below:

**Step 1:** Start with an atom in the state  $|\downarrow, k = 0\rangle$  in the dimerization  $D1$ , and bring it into a coherent superposition state  $(|\uparrow, k = 0\rangle + |\downarrow, k = 0\rangle)/\sqrt{2}$  using a MW  $\pi/2$ -pulse. Then apply a magnetic field gradient to create a constant force in opposite directions for the two spin components which leads to Bloch oscillations. The atomic wavepacket thus evolves into the coherent superposition state  $1/\sqrt{2}(|\uparrow, k\rangle + e^{i\delta\varphi}|\downarrow, -k\rangle)$ . When both reach the band edge, the differential phase between the two states is given by  $\delta\varphi = \varphi_{\text{Zak}} + \delta\varphi_{\text{Zeeman}}$  (as in the previous protocol the dynamical phases cancel out).

**Step 2:** To eliminate the Zeeman phase difference, apply a spin-echo  $\pi$ -pulse at this point and also switch dimerization from  $D1 \rightarrow D2$ . For atoms located at the band edge  $k = \pm G/2$ , this non-adiabatic dimerization switch induces a transition to the excited

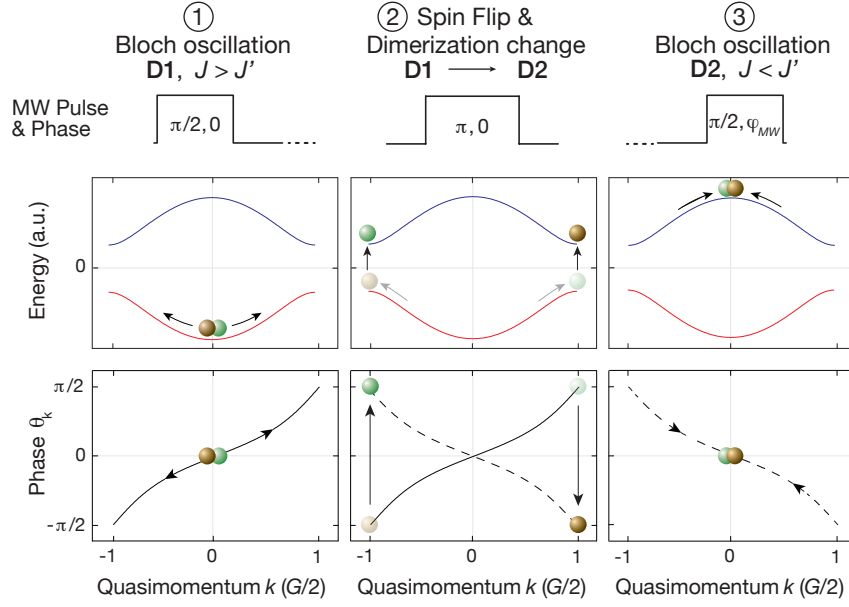


Figure 4.2: Experimental proposal for measuring the Zak phase  $\varphi_{Zak}^{D1} - \varphi_{Zak}^{D2} = \pi$ . Energy band, MW pulses and state evolution of a single atom in a superposition of two spin-states with opposite magnetic moment (brown and green balls) during the three-step echo sequence described in the text. The winding of the state vector with  $k$  is given by  $\theta_k$  (solid line dimerization D1, dashed line dimerization D2).

band of the SSH model (see Eq. 3.34).

**Step 3:** The sequence is finally completed by letting the spin components further evolve in the upper band until they return to  $k = 0$ . At this point in time, apply a final  $\pi/2$ -pulse with phase  $\varphi_{MW}$  to interfere the two spin components and read out their relative phase  $\delta\varphi$  through the resulting Ramsey fringe. The change in dimerization occurring at the mid-point of the echo sequence is crucial in order not to cancel the Zak phase in addition to the Zeeman phase. Due to the opposite windings of the Bloch states in the upper and lower bands with quasimomentum  $k$  (Fig. 4.2), the resulting phase shift encoded in the Ramsey fringe is thus given by:  $\delta\varphi = \varphi_{Zak}^{D1} - \varphi_{Zak}^{D2}$ .

The spin-echo  $\pi$ -pulse in the second step is important because it removes the Zeeman phase and therefore it makes the full experimental sequence robust against magnetic field fluctuations, provided that the field does not fluctuate on time scales comparable to the Bloch oscillation time.

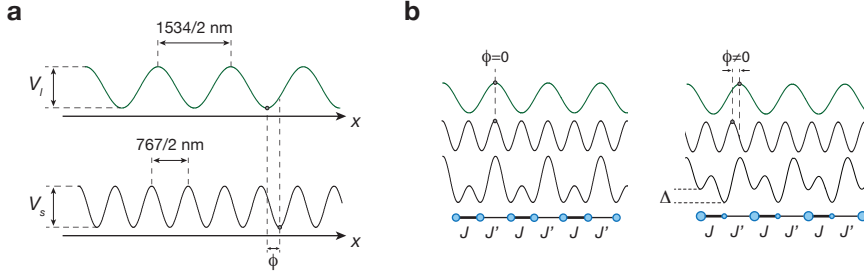


Figure 4.3: Experimental setup for the realization of a dimerized system. **(a)** Two superimposed standing waves of wavelengths  $\lambda_s/\lambda_l$  and relative phase  $\phi$  create a superlattice potential **(b)**. That potential consists of an array of double wells with hopping terms  $J$  and  $J'$ . By adjusting the relative phase  $\phi$ , an energy offset  $\Delta$  can be introduced on each double well, allowing for the realization of the SSH model (left,  $\Delta = 0$ ) and the Rice-Mele Model (right,  $\Delta \neq 0$ ).

## 4.2 Experimental measurement of the Zak phase

### 4.2.1 Experimental setup to realize the dimerized system

In order to realize the Hamiltonian of the SSH and Rice-Mele models, we loaded a Bose-Einstein condensate of  $^{87}\text{Rb}$  atoms into a one-dimensional optical superlattice potential. This potential was formed by superimposing two standing optical waves of wavelengths  $\lambda_s = 767\text{ nm}$  and  $\lambda_l = 1534\text{ nm}$  that generate a lattice potential of the form  $V(x) = V_l \sin^2(k_l x + \phi/2) + V_s \sin^2(2k_l x + \pi/2)$ , where  $k_l = 2\pi/\lambda_l$  and  $V_{s/l}$  are the corresponding strengths of the two standing waves (see Fig. 4.3a). By controlling the phase  $\phi$  between the two waves, different lattice configurations can be realized. For the phase  $\phi = 0$  the SSH model is realized. In that case the optical potential corresponds to an array of double wells, where the coupling between two consecutive double wells is  $J'$  and between the wells of each single double well is  $J$ , and the length of the unit cell is  $d = \lambda_l/2$  (see Fig. 4.3b). In the directions transverse to the lattice there is only a weak harmonic confinement on the order of  $2\pi \cdot 25\text{ Hz}$ , and therefore the interactions can be safely neglected. In the tight-binding regime, the system is described by the SSH Hamiltonian:

$$\hat{H} = - \sum_n (J \hat{a}_n^\dagger \hat{b}_n + J' \hat{a}_n^\dagger \hat{b}_{n-1} + \text{h.c.}), \quad (4.2)$$

which has been described in the previous chapter. If the phase  $\phi = \pi$  is chosen, then the resulting potential is shifted by one lattice site towards one direction, swapping the values of  $J$  and  $J'$ , which is equivalent to changing the dimerization from  $D1$  to  $D2$ . Such a swap is a necessary tool for implementing the second step of our protocol to measure  $\delta\varphi_{\text{Zak}}$ . In the experiment, an instantaneous swap of the values of  $J$  and  $J'$  is implemented by using a second lattice of wavelength  $\lambda_l = 1534\text{ nm}$ , which has a relative phase of  $\phi' =$

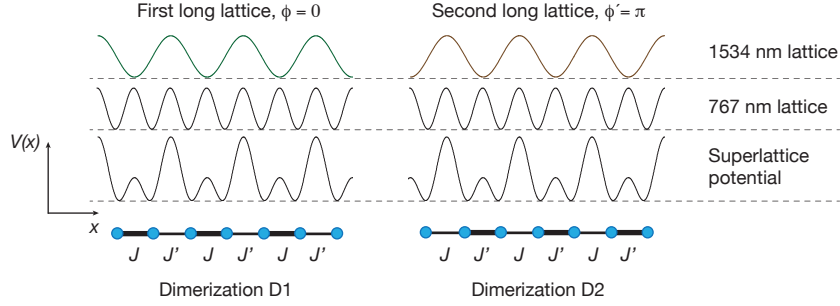


Figure 4.4: Experimental setup used to instantaneously swap the dimerization from  $D1$  to  $D2$ . It consists of a short lattice of wavelength  $\lambda_s$  and two long lattices of wavelength  $\lambda_l$ . The relative phases  $\phi$  and  $\phi'$  of the long lattices with respect to the short lattice can be independently controlled. For  $\phi = 0$  the first long lattice in combination with the short lattice create a dimerized system with dimerization  $D1$ . The second long lattice, with  $\phi' = \pi$ , combined with the short lattice realizes the  $D2$  phase of the dimerized system.

$\pi$  respect to the lattice with  $\lambda_s = 767$  nm. Therefore by switching off the original lattice at  $\lambda_l = 1534$  nm and switching on the second one, one can instantaneously perform the swapping (see Fig. 4.4).

#### 4.2.2 Experimental sequence

To implement the second protocol to measure the Zak phase we used the following experimental sequence:

We started by loading a Bose-Einstein condensate of about  $5 \times 10^4$   $^{87}\text{Rb}$  atoms in the Zeeman state  $|F = 1, m_F = -1\rangle = |\downarrow\rangle$  in 200 ms into a dimerized 1D lattice of  $V_l = 13E_{r,l}$ ,  $V_s = 4E_{r,s}$  and  $\phi = 0$ , where  $E_{r,i} = \hbar^2/2m\lambda_i$ ,  $i = l, s$ . Thereafter, a magnetic field gradient of  $f = 1.18(4)$  kHz/d was ramped up in 1.5 ms, and subsequently a  $3\text{-}\mu\text{s}$  MW  $\pi/2$ -pulse coupling to the Zeeman state  $|F = 2, m_F = -1\rangle = |\uparrow\rangle$  was applied. After half of a Bloch oscillation period ( $425 \mu\text{s}$ ), when the atoms were at the edges of the band, a  $\pi$ -pulse was applied and the dimerization was swapped. After an additional half a Bloch period the atoms returned to  $k = 0$  and a final  $\pi/2$ -pulse with a phase  $\varphi_{MW}$  was applied. At the end of the sequence we measured the population fraction of each of the two spin components by using time-of-flight imaging with a Stern-Gerlach gradient field applied during the expansion to separate the different Zeeman states.

The dimerization swap was achieved by quickly switching off the first long lattice with phase  $\phi = 0$  and ramping up the second long lattice with a phase  $\phi' = \pi$  within  $10 \mu\text{s}$  (see Fig. 4.4). As the dimerization swap time is much shorter than the Bloch oscillation time, it can be considered instantaneous and therefore does not introduce

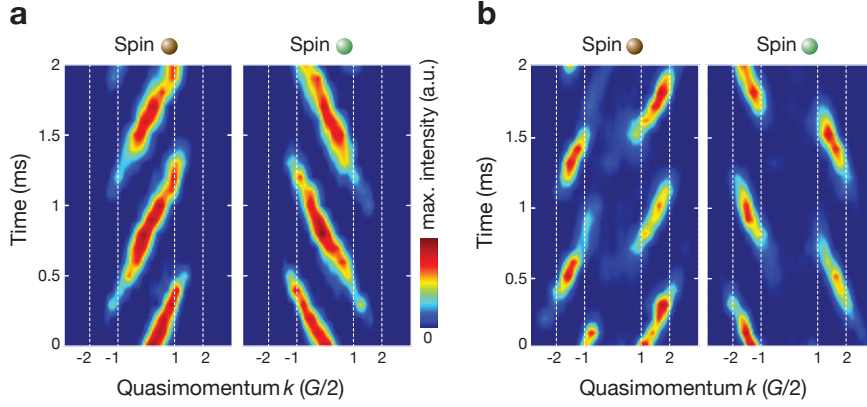


Figure 4.5: Time-of-flight momentum distributions taken for different evolution times of the spin-dependent Bloch oscillations in the lower (a) and upper energy band (b) used in the experiment. Each momentum point is an average of three identical measurements.

any dynamical phase. Furthermore, even if this process were to induce an extra phase, then it would be the same for both spin components and would cancel out in the Ramsey interferometry. In section 4.3 the experimental results of the measurements of the Zak phase in the Rice-Mele Hamiltonian will be presented, and it will be shown that within the experimental uncertainty the dimerization swap does not induce any extra phase.

Figure 4.5 shows images of the momentum distribution of the atoms during the spin-dependent Bloch oscillations in the lower and upper energy bands. Note the opposite evolution in momentum space due to the opposite magnetic moments of the two spin-states. Atoms in the upper energy band are characterized by a distinctively different momentum pattern from atoms in the lower energy band (see also Fig. E.2). The Bloch oscillation period of  $\tau_{\text{Bloch}} = 0.85(3)$  ms was chosen to be slow enough that non-adiabatic Landau-Zener transitions at the band edge are negligible ( $< 1\%$ ), while still maintaining an overall fast evolution time to minimize decoherence effects. Due to experimental imperfections, a small fraction (less than 10%) was transferred to higher bands.

In the experiment, for each measured fringe we also took a reference fringe for which the total geometric phase was zero. The sequence used to obtain these fringes consisted of following the steps one to three of the protocol described above, with the difference being that the dimerization was not swapped in the second step. As a consequence, the spin components return to  $k = 0$  in the lowest band and the geometrical phase is cancelled out, i.e.  $\delta\varphi = 0$ . The phase difference between the fringe and its reference is directly equal to  $\varphi_{\text{Zak}}^{D1} - \varphi_{\text{Zak}}^{D2}$ . The reason why we took the reference fringe is because the initial phase of the Ramsey fringe can also be affected by imperfections in the Ramsey sequence (see below).

A typical result for the two Ramsey fringes obtained with and without dimerization swapping during the state evolution can be seen in Fig. 4.6a. Each plotted value for a

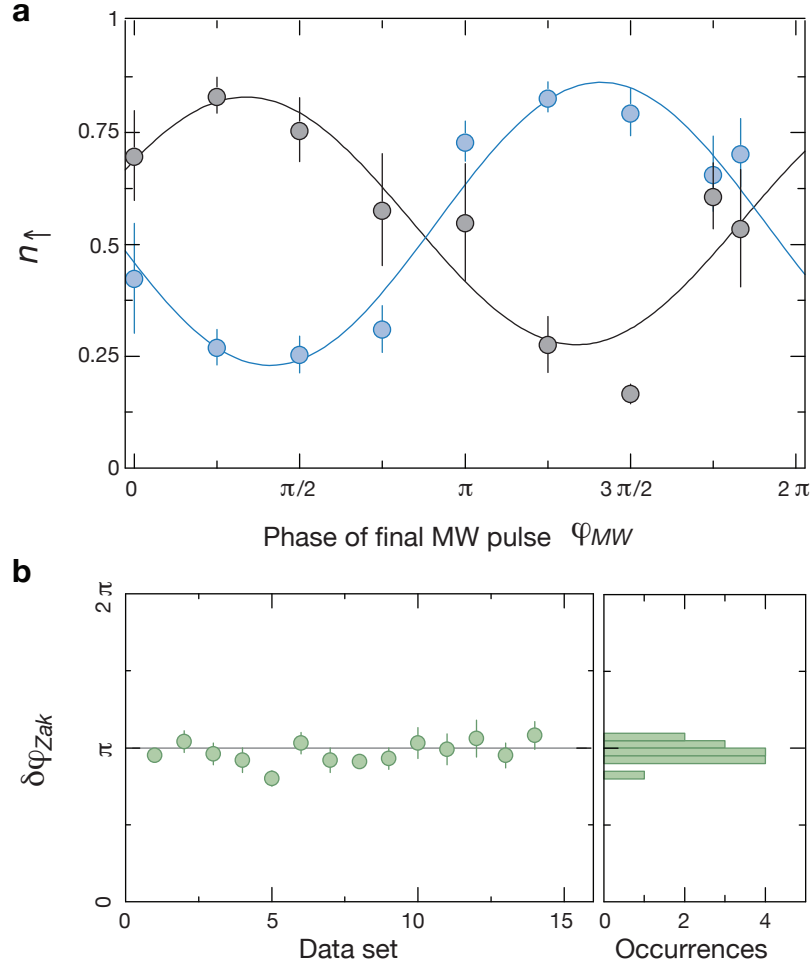


Figure 4.6: Determination of the Zak phase. **(a)** Following the sequence described in the text, the atom number in the two spin states  $N_{\uparrow,\downarrow}$  is measured and the fraction of atoms in the  $|\uparrow\rangle$  spin state  $n_{\uparrow} = N_{\uparrow}/(N_{\uparrow} + N_{\downarrow})$  is plotted as a function of the phase of the final microwave  $\pi/2$ -pulse. Blue (black) circles correspond to the fringe in which the dimerization was (not) swapped, and the corresponding solid lines are sinusoidal fits to the data, where the free parameters were the amplitude, offset and initial phase. The difference in phase of the two fits to the Ramsey fringes yields the Zak phase difference  $\delta\varphi_{Zak} = \varphi_{Zak}^{D1} - \varphi_{Zak}^{D2}$ . In order to reduce the effect of fluctuations, every data point is an average of five individual measurements and the error bars show the standard deviation of the mean. The phase of the reference fringe (black) is determined by a small detuning of the microwave pulse. **(b)** Measured relative phase for 14 identical experimental runs (left), which give an average value of  $\delta\varphi_{Zak} = 0.97(2)\pi$ . The corresponding histogram is shown on the right with a binning of  $0.05\pi$ . The  $1\sigma$ -width of the resulting distribution is  $\sigma = 0.07\pi$ .

given phase  $\varphi_{MW}$  is an average over five identical measurements in order to reduce the effect of residual fluctuations. We performed a further statistical analysis by recording 14 independent Ramsey fringes for the two configurations. The phase differences obtained are shown in Fig. 4.6b together with the corresponding histogram. From these individual measurements we determine the geometric phase difference between the two dimerized configurations to be

$$\delta\varphi = 0.97(2)\pi,$$

in excellent agreement with theory (as discussed in the previous chapter). The uncertainty in the recorded value denotes the standard error of the mean obtained from the distribution function (Fig. 4.6b) and it is mainly determined by experimental imperfections in the control of the underlying lattice potentials, particularly of the relative phase  $\phi$  between the two standing waves.

The initial phase of the measured fringes was affected by a reproducible 80-kHz drift in the offset magnetic field during the time of a full Bloch oscillation. Due to this, the three MW pulses were not all on resonance. The first (last)  $\pi/2$ -pulse was detuned by  $-40$  kHz (40 kHz) and the intermediate  $\pi$ -pulse was on resonance. This detuning also leads to a reduced maximum contrast of the Ramsey fringes of 0.8(1). The drift in the offset magnetic field also adds a constant value to the Zeeman phase  $\varphi_{Zeeman}$ , which is independent of the change of dimerization, and therefore it does not affect the phase difference  $\delta\varphi$ . The contrast of the Ramsey fringes is further reduced by the detuning across the cloud created by the magnetic field gradient. The Fourier-transform limited linewidth of the resonance is 150(20) kHz, which is about two times larger than the MW coupling strength of 80 kHz, and therefore this could lead to a further reduction of the contrast by 10-20%.

The two different Zeeman states used for the measurements have a different light shift, and therefore the tunneling amplitudes are slightly different for both components. However, as long as the relation  $J > J'$  or  $J' > J$  holds for each component, the Zak phase is not affected, because as a topological invariant it is independent of the specific values of  $J$  and  $J'$ , i.e. as long as the gap is not closed the Zak phase is not affected. On the other hand, the dynamical phases are going to be different and they might not cancel for both spin components. A calculation of the dynamical phases shows that one would need a difference larger than 80% between the ratios  $J/J'$  seen by the two components to obtain a drift of the measured Zak phase on the order of the current experimental error. This difference is much larger than the differential light shift for the involved transitions, which is on the order of 0.1%, and therefore it can be safely neglected.

The quadratic Zeeman shift for the two spin components used in the experiment could also affect the measured Zak phase. However, for the experimental magnetic field offset of 4 G, the difference in the magnetic gradients for the two components gives a Bloch oscillation time difference of  $3 \mu\text{s}$ , which is an order of magnitude smaller than

the experimental error of  $\pm 30 \mu\text{s}$  for the Bloch oscillation time. The effect of this is that the two spin components arrive at the band edges at slightly different times which leads to an imperfect atom transfer to the upper band, but it is still larger than 99%.

### 4.2.3 Edge states and trapping effects

In section 3.3.4 it was shown that for a finite size SSH system, the value of the Zak phase underlies the presence of edge states. In order to observe this, one would need to realize a finite size system limited by hard walls at the edges, something that is currently not available in our setup. The new generation of experiments under construction will potentially be able to recreate the hard-wall conditions and confirm the presence of edge states. For those experiments, it is interesting to ask what would be the necessary power law potential such that the system behaves as a finite size system. When a power law potential  $(r/r_0)^\gamma$  is present, we find the absence or presence of edge states to still be clearly visible down to power laws of about  $\gamma = 10 - 12$  compared to the ideal box-potential confinement (see Fig. 4.7 for  $\gamma = 12$ ). Such system should also clearly allow one to observe charge fractionalization although the edge states spread out over a larger region for lower gamma and will reduce the value of the measured fractional charge (relative to the background density of 1/2 in a half filled band case). Clearly, a situation with hard walls would be favorable for experiments.

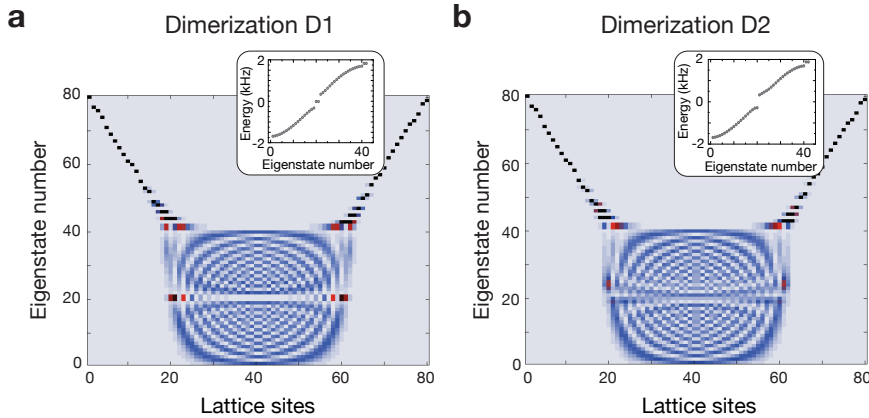


Figure 4.7: Density plot for the different eigenstates for the dimerizations D1 **(a)** and D2 **(b)** in a finite size system with 80 lattice sites, coupling  $J/J' = 1\text{kHz}/0.7\text{kHz}$  and trapping potential of the form  $(r/r_0)^\gamma$  with  $\gamma = 12$  and  $r_0 = 20$  lattice sites. The horizontal axis represents the lattice sites and the vertical axis the eigenstate number. The insets show the energies as a function of the eigenstate number up to 40. For the dimerization D1 there are two isolated eigenenergies that correspond to the two visible localized edge states. For the dimerization D2 there is no isolated eigenstate and no visible localized state.

## 4.3 Experimental measurement of fractional Zak phases

### 4.3.1 Experimental sequence and results

The results presented in the previous section correspond to a dimerized lattice which models polyacetylene, where the phase difference  $\delta\varphi_{Zak} = \pi$  between the two possible polyacetylene phases indicates that the two phases correspond to different topological classes. In this section we will show our results for a dimerized lattice with staggering, which corresponds to a linear conjugated diatomic polymer [155] and is captured by the Rice-Mele Hamiltonian described in the previous chapter:

$$\hat{H} = -\sum_n (J\hat{a}_n^\dagger\hat{b}_n + J'\hat{a}_n^\dagger\hat{b}_{n-1} + \text{h.c.}) + \Delta\sum_n (\hat{a}_n^\dagger\hat{a}_n - \hat{b}_n^\dagger\hat{b}_n). \quad (4.3)$$

In this case, the energy offset  $\Delta$  displaces the pseudo-spin Bloch vectors away from the equatorial plane, resulting in an additional dependence of the Zak phase on the offset  $\Delta$  and the band index (see Fig. 4.8 and section 3.3):

$$\mathbf{u}_{-,k} = \begin{pmatrix} \sin \frac{\gamma_k}{2} \\ \cos \frac{\gamma_k}{2} e^{-i\theta_k} \end{pmatrix}, \quad \mathbf{u}_{+,k} = \begin{pmatrix} -\cos \frac{\gamma_k}{2} \\ \sin \frac{\gamma_k}{2} e^{-i\theta_k} \end{pmatrix}, \quad \gamma_k = \arctan \frac{\varepsilon_k}{\Delta}. \quad (4.4)$$

To probe the dependence of  $\varphi_{Zak}$  on  $\Delta$ , an experimental sequence similar to the one described in the previous section was performed. However, instead of swapping the dimerization from D1 to D2, an energy offset  $|\Delta| < 2J$  was introduced for one half of the sequence (see Fig. 4.8). Thereafter, because of the spin-echo pulse, the wavepackets return to  $k = 0$  in the lowest band. Although the system completes a full Bloch oscillation in the lowest band, the total geometric phase acquired is not zero, because the Bloch vector is displaced from the equatorial plane during one half of the sequence and the Zak phase is changed from  $\varphi_{Zak}$  to  $\varphi_{Zak}(\Delta)$ . The resulting phase in the Ramsey fringe is thus given by  $\delta\varphi = \varphi_{Zak} - \varphi_{Zak}(\Delta)$ . A reference fringe with  $\Delta = 0$  was also taken, for which  $\delta\varphi = 0$ . As before, the phase difference between these two fringes for atoms in the lower band allows us to determine the relative phase  $\varphi_{Zak} - \varphi_{Zak}(\Delta)$ .

During the non-adiabatic switching of the superlattice potential at step 2 of the experimental sequence, some of the atoms are transferred to the higher band and acquire a different geometric phase. However, taking into account this contribution to the measured phase difference enabled us to extract the relative phase  $\delta\varphi$  from our data (see section 4.3.2). As shown in Fig. 4.9, we find good agreement between the measured and predicted values of the fractional Zak phase. Moreover, for  $\Delta = 0$  we find that within experimental error  $\varphi_{Zak} - \varphi_{Zak}(\Delta) = 0$ , which indicates that the process of switching on the second superlattice does not introduce additional phases.

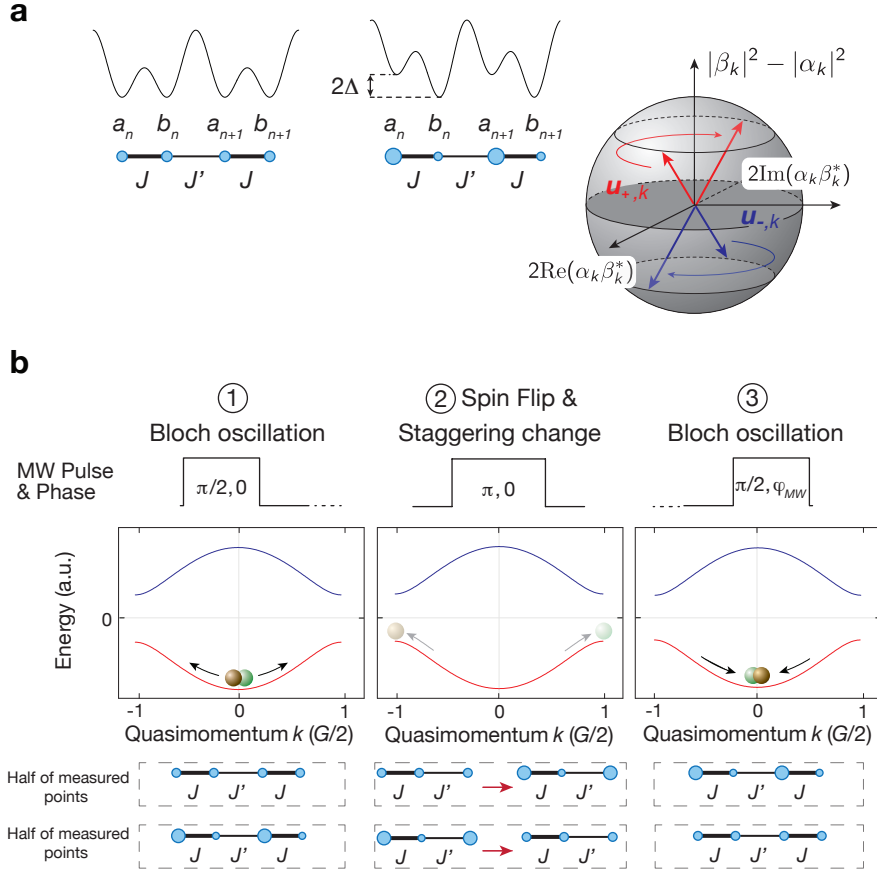


Figure 4.8: Fractional Zak phase. **(a)** Lattice potential without and with an on-site energy staggering  $\Delta$ . When  $\Delta = 0$  the Zak phase is  $\varphi_{\text{Zak}}(\Delta = 0) = \pi/2$ . As  $\Delta$  increases, the pseudo-spin vectors move away from the equatorial plane and the value of  $\varphi_{\text{Zak}}(\Delta)$  decays rapidly to zero. The energy offset  $\Delta$  is achieved by choosing  $\phi \neq 0$  (see also Fig. 4.3). **(b)** Experimental sequence. In the first step the atoms undergo Bloch oscillations in the lowest band until they reach the band edge. In step 2 the spin is flipped and the staggering  $\Delta$  is introduced/removed. In the last step the atoms return to  $k = 0$  in the lowest band and a final MW pulse with a phase  $\varphi_{MW}$  is applied. As illustrated at the bottom of the figure, for half of the measured points the sequence started with an energy staggering  $\Delta \neq 0$  that was changed to  $\Delta = 0$  in step 2, and the other way around for the second half. Note that for this sequence only the dimerization  $D1$  was used.

### 4.3.2 Extracting the phase difference $\varphi_{\text{Zak}} - \varphi_{\text{Zak}}(\Delta)$

In this section we explain how the value of  $\varphi_{\text{Zak}} - \varphi_{\text{Zak}}(\Delta)$  was extracted from the measured fringes for Fig. 4.9. Due to a fraction of atoms transferred to the upper band when  $\Delta \neq 0$ , the phase difference between the two Ramsey fringes deviates from  $\varphi_{\text{Zak}} - \varphi_{\text{Zak}}(\Delta)$ . The reason for this is that the fraction of atoms in the upper band acquires a different geometric phase  $\varphi_{\text{Zak},+}(\Delta) = \pi - \varphi_{\text{Zak},-}(\Delta)$  (see Eq. 3.36) than the fraction in the lower band. Therefore, when measuring the Ramsey fringe, both phases

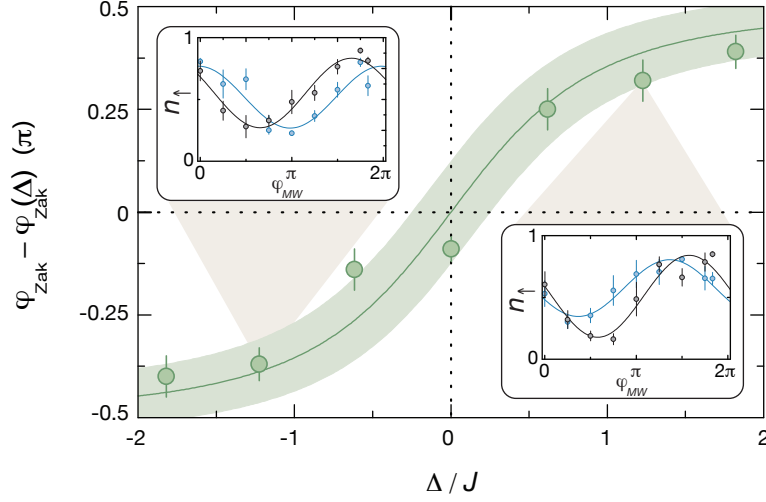


Figure 4.9: Fractional Zak phase. Measured phase difference  $\varphi_{Zak} - \varphi_{Zak}(\Delta)$  as a function of  $\Delta$ . Each individual point was obtained from four individual measurements. The vertical error bars represent the standard error of the mean. The green line is the theoretical prediction and the shaded area indicates the uncertainties in the calibration of the energy offset  $\Delta$ . The insets show a typical Ramsey fringe for  $\Delta/J = -1.2$  (left) and  $\Delta/J = 1.2$  (right), which were used to extract the relative phase  $\delta\varphi$ . The blue (black) fringes correspond to measurements with (without) staggering.

come into play as explained below.

As described in section 4.3.1, for half of the measured points during the first part of the Bloch oscillation the atoms evolve in the lower band of the dimerized system with  $\Delta = 0$  (for the second half of the measured points the atoms start in the lower band with  $\Delta \neq 0$ , which gives essentially the same result). When they reach the edge of the band, the wave function is

$$|\psi\rangle = \frac{1}{\sqrt{2}} (|\uparrow, -G/2\rangle_- e^{i\varphi_{Zak}/2} + |\downarrow, G/2\rangle_- e^{-i\varphi_{Zak}/2}),$$

where  $\varphi_{Zak} = \varphi_{Zak,-}(\Delta = 0)$ . For simplicity, the Zeeman phase is not written, as it is in any case cancelled due to the spin-echo  $\pi$ -pulse. When the energy offset  $\Delta$  is introduced, a fraction of atoms is transferred to the upper band. The upper- and lower-band populations  $n_{\pm}$  after such a non-adiabatic turn on of the staggering  $\Delta$  can be obtained by projecting the lower-band eigenstates with  $\Delta = 0$  onto the states with  $\Delta \neq 0$  (see Eq. 3.32). They are given by

$$n_{\pm} = \frac{1 \mp \sin(\gamma_k)}{2} = \frac{\tilde{\varepsilon}_k \mp \varepsilon_k}{2\tilde{\varepsilon}_k}, \quad (4.5)$$

where all the quantities here are defined for the final non-zero value of  $\Delta$  (Fig. 4.10).

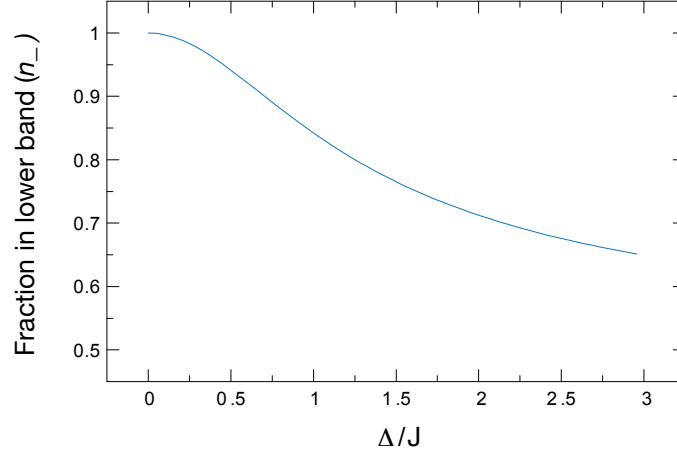


Figure 4.10: Theoretically calculated atom fraction in the lower band ( $n_-$ ) as a function of the energy offset in units of  $J$ . As  $\Delta/J$  increases, the fraction transferred to the upper band ( $n_+$ ) also increases. In the limit  $\Delta/J \rightarrow \infty$ ,  $n_- \rightarrow 0.5$ .

Then, when the MW  $\pi$ -pulse is applied and the energy offset  $\Delta$  is quickly introduced, the spins are flipped and the populations in the bands are  $n_{\pm}$ , resulting in the wave function

$$|\psi\rangle = \frac{1}{\sqrt{2}} \left( \sqrt{n_-} | -G/2 \rangle_- + \sqrt{n_+} | -G/2 \rangle_+ \right) e^{i\varphi_{\text{Zak}}/2} |\downarrow\rangle \\ + \frac{1}{\sqrt{2}} \left( \sqrt{n_-} | G/2 \rangle_- + \sqrt{n_+} | G/2 \rangle_+ \right) e^{-i\varphi_{\text{Zak}}/2} |\uparrow\rangle.$$

In the second half of the Bloch oscillation the particles return to  $k = 0$  and the fraction in the upper (lower) band picks up a phase  $\varphi_{\text{Zak},+}(\Delta)$  ( $\varphi_{\text{Zak},-}(\Delta)$ ), such that the resulting state vector is:

$$|\psi\rangle = \frac{1}{\sqrt{2}} \left\{ \sqrt{n_-} |0\rangle_- e^{-i\varphi_{\text{Zak},-}(\Delta)/2} + \sqrt{n_+} |0\rangle_+ e^{-i\varphi_{\text{Zak},+}(\Delta)/2} \right\} e^{i\varphi_{\text{Zak}}/2} |\downarrow\rangle \\ + \frac{1}{\sqrt{2}} \left\{ \sqrt{n_-} |0\rangle_- e^{i\varphi_{\text{Zak},-}(\Delta)/2} + \sqrt{n_+} |0\rangle_+ e^{i\varphi_{\text{Zak},+}(\Delta)/2} \right\} e^{-i\varphi_{\text{Zak}}/2} |\uparrow\rangle.$$

Finally, a  $\pi/2$ -pulse with a MW phase is applied, which rotates the spins according to  $|\uparrow\rangle \rightarrow \frac{1}{\sqrt{2}}(e^{-i\varphi_{\text{MW}}/2} |\uparrow\rangle + e^{+i\varphi_{\text{MW}}/2} |\downarrow\rangle)$  and  $|\downarrow\rangle \rightarrow \frac{1}{\sqrt{2}}(e^{i\varphi_{\text{MW}}/2} |\uparrow\rangle + e^{-i\varphi_{\text{MW}}/2} |\downarrow\rangle)$ . After this pulse, the total population in  $|\uparrow\rangle$  is given by:

$$n_{\uparrow} = \frac{1}{2} \left\{ 1 + n_- \cos(\varphi_{\text{Zak}} - \varphi_{\text{Zak},-}(\Delta) + \varphi_{\text{MW}}) + n_+ \cos(\varphi_{\text{Zak}} - \varphi_{\text{Zak},+}(\Delta) + \varphi_{\text{MW}}) \right\}, \quad (4.6)$$

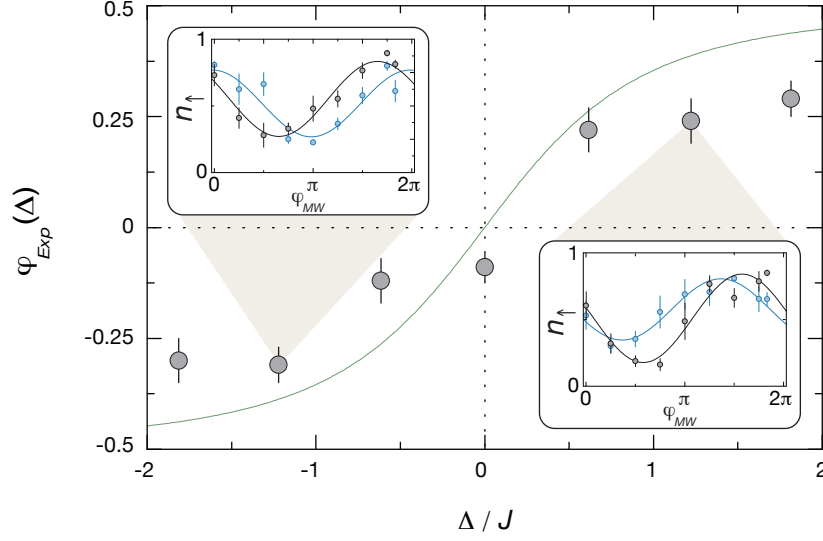


Figure 4.11: Measured phase difference  $\varphi_{Exp}$  as a function of the energy offset in units of  $J$ . The green line shows the predicted value of  $\varphi_{Zak} - \varphi_{Zak}(\Delta)$  when there is no population transfer to the upper band.

and a similar expression for  $n_{\downarrow}$ . The Ramsey fringe is obtained by measuring the population in each spin component as a function of the MW phase  $\varphi_{MW}$ .

For negligible  $n_{+}$  the phase of the Ramsey fringes directly corresponds to  $\varphi_{Zak} - \varphi_{Zak,-}(\Delta)$ . For any finite value of  $n_{+}$ , one can recast Eq. 4.6 in the form  $A + B \cos(\varphi_{Exp} + \varphi_{MW})$  and solve for  $\varphi_{Zak} - \varphi_{Zak,-}(\Delta)$  using the relation  $\varphi_{Zak,+}(\Delta) = \pi - \varphi_{Zak,-}(\Delta)$  and the theoretical values of  $n_{\pm}$ , where  $\varphi_{Exp}$  is the measured phase difference between the Ramsey fringes. The resulting values of  $\varphi_{Zak} - \varphi_{Zak,-}(\Delta)$  are displayed in Fig. 4.9, and the values of  $\varphi_{Exp}$  are shown in Fig. 4.11.

### 4.3.3 Symmetries and generalizations of the measurement scheme

For the measurements presented here, we made use of special symmetries in our Hamiltonian that allowed us to extract the phase difference between the two topologically distinct phases. This was the simplest way to address the problem of fluctuating magnetic fields in the laboratory. In principle, our scheme does not require the use of these special symmetries if sufficiently stable magnetic fields are achieved. In that case, one could directly implement the protocol presented in 4.1.1 and the dynamical phase would be cancelled for any time-reversal invariant Hamiltonian. Furthermore, in the absence of any symmetry in the band, the dynamical phase could be still isolated from the geometric phase by analyzing the Ramsey phase as a function of the Bloch oscillation velocity.

We also would like to note that while the Ramsey fringe only measures the Zak phase

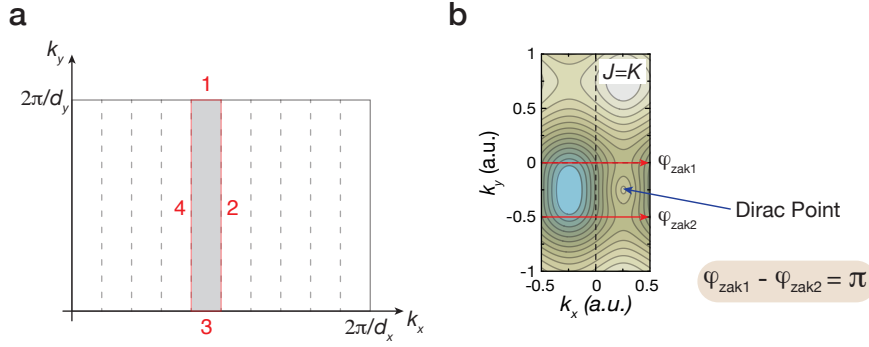


Figure 4.12: Generalization of the protocol to two-dimensional systems. **(a)** Brillouin zone of a generic two-dimensional lattice. The Berry phase associated with the grey area is equal to the difference between the Zak phases along the path 2 and 4, because the ones along 1 and 3 cancel with each other. Due to this, the change in the Zak phase along the  $k_y$  direction as a function of  $k_x$  is related to the Chern number of the Band, i.e. the Chern number is equal to the winding number of the Zak phase across the Brillouin zone **(b)** Energy dispersion relation of the staggered flux lattice corresponding to the reference [45]. By measuring the Zak phase for the highlighted paths one can obtain the  $\pi$  Berry phase corresponding to the Dirac point.

modulo  $2\pi$ , a complete characterization can be achieved by evolving from a reference Hamiltonian into a desired Hamiltonian without closing a gap in the energy spectrum and monitoring the evolution of the Zak phase.

The protocol presented here to measure the Zak phase can be easily extended to two-dimensional systems and used to fully characterize the band topology (see Fig. 4.12), a proposal which has been developed by D. Abanin and collaborators [66]. The idea of the protocol is to measure the Zak phase for different parallel paths and then use the relation between the Chern number and the Zak phase to extract the Chern number from these values. Furthermore, they propose using the technique to measure the  $\pi$  Berry phase for a trajectory enclosing a Dirac point, an idea that has been recently implemented in graphene-like optical lattices [186].

## 4.4 Conclusion

In conclusion, we have presented a general approach for studying topological properties of Bloch bands in optical lattices and demonstrated its versatility through a first measurement of the topological invariant in topologically non-trivial Bloch bands. Topologically distinct many-body phases can arise from such topologically distinct Bloch bands when the bands are filled with fermions. Making use of the recently demonstrated control of optical potentials at the single-site level [187], one could realize domain walls or sharp boundaries in the dimerized lattice that would allow the direct

study of edge states [188, 189] and fractional charges for non-interacting fermions or hardcore bosons [65, 152, 153, 190, 191].

Although in this work we focused on one-dimensional systems, our technique can easily be extended to two-dimensional systems, where the change of the Zak phase in the Brillouin zone gives the topological density of the Bloch band [66]. This enables measurements of both the Chern number of topological bands and the  $\pi$ -flux associated with a Dirac point. Additionally, we expect that this idea could be extended to measure the non-Abelian Berry phase in Bloch bands (such as in a system with the quantum spin Hall effect [192]), to study Floquet states in periodically driven systems [104, 193, 194], and to quasiparticles in unconventional superconductors, such as  $d$ -wave superconductors, which have a Dirac dispersion at the nodal points [195]. Overall, our work indicates that cold atomic systems provide a versatile platform for studying topological states of matter, and establishes a novel method for probing their properties.



## Chapter 5

# Analog of the Meissner effect in flux ladders

In this chapter, we begin with a short introduction to the Meissner effect in superconductors to then connect with an analog effect that is present in a ladder system exposed to an artificial external magnetic field. It will be shown that the flux ladder possesses two different phases: the Meissner phase, where the system presents a uniform chiral current along the legs of the ladder, and a vortex phase, where the currents in the ladder exhibit a vortex structure. These two phases have some analogies with the Meissner and Abrikosov vortex phases present in a superconductor.

### 5.1 Introduction to the Meissner effect

The electrical resistivity of metals decreases with decreasing temperature. Despite vibrations, for an ideal crystal where there are no defects or impurities, the resistivity vanishes at  $T = 0$  and stays finite for finite temperatures. However, due to imperfections in the crystal, the transport relaxation times are finite even at zero temperature and the conductivity stays finite even at zero temperature. It was therefore a big surprise when in 1911, H. Kamerlingh Onnes observed that the resistivity of mercury dropped to a very low value (zero within experimental error) at a temperature of around  $T = 4.2K$  (see Fig. 5.1) [196]. This property, called superconductivity, for which the resistivity dropped suddenly to zero at some critical temperature  $T_c$ , was later on confirmed to be present in a large variety of metals.

The drop in resistivity was only one of the hallmark features defining the transition to the superconducting state. In 1933, Meissner and Ochsenfeld observed another phenomena appear in the superconducting phase: a superconductor behaves like a perfect diamagnet [69]. When a superconductor at  $T > T_c$  is placed in an external magnetic field, the field lines penetrate its core. However, when it is cooled below the critical tem-

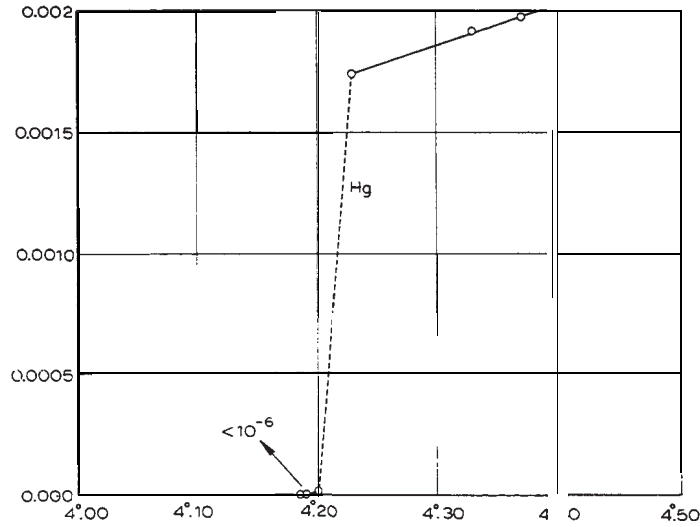


Figure 5.1: Temperature dependence of the resistivity of mercury. For  $T > 4.2\text{K}$  the resistivity is finite, and when  $T$  is decreased to around  $T_c = 4.2\text{K}$ , the resistivity suddenly drops to zero and the system enters into a superconducting phase. (Image extracted from H. K. Onnes' Nobel lecture [197]).

perature, it enters into the superconducting state and the superconductor fully repels the magnetic field from its core (see Fig. 5.2a). This behavior can be explained by the presence of currents in a thin layer on the surface of the superconductor, which are induced by the external magnetic field. These currents create a magnetization that cancels the applied field in the core of the superconductor. There are different types of superconductors [198, 199]. For a superconductor of type I (see Fig. 5.2b), when the applied external magnetic field  $H_{ext}$  is smaller than the critical field  $H_{c1}$ , the system finds itself in the so-called Meissner state, where the magnetization  $M$  is proportional to  $H_{ext}$  and there is full screening of the applied field. For  $H_{ext} > H_{c1}$  the magnetization suddenly drops to zero and the material is in a normal state. On the other hand, for a type II superconductor (see Fig. 5.2c), there are two critical fields  $H_{c1}$  and  $H_{c2}$ . If  $H_{ext} < H_{c1}$ , the material is in the Meissner state and the magnetization is proportional to the external field. For  $H_{c1} < H_{ext} < H_{c2}$ , the system is in the Abrikosov-vortex phase [200], and the surface currents only partially screen the applied field. In this case, the superconducting state presents a vortex structure through which the external field can penetrate. Finally, for  $H_{ext} > H_{c2}$ , the system is in a normal state where no screening is present at all.

A full microscopic description of the Meissner effect and superconductivity is given by BCS theory [70], which explains that at very low temperature, electrons with attractive interactions form the so-called Cooper pairs and behave like bosonic particles which can undergo Bose-Einstein condensation. A more phenomenological description of the

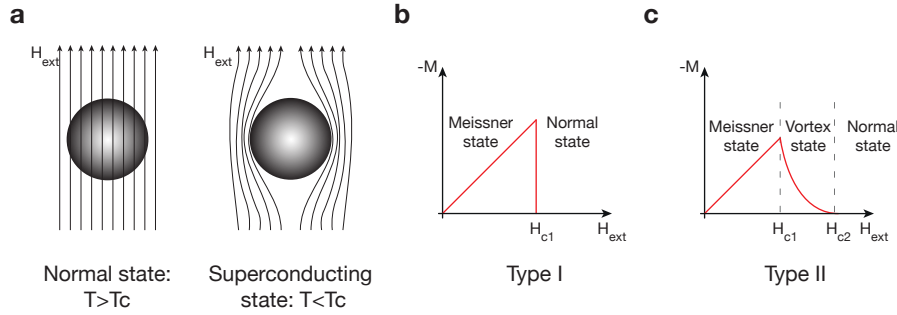


Figure 5.2: Meissner effect. **(a)** Magnetic field lines around a material in a normal state (left) and superconducting state (right). **(b), (c)** Magnetization of a type I (b) and a type II (c) superconductor as a function of the applied field. For the type I case, when  $H_{ext} < H_{c1}$ , the material is in a superconducting state and there is full screening of the applied field, and when  $H_{ext} > H_{c1}$ , the material is in a normal state and the external field fully penetrates the sample. For a type II superconductor there is an intermediate state that corresponds to  $H_{c1} < H_{ext} < H_{c2}$  in which the external field is only partially screened.

Meissner effect is provided by the London equations [201]. In 1935, the brothers Fritz and Heinz London proposed the following system of equations to describe the electric and magnetic properties of superconductors

$$\frac{d\mathbf{j}}{dt} = \frac{ne^2}{m}\mathbf{E}, \quad \nabla \times \mathbf{j} = -\frac{ne^2}{m}\mathbf{B}, \quad (5.1)$$

where  $n$ ,  $m$ ,  $e$  and  $\mathbf{j}$  are respectively the density, mass, electric charge and current of the particles in the superconducting state, and  $\mathbf{B}$  and  $\mathbf{E}$  are the magnetic and electric field in the superconductor. The Maxwell equations tell us that  $\frac{1}{\mu_0}\nabla \times \mathbf{B} = \mathbf{j}$ , which, together with the second London equation, gives

$$\nabla \times \nabla \times \mathbf{B} = -\frac{1}{\lambda_L^2}\mathbf{B}, \quad (5.2)$$

where  $\lambda_L^2 = m/(ne^2\mu_0)$  is called the London penetration length. If we apply a uniform magnetic field  $B_0$  in the  $z$ -direction to a system where half of the volume ( $x > 0$ ) is filled with a superconducting material and the other half ( $x < 0$ ) with a normal material, then the solution to Eq. 5.2 is

$$B_z(x) = \begin{cases} B_0 & x < 0, \\ B_0 e^{-x/\lambda_L} & x > 0. \end{cases} \quad (5.3)$$

It implies that the magnetic field decays exponentially fast inside the superconductor, with a decay constant given by the London penetration length. Additionally, from the Maxwell equations, one can obtain the corresponding current circulating in the superconductor:

$$j = \frac{1}{\mu_0 \lambda_L} B_0 e^{-x/\lambda_L}, \quad (5.4)$$

which also decays exponentially inside the superconductor. This current is proportional to the applied field and produces a field that screens the external field inside the superconductor, which explains the basic mechanism of the Meissner effect.

## 5.2 Meissner-like effect in a ladder

A ladder consists of two coupled one-dimensional systems and takes its name from its geometrical aspect. When it is exposed to a magnetic field, very interesting physics appears because it is the smallest possible system that exhibits topological properties that are closely connected to the integer quantum Hall effect, i.e. the chiral modes of the flux ladder are in correspondence with the edge states of the quantum Hall effect [202]. Previously, these ladder systems have been theoretically studied within the context of Josephson junctions arrays, where it has been first suggested that there is an analogy between this system and the Meissner effect [203–211] and also in the context of ultracold atoms exposed to an artificial magnetic field [202, 211–214].

### 5.2.1 Ladder in a magnetic field

The ladder system considered here consists of non-interacting bosonic particles in an infinitely extended two-leg ladder geometry subject to a magnetic flux  $\phi$  per plaquette (see Fig. 5.3). Along the horizontal direction, the coupling term is  $K$ , which is homogeneous through the system. Along the vertical direction, the spatially dependent complex coupling term is  $J_{\ell;\mu} = J e^{\pm i\varphi}$ , where  $\ell$  denotes the lattice site and  $\mu = (L, R)$  stands for the left and right leg of the ladder. The plus sign corresponds to the left leg and the minus to the right one. The Hamiltonian describing this system is

$$H = -J \sum_{\ell} \left( e^{i\varphi} \hat{a}_{\ell+1;L}^{\dagger} \hat{a}_{\ell;L} + e^{-i\varphi} \hat{a}_{\ell+1;R}^{\dagger} \hat{a}_{\ell;R} \right) - K \sum_{\ell} \left( \hat{a}_{\ell;L}^{\dagger} \hat{a}_{\ell;R} \right) + \text{h.c.}, \quad (5.5)$$

where the operator  $\hat{a}_{\ell;\mu}$  annihilates a particle at site  $\ell$  in the left or right leg of the ladder.

The complex phases in the coupling terms are called Peierls phases and are associated with the magnetic field that pierces the system through the expression  $J_{\ell;\mu} = |J_{\ell;\mu}| e^{-ie/\hbar \int_{\ell}^{\ell+1} \mathbf{A} \cdot d\mathbf{l}}$ , where  $\mathbf{B} = \nabla \times \mathbf{A}$  [215, 216]. Thus, if one considers a closed path on a single plaquette as shown in Fig. 5.4, the total magnetic flux through the loop is

$$\phi = \varphi_1 + \varphi_2 - \varphi_3 - \varphi_4, \quad (5.6)$$

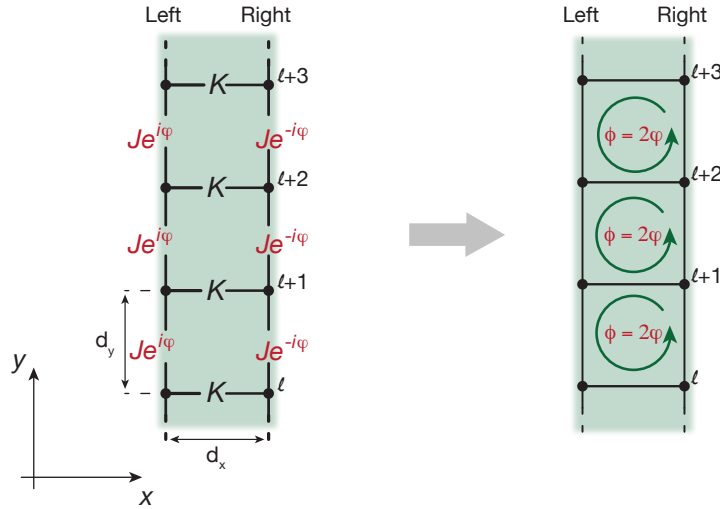


Figure 5.3: Schematic of a ladder system. The ladder system with its corresponding coupling terms is displayed on the left side. The ladder with the corresponding effective flux  $\phi = 2\varphi$  associated with the complex phases of the coupling terms is shown on the right side. The lattice constants are given by  $d_{x,y}$ .



Figure 5.4: Single plaquette with complex phases to illustrate the total phase picked up by a particle that travels along a closed loop around the plaquette. The corresponding effective magnetic flux is then given by the sum of these phases.

and it is given in units of  $\phi_0/(2\pi)$ , where  $\phi_0 = h/e$  is the flux quantum. Using this relation in our Hamiltonian, one can see that the magnetic flux is  $\phi = 2\varphi$ .

The eigenstates of H can be calculated by introducing the momentum operators

$$\hat{a}_{q;\mu} = \sum_{\ell} e^{iq\ell d_y} \hat{a}_{\ell;\mu}, \quad (5.7)$$

and solving the Schrödinger equation for the ansatz  $|\psi_q\rangle = (\alpha_q \hat{a}_{q;L}^\dagger + \beta_q \hat{a}_{q;R}^\dagger) |0\rangle$ . The final equations for  $\alpha_q$  and  $\beta_q$  can be written as

$$\begin{pmatrix} 2J\cos(\varphi - qd_y) & K \\ K & 2J\cos(\varphi + qd_y) \end{pmatrix} \begin{pmatrix} \alpha_q \\ \beta_q \end{pmatrix} = \varepsilon_q \begin{pmatrix} \alpha_q \\ \beta_q \end{pmatrix}. \quad (5.8)$$

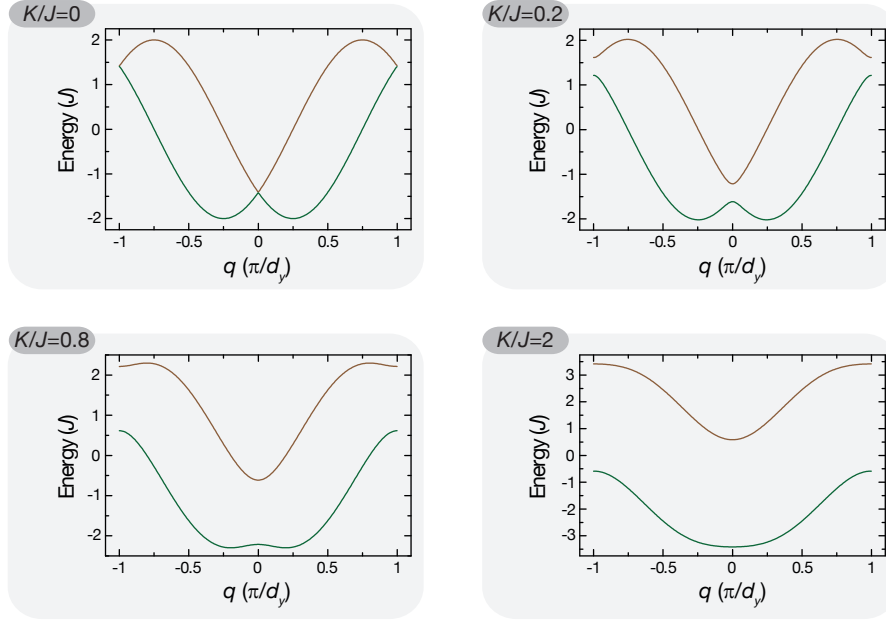


Figure 5.5: Energy bands for different values of  $K/J$  and constant flux  $\phi = \pi/2$ . For  $K = 0$ , the two legs are isolated and the bands correspond to the independent bands of the two legs, shifted from  $q = 0$  due to the complex phases in the tunneling terms. When  $K > 0$ , a gap opens and the two independent bands start mixing with each other. For  $K/J < (K/J)_c$ , the lowest band presents two minima at  $\pm q_{K/J}$  and for  $K/J > (K/J)_c$  there exists a single minimum at  $q = 0$ .

The corresponding solution gives two energy bands:

$$\varepsilon_q = 2J\cos(qd_y)\cos(\varphi) \pm \sqrt{K^2 + 4J^2\sin^2(\varphi)\sin^2(qd_y)}. \quad (5.9)$$

The properties of the bands depend on the ratio  $K/J$ . When  $K = 0$ , the two legs are completely isolated and the band structure of the system corresponds to the one of the individual legs (see Fig. 5.5). Each of the legs is a one-dimensional periodic system and possesses an energy band whose minimum is shifted from  $q = 0$  due to the presence of the complex tunneling terms  $J_{\ell;\mu}$ . For finite coupling  $K$ , a gap equal to  $2K$  opens at  $q = 0$  and at  $q = \pm(\pi/d_y)$  and the lowest band presents two minima located at  $\pm q_{K/J}$ , whose value depends on  $K/J$  and  $\varphi$ . When the ratio  $K/J$  is larger than the critical value  $(K/J)_c = 2\sin^2(\varphi)/\cos(\varphi)$ , the lowest band has a single minimum at  $q = 0$ .

The population fractions on the left and right side of the ladder are  $n_\mu = N^{-1} \sum_\ell \langle \hat{a}_{\ell;\mu}^\dagger \hat{a}_{\ell;\mu} \rangle$ , where  $N$  is the total number of particles. For the eigenstate  $|\psi_q\rangle = (\alpha_q \hat{a}_{q;L}^\dagger + \beta_q \hat{a}_{q;R}^\dagger) |0\rangle$ , one can write the population densities as  $n_L = |\alpha_q|^2$  and  $n_R = |\beta_q|^2$ , from which one can see that these densities depend on the quasimomentum  $q$ , on  $K/J$  and on  $\varphi$ . As a general characteristic, at  $q = 0$  the relation  $n_L = n_R$  holds, and when decreasing (increasing)  $q$  to negative (positive) values, the density on the left (right) leg increases.

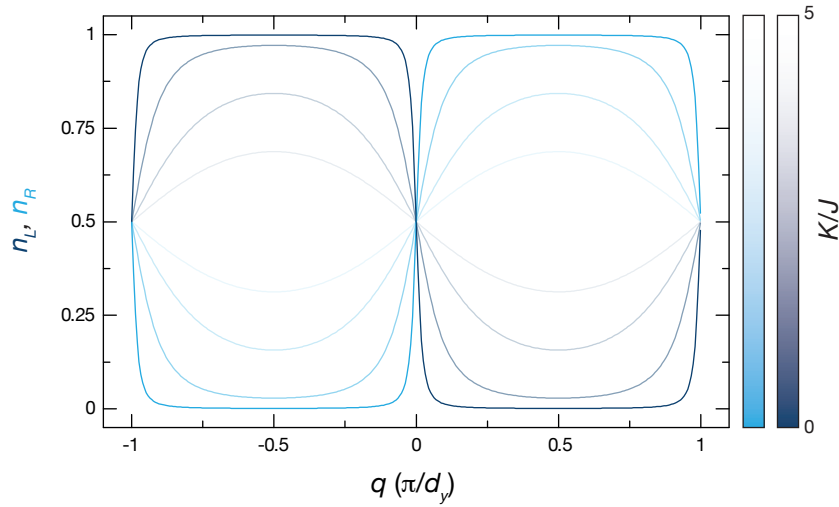


Figure 5.6: Population fractions on the legs of the ladder for different values of  $K/J$  as a function of the quasimomentum  $q$  for the lowest band and for a fixed flux  $\phi = 2\varphi = \pi/2$ . For a given value of  $K/J$ , the density on the left leg is larger (smaller) than the one on the right leg when  $q < 0$  ( $q > 0$ ). As  $K/J$  is increased, the left-right population difference decreases.

In Fig. 5.6, one can see the left-right density fraction for different values of  $q$  and  $K/J$  and for a fixed flux  $\phi = 2\varphi = \pi/2$ . When  $K/J \ll 1$ , the difference between  $n_L$  and  $n_R$  is more pronounced and gets smaller for higher values of  $K/J$ .

### 5.2.2 Currents in ladders

The Hamiltonian of a particle of charge  $e$  and mass  $m$  exposed to an electromagnetic field described by the vector potential  $\hat{\mathbf{A}}$  and the scalar potential  $V_0$  is

$$\hat{H} = \frac{1}{2m} [\hat{\mathbf{p}} - e\hat{\mathbf{A}}(\hat{\mathbf{r}}, t)]^2 + eV_0(\hat{\mathbf{r}}, t) + U(\hat{\mathbf{r}}), \quad (5.10)$$

where  $\hat{\mathbf{p}} = -i\hbar\nabla$  is the momentum operator and  $U(\hat{\mathbf{r}})$  is any other potential to which the particle is exposed. For a given state  $\psi$ , the probability current can be expressed as

$$\mathbf{j}(\mathbf{r}) = \text{Re}\{e\psi^*(\hat{\mathbf{v}}\psi)\}, \quad \hat{\mathbf{v}} = \frac{1}{m} (\hat{\mathbf{p}} - e\hat{\mathbf{A}}). \quad (5.11)$$

It is well known that the vector potential is a gauge dependent quantity in the sense that any other vector potential of the form  $\mathbf{A}' = \mathbf{A} + \nabla f(\mathbf{r})$  produces the same magnetic field  $\mathbf{B} = \nabla \times \mathbf{A}$ . However, this gauge dependence is not shared by the current because the gauge transformation also affects the wavefunction and leaves the current gauge invariant.

When the lattice potential of the ladder is present, i.e. when  $U(\hat{\mathbf{r}})$  is the periodic potential that creates the ladder lattice structure, the current operators in the tight-binding model for each bond of the lattice take the form [217]:

$$\hat{\mathbf{j}}_\ell^x = -i\frac{d_x}{\hbar} \left( \hat{a}_{\ell;R}^\dagger \hat{a}_{\ell;L} H_{\ell;L \rightarrow R} - \text{h.c.} \right), \quad \hat{\mathbf{j}}_{\ell;\mu}^y = -i\frac{d_y}{\hbar} \left( \hat{a}_{\ell+1;\mu}^\dagger \hat{a}_{\ell;\mu} H_{\ell \rightarrow \ell+1;\mu} - \text{h.c.} \right), \quad (5.12)$$

where  $H_{\ell;L \rightarrow R} = \langle 0 | a_{\ell;R} \hat{H} a_{\ell;L}^\dagger | 0 \rangle$  is the Hamiltonian matrix element connecting the sites  $(\ell; L)$  and  $(\ell; R)$ , and  $H_{\ell \rightarrow \ell+1;\mu} = \langle 0 | a_{\ell+1;\mu} \hat{H} a_{\ell;\mu}^\dagger | 0 \rangle$  is the matrix element connecting the sites  $(\ell; \mu)$  and  $(\ell + 1; \mu)$ .

For a general state  $|\psi\rangle = \sum_{\ell;\mu} c_{\ell;\mu} \hat{a}_{\ell;\mu}^\dagger | 0 \rangle$ , the expectation values of the currents take the form

$$\mathbf{j}_\ell^x = \frac{2d_x}{\hbar} \text{Im} \left( c_{\ell;R}^* c_{\ell;L} H_{\ell;L \rightarrow R} \right), \quad \mathbf{j}_{\ell;\mu}^y = \frac{2d_y}{\hbar} \text{Im} \left( c_{\ell+1;\mu}^* c_{\ell;\mu} H_{\ell \rightarrow \ell+1;\mu} \right). \quad (5.13)$$

Finally, one can define the chiral current in the ladder as the average of the differences between the currents on the left and right legs [202]:

$$\mathbf{j}_C = N_{leg}^{-1} \sum_{\ell} (\mathbf{j}_{\ell;L}^y - \mathbf{j}_{\ell;R}^y), \quad (5.14)$$

where  $N_{leg}$  is the length of the ladder and the sum runs over all the lattice sites of the ladder.

Using the expressions given in Eq. 5.13, one can calculate the currents in the ladder for the ground state. When  $K/J > (K/J)_c$ , the ground state is  $|\psi_{q=0}\rangle = (\alpha_0 \hat{a}_{0;L}^\dagger + \beta_0 \hat{a}_{0;R}^\dagger) | 0 \rangle$ . The currents for that state are

$$\mathbf{j}_\ell^x = 0, \quad \mathbf{j}_{\ell;L}^y = \frac{Jd_y}{\hbar} |\alpha_0|^2 \sin(\varphi), \quad \text{and} \quad \mathbf{j}_{\ell;R}^y = -\frac{Jd_y}{\hbar} |\beta_0|^2 \sin(\varphi), \quad (5.15)$$

and the chiral current is given by

$$\mathbf{j}_C = \frac{Jd_y}{\hbar} (|\alpha_0|^2 + |\beta_0|^2) \sin(\varphi). \quad (5.16)$$

When  $K/J < (K/J)_c$ , the lowest band presents two degenerate energy minima at  $\pm q_{K/J}$  and therefore the ground state is not unique. As it will be explained in the next chapter, our experimental results are compatible with a population of a symmetric superposition state of the form

$$|\psi_g\rangle = \left( |\psi_{q_{K/J}}\rangle + e^{i\theta} |\psi_{-q_{K/J}}\rangle \right) / \sqrt{2}. \quad (5.17)$$

At the end of the next section, it will be shown that  $\theta$  only shifts the wavefunction globally and therefore one can choose  $\theta = 0$ . For this state, the currents along the bonds are

$$\begin{aligned}
\mathbf{j}_{\ell;L}^y &= + \frac{Jd_y}{\hbar} [|\alpha_{q_{K/J}}|^2 \sin(d_y q_{K/J} + \varphi) + |\alpha_{-q_{K/J}}|^2 \sin(-d_y q_{K/J} + \varphi) \\
&\quad - 2|\alpha_{q_{K/J}}||\alpha_{-q_{K/J}}| \cos(d_y q_{K/J}(2\ell + 1)) \sin(\varphi)], \\
\mathbf{j}_{\ell;R}^y &= + \frac{Jd_y}{\hbar} [|\beta_{q_{K/J}}|^2 \sin(d_y q_{K/J} - \varphi) + |\beta_{-q_{K/J}}|^2 \sin(-d_y q_{K/J} - \varphi) \\
&\quad + 2|\beta_{q_{K/J}}||\beta_{-q_{K/J}}| \cos(d_y q_{K/J}(2\ell + 1)) \sin(\varphi)], \\
\mathbf{j}_{\ell}^x &= - \frac{Kd_x}{\hbar} \sin(d_y q_{K/J}(2\ell + 1)) [|\alpha_{q_{K/J}}||\beta_{-q_{K/J}}| - |\alpha_{-q_{K/J}}||\beta_{q_{K/J}}|]. \quad (5.18)
\end{aligned}$$

To calculate the chiral current one can neglect the terms proportional to  $\cos(d_y q_{K/J}(2\ell + 1))$  because for  $K/J < (K/J)_c$ , the quasimomentum  $q_{K/J}$  cannot be zero nor  $\pi/d_y$  and therefore those terms are negligible when averaging over the system size. Then, the chiral current takes the form

$$\mathbf{j}_C = \frac{2Jd_y}{\hbar} [|\alpha_{q_{K/J}}|^2 \sin(d_y q_{K/J} + \varphi) + |\alpha_{-q_{K/J}}|^2 \sin(-d_y q_{K/J} + \varphi)], \quad (5.19)$$

where the relations  $|\alpha_{\pm q_{K/J}}| = |\beta_{\mp q_{K/J}}|$  were used.

### 5.2.3 Meissner-like effect in the ladder

In this section we will show that a flux ladder possesses two phases which are distinguished by the current structure along the bonds. For  $K/J > (K/J)_c$ , the system is in a Meissner-like phase, where the currents are maximal and circulate in opposite directions along the two legs of the ladder. When  $K/J < (K/J)_c$ , the system is in a vortex phase, where the currents along the bonds form a vortex structure. Furthermore, we will show that for a fixed  $K/J$ , the chiral current increases with the flux like in the Meissner phase in a superconductor, and if the flux is larger than some critical flux, then the chiral current decreases like in the Abrikosov-vortex phase present in a type II superconductor.

In order to understand the connection between the current behavior in the two regimes and the Meissner effect, it is better to define a critical flux  $\phi_c$ . Since the critical ratio  $(K/J)_c = 2\sin^2(\varphi)/\cos(\varphi)$  depends on the flux, for a given  $K/J$  one can define the critical flux as the flux that one needs in order to have  $(K/J)_c = K/J$ . Under this definition, if  $\phi < \phi_c$ , then  $K/J > (K/J)_c$  and Eq. 5.16 holds, and if  $\phi > \phi_c$ , then  $K/J < (K/J)_c$  and Eq. 5.19 holds.

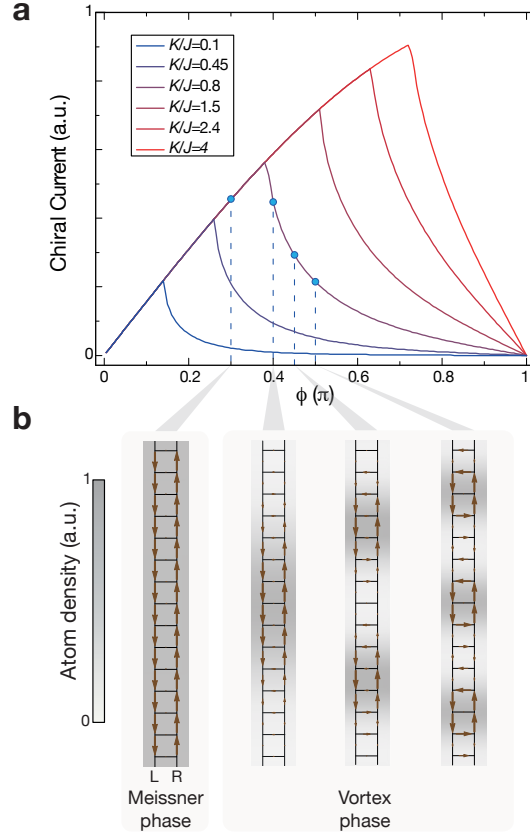


Figure 5.7: **(a)** Chiral current amplitude as a function of the flux. In the Meissner phase, the current increases with flux until the flux reaches the critical value  $\phi_c$  and the system enters into the vortex phase where the current decreases with the flux. **(b)** Theoretically calculated individual currents and particle densities for the different values of  $\phi$  marked in (a) and for  $K/J = 0.8$ . In the vortex phase, the wavefunction exhibits a vortex structure for the currents, whose period decreases with the flux, and the atom density becomes modulated with the same periodicity. In the Meissner phase, on the other hand, the size of the vortex is infinite and the density is uniform. The thickness and length of the arrows denotes the current strength, which is normalized to the maximum current for each flux. To clearly illustrate the modulation of the density, a homogeneous offset was subtracted from the density and the remaining modulation was renormalized for each flux.

Figure 5.7 shows the chiral current  $\mathbf{j}_C$  as a function of the flux for different values of  $K/J$ . For  $\phi < \phi_c$  ( $K/J > (K/J)_c$ ), the ground state of the Hamiltonian exhibits a Meissner phase with maximal and opposite currents along the legs of the ladder. Increasing the flux leads to increasing edge currents up to the critical flux  $\phi_c$  beyond which the current abruptly starts to decrease. At this point the system enters a vortex phase with decreasing edge currents. Such a behavior parallels the one of the Meissner effect in a type-II superconductor and its transition into an Abrikosov vortex lattice phase. In this case,  $\phi_c$  is the flux associated with the critical field  $\mathbf{H}_{c1}$ , and there is no

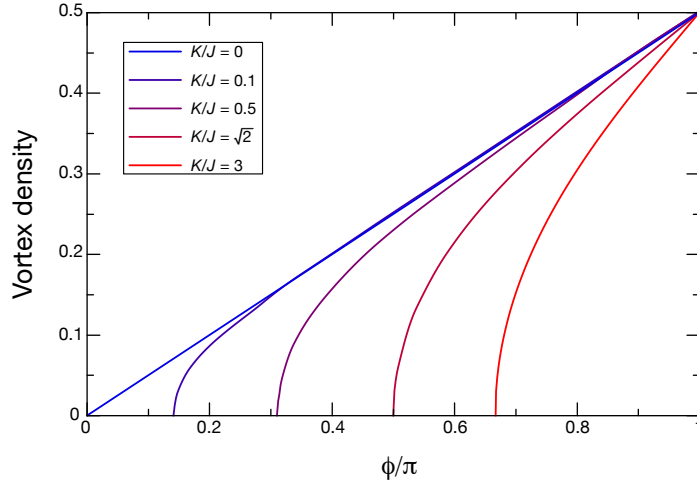


Figure 5.8: Density of vortices per plaquette as a function of the flux for different values of  $K/J$  showing the transition from the vortex-free Meissner phase to a vortex phase with finite vortex density for  $\phi > \phi_c$ . In terms of  $K/J$ , when  $K/J < (K/J)_c$ , there is a single infinitely large vortex and the density of vortices is zero, and for  $K/J \ll 1$ , the vortex density increases almost linearly with the flux.

critical flux corresponding to  $\mathbf{H}_{c2}$ .

It is important to remark on a fundamental difference between the flux ladder system and the Meissner effect. In the former, due to the charge-neutrality of the atoms, the current does not have any back-action onto the system and therefore there is no real screening of the magnetic field. Furthermore, the solution corresponds to the ground state of a single particle Hamiltonian, and therefore the current amplitude depends on the density of particles in the system. On the other hand, in the Meissner effect, the current screens the external magnetic field, and it is a many-body solution to the Hamiltonian. Other systems that present an analogy to the Meissner effect have been studied within the context of rotating superfluids. In the Hess-Fairbank effect, a superfluid is placed in a thin rotating annulus and there is a critical rotation frequency beyond which vortex-line singularities appear in the superfluid [218].

The density of vortices in the ladder as a function of the flux can be estimated using Eqs. 5.18 (see Fig. 5.8). In the Meissner phase, where the flux is smaller than the critical flux, the density of vortices is zero because there is a single infinitely large vortex in the system. In the vortex phase, the number of vortices increases rapidly with the flux. In the limit of very large fluxes, the vortex density approaches the one of decoupled ladders ( $K = 0$ ) and increases linearly with the applied flux.

The Meissner to vortex phase transition can be also observed for a fixed flux by changing the ratio  $K/J$ . Figure 5.9 shows a two-dimensional phase diagram of the

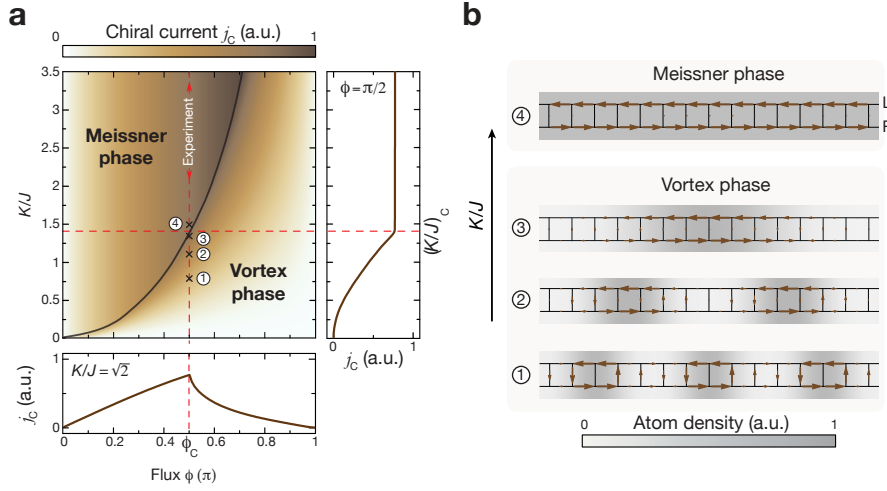


Figure 5.9: Phase diagram of ladder currents. **(a)** Chiral current strength along the legs of the ladder as a function of the flux and the ratio  $K/J$  calculated for the ground state of a ladder with 300 sites and periodic boundary conditions. The solid line shows the critical boundary that separates the Meissner and the vortex phase. The lower graph shows a profile of the current for a fixed value of  $K/J = \pi/2$ . In the Meissner phase, the current increases with flux, until a critical flux  $\phi_c$  is reached after which the system transitions into a vortex phase where the chiral current decreases with flux. The graph on the right is a profile line for a fixed flux  $\phi = \pi/2$ , as used in the experiment. In that case, the chiral current increases in the vortex phase when increasing  $K/J$  until one enters the Meissner phase at the critical point  $(K/J)_c$  where the current saturates. **(b)** Theoretically calculated individual currents and particle densities for the different values of  $K/J$  marked in (a), showing the same features for the currents as in Fig. 5.7b.

chiral current strength as a function of the flux and  $K/J$ . There, one can see that the chiral current increases as a function of  $K/J$  and becomes saturated when entering into the Meissner phase. Additionally, the current along the bonds has the same vortex structure as for Fig. 5.7. In the next chapter it will be shown that in our experiment we cannot easily change the flux. Then, to observe the transition from the Meissner to the vortex phase a different strategy had to be followed, which consisted in measuring the chiral current as a function of the rung-to-leg coupling ratio  $K/J$ .

As mentioned before, there are two degenerate ground states in the vortex phase and therefore the ground state of the system is not unique. As can be seen in Fig. 5.10, the ground state  $|\psi_{q_{K/J}}\rangle$  ( $|\psi_{-q_{K/J}}\rangle$ ) populates mostly the left (right) leg. On the other hand, the superposition state  $|\psi_g\rangle = (|\psi_{q_{K/J}}\rangle + e^{i\theta}|\psi_{-q_{K/J}}\rangle) / \sqrt{2}$  exhibits the already mentioned vortex structure. The only role of the phase  $\theta$  is to displace the entire wavefunction along the legs and therefore does not affect the value of the currents.

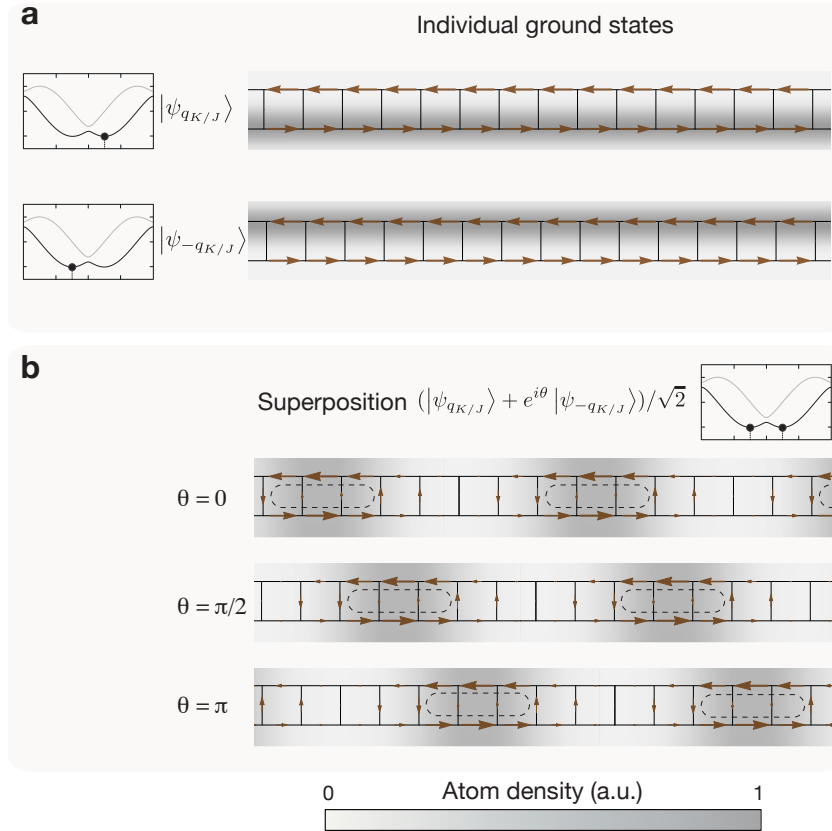


Figure 5.10: Currents and densities for different ground states. **(a)** Current strength and population density for the individual ground states  $|\pm q_{K/J}\rangle$  for  $K/J = 0.4$ . For smaller and smaller values of  $K/J$ , the population gets increasingly concentrated on a single leg of the ladder, right leg for  $|q_{K/J}\rangle$  and left leg for  $| -q_{K/J}\rangle$ . **(b)** Current strengths and wavefunction density for the superposition state calculated for different values of  $\theta$ . The only effect of  $\theta$  is to shift the wavefunction without affecting the average current and density values. For a better illustration of the spatial density modulation, a constant density offset was subtracted and the remaining modulation was renormalized for each  $K/J$ .

### 5.2.4 Momentum distribution

It will be shown in the next chapter that, in the experiment, we have the possibility of measuring the momentum distribution of the atomic state after a time-of-flight expansion. In this section we explain the expected momentum distribution for the flux ladder that we have experimentally realized.

For a given quasimomentum  $q$ , the momentum distribution of the eigenstate  $|\psi_q\rangle = (\alpha_q \hat{a}_{q;L}^\dagger + \beta_q \hat{a}_{q;R}^\dagger) |0\rangle$  has a single peak in the first Brillouin zone located at  $k = q$ . As can be seen in Fig. 5.11a, in the Meissner phase, the system possesses a single minimum in the lowest band structure at  $q = 0$ , and therefore the ground state has a single real momentum peak at  $k = 0$ . In the vortex phase there are two minima at  $\pm q_{KJ}$  and

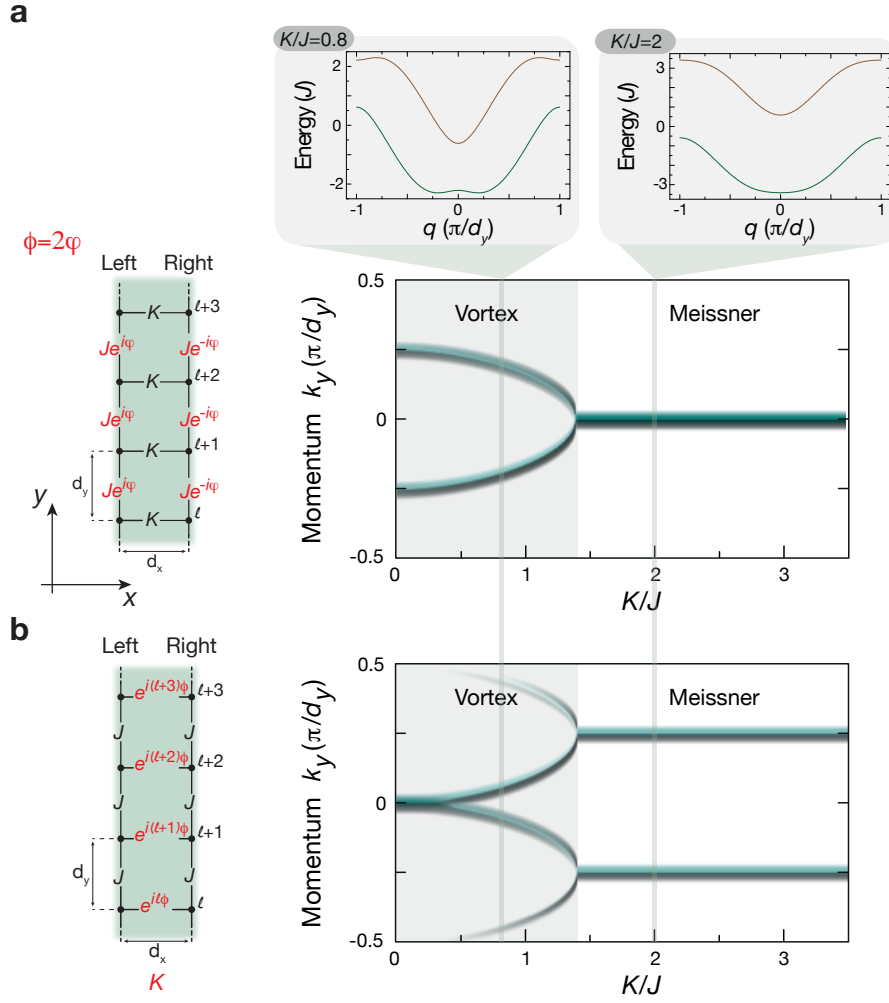


Figure 5.11: Momentum distribution for the theoretical **(a)** and experimental **(b)** gauge. In the theory gauge, there is a single real momentum peak in the Meissner phase and two peaks in the vortex phase. In the experimental gauge, for each quasimomentum  $q$ , there are two corresponding real momentum peaks. Therefore, in the Meissner and vortex phases, there are two and four momentum peaks, respectively.

therefore the ground state  $|\psi_g\rangle = (|\psi_{q_{K/J}}\rangle + e^{i\theta} |\psi_{-q_{K/J}}\rangle) / \sqrt{2}$  has two peaks at  $k = \pm q_{K/J}$ .

In the next chapter, we will present our experimental setup, where it will be shown that we create a ladder system with a flux of  $\pi/2$  per plaquette but in a different gauge (see Fig. 5.11b). In our experiment, the complex hopping terms are oriented along the rungs of the ladder, while along the legs of the ladder, there is normal tunneling with amplitude  $J$ . There are many observables that are gauge-independent, like the currents and densities. However, the momentum distribution is a gauge-dependent quantity, and therefore it has to be calculated for the experimental gauge.

From the relation between the vector potential and the complex hopping terms, i.e.  $J_{\ell,\mu} = |J_{\ell,\mu}| e^{-ie/\hbar \int_{\ell}^{\ell+1} \mathbf{A} \cdot d\mathbf{l}}$ , one can see that the vector potentials that produce the theoretical and experimental gauges are  $\mathbf{A}_T = \frac{\phi_0}{8d_x d_y} (0, 2x - d_x, 0)$  and  $\mathbf{A}_E = -\frac{\phi_0}{8d_x d_y} (2y, 0, 0)$ , respectively. These two quantities are related by a gauge transformation of the form  $\mathbf{A}_E = \mathbf{A}_T + \nabla f(x, y)$ , and by definition they produce the same magnetic field  $\mathbf{B} = \frac{\phi_0}{8d_x d_y} (0, 0, 2)$ . As it is known from quantum mechanics, a gauge transformation transforms the wavefunction according to  $\psi \rightarrow e^{ief(x,y)/\hbar} \psi$ . Then, the density of the wavefunction is not affected but the momentum distribution could be modified. From  $\mathbf{A}_T$  and  $\mathbf{A}_E$  one can obtain that  $f(x, y) = -\frac{\phi_0}{8d_x d_y} y(2x - d_x)$ . Therefore, the eigenstates are transformed to our experimental gauge as follows:

$$\begin{aligned} |\psi_q\rangle_T &= (\alpha_q \hat{a}_{q;L}^\dagger + \beta_q \hat{a}_{q;R}^\dagger) |0\rangle = \alpha_q \sum_{\ell} e^{iq\ell d_y} \hat{a}_{\ell;L}^\dagger + \beta_q \sum_{\ell} e^{iq\ell d_y} \hat{a}_{\ell;R}^\dagger \\ \rightarrow |\psi_q\rangle_E &= \alpha_q \sum_{\ell} e^{i(q + \frac{\pi}{4d_y})\ell d_y} \hat{a}_{\ell;L}^\dagger + \beta_q \sum_{\ell} e^{i(q - \frac{\pi}{4d_y})\ell d_y} \hat{a}_{\ell;R}^\dagger. \end{aligned} \quad (5.20)$$

From the equation above one can infer that in the experimental gauge, for each quasi-momentum  $q$ , there are two real momentum peaks in the first Brillouin zone located at  $k = q \pm \frac{\pi}{4d_y}$ , and their weights are  $\alpha_q$  and  $\beta_q$ , respectively. Figure 5.11b shows the expected momentum distribution in the experimental gauge for different values of  $K/J$ . In the Meissner phase, there are two peaks at  $k = 0 \pm \frac{\pi}{4d_y}$ , and in the vortex phase, there are four peaks at  $k = q_{K/J} \pm \frac{\pi}{4d_y}$  and at  $k = -q_{K/J} \pm \frac{\pi}{4d_y}$ .

### 5.3 Spin-orbit coupling mapping

Spin-Orbit Coupling (SOC) links a particle's velocity to its quantum mechanical spin and is essential in many condensed matter phenomena. SOC is crucial for the spin-Hall effect [219, 220] and topological insulators [156, 192, 221]. In the last decade, it has become a very active field of research since Kitaev [222] noticed that Majorana fermions should not couple too much to external noise and should be protected from decoherence, making them especially suited for quantum information and quantum memories. Spin-orbit coupled superconductors in a magnetic field could host Majorana fermions [223], which motivates experimentalists to push into that direction. In the context of ultracold atoms, SOC has been only recently realized for bosons [224] and for fermions [225], but only for one form of SOC. There are several theoretical proposals on how to engineer more general forms of SOC, and it still remains a challenge for the experimentalists to implement them in the lab.

A very well known example of SOC is the shift of the electron's atomic energy level due to the coupling between the electron's spin and the magnetic field generated by the atomic nucleus. In this example, the electrically charged nucleus produces an electric

field  $\mathbf{E}$ , which in the reference frame of the electron is seen as a magnetic field  $\mathbf{B} = -\frac{\mathbf{v} \times \mathbf{E}}{c^2}$ . The magnetic moment energy of the electron  $-\boldsymbol{\mu} \cdot \mathbf{B}$  then couples the electron's spin with the momentum, giving rise to the SOC term  $\mathbf{L} \cdot \mathbf{S}$ . A more condensed-matter related example is the Rashba effect [226], which takes place when a moving particle is placed in the presence of a static electric field  $\mathbf{E}_{ext}$ . In the reference frame of the particle, which has a momentum  $\mathbf{k}$ , the electric field gives rise to a momentum dependent magnetic field  $\mathbf{B}_{ext}(\mathbf{k}) = (-k_y, k_x, 0)\hbar E_{ext}/mc^2$ . As in the previous example, the SOC comes from the energy of the particle's magnetic moment in the magnetic field  $-\boldsymbol{\mu} \cdot \mathbf{B}_{ext}$ , which is proportional to  $k_y\hat{\sigma}_x - k_x\hat{\sigma}_y$ , where  $\hat{\sigma}_i$ ,  $i \in (x, y, z)$  are the Pauli matrices. Due to the Rashba SOC, the original parabolic dispersion relation of a free particle is split into two branches:

$$E = \frac{k^2}{2m} \pm \alpha k, \quad (5.21)$$

where  $\alpha$  denotes the strength of the Rashba coupling term. In 2D solids, there is a second type of SOC, known as Dresselhaus [227], which involves a term of the form  $-k_y\hat{\sigma}_x - k_x\hat{\sigma}_y$ . When the Rashba and Dresselhaus terms are present and have the same strength, the total Hamiltonian of a free particle can be written as

$$\hat{H} = \frac{\hbar^2 \mathbf{k}^2}{2m} + \frac{B_z}{2}\hat{\sigma}_z + \alpha k_x \hat{\sigma}_y, \quad (5.22)$$

where  $B_z$  represents a magnetic offset field along  $z$ . As can be seen in Fig. 5.12a, when  $B_z = 0$ , the energy corresponds to the two shifted parabolas due to the SOC term. When the magnetic offset  $B_z$  is increased, the two branches start to mix with each other (mixing of the spin components due to  $\hat{\sigma}_x$ ) and a gap opens. In the very strong magnetic offset regime, the SOC effect is less visible and the two spin components are completely mixed.

The flux ladder system can be mapped onto a SOC system where the legs of the ladder play the part of pseudo-spins [202, 228]. In order to see this, one can take the Hamiltonian 5.5 and write it in the momentum representation using the expansion given in Eq. 5.7:

$$\hat{H} = -2J \sum_q \hat{\mathbf{c}}_q^\dagger \mathcal{H}(q) \hat{\mathbf{c}}_q, \quad (5.23)$$

with  $\hat{\mathbf{c}}_q^\dagger = (\hat{a}_{q,L}^\dagger, \hat{a}_{q,R}^\dagger)$  and the Hamiltonian matrix

$$\mathcal{H}(q) = \cos(\varphi)\cos(q)\hat{\mathbb{1}} + \frac{K}{2J}\hat{\sigma}_x + \sin(\varphi)\sin(q)\hat{\sigma}_z. \quad (5.24)$$

This Hamiltonian is very similar to 5.22, with the only difference being that due to the lattice structure, it is written in quasimomentum space, and the momentum term  $k$  is replaced by the velocity of the particle in the lattice, given by  $\sin(q)$ . In the flux ladder,

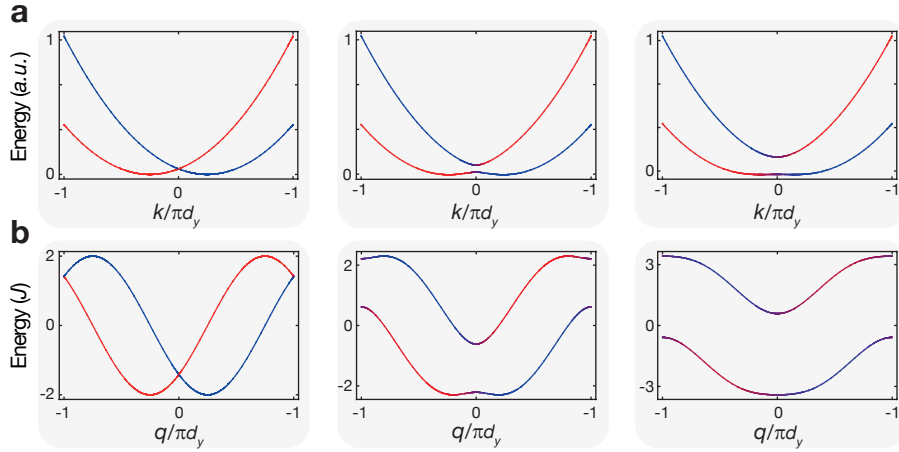


Figure 5.12: Energy dispersion relation for a free particle with SOC **(a)** and the flux ladder system **(b)**. The blue-red color scale represents the population fraction of the spin/pseudo-spin. For small offset field  $B_z$  (coupling ratio  $K/J$ ) the energy corresponds to two shifted free energy parabolas (a) and two shifted lattice dispersion relations (b). When the offset (coupling) is increased, the two components mix with each other.

the ratio  $K/J$  plays the role of  $B_z$  in Eq. 5.22. For small  $K/J$ , the two legs of the ladder are weakly coupled and the energy of the system corresponds to two lattice energy bands shifted due to the flux (see Fig. 5.12). As  $K/J$  is increased, the two legs are more and more coupled and therefore the two pseudo-spin components are more and more mixed.



## Chapter 6

# Measurements of chiral Meissner currents in the flux ladder

In this chapter, we describe the experimental sequence used to prepare the ground state of the flux ladder and then to measure the chiral Meissner currents by using a projection technique. The results show that the current behaves very differently in the Meissner and vortex phase, confirming our theoretical model. At the end of the chapter, we present our results on the momentum distribution measured after time-of-flight expansion, which also shows the transition from the vortex to the Meissner phase.

### 6.1 Experimental realization of the flux ladder

In this experiment, laser-assisted tunneling to engineer the Peierls phases in the complex tunneling terms was used, which created an artificial magnetic field in the ladders. Within the context of this thesis, we will not discuss the details of the theory behind the laser-assisted tunneling, but rather focus only on the physics that it allows us to realize. A more detailed explanation of this method will be explained in the thesis of M. Aidelsburger [229]. There, our previous experiments will be discussed where laser-assisted tunneling was used to engineer artificial magnetic fields [45, 47, 230].

#### 6.1.1 Experimental setup

In our experiment, we load a Bose-Einstein condensate of  $^{87}\text{Rb}$  bosonic atoms into a three dimensional optical lattice potential. The lattice potential is composed of a standing wave along the  $y$  direction with a wavelength of  $\lambda_s = 767\text{ nm}$  and a superposition of a short and a long standing wave of  $\lambda_s$  and  $\lambda_l = 2\lambda_s$  along the  $x$  direction. Additionally, a weak standing wave of  $\lambda_z = 844\text{ nm}$  along the  $z$  direction is used, which does not isolate

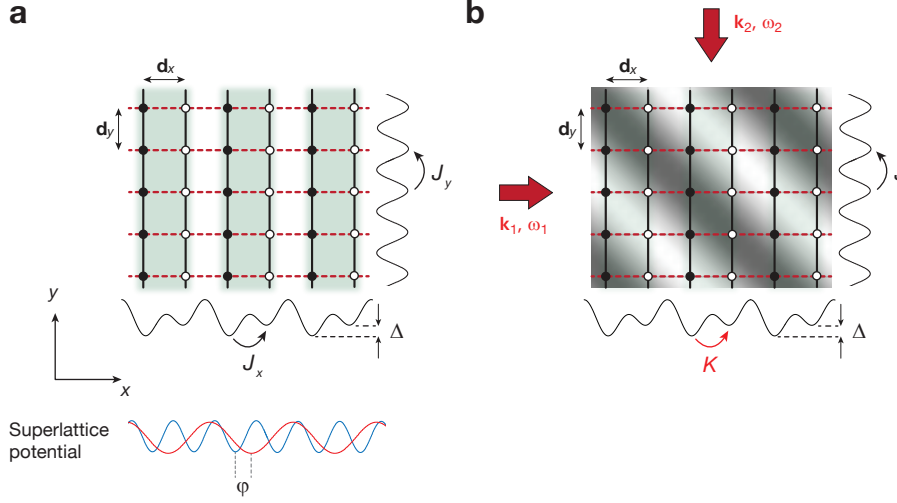


Figure 6.1: Experimental setup used to create the flux ladder. **(a)** The experiment consist of a one-dimensional array of ladders in the  $xy$ -plane with lattice constants given by  $d_{x,y}$ . Along the  $y$  direction, a single standing wave creates a lattice potential with coupling  $J_y$ . Along the  $x$  direction, two standing waves are superimposed to create a superlattice potential, which forms an array of isolated double wells with a left-right coupling and energy difference  $\Delta$  and  $J_x$ , respectively. The long (short) standing wave is red (blue) detuned with respect to the atomic transition, and their relative phase is denoted by  $\varphi$  [29]. **(b)** An effective homogeneous magnetic field is realized in each ladder by using a pair of interfering beams (red arrows) whose frequency difference is on resonance with the energy gap  $\Delta$ , i.e.  $\omega = \omega_2 - \omega_1 = \Delta/\hbar$ . The running-wave modulates the on-site energy on each lattice site and through laser-assisted tunneling, restores the left-right tunneling, resulting in the effective couplings  $K$  and  $J$  along  $x$  and  $y$ , respectively.

different planes. Along the  $x$  direction, this results in a superlattice potential of the form  $V(x) = V_{lx}\sin^2(k_l x + \varphi/2) + V_x\sin^2(k_s x)$ , where  $k_i = 2\pi/\lambda_i$ ,  $i \in \{s, l\}$  and  $\varphi$  is the phase difference between the long and short standing waves (see Fig. 6.1a). The values of  $V_{lx/x}$  and the phase  $\varphi$  were chosen to have an array of isolated double well potentials along  $x$ , where each individual double well corresponds to a single realization of the ladder. By adjusting the phase  $\varphi$ , the double wells were tilted to have an energy difference  $\Delta$  between the left and right wells. In the limit of  $J_x \ll \Delta$ , where  $J_x$  is the left-right bare coupling, the tunneling inside each double well is inhibited. In order to induce left-right tunneling inside each double well, we used a pair of far-detuned beams with wavevectors  $\mathbf{k}_{1,2}$  and frequency difference  $\omega = \omega_2 - \omega_1$  (see Fig. 6.1b and section 2.1.5). These two beams create a running-wave that modulates the underlying lattice structure and induces left-right laser-assisted tunneling. The mechanism behind the laser-assisted tunneling is that whenever a particle on the left well (left leg of the ladder from now on) hops to the right leg, it absorbs a photon from one of the beams and releases a photon into the other one. The energy difference between these two photons bridges the left-right energy gap  $\Delta$ , i.e.  $\hbar\omega = \Delta$ , and in addition, the particle receives a net momentum

kick. When the hopping is in the opposite direction, i.e. from right to left, the direction of the momentum kick is reversed. Therefore, the particle behaves like an electron in a magnetic field.

The time-dependent Hamiltonian of a single ladder is

$$\hat{H}_t = -J_y \sum_{\ell,\mu} \hat{a}_{\ell;\mu}^\dagger \hat{a}_{\ell+1;\mu} - J_x \sum_{\ell} \hat{a}_{\ell;L}^\dagger \hat{a}_{\ell;R} + \Delta \sum_{\ell} \hat{n}_{\ell;R} + V_{\mathbf{k}}^0 \sum_{\ell,\mu} \cos(\omega t + \phi_{\ell;\mu}) \hat{n}_{\ell;\mu} + \text{h.c.}, \quad (6.1)$$

where  $\mu \in \{L, R\}$  denotes the left and right legs of the ladder,  $\ell$  indicates the lattice sites along the ladder and  $J_y$  is the bare tunneling along the  $y$  direction. The first and second terms are simply the kinetic energies along the  $y$  and  $x$  direction, respectively. The third term corresponds to the left-right energy difference  $\Delta$ , and the last term is the time dependent modulation of the potential given by the running-wave beams, where  $V_{\mathbf{k}}^0$  is the amplitude of the modulation and  $\phi_{\ell;\mu}$  is the phase of the running-wave on the different lattice sites. Here we neglect any kind of interparticle interaction (in section 6.3.4 we present a discussion about the interaction energies in this system). Using Floquet theory [231, 232], an effective time-averaged Hamiltonian can be derived, which is time-independent

$$\hat{H} = -J \sum_{\ell,\mu} \hat{a}_{\ell;\mu}^\dagger \hat{a}_{\ell+1;\mu} - K \sum_{\ell} e^{i\ell\pi/2} \hat{a}_{\ell;L}^\dagger \hat{a}_{\ell;R} + \text{h.c.} \quad (6.2)$$

Here the effective coupling terms are

$$\begin{aligned} J &= J_y \mathcal{J}_0(V_{\mathbf{k}}^0/(\sqrt{2}\Delta)) \approx J_y, \\ K &= J_x \mathcal{J}_1(V_{\mathbf{k}}^0/(\sqrt{2}\Delta)) \approx J_x V_{\mathbf{k}}^0/(2\sqrt{2}\Delta), \end{aligned} \quad (6.3)$$

where  $\mathcal{J}_i(x)$  denote the Bessel functions of the first kind. This effective Hamiltonian is only valid in the limit  $J_x, J_y \ll \Delta$ . The spatially-dependent phase factors  $e^{i\ell\pi/2}$  have their origin in the phases  $\phi_{\ell;\mu}$  of the running-wave (see Fig. 6.2). The corresponding flux can be obtained by considering a closed loop around a plaquette as was explained in the previous chapter. For our system we obtain a flux of  $\phi = (\ell + 1)\pi/2 - \ell\pi/2 = \pi/2$  per plaquette. By changing the angle between the beams or changing their wavelength one can in principle engineer any desired flux.

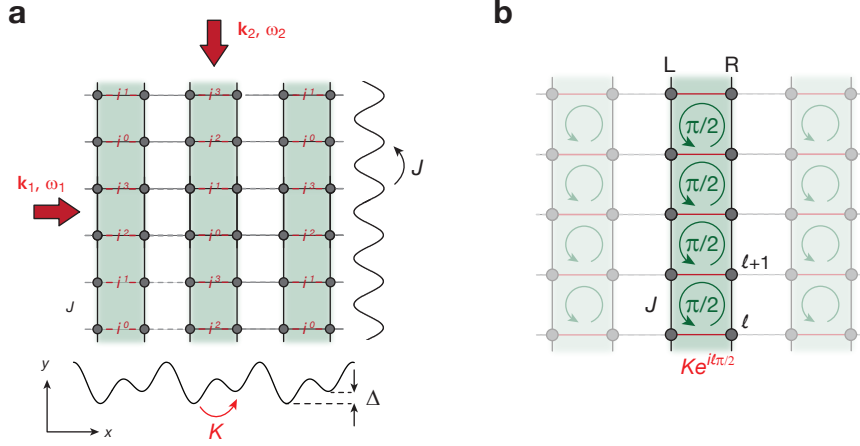


Figure 6.2: Schematics of the effective ladder system. **(a)** The effective Hamiltonian corresponds to an array of ladders in the  $xy$ -plane, where the effective coupling along the  $x$  and  $y$  direction are  $J$  and  $K$ . Along the  $y$  direction there is an additional phase in the hopping terms that gives rise to the artificial magnetic field. This phase comes from the original spatially-dependent phase of the running-wave. **(b)** Diagram of the independent ladders with the corresponding hopping terms and phases. The flux per plaquette is equal to  $\pi/2$ .

## 6.2 Experimental sequence and projection into isolated double wells

### 6.2.1 Experimental sequence

In order to measure the chiral currents in the flux ladder, it is first necessary to populate the ground state of the system. The experimental sequence used to do this is the following (see Fig. 6.3). A BEC of about  $5 \times 10^4$   $^{87}\text{Rb}$  atoms was first loaded adiabatically in 200 ms into a three-dimensional lattice with  $V_{lx} = 25(1) E_{rl}$ ,  $V_y = 7.0(2) E_{rs}$  and  $V_z = 5.0(2) E_{rz}$ , where  $E_{ri} = \hbar^2 / (2m\lambda_i^2)$ ,  $i \in \{s, l, z\}$ . The tilted ladders were then formed by ramping up the short lattice along  $x$  to its final value  $V_x = 3.2(1) E_{rs}$  in 20 ms, where the phase  $\varphi$  of the superlattice along  $x$  was chosen such that the offset was  $\Delta/h = 5.57(4)$  kHz and all atoms ended up on the left side of the ladders. In the next step, laser-assisted tunneling between the initially isolated legs of the ladders was switched on by ramping up the running-wave beams to  $V_K^0 = 4.1(2) E_{rK}$  corresponding to  $K/J = 2.1(1)$  in 10 ms, where  $E_{rK} = \hbar^2 / (2m\lambda_K^2)$  and  $\lambda_K = 2\lambda_s$ . After a holding time of 5 ms that ensures an equal left-right distribution of atoms (see below), the running-wave beams were changed to their final value within 10 ms. After a subsequent holding time of 10 ms, the atoms were in the ground state of the flux ladder system. The initial ramp of the running-wave beams amplitude to the value  $K/J = 2.1$  is there to ensure an initially equal population on both legs. During the following holding time, there is a left-right population oscillation between the legs, which is completely damped after the

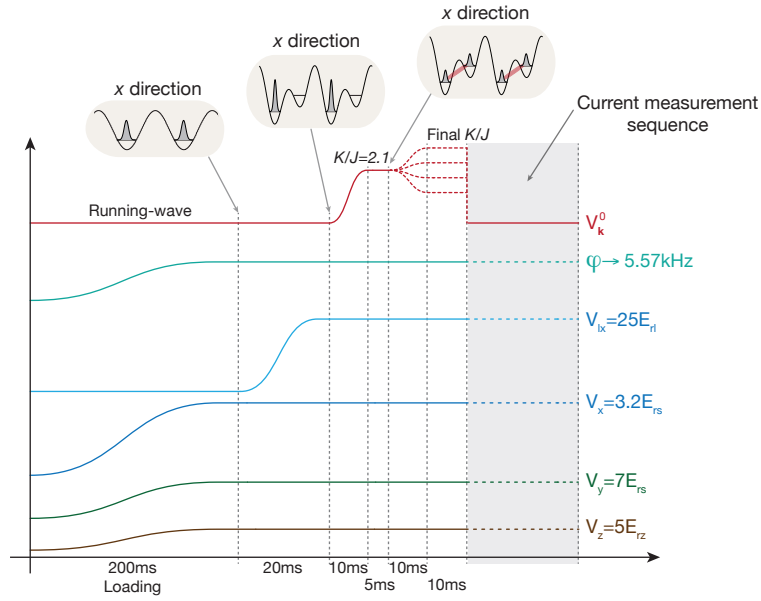


Figure 6.3: Experimental sequence to prepare the ground state of the flux ladder. Initially all the atoms are loaded into a three-dimensional lattice, where there are no double wells. Next, the short lattice along  $x$  is ramped up, realizing an array of tilted ladders. Then, as shown in the figure, the running-wave beams are ramped up to restore the left-right inter-leg tunneling and populate the ground state of the flux ladder for a particular value of  $K/J$ .

holding time. The last ramp to the final value of  $K$  and subsequent holding time bring the system to the ground state of the flux ladder for that particular  $K$ .

Once the ground state is populated, we project the wavefunction into isolated double wells along the  $y$  direction and measure the average even-odd population oscillations, from which we can extract the chiral current that corresponds to the original state before the projection, as will be explained in section 6.2.2. The experimental sequence used for the projection is shown in Fig. 6.4. It was done by suddenly switching off the running-wave beams followed by ramping up a long lattice of wavelength  $\lambda_l$  along  $y$  to  $V_{ly} = 18.0(8)E_{rl}$  in 0.2 ms. During this same time, the short lattice along  $x$  was increased to  $V_x = 10.0(3)E_{rs}$  to isolate the legs of the ladders. Following a variable holding time between 0 and 2 ms, where the atoms oscillate in the double wells, the even-odd atom fraction on each leg was determined using the site-resolved band mapping technique described in the next paragraph.

After the projection into isolated double wells along  $y$ , the system consists of an array of isolated  $2 \times 2$  plaquettes with negligible tunneling between the legs of the ladders (see Fig. 6.5a). The occupation numbers in the four sites of each plaquette on the even/odd and left/right (L/R) locations are denoted by  $N_{\text{odd};L}$ ,  $N_{\text{odd};R}$ ,  $N_{\text{even};L}$ , and  $N_{\text{even};R}$ . These occupation numbers are extracted by transferring the populations to different Bloch bands, similar to the technique described in refs. [29, 53, 233, 234] (see

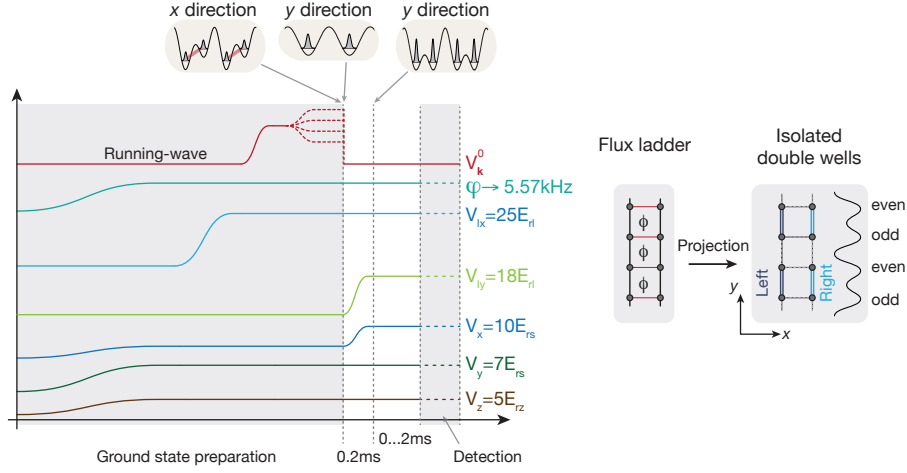


Figure 6.4: Experimental sequence to project the ground state of the flux ladder into isolated double wells along  $y$ . After preparing the ground state of the flux ladder (left grey shaded area), the running-wave beams are switched off and a second superlattice along the  $y$  direction is ramped up to split up the system in an array of isolated double wells.

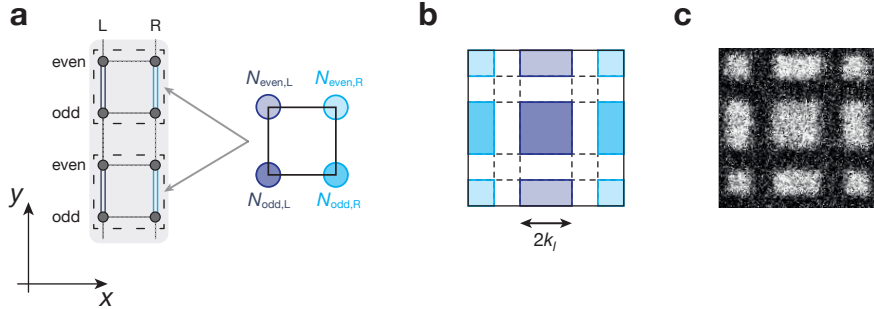


Figure 6.5: **(a)** Schematic drawing of a four-site square plaquette labeled by the corresponding occupation numbers. **(b)** Brillouin zones of the 2D lattice ( $k_l = 2\pi/\lambda_l$ ). **(c)** Typical momentum distribution obtained after the band-mapping sequence, measured after 10 ms of time-of-flight.

also appendix C). A subsequent band mapping allows us to determine the populations in different Bloch bands by counting the corresponding atom numbers. The colors in Fig. 6.5 illustrate the connection between the long-lattice Brillouin zones and the corresponding lattice sites. The evolutions  $N_{\text{odd};L}(t)$  and  $N_{\text{even};L}(t)$  ( $N_{\text{odd};R}(t)$  and  $N_{\text{even};R}(t)$ ) are used to evaluate the amplitude of the currents in the left (right) leg of the ladders and  $n_{\text{odd};\mu}(t) = N_{\text{odd};\mu}(t)/(N_{\text{even};\mu}(t) + N_{\text{odd};\mu}(t))$  with  $\mu = L, R$ .

### 6.2.2 Relation between currents and oscillations in isolated double wells

After the ground state wavefunction has been projected into the isolated double wells along the  $y$  direction, there is a subsequent even-odd population oscillation in each double well, which depends on the coefficients of the projected wavefunction. Let us assume that the wavefunction can be written as  $|\psi\rangle = \sum_{\ell} c_{\ell;L} \hat{a}_{\ell;L}^{\dagger} |0\rangle + c_{\ell;R} \hat{a}_{\ell;R}^{\dagger} |0\rangle$ , and let us consider the evolution on a single double well located between the sites  $\ell$  and  $\ell + 1$  on the left leg of the ladder. Directly after the projection, the wavefunction on that double well is  $|\psi\rangle_{\ell;L} = c_{\ell;L} \hat{a}_{\ell;L}^{\dagger} |0\rangle + c_{\ell+1;L} \hat{a}_{\ell+1;L}^{\dagger} |0\rangle$ . The dynamics on each double well is governed by the Hamiltonian

$$\hat{H}_{DW} = -J_{DW} \hat{a}_{\ell;L}^{\dagger} \hat{a}_{\ell+1;L} + \text{h.c.}, \quad (6.4)$$

where  $J_{DW}$  is the coupling between the even and odd wells. From there one can calculate the time evolution of the populations in the double wells

$$|c_{\ell;L}|^2(t) = \frac{1}{2} [1 + \{|c_{\ell;L}|^2 - |c_{\ell+1;L}|^2\} \cos(2J_{DW}t/\hbar) - 2 \text{Im}(c_{\ell;L}^* c_{\ell+1;L}^*) \sin(2J_{DW}t/\hbar)]. \quad (6.5)$$

The first term is proportional to the initial population imbalance. The amplitude of the second oscillating term is proportional to the current originally on that bond (Eq. 5.13), i.e.

$$\mathbf{j}_{\ell;L}^y = \frac{2d_y}{\hbar} \text{Im}(c_{\ell+1;L}^* c_{\ell;L} H_{\ell \rightarrow \ell+1;L}) \propto 2 \text{Im}(c_{\ell;L}^* c_{\ell+1;L}^*). \quad (6.6)$$

This is valid only because the Hamiltonian elements  $H_{\ell \rightarrow \ell+1;\mu}$  of the flux ladder are real and equal to  $J$ . It is important to remark here that we are considering the current that corresponds to the ground state of the flux ladder, and therefore to calculate it, one has to use the Hamiltonian terms of the flux ladder and not the ones after the projection. A second important point is that if one performed this measurements with a Hamiltonian in the theoretical gauge described in the previous chapter, then the Hamiltonian element  $H_{\ell \rightarrow \ell+1;L}$  would be  $J e^{i\pi/4}$  and therefore the oscillation amplitude  $2 \text{Im}(c_{\ell;L}^* c_{\ell+1;L}^*)$  would not be proportional to the current.

In the experiment, we do not have the possibility of measuring the time evolution on each individual double well, but rather the average quantities  $n_{\text{even};\mu}(t) = \sum_{\ell} |c_{2\ell;\mu}|^2(t)$  and  $n_{\text{odd};\mu}(t) = \sum_{\ell} |c_{2\ell+1;\mu}|^2(t)$ , which are the even and odd average oscillation amplitudes on the left and right leg of the ladder. From Eq. 6.5 one obtains

$$n_{\text{even};L}(t) = \frac{1}{2} [1 + \{n_{\text{even};L} - n_{\text{odd};L}\} \cos(2J_{DW}t/\hbar) - \frac{j_L}{J d_y / \hbar} \sin(2J_{DW}t/\hbar)], \quad (6.7)$$

with  $n_{\text{even/odd};L} = n_{\text{even/odd};L}(t = 0)$  and  $j_L = N_{\text{leg}}^{-1} \sum_{\ell} j_{2\ell;L}^y$  is the average current on the left leg of the ladder and where an equivalent expression is valid for the right leg. To obtain Eq. 6.7, only the double wells in which the wavefunction is projected were considered, i.e. every other bond along the  $y$  direction, as shown in Fig. 6.4. This explains why only the even terms appear in the definition of  $j_L$ .

In order to extract the average current  $j_\mu$  one could look at the amplitude of  $n_{\text{even};\mu}(t)$  at the specific times  $t = \pi\hbar/(2J_{DW})$ , for which  $\cos(2J_{DW}t/\hbar)$  is zero and  $\sin(2J_{DW}t/\hbar)$  is one [214]. This approach is difficult to follow in the experiment because during the projection time, which is very short but finite, there could be some time evolution that introduces some complication in the determination of the time  $t = 0$ .

A numerical calculation of the quantity  $n_{\text{even};\mu} - n_{\text{odd};\mu}$  for our experimental parameters predicts that this quantity is zero for the range of the ratio  $K/J$  and flux used in the experiment. The vanishing of  $n_{\text{even};\mu} - n_{\text{odd};\mu}$  is due to the fact that it is an averaged quantity over the different bonds along the legs, and therefore it averages out (the wavefunction density is periodic along the legs and it does not favor any specific site). Therefore, from the numerical calculations one can state that

$$n_{\text{even};\mu}(t) = \frac{1}{2} \left[ 1 - \frac{j_\mu}{Jd_y/\hbar} \sin(2J_{DW}t/\hbar) \right], \quad (6.8)$$

which means that the oscillation amplitude is proportional to the average current.

It will be shown in the next section that due to experimental imperfections in the system, the averaged population imbalance  $n_{\text{even};\mu} - n_{\text{odd};\mu}$  is very small but it does not fully average out. This means that for small currents  $j_\mu$ , the time evolution of  $n_{\text{even};\mu}(t)$  will be more strongly affected by the population imbalance and its phase and amplitude will be modified. However, if one assumes that the wavefunction density is the same on both legs, i.e.  $n_{\text{even/odd};L} = n_{\text{even/odd};R}$ , which is a reasonable assumption considering that the symmetric superposition solutions (Eq. 5.17) for the ground state of the flux ladder exhibit that symmetry, then one can calculate the chiral current by

$$\begin{aligned} n_{\text{even};L}(t) - n_{\text{even};R}(t) &= \frac{1}{2} \left[ \frac{j_R}{Jd_y/\hbar} \sin(2J_{DW}t/\hbar) \right] - \frac{j_L}{Jd_y/\hbar} \sin(2J_{DW}t/\hbar) \\ &= \frac{j_C}{2Jd_y/\hbar} \sin(2J_{DW}t/\hbar), \end{aligned} \quad (6.9)$$

where the population imbalance terms cancel with each other. Therefore, by subtracting the oscillations on the left and right legs, one obtains an oscillation whose amplitude is proportional to the chiral current  $j_C$ , where here the chiral current runs only over the projected double wells. A numerical calculation shows that for the parameters used in our experiment, the difference between averaging over all the bonds and averaging over every other bond is negligible. There is a regime at which the periodicity of the vortex

structure is on the order of a single bond, and therefore in that case the chiral current averaged over every other bond would depend on which bonds would be taken for the projection. However, that regime is not accessed in our experiment.

## 6.3 Measurements of chiral Meissner currents

### 6.3.1 Rabi oscillations in double wells

Using the experimental sequence described in section 6.2.1, the system was prepared in the ground state of the flux ladder with  $K/J = 330(20) \text{ Hz}/150(10) \text{ Hz} = 2.2(1)$ , which corresponds to the Meissner phase, and then by projecting into isolated double wells, the corresponding even-odd time evolution of  $n_{\text{odd};\mu}$  was measured. The results are presented in Fig. 6.6a. The first thing to note is that both oscillations are out of phase by  $\pi$ , which indicates two things. The first one is that the current flows in opposite directions along the legs of the ladder, indicating a non-zero chiral current, which is expected from the theory calculations as shown in Fig. 5.9b. The second point is that the fact that they are within the experimental error out of phase by  $\pi$  indicates that  $n_{\text{even};\mu} - n_{\text{odd};\mu} \ll j_{\mu}$  and therefore the oscillations are dominated by the current term. Figure 6.6b shows the time evolution of  $n_{\text{odd};\mu}$  when the flux is reversed to  $-\pi/2$ . In that case, the phases of  $n_{\text{odd};L}$  and  $n_{\text{odd};R}$  are also reversed. This demonstrates that the flux ladder exhibits a chiral edge current in the ground state whose chirality is reversed when inverting the direction of the flux, in agreement with the theoretical expectation.

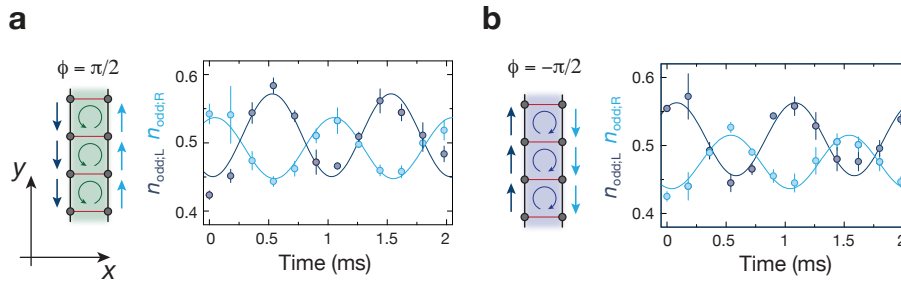


Figure 6.6: Time evolution of the population fractions  $n_{\text{odd};L}$  (dark blue) and  $n_{\text{odd};R}$  (light blue) for  $K/J = 2.2(1)$  and for the fluxes  $\phi = \pi/2$  (a) and  $\phi = -\pi/2$  (b). When the flux is  $+\pi/2$  ( $-\pi/2$ ) the edge current flows counterclockwise (clockwise). The small initial phase offsets of  $n_{\text{odd};\mu}$  are caused by the finite projection time. Each experimental point is an average over three measured values and the error bars depict the corresponding standard deviations. The solid lines are sinusoidal fits to the experimental data, where the frequency was fixed to the calibrated double well coupling  $2J_{DW}/h = 0.99(7) \text{ kHz}$ .

The presence of chiral currents in the ladder is only due to the artificial magnetic field. The ground state wavefunction of a ladder without flux is homogeneous through

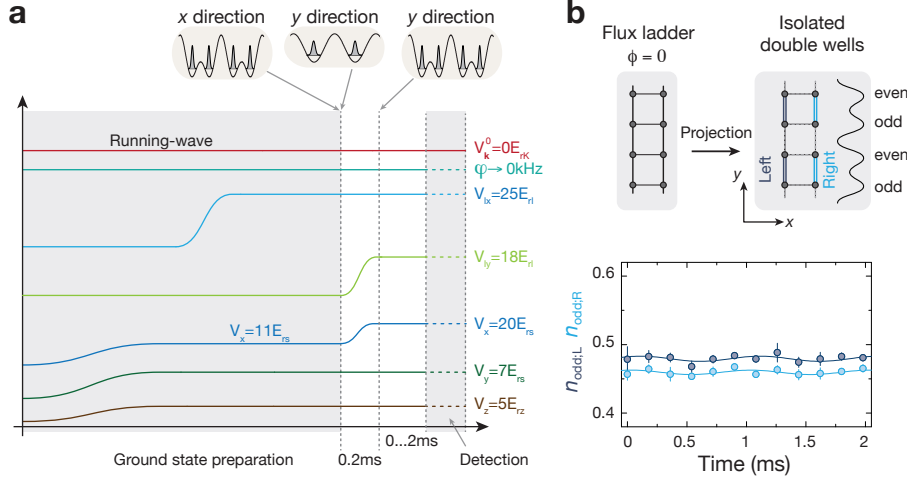


Figure 6.7: Experimental sequence and results for the ladder without flux. **(a)** Experimental sequence for the ground state preparation and projection into double wells used for the ladder without flux. In this sequence, the running-wave beams were not used, and there was no left-right energy tilt. **(b)** Schematic of the ladder without flux together with the experimental results. Each experimental point is an average over three experimental measurements and the error bars indicate the corresponding standard deviations. The solid lines are sinusoidal fits to the experimental data, where the frequency was fixed to the calibrated double well coupling  $2J_{DW}/h = 0.99(7)$  kHz.

the ladder and no chiral currents are present. In order to confirm this, the currents for a ladder without flux were also measured. The experimental sequence used was the same as for the flux ladder, but with  $\Delta = 0$ ,  $V_x = 11.0(3)E_{rs}$  and without running-wave beams. The resulting ladders had a bare coupling along the rungs of  $J_x/h = 250(10)$  Hz, and the total flux was zero due to the absence of the Peierls phases in the hopping terms. The projection sequence into isolated double wells in this case differed from the one described in 6.2.1 in that  $V_x$  was ramped to  $20E_{rs}$  instead of  $10E_{rs}$  to prevent left-right tunneling (see Fig.6.7a). The results are displayed in Fig. 6.7b, where one can see that the oscillation amplitude is negligible within the experimental error. Moreover, there are no out of phase oscillations which would be present for a system with non-zero chiral current.

The lifetime of the currents in the flux ladder can be obtained by measuring the amplitude of the chiral currents as a function of a holding time, which is directly before the projection into isolated double wells. The experimental results are shown in Fig. 6.8, where the measurements were performed for  $K/J = 2.1(1)$ , and the amplitude of the chiral current was extracted from the individual oscillations  $n_{\text{odd};L}$  and  $n_{\text{odd};R}$  as described in Eq. 6.9. Fitting an exponential decay to the data results in a lifetime of  $39(7)$  ms. The two main mechanisms leading to the damping of the measured oscillations

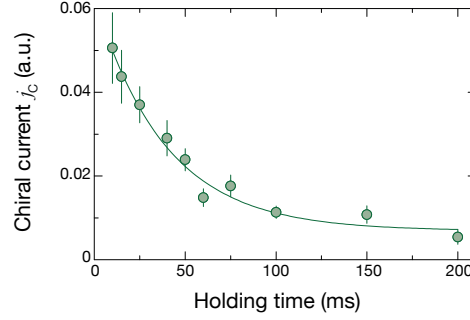


Figure 6.8: Measured chiral current amplitude for  $K/J = 2.1(1)$  as a function of a holding time before projecting into double wells. The data points were evaluated through  $\mathbf{j}_C = \mathbf{j}_L - \mathbf{j}_R \propto |I_L - e^{i\Delta\varphi} I_R|$ , where  $I_\mu$  are the amplitudes of the oscillations  $n_{\text{odd};\mu}$  and  $\Delta\varphi$  their relative phase. All data points were extracted from two individual measurements of  $n_{\text{odd};L}$  and  $n_{\text{odd};R}$ , where we averaged the two independently fitted amplitudes  $I_\mu$  and calculated the resulting standard deviations to obtain the error bars. The solid line is a fit of an exponential decay to the data, which gives a lifetime of 39(7) ms.

tions are most likely heating caused by the running-wave beams and decoherence or inhomogeneous dephasing between the individual ladders relative to each other, as the measured amplitude is averaged over the entire system.

### 6.3.2 Results of the measurements of the chiral Meissner currents

In order to probe the phase diagram shown in Fig. 5.9, we studied the change of the chiral current amplitude when increasing the ratio  $K/J$  for a constant flux  $\phi = \pi/2$ . On each leg of the ladder, we measured  $n_{\text{odd};\mu}(t)$  and fitted its amplitude  $I_\mu$  and phase  $\varphi_\mu$  for different values of  $K$  and constant  $J$ . As explained in section 6.2.2, to extract the chiral current, we made use of the left-right symmetry of the wavefunction density, i.e.  $n_{\text{even}/\text{odd};L}(0) = n_{\text{even}/\text{odd};R}(0)$ , from which we obtain  $\mathbf{j}_C = \mathbf{j}_L - \mathbf{j}_R \propto |I_L - e^{i\Delta\varphi} I_R|$ , with  $\Delta\varphi = \varphi_L - \varphi_R$ . As shown in Fig. 6.9a, in the vortex phase, the chiral current increases when increasing  $K/J$  up to the critical point  $(K/J)_c = \sqrt{2}$  at which the system enters the Meissner phase indicated by a saturation of the chiral current. For a comparison with theory, we fitted the theoretically predicted behavior with amplitude and offset as free fit parameters and find good agreement between theory and experiment. The amplitude of the chiral current was found to be 14% of the theoretically expected value. Some possible reasons for this reduction in amplitude are the inhomogeneities in the system, imperfect projection of the ladder ground state into the double wells, interactions in the system, heating produced by the running-wave beams, and also the presence of tubes in the transverse ( $z$ ) direction where there is a very weak lattice.

In Figure 6.9b we plot the phase differences  $\Delta\varphi$  for the different values of  $K/J$ . There

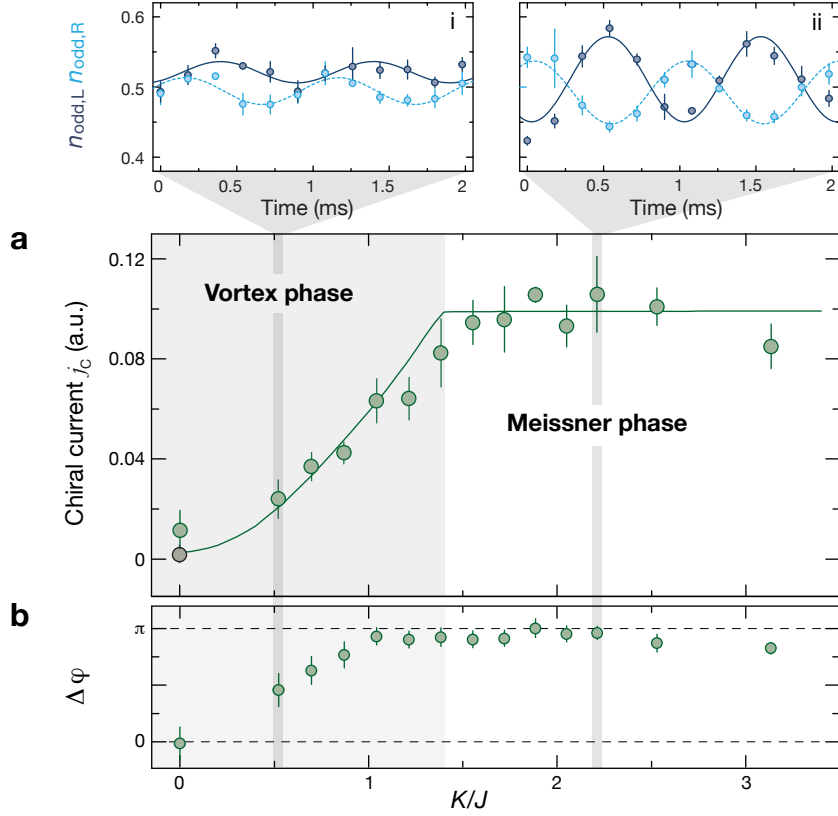


Figure 6.9: Chiral current as a function of  $K/J$ . **(a)** Average chiral current  $j_C$  obtained from sinusoidal fits to the individual oscillations of  $n_{\text{odd};\mu}(t)$  for different values of  $K/J$ . The darker (lighter) area indicates the vortex (Meissner) phase. The solid green line is a theory curve fitted to the experimental data, which was calculated using the Hamiltonian of Eq. 6.2. The fitted amplitude and offset were 0.14(1) and 0.001(2) respectively. The gray point was measured in a ladder with  $\phi = 0$  where the chiral current is zero. The two insets above show the average of three individual oscillations for  $K/J = 0.52(7)$  (i) and for  $K/J = 2.2(1)$  (ii). **(b)** Phase difference  $\Delta\varphi$  between the oscillations  $n_{\text{odd};L}(t)$  and  $n_{\text{odd};R}(t)$  for different values of  $K/J$ . We observe that  $\Delta\varphi \approx \pi$  for  $K/J > 1$  and decreases when  $K/J \lesssim 1$ . All data points were extracted from three individual measurements of  $n_{\text{odd};\mu}(t)$ . For the chiral current, the data points were evaluated through  $|I_L - e^{i\Delta\varphi} I_R|$ , where we averaged the three independently fitted amplitudes  $I_\mu$  and calculated the resulting standard deviations. For the phase measurements, we fitted the phase of the average of the three independent oscillations and from the errors of the fits we determined the error bars.

one can observe that when  $K/J > 1$ , the value of  $\Delta\varphi$  is close to  $\pi$ . This is to be expected, as explained in Eqs. 6.8 and 6.9, when the averaged initial population imbalance on neighboring sites on the double wells is negligible and a chiral current is present in the system. For values of  $K/J < 1$ , we find that  $\Delta\varphi$  decreases, most likely due to the fact that the smaller and smaller leg currents for decreasing  $K/J$  lead to a larger effect of any

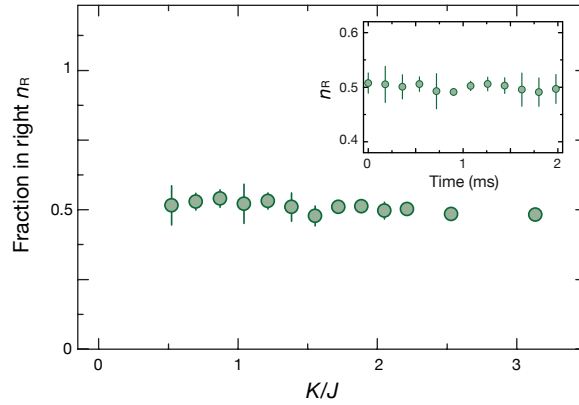


Figure 6.10: Fraction of atoms in the right leg of the ladders for the current measurements shown in Fig. 6.9. All data points are an average over three independent measurements, in which the atom fraction was averaged over the entire evolution and the error bars indicate the standard deviations. The inset shows the time evolution after the projection into the double wells for  $K/J = 2.2(1)$ , corresponding to the measurements shown in Fig. 6.6a. Each point is an average over three individual measurements and the errors are the corresponding standard deviations.

initial population imbalance on the phase of the double well oscillations (see Eqs. 6.8 and 6.9).

In the previous chapter it was mentioned that the ground state in the vortex phase is degenerate and that the distribution of currents on the bonds of the ladder depends on the particular populated state. As it was shown in Fig. 5.10, the ground state  $|q_{K/J}\rangle$  ( $|-q_{K/J}\rangle$ ) has more population on the right (left) leg of the ladder, and therefore if in the experiment only one of the states is populated, then the left-right leg population will not be balanced. The site-resolved detection technique, which is used to determine the atom number on the different sites of the plaquettes, allows for a simultaneous measurement of currents as well as atom populations on the left and right legs of the ladders. Figure 6.10 shows the fraction of atoms on the right leg for the current measurements of Fig. 6.9a, proving that the number of atoms is the same on both legs after the preparation of the final state, which started with all atoms initially in the left leg. In addition, no changes in the left-right distribution were observed during the oscillations in the double wells, which is expected since both legs are essentially decoupled during this time. These results indicate that the experiment equally populates both ground states, either in a coherent superposition state of the form  $|q_{K/J}\rangle + e^{i\theta} |-q_{K/J}\rangle$ , or in a way such that half of the ladders are in the  $|q_{K/J}\rangle$  state and the other half in the  $|-q_{K/J}\rangle$  state. The state preparation, which is symmetric on all the ladders, should favor the population of the superposition state.

In Figure 6.9a the results of the chiral current measurements are shown, which are

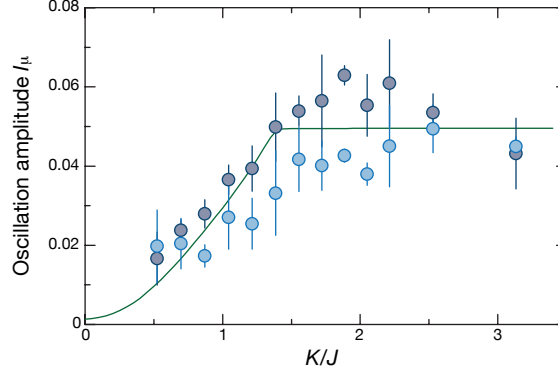


Figure 6.11: Measured oscillation amplitudes  $I_\mu$  on the left (dark blue) and right (light blue) legs of the ladder. Each data point is an average over three individual measurements. The error bars denote the standard deviation of the individual measurements. The solid line is the fit of the theoretically calculated chiral current amplitude (divided by two) to our data from Fig. 6.9 of the main text. The experimental amplitudes are  $\sim 14\%$  of the predicted ones for a single non-interacting ladder.

obtained from the individual oscillations  $n_{\text{odd};\mu}$ . The corresponding amplitudes  $I_\mu$  of  $n_{\text{odd};\mu}$  are displayed in Fig. 6.11, where one can see that typically  $I_L > I_R$ . One possible reason could be that since the particles on the right leg are transferred to a higher band along the  $x$  direction during the detection technique, an imperfection in the transfer could produce some left-right asymmetry. Another possible reason is the eventual presence of a one-directional current in the ladder flowing downwards on both legs of the ladder. Such a current would then enhance the current on the left leg and decrease it on the right one. By writing  $j_L = j_L^0 + j_{\text{dir}}$  and  $j_R = j_R^0 - j_{\text{dir}}$  one can estimate from the experimental data the amplitude of a possible one-directional current  $j_{\text{dir}}$ . This calculation yields a value smaller than 20% of the maximum measured oscillation amplitude. The presence of that current would not affect the chiral current, because for the chiral current, the difference between the current on the left and right legs is calculated, canceling any one-directional current.

When preparing the experimental sequence, we noted that when the weak lattice along the  $z$  direction was removed, i.e.  $V_z = 0 E_{yz}$ , then the currents in the ladder without flux were not zero, but there was an in phase oscillation of  $n_{\text{odd};L}$  and  $n_{\text{odd};R}$  whose amplitude depended on the holding time before projecting into isolated double wells (see Fig. 6.12). This current was produced by a small sloshing of the entire atomic cloud in the trap with lattice, and depending to the holding time, it resulted in a zero, positive or negative current, but it never yielded an out of phase oscillation and therefore no chiral current was present. The presence of the weak lattice along  $z$  helped to hold the atomic cloud and extinguish the one directional currents as shown in Fig. 6.7; therefore,

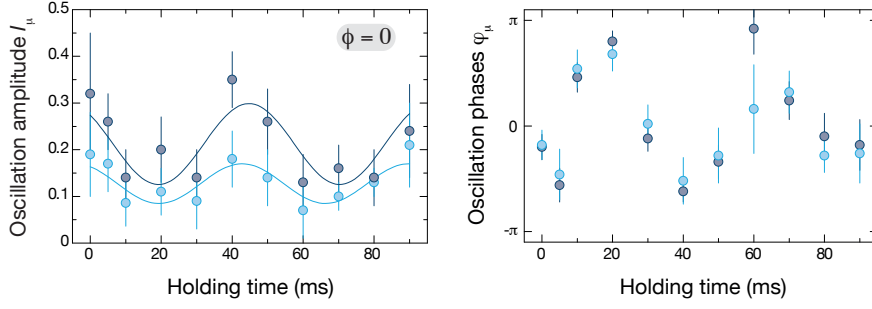


Figure 6.12: Measured oscillation amplitudes  $I_\mu$  and phases  $\varphi_\mu$  on the left (dark blue) and right (light blue) legs of the ladders without flux and without transverse lattice along  $z$  as a function of a holding time before the projection into isolated double wells. The amplitudes  $I_\mu$  oscillate in phase because of a sloshing of the entire atomic cloud in the trap with a lattice. Similarly, the phases  $\varphi_\mu$  change from positive to negative whenever the atomic cloud changes its direction of movement. When the weak lattice of  $V_z = 5 E_{rz}$  was present, the oscillation amplitudes  $I_\mu$  were zero, indicating that there was no one-directional current in the ladder. Each data point corresponds to the amplitude of a single oscillation, and the error bars depict the errors of the fits.

the weak lattice along  $z$  was kept on during the experimental sequence used for the measurements of the chiral currents in the flux ladders.

### 6.3.3 Calibration of laser-assisted tunneling

The calibration of the value of the effective couplings  $K$  and  $J$  as a function of the running-wave beam amplitude  $V_k^0$  was done as follows. For the effective coupling  $K$ , we first performed a spectroscopy measurement to determine the value of the tilt  $\Delta$ , and then a left-right Rabi oscillation in isolated double well potentials to calibrate the effective coupling (see Fig. 6.13a). For the spectroscopy measurements, we first loaded the atoms into a three dimensional lattice configuration consisting of the short lattice along the  $y$  direction with a strength  $V_y = 30(1) E_{rs}$ , the lattice along  $z$  with  $V_z = 30(1) E_{rz}$  and the long lattice along  $x$  with  $V_{lx} = 30(1) E_{rl}$ . Then a filtering sequence was performed which removed all the atoms from the double-occupied lattice sites, leaving the system with either zero or one atom per lattice site [29, 76, 235, 236]. Next, the short lattice along  $x$  was ramped up in 2 ms to  $V_x = 5.0(2) E_{rs}$ , splitting the sites into double well potentials with a tilt  $\Delta$ . At this point in the sequence, each isolated double well had a single atom loaded on the left well. Once in this configuration, the short lattice was quickly decreased in 0.1 ms to the final value of  $V_x = 3.2(1) E_{rs}$  and the running wave beams were instantly ramped up to  $V_k^0$  and kept in this configuration for a holding time  $\tau = 600 \mu s$ . By measuring the atom fraction  $n_{\text{right}}$  transferred to the right well as

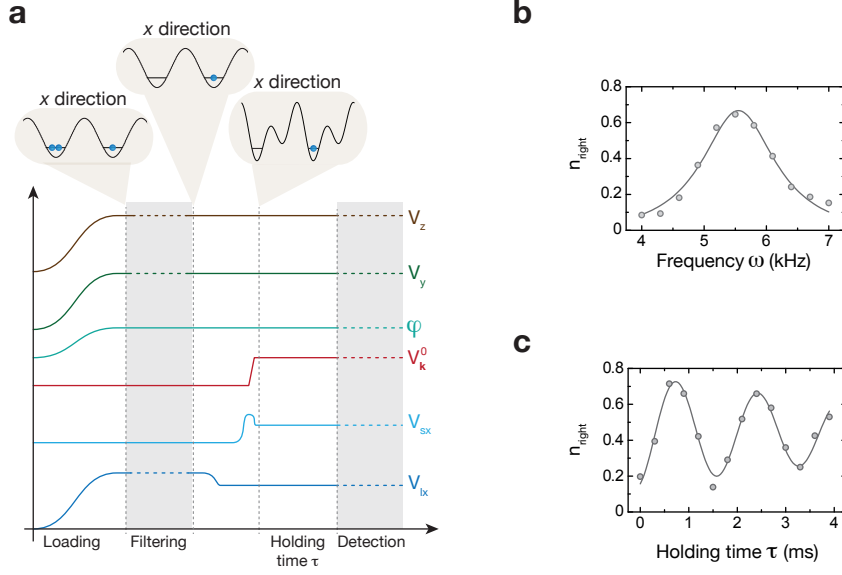


Figure 6.13: Experimental sequence for the calibration of  $K$ . **(a)** Experimental sequence used for the spectroscopy/Rabi oscillation measurements. **(b)** Atom fraction transferred to the right well as a function of the frequency of the running-wave beams as measured in the spectroscopy sequence. For these measurements, the sequence shown in (a) was used, where the holding time was fixed to  $\tau = 600 \mu\text{s}$  and the frequency  $\omega$  was varied. **(c)** Atom fraction transferred to the right well as a function of the holding time for the fixed resonant frequency  $\hbar\omega = \Delta$ . In this case, the resonant frequency obtained in (b) was used and the holding time  $\tau$  was varied.

a function of the frequency, we were able to determine the resonant frequency at which  $\hbar\omega = \Delta$  (see Fig. 6.13b). The measured value of the tilt was typically  $\Delta/h \sim 5.6 \text{ kHz}$ . The right atom fraction was measured by transferring the atoms on the right to a higher band along  $x$  and then applying a subsequent band-mapping technique (see end of section 6.2.1).

To calibrate the value of  $K$ , exactly the same sequence as described above was used, but instead of changing the frequency and fixing the holding time  $\tau$ , we chose the resonant driving frequency  $\hbar\omega = \Delta$  and measured the atom fraction  $n_{\text{right}}$  transferred to the right well as a function of the holding time (see Fig. 6.13c). The frequency of the left-right Rabi oscillation is equal to twice the strength of the laser-induced coupling. By repeating this measurement for different amplitudes  $V_{\mathbf{k}}^0$  of the running-wave beams and fitting the oscillation frequency, the calibration curve shown in Fig. 6.14 was obtained. For a typical value of  $V_{\mathbf{k}}^0 = 4.1(2) E_{rK}$ , with  $E_{rK} = \hbar^2 / (2m\lambda_K^2)$ ,  $\lambda_K = 2\lambda_s$ , we obtain an effective coupling  $K/h = 310(20) \text{ Hz}$ .

From Eq. 6.3 one can see that  $J \approx J_y$ , and that the deviation is larger for larger driving amplitudes  $V_{\mathbf{k}}^0$ . Since along the  $y$  direction there is only a single short lattice, one cannot easily calibrate  $J$  in the same way as it was done for  $K$ . However, one can estimate the

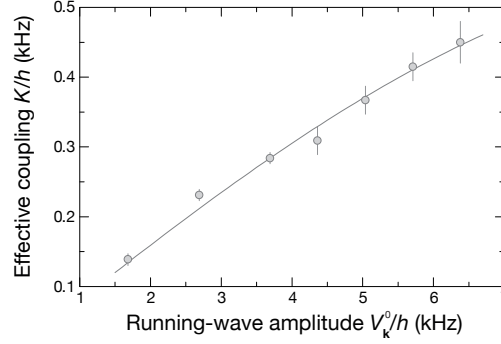


Figure 6.14: Calibration of laser-assisted tunneling  $K$ . For each value of  $V_{\mathbf{k}}^0$  the frequency of the left-right Rabi oscillation was fitted. The error bars are the errors of the fitted frequencies. The solid line is a fit to the data of a Bessel function of the first kind  $\mathcal{J}_1(x)$  (see Eq. 6.3). For each measured point we first performed a spectroscopy measurement to determine the resonant frequency at which  $\hbar\omega = \Delta$ , which was typically around 5.6 kHz. The calculated bare tunneling in the double wells was  $J_x/h = 2.2(2)$  kHz.

relative deviation of  $J$  with respect to  $J_y$ . In order to do this, the experimental sequence shown in Fig. 6.15a was used. First the atoms were loaded into a three dimensional lattice with  $V_x = 30(1) E_{rs}$ ,  $V_z = 30(1) E_{rz}$  and  $V_{ly} = 18.0(7) E_{rl}$  and then a filtering sequence to remove double occupancies was performed. Next, by ramping the short lattice along  $y$  to  $V_y = 20.0(7) E_{rs}$  in 20 ms, each single lattice site was split into double wells along  $y$ , where an initial tilt  $\Delta_y$  along that direction was used to load all the atoms into the left well. Subsequently, the energy tilt  $\Delta_y$  was set to zero in 20 ms and directly after this, the short lattice was ramped down in 0.1 ms to  $V_y = 7 E_{rs}$  and the atoms were held in this configuration during a holding time  $\tau$ . During this time, the running-wave beams were on with a frequency  $\omega/h = 5.6(4)$  kHz, which was the typical frequency used for all the chiral current measurements, and the atoms underwent left-right Rabi oscillations. As above, the frequency of the oscillation is twice the effective coupling. Therefore, by repeating this sequence for different values of  $V_{\mathbf{k}}^0$  and fitting the oscillation frequency, we were able to extract the ratio  $J_{dw}(V_{\mathbf{k}}^0)/J_{dw}(0)$  and then obtain the calibrated curve through  $J(V_{\mathbf{k}}^0) = J_y * J_{dw}(V_{\mathbf{k}}^0)/J_{dw}(0)$ , where  $J_{dw}(V_{\mathbf{k}}^0)$  is the measured coupling in the double well and  $J_y$  is the bare coupling along  $y$  in the flux ladder system (see Fig. 6.15b).

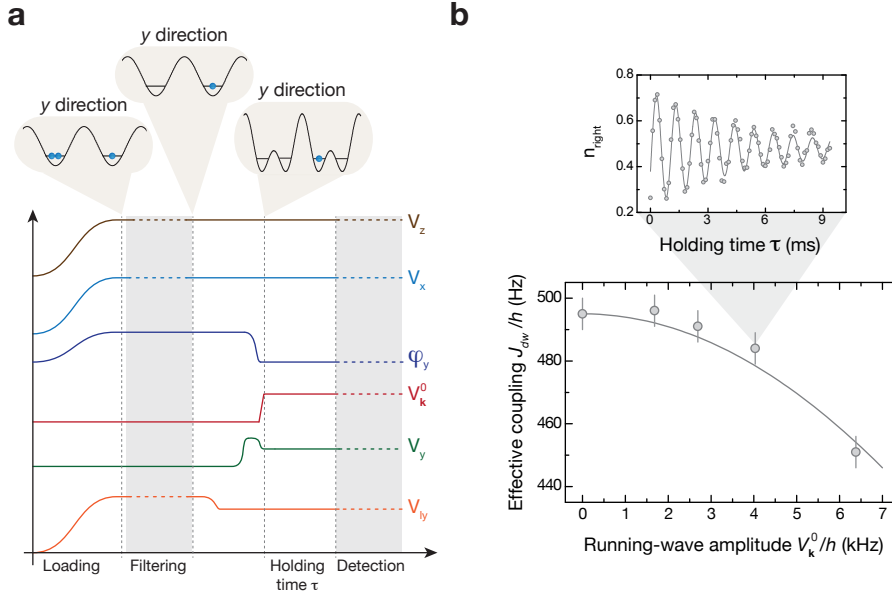


Figure 6.15: Experimental sequence for the calibration of  $J$ . **(a)** Experimental sequence used for the Rabi oscillation measurements. **(b)** Calibration of coupling  $J$ . For each value of  $V_k^0$ , the frequency of the Rabi oscillation was fitted. Each point was obtained from a single oscillation and the error bars are the errors of the fitted frequencies. The solid line is a fit to the data of a Bessel function of the first kind  $\mathcal{J}_0(x)$  (see Eq. 6.3). Inset: Rabi oscillation for the running-wave amplitude  $V_k^0/h = 4.0(3)$  kHz. The solid line is a damped sinusoidal fit to the data. The typical decay constant of the oscillations was 3 ms.

### 6.3.4 Interaction energy

The physics of the Meissner-like effect in bosonic flux ladders described in the previous chapter is a single-particle effect, in the sense that any kind of interparticle interaction is neglected. Therefore, in the experiment, the interactions have to be as small as possible to be in the non-interacting regime. One possibility could be to use Feshbach resonances to fully suppress the interactions, but unfortunately, that is not easily available for the atomic species used in our experiment ( $^{87}\text{Rb}$ ). Another possibility is to deconfine the wavefunction as much as possible along the  $z$  direction, such that the particles are less likely to interact. In the experiment we followed this approach by using a weak lattice along the  $z$  direction (more ideally, one could simply put a weak harmonic confinement along the  $z$  direction instead of a weak lattice, but as it will be explained in Fig. 6.12, it was not experimentally convenient in our setup). In the mean field approximation, one can write the interaction energy per lattice site as (see section 2.3.3)

$$U = \frac{4\pi\hbar^2 a}{m} \int d^3\mathbf{x} |\psi(\mathbf{x})|^4, \quad (6.10)$$

where  $\psi(\mathbf{x})$  is the wavefunction corresponding to a single lattice site of the three-dimensional lattice,  $m$  is the mass of  $^{87}\text{Rb}$  and  $a$  is the scattering length. The interaction energy can be numerically calculated for an infinite three-dimensional lattice by replacing  $\psi(\mathbf{x})$  with the product of the Wannier functions along the three directions, i.e.  $\psi(\mathbf{x}) = w_x(x) * w_y(y) * w_z(z)$ . For the lattice parameters of the ladder (see next section), this gives a total interaction energy of 1.06(5) kHz.

One can then estimate the interaction energy per single lattice site of the ladder, where by single site of the ladder we mean a site of the ladder together with all the sites that lie in the same line along the  $z$  direction. A complete Thomas-Fermi numerical calculation including the total number of particles ( $N = 5 \times 10^5$ ), the trapping frequencies along  $x$ ,  $y$  and  $z$  ( $\omega_x = \omega_y \approx 2\pi * 25$  Hz,  $\omega_z \approx 2\pi * 40$  Hz) and the interaction energy per lattice site 1.06(5) kHz yields a value of  $U_{2D}/h = 50$  Hz for the interaction energy in the flux ladder. This results in a ratio  $U_{2D}/J = 50$  Hz/150 Hz = 1/3. In addition, owing to the large particle number per single site tube, one can conclude that the system should remain in the weakly interacting regime for the parameters used in the experiment. This calculation also gives an effective system size of 35 lattice sites along  $z$  and 40 lattice sites along  $x$  and  $y$ .

## 6.4 Measurements of the momentum distribution after free expansion

In a second series of measurements, we investigated the momentum distribution along the  $y$  direction of the flux ladder system after time-of-flight expansion as a function of  $K/J$ . In section 5.2.4, it was shown that in the experimentally realized gauge, each quasi-momentum  $q$  has two real momentum components in the first Brillouin zone located at  $k_y = q \pm \pi/(4d_y)$  [228]. Therefore, for the Meissner phase where the lowest energy band has a single ground state at  $q = 0$ , the momentum peaks are located at  $k_y = \pm \pi/(4d_y)$ . In the vortex phase, the energy band has two ground states at  $\pm q_{K/J}$  that depend on the ratio  $K/J$ , and correspondingly four momentum peaks at  $k_y = q_{K/J} \pm \pi/(4d_y)$  and  $k_y = -q_{K/J} \pm \pi/(4d_y)$  are expected (see Fig. 5.11 and Fig. 6.16). When  $K/J \ll (K/J)_c$ , the two outer peaks at  $k_y = \pm q_{K/J} \pm \pi/(4d_y)$  vanish and the two inner peaks converge to  $k_y = 0$ .

In order to study the momentum distribution behavior, the same experimental sequence as for measuring the chiral currents was used, but instead of projecting into isolated double wells along  $y$ , the atoms were directly released from the trap and the momentum distribution after time-of-flight was determined. As displayed in Fig. 6.16b, for the Meissner phase, we observe the two expected peaks, but in the vortex phase we only observe the two inner peaks and cannot resolve the position of the outer peaks. The

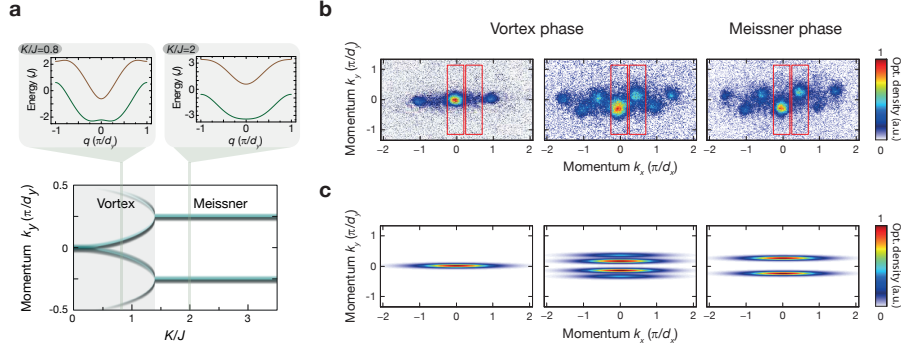


Figure 6.16: Measured and expected momentum distribution after time-of-flight expansion. **(a)** Band structure and corresponding position of the momentum peaks along the  $y$  direction as a function of the ratio  $K/J$ . **(b)** Time-of-flight images of the momentum distribution and **(c)** theoretically calculated momentum distributions for  $K/J = 0.00(1)$  (left),  $1.28(5)$  (center) and  $2.1(1)$  (right). Along the  $x$  direction a simple Gaussian was assumed.

reason for this is that close to the critical point, the two peaks at  $k_y = \pm q_{K/J} + \pi/(4d_y)$  (and at  $k_y = \pm q_{K/J} - \pi/(4d_y)$ ) are too close to each other, and the band flatness combined with the finite temperature do not allow to resolve the two peaks. On the other hand, for  $K/J \ll (K/J)_c$ , where one could expect to resolve them, the peaks are well separated but the outer peaks vanish. In our experiment, we also observe interference effects along the horizontal direction, which are caused by a residual coherence between individual ladders (see last paragraph of this section).

For the analysis of the momentum distributions, we therefore fitted the position of the two inner peaks and measured their relative distance as a function of  $K/J$ . In the analysis, we first selected two boxes around the two peaks at the center (shown in Fig. 6.16b) and integrated the signal along the horizontal direction for each box independently. Then we fitted a Gaussian function to each of the two integrated signals and extracted the two peak positions  $k_{y1}$  and  $k_{y2}$  and the widths  $\sigma_1$  and  $\sigma_2$ . We discarded all the images with a width  $\sigma = \sqrt{\sigma_1^2 + \sigma_2^2} > 0.4k_y$ , for which the peak identification was not reliable anymore, and then calculated the peak separations  $k_{y1} - k_{y2}$ . As can be seen in Fig. 6.17, we obtain a reasonable agreement with the theoretically calculated peak separation, displaying an increasing peak separation in the vortex phase and a saturated separation in the Meissner phase.

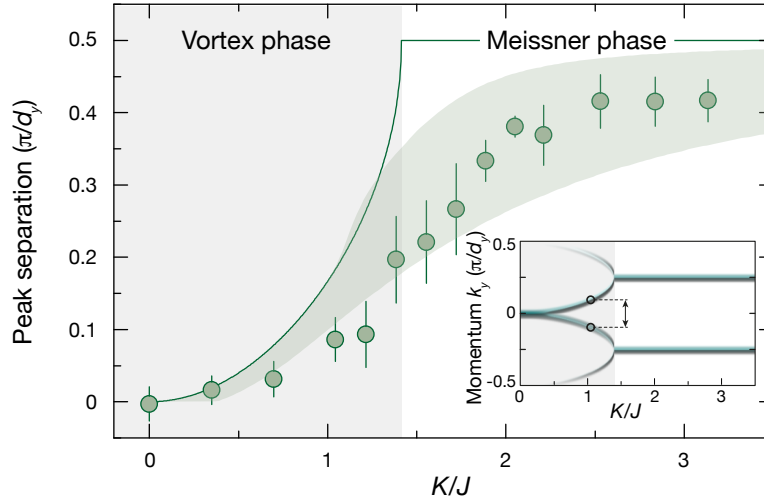


Figure 6.17: Relative position of the momentum peaks. Experimental peak separation between inner peaks as a function of  $K/J$  fitted from the time-of-flight images. Each point corresponds to an average of 5-40 individual measurements and the error bars are the standard deviations. The solid line is the theoretically calculated peak separation, where there is no free parameter. The light green shaded area shows the peak separation calculated for a system with a density of 25 particles per single site of the ladder and for a temperature range from 10 nK to 30 nK. The inset shows the expected momentum distribution along  $y$  as a function of  $K/J$ , and the black circles highlight the measured peak separation.

The small reduction in amplitude can be explained by considering the finite temperature of the system, which slightly reduces the separation of the momentum peaks. There is a two-fold reason for the reduction in the separation due to finite temperature: Non-zero temperature implies population of a fraction of the energy band, which means that, due to our experimental gauge, the maximum of the peaks are shifted closer to each other (see caption in Fig. 6.18). The second reason is that the peaks get broader and are then more strongly affected by the Wannier envelope in the time-of-flight expansion, which also shifts the peaks to a closer position (see caption in Fig. 6.19). To quantitatively estimate the peak separation for the flux ladder with finite temperature, we considered a ladder system with a density of 25 particles per single site of the ladder, and using a Bose-Einstein distribution, we calculated the occupation fraction of the different quasimomentum states and the corresponding momentum distribution for temperatures between 10 nK and 30 nK. The results are illustrated by the shaded green area in Fig. 6.17, where the effect of the Wannier envelope was also included in the calculation.

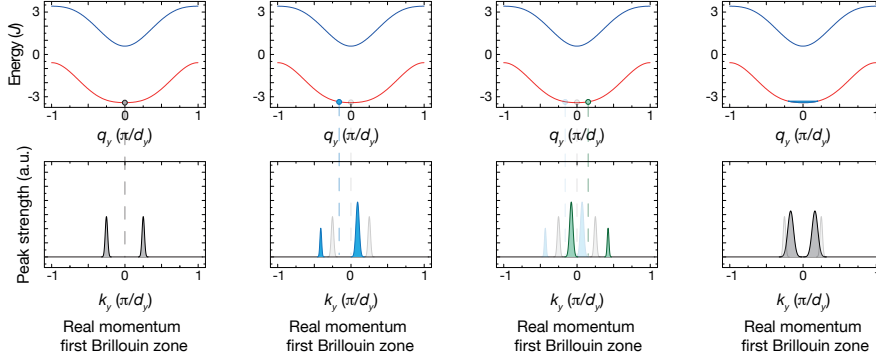


Figure 6.18: Finite temperature effect on the peak separation. When the quasimomentum  $q = 0$  is populated there are two equally strong real momentum components at  $k = \pm\pi/(4d_y)$  in the first Brillouin zone. For  $q \neq 0$  the two real momentum peaks are at  $k_y = q \pm \pi/(4d_y)$ , but they have different weights, given by  $|\alpha_q|^2$  and  $|\beta_q|^2$  (see Eq. 5.20). For  $q < 0$ ,  $|\alpha_q| > |\beta_q|$  and therefore the peak at  $k = q + \pi/(4d_y)$  is stronger than the one at  $k = q - \pi/(4d_y)$ . The opposite occurs for  $q > 0$ . For a finite temperature, the system populates a fraction of the band, and due to this asymmetry in the weights of the peaks, when adding up all the contributions, the peak separation is reduced.

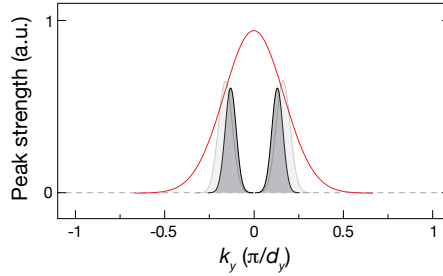


Figure 6.19: Effect of the Wannier envelope on the measured peak separation. In the time-of flight expansion, the momentum distribution of the wavefunction in the ladder is multiplied by the Wannier envelope that corresponds to the lattice configuration used in the experiment (see [18, 237] and appendix A). If the width of the momentum peaks is comparable to the one of the Wannier envelope, then the peaks are shifted closer to each other. This effect is present in our experiment, where due to the finite temperature of the system, the average experimentally measured width of the momentum peaks is  $\sigma \sim 0.32k_y$  (see Fig. 6.20), which is comparable to the measured width of the Wannier envelope  $\sigma_W \sim 0.5k_y$ .

In Figure 6.20, the measured width  $\sigma$  of the peaks as a function of  $K/J$  is shown. We observed that it increases with  $K/J$  and has a maximum value near the critical point. We attribute this to the presence of the outer peaks at  $k_y = \pm q_{K/J} \pm \pi/(4d_y)$  that have a non-negligible weight near the critical point. Additionally, the energy band becomes very flat near  $(K/J)_c$ , which combined with the finite temperature of the system, increases

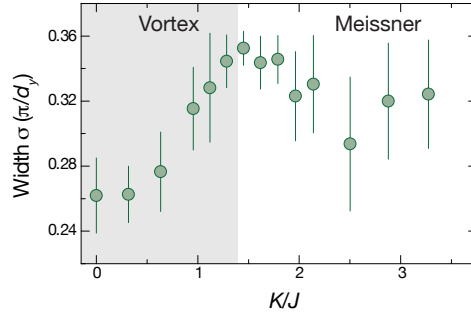


Figure 6.20: Width of the momentum peaks after time-of-flight expansion for the measurements from Fig 6.17. Each point is an average of 5-40 images, and the error bars are the corresponding standard deviations.

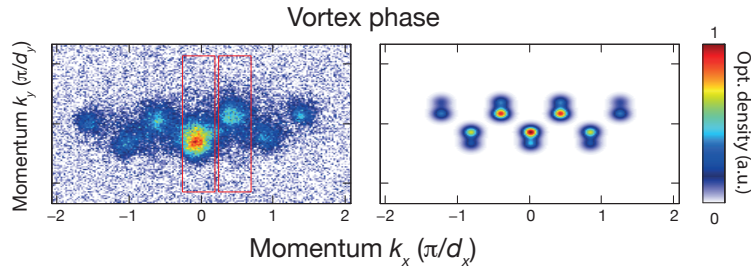


Figure 6.21: Residual interference effects along the horizontal direction. A numerical calculation of the momentum distribution (right image) due to the interference between the ground states of the two types of ladder realizations in the system qualitatively explains the interference effects observed along the horizontal direction (left image).

the width of the peaks.

The interference effects along the horizontal direction seen in the experimental images can be explained by considering a residual coherence between the individual ladders after the state preparation. As one can see in Figure 6.2a, two types of ladders exist which only differ by a global phase factor of  $\pi$  for the coupling along the rungs. Due to the residual coherence after the state preparation, these two types of ladders interfere, yielding the peak structure seen in the experiment (see Fig. 6.21).

## 6.5 Conclusion

The experimental results presented here mark the first demonstration of a low-dimensional Meissner-like effect and the first observation of chiral Meissner edge currents for a bosonic lattice superfluid. This work also demonstrates a very efficient way to implement one type of spin-orbit coupling in one-dimensional ultracold quantum gases.

In future works, it would be intriguing to use the recently developed high resolution imaging [4, 5] to measure the lattice currents in a spatially resolved way. This would enable one to not only directly detect the vortices in the flux ladders, but also measure their full current statistics [214]. Measuring the edge currents precisely would also open intriguing avenues for exploring their connection to the edge states of an integer quantum Hall insulator [228]. Furthermore, one could also hope to realize new many-body phenomena in the strongly interacting limit of a Mott insulator [20, 23], where the existence of chiral Mott insulators [238, 239] and a spin-Meissner effect for two-component systems have been predicted [211]. Detecting the quantum fluctuations [240] of a chiral Mott insulator would enable one to directly probe the chiral currents in this topologically highly non-trivial insulating phase.

## Chapter 7

# Resonating valence bond states in plaquettes

In this chapter, we discuss the realization of minimum instances of a Resonating Valence Bond state (RVB) in four-well plaquettes. In the first part, the concept of RVB states is reviewed, first within the context of chemical bonds and then in the context of condensed matter as candidates for explaining high  $T_c$  superconductivity. Then the spin model for atoms in plaquettes with dominating interactions is described as well as the spin Hamiltonian and its physics. Finally, the experimental results on the measurement of RVB states in plaquettes are given.

## 7.1 Introduction to resonating valence bond states

### 7.1.1 Quantum resonances in chemistry

In his theory of chemical bonds, L. Pauling [73, 241] developed a method to explain the chemical structure and properties of certain organic molecules. In that theory he introduced the concept of quantum resonance: a quantum superposition of resonant structures with different arrangements of the quantum bonds. Benzene ( $C_6H_6$ ) is a particular molecular structure whose bond configuration is explained by this theory. It consists of six C atoms forming a hexagonal pattern on the  $xy$ -plane, each of them in turn connected to a H atom, as illustrated in Fig. 7.1. The electronic configurations of C and H are  $1S^22S^22P_x^12P_y^1$  and  $1S^1$ , respectively. Therefore, the H atoms can share their valence electron, and the C atom has to join to three other atoms, resulting three  $sp^2$  orbitals due to hybridization. The two more likely configurations that can be formed are displayed in Fig. 7.1. Each of them consists of one C atom forming two  $\sigma$  and one  $\Pi$  bonds with another two C atoms, and one  $\sigma$  bond with one H atom.

The shared electrons that form the valence bonds are in a singlet configuration,

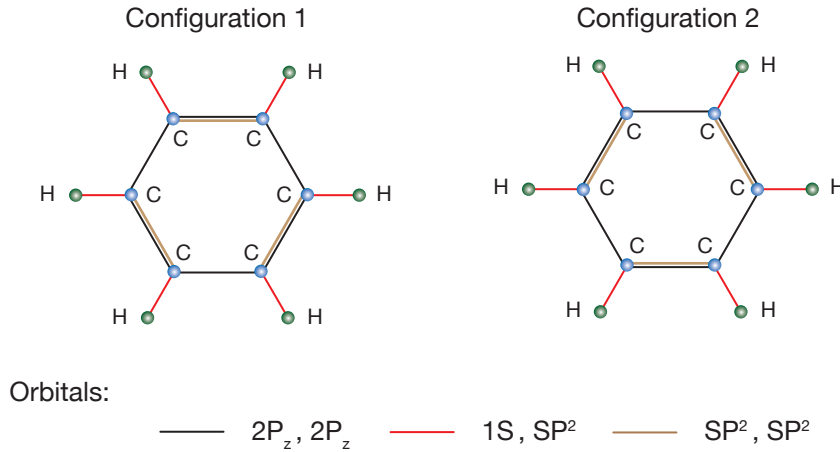


Figure 7.1: Benzene molecule. The two bond configurations of the molecule are illustrated, which differ in a rotation by  $60^\circ$ . The  $\sigma$  bonds CH are formed by the orbitals  $1S$  and  $SP^2$ , the  $\sigma$  bonds CC by two  $SP^2$  orbitals and the  $\Pi$  bonds CC by two  $P_z$  orbitals. Independently, none of the structures can explain the chemical properties of benzene; however, the quantum superposition of them does.

meaning that their spin wavefunction is described as

$$|\psi\rangle = \frac{1}{\sqrt{2}}(|\uparrow\rangle_1 \otimes |\downarrow\rangle_2 - |\downarrow\rangle_1 \otimes |\uparrow\rangle_2), \quad (7.1)$$

where the subindexes indicate the particle number.

The chemical properties of benzene cannot be explained by the two independent configurations, and since they only differ by a rotation of  $60^\circ$ , there is no reason for the system to choose one or the other configuration. The solution given by the resonance theory is that the benzene is in a quantum superposition of the states that correspond to both configurations, i.e.

$$|\psi\rangle_{Benzene} = \frac{1}{\sqrt{2}}(|\psi\rangle_{Conf 1} + |\psi\rangle_{Conf 2}), \quad (7.2)$$

where  $|\psi\rangle_{Conf 1/2}$  are the wavefunctions of the configurations 1/2, and  $|\psi\rangle_{Benzene}$  is the wavefunction of the benzene. Therefore, the singlet electronic configurations on the bonds are “resonating” between the two configurations.

### 7.1.2 RVB states in condensed matter

The Heisenberg Hamiltonian is used to describe a system of  $N$  particles that are site localized in a lattice and that interact via spin-spin interactions, through which the energy associated with them depends on whether they point in the same or in opposite directions. The explicit form of the Hamiltonian of the Heisenberg antiferromagnet is

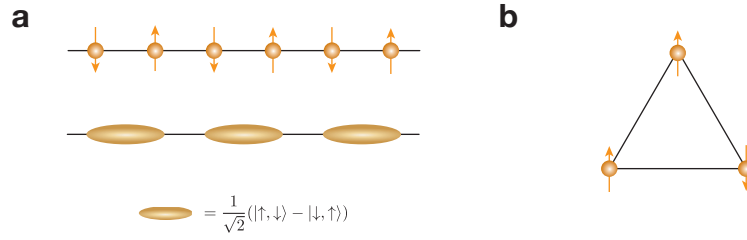


Figure 7.2: Competing mechanism in the Heisenberg antiferromagnet model for different geometries. **(a)** Spins on a one-dimensional chain with Néel ordering (top) and singlet covering (bottom). In this case, the Néel ordering is not energetically favored. **(b)** Frustration in a triangular lattice. In order to minimize the energy the system tends to put neighboring spin with antiparallel orientation. For the triangular lattice this cannot be satisfied for every pair of neighboring spins, and the system is frustrated.

$$\hat{H} = J \sum_{\langle i,j \rangle} \vec{S}_i \cdot \vec{S}_j, \quad (7.3)$$

where  $\vec{S}_i$  denotes the spin operator on the site  $i$ ,  $J > 0$  is the coupling constant and  $\langle i,j \rangle$  are pairs of next neighbor sites. The ground state properties of this Hamiltonian are not well understood except in the one-dimensional case, where the exact solution is available, which is the so called Bethe ansatz [242]. For higher dimensions, different mechanisms compete, and the solution depends also on the particular geometry of the system. To understand this, let us consider the Heisenberg model for a one-dimensional chain with  $S = 1/2$ . For a Néel state, where all the spins on even sites are up and the ones on odd sites are down, the energy per site is given by  $-J/4$  (see Fig. 7.2a). On the other hand, for a state consisting of an array of singlet dimers consecutively ordered on the chain, the total energy per site is  $-3J/8$ . According to this, the Néel state is not energetically favored in the one-dimensional chain. For higher dimensions, this is not always true, and the Néel state is sometimes favored. Consider for example the case of a three-dimensional lattice. In this case, the energy per site of the Néel state is  $-3J/4$ , while the array of dimers forming singlet bonds still has the same energy per site  $-3J/8$ , and therefore it is not favored. However, for the case of two-dimensional lattices, the energies per site are  $-J/2$  and  $-3J/8$ , respectively, for the Néel state and the array of dimers. Since these energies are comparable, the two states compete. In 1973, Anderson [74] studied the Heisenberg model in a two-dimensional triangular lattice with spin  $s = 1/2$ . This system has the particularity that a perfect Néel state with opposite spins on neighboring sites cannot exist due to the lattice geometry (see Fig. 7.2b), and the system is frustrated, meaning that there are different ways of setting the spin orientations on the sites in order to minimize the energy. Anderson proposed a certain type of states

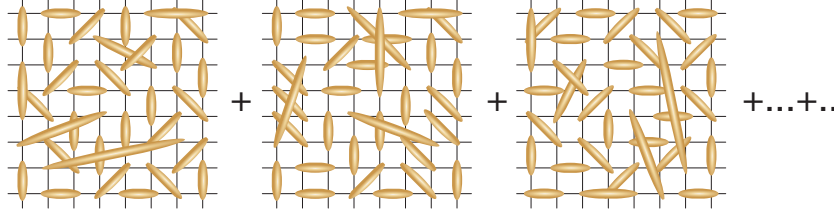


Figure 7.3: Resonating valence bond states in a two-dimensional crystal. RVB states are created by a superposition of many lattice coverings as the ones shown here. Each covering consists of a lattice with exactly one spin one-half particle per site, being each particle paired with exactly a second particle, forming a singlet state. The bonds can be formed not only between next neighbor particles, but also by particles located on any pair of sites.

called Resonating Valence Bond (RVB) states as candidates for the ground state of the triangular lattice. RVB states are defined as a superposition of many singlet coverings  $|\psi_\alpha\rangle$  on a lattice (see Fig. 7.3)

$$|\psi_{RVB}\rangle = \sum_{\alpha} c_{\alpha} |\psi_{\alpha}\rangle, \quad (7.4)$$

where each singlet covering is defined as the product state of singlet states, i.e.

$$|\psi_{\alpha}\rangle = |s_{\alpha 1, \alpha 2}\rangle \otimes |s_{\alpha 3, \alpha 4}\rangle \otimes \dots \otimes |s_{\alpha(N-1), \alpha N}\rangle, \quad (7.5)$$

with  $|s_{i,j}\rangle = (|\uparrow, \downarrow\rangle - |\downarrow, \uparrow\rangle)/\sqrt{2}$  denoting a singlet state created by the spins on the sites  $i$  and  $j$ , and  $(\alpha 1, \dots, \alpha N)$  being a permutation of the indexes  $(1, \dots, N)$ . Up to now, besides the one-dimensional chain, there is no known spin Hamiltonian with full  $SU(2)$  spin-rotational symmetry which is known to have a RVB ground state.

The concept of RVB states gained major importance shortly after the discovery of high- $T_c$  superconductivity by Bednorz and Müller in 1986 [243]. This phenomenon cannot be explained by the conventional BCS theory [72], and it was suggested by Anderson [50] that the mechanism leading to superconductivity could originate from the singlet pairs in the RVB state which become mobile and superconducting under doping. The idea was that in all the high- $T_c$  superconductors, there is a layered structure made up of one or more copper-oxygen planes, where superconductivity takes place. Each of these planes is in a Mott insulator state, where conductivity is inhibited by electron-electron repulsion and the particles are site localized. In this regime the physics is purely dictated by the spin degrees of freedom. The Hubbard Hamiltonian for spin one-half particles in the strongly interacting regime describes well the physics on the planes. It can be proven (see next section) that at half-filling, this Hamiltonian can be

mapped onto an antiferromagnetic Heisenberg Hamiltonian, as the one described in Eq. 7.3. Even though the ground state of the Heisenberg Hamiltonian is not known in general, it is believed that the ground state is the RVB state under doping [50].

## 7.2 Spin Hamiltonian with ultracold atoms in optical plaquettes

Let us consider an ultracold gas of bosonic atoms in two internal states loaded into a two-dimensional superlattice structure whose elementary cell is a plaquette made out of four wells arranged in a square pattern, as shown in Fig. 7.4. In the regime in which the tunneling amplitudes between adjacent plaquettes is strongly suppressed, the system can be regarded as a collection of independent replicas of a single plaquette, the object of our study. The Hamiltonian describing the system is

$$\begin{aligned} \hat{H}_0 = & - \sum_{\sigma=\uparrow,\downarrow} \left[ J_x^0 (\hat{a}_{\sigma A}^\dagger \hat{a}_{\sigma B} + \hat{a}_{\sigma C}^\dagger \hat{a}_{\sigma D}) + J_y^0 (\hat{a}_{\sigma B}^\dagger \hat{a}_{\sigma C} + \hat{a}_{\sigma D}^\dagger \hat{a}_{\sigma A}) \right] + \text{h.c.} \\ & + U/2 [\hat{n}_A(\hat{n}_A - 1) + \hat{n}_B(\hat{n}_B - 1) + \hat{n}_C(\hat{n}_C - 1) + \hat{n}_D(\hat{n}_D - 1)], \end{aligned} \quad (7.6)$$

where  $\hat{a}_{\sigma\mu}^\dagger$  are the creation operators for a particle with spin  $\sigma$  on the site  $\mu$ , with  $\sigma = \uparrow, \downarrow$  and  $\mu = A, B, C, D$  denoting the sites of the plaquette (see Fig. 7.4), and  $U$  is the spin-independent on-site interaction energy. The hopping terms along the  $x$ - and  $y$ -directions are given by  $J_x^0 \geq 0$  and  $J_y^0 \geq 0$ , respectively.

At half filling and when the on-site interaction  $U$  dominates over the tunneling amplitudes  $J_x^0$  and  $J_y^0$  between wells in a plaquette, atoms are site localized one per site and the physics is governed by the remaining four effective  $\frac{1}{2}$ -spins, which interact with their next neighbors via a ferromagnetic Heisenberg interaction of the form  $J \vec{S}_i \cdot \vec{S}_j$ , with  $J = -4(J^0)^2/U$  and  $J^0$  being the bare hopping term connecting the sites  $i$  and  $j$  [30, 244–247]. The effective spin- $\frac{1}{2}$  operators are given by

$$\begin{aligned} S_i^x &= (\hat{a}_{\uparrow i}^\dagger \hat{a}_{\downarrow i} + \hat{a}_{\downarrow i}^\dagger \hat{a}_{\uparrow i})/2, \\ S_i^y &= (\hat{a}_{\uparrow i}^\dagger \hat{a}_{\downarrow i} - \hat{a}_{\downarrow i}^\dagger \hat{a}_{\uparrow i})/2, \\ S_i^z &= (\hat{n}_{\uparrow i} - \hat{n}_{\downarrow i})/2, \end{aligned} \quad (7.7)$$

and the total plaquette spin Hamiltonian is

$$\hat{H} = J_x (\vec{S}_A \cdot \vec{S}_B + \vec{S}_C \cdot \vec{S}_D) + J_y (\vec{S}_B \cdot \vec{S}_C + \vec{S}_D \cdot \vec{S}_A), \quad (7.8)$$

with  $J_x = -4(J_x^0)^2/U$  and  $J_y = -4(J_y^0)^2/U$ .

To gain insight into the RVB states on a plaquette, it is convenient to write the Heisenberg interaction in terms of the swap operator  $\hat{X}_{ij} = 2\vec{S}_i \cdot \vec{S}_j + 1/2$ , a unitary operator

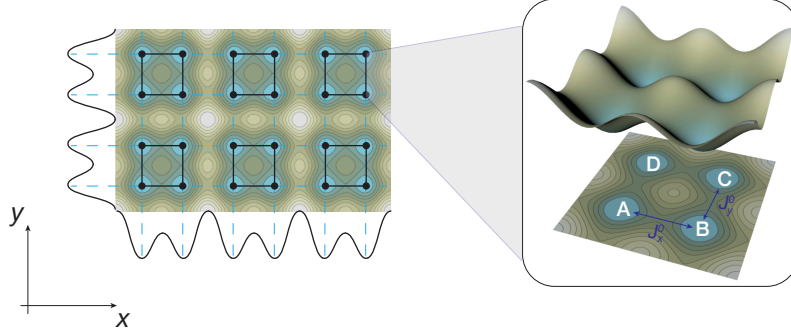


Figure 7.4: Superlattice potential used to create an array of isolated four-site plaquettes. By choosing the barrier between plaquettes high enough, each plaquette can be considered as an independent system. On the right, one can see in detail the plaquette potential and the different lattice sites. In the figure,  $J_x^0$  and  $J_y^0$  denote the bare hopping terms along the horizontal and vertical directions, respectively.

that exchanges the states of the spins on the sites  $i$  and  $j$ . The plaquette Hamiltonian then takes the form:

$$\hat{H} = J_x \hat{X}_x + J_y \hat{X}_y, \quad (7.9)$$

where  $\hat{X}_{x(y)}$  involves exchanges of two spins along an  $x$  ( $y$ )-bond:  $\hat{X}_x = (\hat{X}_{AB} + \hat{X}_{CD})/2$ ,  $\hat{X}_y = (\hat{X}_{AD} + \hat{X}_{BC})/2$ . The total Hilbert space is spanned by the states  $|\sigma_1\sigma_2\sigma_3\sigma_4\rangle$ , where  $\sigma_i$  is the spin on the site  $A$ ,  $\sigma_2$  is the spin on the site  $B$ , etc, and where two of the spins are  $|\uparrow\rangle$  and two  $|\downarrow\rangle$ . The action of the exchange operators on these states are

$$\begin{aligned} \hat{X}_x |\sigma_1\sigma_2\sigma_3\sigma_4\rangle &= |\sigma_2\sigma_1\sigma_4\sigma_3\rangle, \\ \hat{X}_y |\sigma_1\sigma_2\sigma_3\sigma_4\rangle &= |\sigma_4\sigma_3\sigma_2\sigma_1\rangle, \\ \hat{X}_{xy} |\sigma_1\sigma_2\sigma_3\sigma_4\rangle &= |\sigma_3\sigma_4\sigma_1\sigma_2\rangle, \end{aligned} \quad (7.10)$$

with  $\hat{X}_{xy} = \hat{X}_x + \hat{X}_y$  the exchange operator along the diagonals.

From now on, we consider solely the subspace of total spin zero, i.e. subspace of states for which  $\sum_{\mu=A,\dots,D} \vec{S}_\mu |\psi\rangle = 0$ . In this subspace, all spins are part of a singlet state or valence bond and it is generated by two states which correspond to arrangements in either vertical  $|00\rangle$  or horizontal bonds  $|\infty\rangle$  (see Fig. 7.5):

$$\begin{aligned} |00\rangle &= (|\uparrow_A\downarrow_D\rangle - |\downarrow_A\uparrow_D\rangle) \otimes (|\uparrow_B\downarrow_C\rangle - |\downarrow_B\uparrow_C\rangle) \\ &= (|\uparrow\uparrow\downarrow\downarrow\rangle - |\uparrow\downarrow\uparrow\downarrow\rangle - |\downarrow\uparrow\downarrow\uparrow\rangle + |\downarrow\downarrow\uparrow\uparrow\rangle), \end{aligned} \quad (7.11)$$

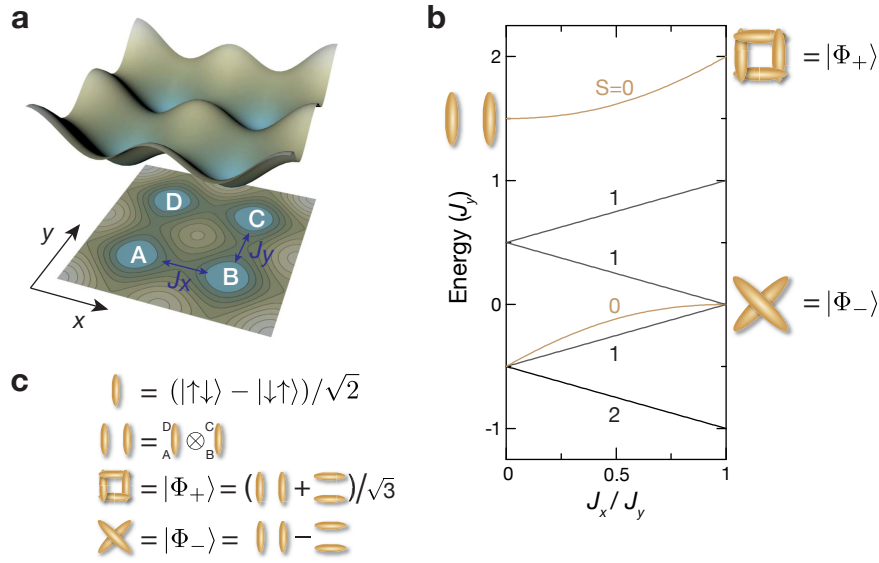


Figure 7.5: Schematics of a single plaquette and energy levels at half filling. **(a)** Scheme of the lattice potential in the  $x, y$  plane, created by a pair of bichromatic optical lattices. Here  $J_x$  and  $J_y$  denote the spin superexchange coupling terms. **(b)** Energy levels of four atoms on a plaquette in a Mott insulating state at half filling, with superexchange spin couplings along  $x$  ( $y$ ) denoted by  $J_x$  ( $J_y$ ). For any ratio  $J_x/J_y$ , the highest energy state is a total spin- $\frac{1}{2}$  singlet. In the case of  $J_x/J_y = 0$ , it corresponds to the valence bond state  $|00\rangle$ , whereas for  $J_x/J_y = 1$  it is the  $s$ -wave RVB state  $|\Phi_+\rangle$ . The other total singlet for  $J_x = J_y$ , which is lower in energy, is the  $d$ -wave RVB state  $|\Phi_-\rangle = |\otimes\rangle$ . **(c)** Symbols used for a singlet bond and for the  $s$ -wave and  $d$ -wave plaquette RVB states.

$$\begin{aligned}
 |\otimes\rangle &= (|\uparrow_A\downarrow_B\rangle - |\downarrow_A\uparrow_B\rangle) \otimes (|\uparrow_C\downarrow_D\rangle - |\downarrow_C\uparrow_D\rangle) \\
 &= (|\uparrow\downarrow\uparrow\downarrow\rangle - |\uparrow\downarrow\downarrow\uparrow\rangle - |\downarrow\uparrow\uparrow\downarrow\rangle + |\downarrow\uparrow\downarrow\uparrow\rangle).
 \end{aligned} \tag{7.12}$$

These two states satisfy  $\langle\otimes|00\rangle = 1/2$ , and therefore they are not orthogonal.

Within this subspace and for identical superexchange couplings  $J_x = J_y \equiv J$ , the Hamiltonian of Eq. 7.9 reduces to  $\hat{H} = J\hat{X}_{xy}$ . As can directly be seen, this diagonal exchange is equivalent to a 90-degree rotation of the plaquette and converts the state  $|00\rangle$  into  $|\otimes\rangle$  and vice-versa, giving rise to a resonance. The eigenstates are then the coherent superpositions (see Fig. 7.5c):

$$\begin{aligned}
 |\Phi_+\rangle &= (|00\rangle + |\otimes\rangle)/\sqrt{3}, \\
 |\Phi_-\rangle &= |00\rangle - |\otimes\rangle.
 \end{aligned} \tag{7.13}$$

These minimum instances of RVB states exhibit no local magnetic order and cannot be distinguished from each other by measuring single-site spin observables. However,

they are distinct with respect to an exchange of two spins along a diagonal: the  $s$ -wave RVB state  $|\Phi_+\rangle$  is symmetric, while the  $d$ -wave RVB state  $|\Phi_-\rangle$  is antisymmetric due to its singlet structure along the diagonals of the plaquette,  $|\Phi_-\rangle = |\otimes\rangle$ .

### 7.3 Experimental realization of the spin Hamiltonian in a plaquette

#### 7.3.1 Loading in plaquettes at half filling

In order to reproduce the spin Hamiltonian given in Eq. 7.9 and prepare spin states with two particles with spin  $|\uparrow\rangle$  and two with  $|\downarrow\rangle$ , the following experimental sequence was employed:

The experiments began with a quasi-pure Bose-Einstein condensate of about  $5 \times 10^4$   $^{87}\text{Rb}$  atoms in the Zeeman state  $|F = 1, m_F = -1\rangle$ . The atoms were loaded into a tetragonal optical lattice potential formed by three mutually orthogonal standing waves with wavelengths  $\lambda_s = 767$  nm (short lattices) along  $x$  and  $y$ , and  $\lambda_z = 844$  nm along  $z$ . Two additional standing waves with wavelengths of  $\lambda_l = 1534$  nm (long lattices) that were superimposed with the short lattices [29] along  $x$  and  $y$  were then used to realize a three-dimensional periodic potential whose elementary cell is a plaquette (see Fig. 7.4). The final lattice depths were chosen to access the Mott insulating regime with at most one atom per lattice site for our total particle number. Due to the fact that imperfections in the system can appear and there may be some plaquettes that are loaded with less than four particles, a special filtering sequence (see appendix G) was employed to be able to extract the signals only from the plaquettes with the right occupation number.

#### 7.3.2 Preparation of the initial state

The initial state used for all the experiments described in this chapter is the singlet state along the vertical bonds  $|00\rangle$ . To prepare this state, the experimental sequence displayed in Fig. 7.6 was used. It started with the plaquettes at half filling with all the atoms in the state  $|F = 1, m_F = 0\rangle$ , a state obtained after the filtering sequence explained in appendix G. First, on each plaquette, the sites along the vertical direction are merged and a Spin-Changing Collisions (SCC) operation is applied [76]. This process brings atom pairs originally in the state  $|F = 1, m_F = 0\rangle$  to the triplet state created by the internal states  $|F = 1, m_F = -1\rangle$  and  $|F = 1, m_F = 1\rangle$ . After that, the sites are split along the vertical direction, creating the triplet state along the vertical bonds

$$\begin{aligned} |00\rangle &= (|\uparrow_A\downarrow_D\rangle + |\downarrow_A\uparrow_D\rangle) \otimes (|\uparrow_B\downarrow_C\rangle + |\downarrow_B\uparrow_C\rangle) \\ &= (|\uparrow\uparrow\downarrow\downarrow\rangle + |\uparrow\downarrow\uparrow\downarrow\rangle + |\downarrow\uparrow\downarrow\uparrow\rangle + |\downarrow\downarrow\uparrow\uparrow\rangle). \end{aligned} \quad (7.14)$$

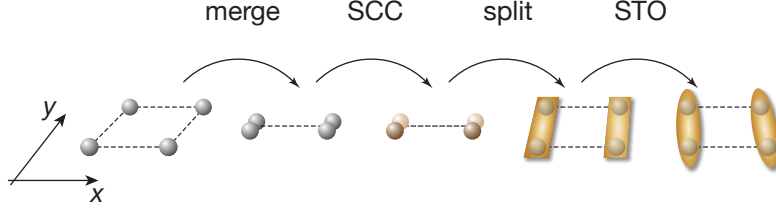


Figure 7.6: Schematics of the preparation of an array of valence bond states  $|00\rangle$  from a unit-filling Mott insulator. The gray, brown and yellow balls represent the internal states  $|F = 1, m_F = 0\rangle$ ,  $|F = 1, m_F = -1\rangle$  and  $|F = 1, m_F = 1\rangle$ , respectively.

Finally, by applying a magnetic field gradient along the  $y$ -direction, Singlet-Triplet Oscillations (STO) [75, 248] are induced, which lead to the following evolution of the state on each plaquette

$$|\psi\rangle = \cos(\omega_G t)|\square\square\rangle + i \sin(\omega_G t)|00\rangle, \quad (7.15)$$

where  $2\hbar\omega_G$  is the energy splitting between the states  $|\uparrow_A\downarrow_D\rangle$  and  $|\downarrow_A\uparrow_D\rangle$  (and also between the states  $|\uparrow_B\downarrow_C\rangle$  and  $|\downarrow_B\uparrow_C\rangle$ ) due to the magnetic field gradient. After a time  $t = \pi/2\omega_G$  the magnetic field gradient inducing the STO is removed and the resulting state is the initial state  $|00\rangle$  (see appendix H for details on the STO sequence). In total we operate in parallel over about  $10^3$  identical plaquettes with unit atom filling. Lattice depths of  $V_{lx} = V_{ly} = 35 E_{rl}$  and  $V_z = 40 E_{rz}$  with  $E_{ri} = \hbar^2/(2m\lambda_i^2)$  ensure negligible atom tunneling between plaquettes.

## 7.4 Measurements of the resonating valence bond states

### 7.4.1 Observation of the valence bond resonance

The valence bond resonance can be observed by initially preparing the state  $|00\rangle$  with  $J_y = 0$  and then suddenly setting  $J_y = J_x$ . As explained in Eq. 7.13, this projects the initial state into the Hamiltonian  $\hat{H} = J\hat{X}_{xy}$ . Since  $\hat{X}_{xy}^2 = 1$ , the evolved quantum state at time  $t$  is

$$|\Psi(t)\rangle = \cos\frac{\omega t}{2}|00\rangle - i \sin\frac{\omega t}{2}|\otimes\rangle, \quad (7.16)$$

and oscillates between the states  $|00\rangle$  and  $|\otimes\rangle$  with frequency  $\omega = 2J_{x(y)}/\hbar$  (see Fig. 7.7a).

To directly observe the valence bond resonance, the initial state  $|00\rangle$  was prepared and then the short-lattice depths were ramped down in  $200\mu\text{s}$  to  $V_x = V_y = 12 E_{rs}$ , resulting in equal couplings  $J_x \simeq J_y = -\hbar \times 120(10)$  Hz and a suppression of first order tunneling as  $|J_{x,y}^0|/U \simeq 1/8$ .

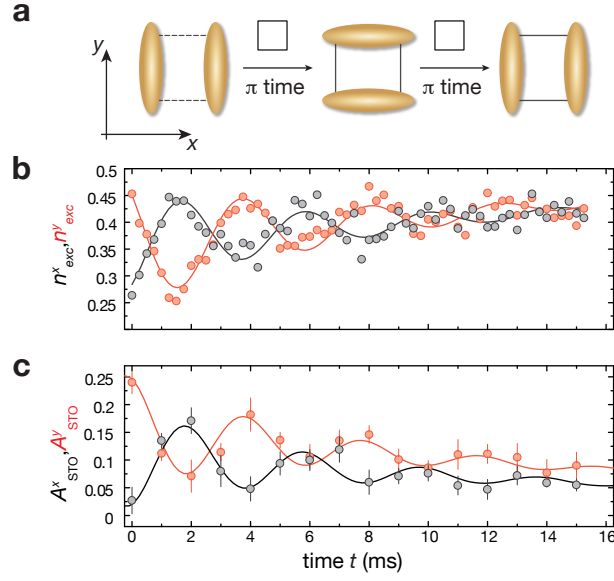


Figure 7.7: Valence bond oscillations in plaquettes. **(a)** Schematics of the valence bond oscillation: starting from  $|00\rangle$ , identical superexchange couplings along  $x$  and  $y$  are switched on, leading to a coherent oscillation between  $|00\rangle$  and  $|\infty\rangle$ . **(b), (c)** Fraction of band excitations  $n_{\text{exc}}^{x,y}$  (b) and STO amplitude  $A_{\text{STO}}^{x,y}$  (c) as a function of the hold time  $t$ . The lattice depths were  $V_x = V_y = 12 E_{rs}$ ,  $V_{lx} = V_{ly} = 30 E_{rl}$ , and  $V_z = 40 E_{rz}$ .

To characterize the state evolution, the projections onto the two valence bond states were measured:

$$\begin{aligned} C_x &= |\langle \Psi(t) | \infty \rangle|^2 = \frac{3}{4} \sin^2(\omega t/2) + \frac{1}{4}, \\ C_y &= |\langle \Psi(t) | 00 \rangle|^2 = \frac{3}{4} \cos^2(\omega t/2) + \frac{1}{4}, \end{aligned} \quad (7.17)$$

which are expected to show oscillations of amplitude  $3/4$ , since  $\langle \infty | 00 \rangle = 1/2$ .

Within the subspace of total singlets, the observable  $C_x$  can be measured by employing two different methods. In the first method, by adiabatically removing the short lattice along the  $x$ -direction, the pairs of double wells along  $x$  are merged. This process transfers the original states in the double wells to the single wells of the long lattice, populating the first and second band. It can be shown that the fraction of band excitation satisfy  $n_{\text{exc}}^x = C_x/2$  (see appendix H). This method can also be applied along the  $y$ -direction.

For the second method, STO [75, 248] are induced along the  $x$ - ( $y$ -) direction by a magnetic-field gradient and the amplitude  $A_{\text{STO}}^x$  ( $A_{\text{STO}}^y$ ) of the oscillation is measured (see appendix H).

As shown in Fig. 7.7, by using the aforementioned methods, a coherent evolution of both  $n_{\text{exc}}^{x,y}$  and  $A_{\text{STO}}^{x,y}$  was indeed observed. This dynamics corresponds to anti-correlated

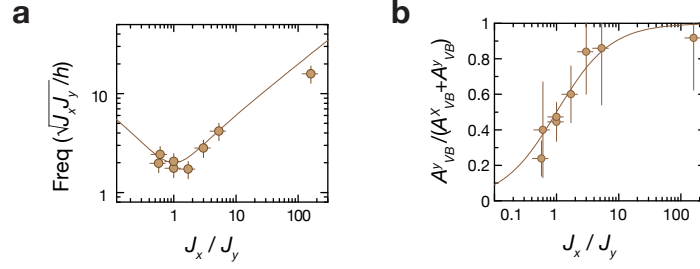


Figure 7.8: Valence bond oscillations for anisotropic couplings. **(a)** Frequency of the valence bond oscillation as a function of  $J_x/J_y$ . **(b)** Ratio  $A_{VB}^y / (A_{VB}^x + A_{VB}^y)$  as a function of  $J_x/J_y$ , where  $A_{VB}^{x,y}$  is the initial amplitude of the valence bond oscillations as shown in Fig. 7.7b. The solid lines are calculated from Eq. 7.9. The horizontal error bars represent the uncertainties in lattice depths and the vertical ones represent the  $1\sigma$  uncertainties of the fits to the STO traces.

oscillations of the projections  $\mathcal{C}_x$  and  $\mathcal{C}_y$  that reveal the periodic swapping of the valence-bond direction. The measured oscillation frequency  $\omega/2\pi = 250(10)$  Hz is compatible with twice the value of the superexchange couplings, in agreement with Eq. 7.16. While the damping of the valence bond oscillation ( $1/e$  decay time of  $6(1)$  ms) could be attributed to inhomogeneities of the different plaquette parameters across the atomic sample, the slow overall increase of  $n_{\text{exc}}^x$  and  $n_{\text{exc}}^y$  could be caused by decoherence within a plaquette.

For the initial state  $|00\rangle$ , the measured STO amplitude is about one half of the expected value  $A_{\text{STO}}^y = 1/2$  (see appendix G). This can be attributed to residual excitations introduced by the site merging, to the residual spatial overlap after time-of-flight between the atoms from the ground and first excited band, as well as to the presence of residual holes in the plaquettes that do not contribute to the STO.

To provide further evidence of the valence-bond dynamics governed by superexchange interactions, the dynamics for anisotropic couplings  $J_x \neq J_y$  was studied. As shown in Fig. 7.8, the measured oscillation frequencies and amplitudes as a function of  $J_x/J_y$  agree well with the values predicted from the Hamiltonian dynamics of Eq. 7.9. Site-resolved population measurements were used to check that throughout the evolution, the four plaquette sites remained equally populated, proving that the dynamics were entirely dominated by the spin degrees of freedom (see [29] and section 7.4.5).

#### 7.4.2 Preparation of the $s$ -wave RVB state

In order to create the  $s$ -wave RVB state  $|\Phi_+\rangle$ , one can make use of the fact that it is adiabatically connected to the initial state  $|00\rangle$  (see Fig. 7.5b). The experimental sequence used to create  $|\Phi_+\rangle$  followed this strategy. It started from the singlet state  $|00\rangle$  in a situation in which  $V_x = 22 E_{rs}$  and  $V_y = 12 E_{rs}$ . For these parameters,  $J_x/J_y$  is negligible

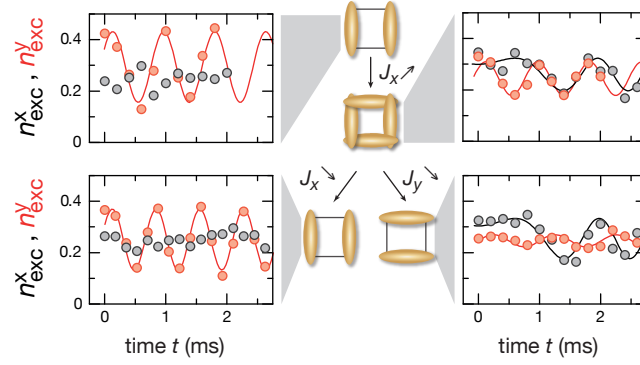


Figure 7.9: Preparation of the  $s$ -wave RVB state. Scheme of the adiabatic conversion  $|00\rangle \rightarrow |\Phi_+\rangle \rightarrow |00\rangle$  or  $|S\rangle$ , together with STO for each state. The STO period along  $x$  is not constant due to an increasing magnetic gradient field during the measurements that was caused by a finite response time of the coils producing the magnetic-field gradient along  $x$ .

and  $|00\rangle$  is an eigenstate of the Hamiltonian in Eq. 7.9. Then, using an exponential ramp,  $V_x$  was decreased within 5 ms to  $12 E_{rs}$ , such that  $J_x = J_y$ . This process adiabatically evolves the initial state and converts it into the  $s$ -wave RVB state.

In order to check the adiabaticity of the lattice-depth ramps, the short lattice along  $x$  ( $y$ ) was then increased to  $22 E_{rs}$  in 5 ms, transforming the RVB state back into a valence-bond state  $|00\rangle$  (or  $|S\rangle$ , respectively). By using STO, the singlet correlations along both directions  $x$  and  $y$  were measured for the initial, intermediate and final states of the ramp  $|00\rangle \rightarrow |\Phi_+\rangle \rightarrow |00\rangle$  or  $|S\rangle$  (see Fig. 7.9). The theoretical expectation amplitudes of these oscillations can be calculated using Eq. H.14 for the corresponding states:

$$\begin{aligned}
 |00\rangle &\rightarrow A_{STO}^y = 1/2, \\
 |\Phi_+\rangle &\rightarrow A_{STO}^y = 1/3, \\
 |S\rangle &\rightarrow A_{STO}^y = 0.
 \end{aligned} \tag{7.18}$$

As expected, for the initial state, oscillations close to maximum amplitude only along  $y$  and none along  $x$  are observed. In the intermediate state, the oscillation amplitudes are approximately equal, as expected for a non-degenerate eigenstate of the Hamiltonian in Eq. 7.9 with symmetric couplings. After the second ramp, depending on whether the superexchange coupling was decreased along  $x$  or  $y$ , singlet correlations mostly along the direction of strong coupling are observed. The measured amplitude of STO in the final state was found to be smaller than in the initial state, due to decoherence in our atomic sample which occurred on a time scale of 30 ms in our setup (see section 7.4.4).

In the RVB state  $|\Phi_+\rangle$ , the projections on the valence bond states are given by  $C_x = C_y = 3/4$ . They can be obtained from the STO amplitudes according to  $C_{x,y} = 1/4 +$

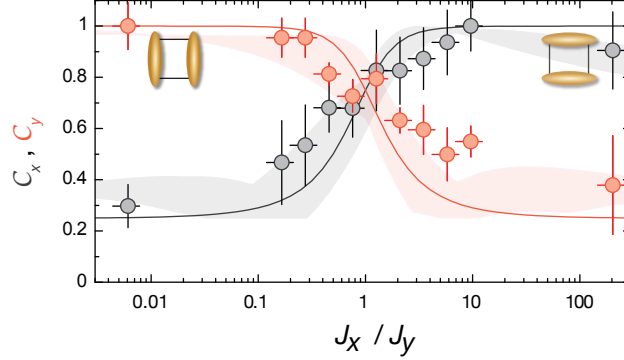


Figure 7.10: Projections  $C_x, C_y$  on the valence bond states as a function of the ratio  $J_x/J_y$  of superexchange couplings, measured from the STO amplitudes. The latter were rescaled in order to give the expected value of 0.5 for the valence bond states  $|\Xi\rangle$  and  $|00\rangle$ , using the data points at  $J_x/J_y = 0.006(2)$  and  $J_x/J_y = 10(3)$ . For the point at  $J_x/J_y = 200(50)$ , the rate of change of the couplings was the largest and adiabaticity was not maintained. The horizontal error bars represent the uncertainties in lattice depths and the vertical error bars represent the  $1\sigma$  uncertainties of the fits to the STO traces. The solid lines are calculated from the eigenstates of the Hamiltonian in Eq. 7.9. The shaded lines are calculated by modeling the experimental ramps using the Schrödinger equation. Their widths represent the uncertainties in the lattice calibration.

$3/2 A_{\text{STO}}^{x,y}$  (see Eq. H.15). By averaging the measured STO amplitudes around  $J_x = J_y$ , we obtain  $C_x = C_y = 0.76(7)$  (see Fig. 7.9), in good agreement with the theoretical prediction.

To further probe the controllability of the system, the projections  $C_x, C_y$  were also measured as a function of the coupling anisotropy  $J_x/J_y$ , by following the adiabatic path  $|00\rangle \rightarrow |\Phi_+\rangle \rightarrow |\psi(J_x/J_y)\rangle$ . The ramping times of both paths was fixed to 5 ms each. As shown in Fig. 7.10, the measurement results are in good agreement with the theoretical values in the adiabatic limit (solid lines). The oscillation amplitudes  $A_{\text{STO}}^{x,y}$  were rescaled in order to give the expected value of 0.5 for the valence bond states  $|00\rangle$  and  $|\Xi\rangle$ , using the data points at  $J_x/J_y = 0.006(2)$  and  $J_x/J_y = 10(3)$ . The rescaling factors were 3.2 and 2.3 for  $C_x$  and  $C_y$ , respectively. The small deviations observed for the case of  $J_x/J_y \gg 1$  are explained by a model that includes the finite ramp time (shaded lines), since adiabaticity is not maintained in this case.

### 7.4.3 Preparation of the $d$ -wave RVB state

The  $d$ -wave RVB state  $|\Phi_-\rangle = |\Xi\rangle$  is not connected by an adiabatic path to the initial state  $|00\rangle$ . However, a different strategy can be used to create  $|\Xi\rangle$  by noting that this state can be obtained from  $|00\rangle$  by exchanging two spins along a bond in the  $x$ -direction:

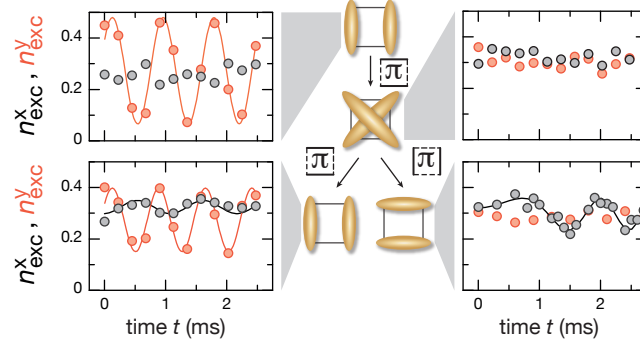


Figure 7.11: Preparation of the  $d$ -wave RVB state. Schematics of the experimental sequence: starting from the state  $|00\rangle$ , the superexchange coupling along  $x$  is suddenly switched on. The  $d$ -wave RVB state  $|\Phi_{-}\rangle$  is obtained at the  $\pi$  time of the subsequent periodic evolution. Measured STO are shown at the  $0$ ,  $\pi$  and  $2\pi$  times of the evolution. For the lower right state, the coupling direction at the  $\pi$  time was inverted.

$$\hat{X}_x|00\rangle = \frac{1}{2}(\hat{X}_{AB} + \hat{X}_{CD})|00\rangle = |\otimes\rangle. \quad (7.19)$$

To implement this unitary operator we made use of the spin Hamiltonian given in Eq. 7.9 with  $J_y = 0$ .

The experimental sequence started by preparing the initial state  $|00\rangle$  in the plaquettes and then suddenly ramping the short lattices to  $V_x = 12 E_{rs}$  and  $V_y = 22 E_{rs}$ , resulting in a negligible coupling ratio  $J_y/J_x$ . The subsequent state evolution is given by

$$|\Psi(t)\rangle = \cos \frac{\omega t}{2} |00\rangle - i \sin \frac{\omega t}{2} |\otimes\rangle, \quad (7.20)$$

with  $\omega = 2J_x/\hbar$ .

For a hold time  $t = \pi/\omega$ , the initial state evolves into  $|\otimes\rangle$  and is characterized by  $\mathcal{C}_x = \mathcal{C}_y = 1/4$  and reduced STO amplitudes  $A_{\text{STO}}^x = A_{\text{STO}}^y = 1/8$ . As shown in Fig. 7.11, in this state, the amplitude of the STO was indeed much reduced, in our case below the noise level. However, the large STO amplitude along  $y$ , observed both in the initial state and after one period of evolution ( $t = 2\pi/\omega$ ), demonstrates the coherence of the evolution and rules out a reduction of contrast at  $t = \pi/\omega$  due to decoherence. Alternatively, after preparing the  $|\Phi_{-}\rangle$  state, the coupling direction was inverted by increasing the short-lattice depth along  $x$  to  $22 E_{rs}$  and decreasing the one along  $y$  to  $12 E_{rs}$  in  $200 \mu\text{s}$ . As shown in Fig. 7.11, a coherent evolution to a state with a large overlap with  $|\otimes\rangle$  was observed, according to the measured STO.

#### 7.4.4 Decoherences in the singlet subspace

In the measurements presented in sections 7.4.2 and 7.4.3, the experimental results show that the amplitudes of the STO at the beginning and at the end of the processes  $|00\rangle \rightarrow |\Phi_+\rangle \rightarrow |00\rangle$  and  $|00\rangle \rightarrow |\Phi_-\rangle \rightarrow |00\rangle$  are reduced. In order to understand this, the decoherence of the highest energy total singlet state was investigated by measuring the fidelity of the adiabatic sweep  $|00\rangle \rightarrow |\Phi_+\rangle \rightarrow |\Xi\rangle$  as a function of the total ramp duration (see Fig. 7.12). The decrease in fidelity for small ramp durations is well accounted for by a numerical calculation of the evolution of the quantum state during the ramp, according to the Hamiltonian in Eq. 7.9. For the ramp duration of 10 ms used for Fig. 7.10, the calculation predicts a fidelity of 0.97 (see inset in Fig. 7.12). The measured decrease of fidelity for longer ramp durations illustrates a decoherence mechanism in our system whose understanding would require further studies.

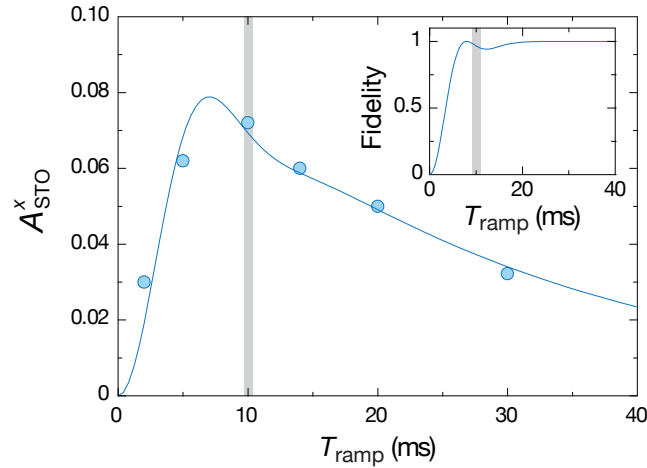


Figure 7.12: Decoherence in the singlet subspace. STO amplitude after an adiabatic sweep  $|00\rangle \rightarrow |\Phi_+\rangle \rightarrow |\Xi\rangle$  as a function of the total ramp duration. The solid line is the product of the sweep fidelity expected without decoherence and of an adjustable exponential decay ( $1/e$  decay time of 27(5)ms). The gray region indicates the ramp duration for the experiment described in section 7.4.2. Inset: Sweep fidelity expected without decoherence, calculated by solving the Schrödinger equation with the Hamiltonian shown in Eq. 7.9.

#### 7.4.5 Population evolution during the dynamics

The parameter regime used for the experiments results in a Hamiltonian dominated by the spin of the particles, and where the population on the different lattice sites should remain constant throughout the spin evolution. In order to corroborate this, the atom numbers on the different sites of the plaquette were detected by applying the mapping sequences along the  $x$  and  $y$  direction described in appendix B. During this sequence, the

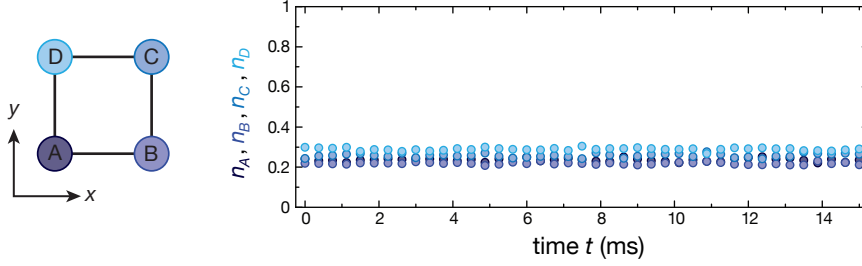


Figure 7.13: Measured population fractions  $n_q = N_q / (\sum_{q'} N_{q'})$ , with  $q = A, B, C$  and  $D$ , on the different lattice sites during the valence bond oscillations for the trace shown in Fig. 7.7. As expected, in the Mott insulating regime, the particles are site-localized and the populations stay constant all through the evolution.

populations  $N_q$  are transferred to different Bloch bands and a subsequent band-mapping technique allows us to determine the population in the Bloch bands by counting the atom numbers in different Brillouin zones. The population imbalance during the valence bond oscillations is shown in Fig. 7.13, where it can be seen that the population in four plaquette sites remained equally populated, proving the purely spin-dynamics during the oscillation.

## 7.5 Conclusions

In conclusion, we have shown direct experimental evidence of a valence-bond quantum resonance in an array of replicas of optical plaquettes by preparing and detecting minimum versions of RVB states. The  $s$ -wave and  $d$ -wave plaquette states created here could be used to encode a minimum instance of a topologically protected qubit. When stabilized by a Hamiltonian  $H = J(\hat{X}_x + \hat{X}_y + \hat{X}_{xy})$ , corresponding to a situation in which superexchange interaction takes also place along the diagonal bonds, these two states form a degenerate two level system which is immune to local decoherence arising, for instance, from on-site fluctuations of the external magnetic field. Such an arrangement could also be directly adapted to a setting of four coupled quantum dots to realize protected qubits in a solid state setting [249]. Further extensions enabled by this work include the adiabatic connection of the plaquette RVB and valence bond solid states, or the study of their non-equilibrium dynamics upon instantaneous coupling in quantum ladders or extended two-dimensional systems. Moreover, the plaquette tools developed here could be used as building blocks for more complex protocols leading to a variety of topologically ordered states, like Laughlin states or string net condensates [248, 250]. Finally, we note that all presented results could also be obtained using fermions instead

---

of bosons, where the singlet valence bond is the true ground-state of a two-spin dimer. In this case, the adiabatic connection of isolated RVB states could lead to the formation of a *d*-wave superfluid upon doping [77–79].



## Chapter 8

# Conclusions and Outlook

In this thesis, new experiments that deal with the simulation of condensed matter systems with ultracold atoms were presented. Novel techniques to generate artificial magnetic fields, to measure currents along the bonds of a lattice and to determine topological invariants in Bloch bands were studied. The methods presented here illustrate the potential of ultracold atoms as a versatile platform to investigate topological states of matter, as they allow for the extraction of observables that are otherwise inaccessible in a real material.

The measurement of the Zak phase was enabled through the use of a one-dimensional superlattice potential to recreate a dimerized system described by the SSH Hamiltonian, which models polyacetylene molecules. This Hamiltonian has two different topological phases that depend on the dimerization. A novel interferometric technique that involves Ramsey interferometry and Bloch oscillations was developed to extract the Zak phase of a Bloch band. The first approach to measure the Zak phase on a single band using the interferometric protocol was hindered by the experimental instability of the external magnetic field in the system. To overcome this difficulty, a modified protocol that involves two Bloch bands in different dimerizations and the use of an echo  $\pi$ -pulse was developed. The modified protocol is robust against magnetic field fluctuations and furthermore allows for the direct measurement of the Zak phase difference between the two topologically distinct phases of the SSH model. The experimentally measured value of the phase difference was  $0.97(2)\pi$ , in agreement with the theoretically expected value of  $\pi$ . This phase difference indicates the different topological character of the two dimerizations.

By adding a staggered energy tilt along the superlattice potential, the Rice-Mele Hamiltonian was realized, which models conjugated diatomic polymers. In this case, the Zak phase is no longer quantized in units of  $\pi$ . The interferometric protocol applied to this system allows for the extraction of the fractional Zak phase as a function of the strength of the energy staggering. The results of the measurements were quantitatively

consistent with the theoretical calculations.

Making use of the recently demonstrated single-site-resolved detection and manipulation techniques [4, 5] in a SSH model, sharp boundaries could be introduced in the system which could enable the preparation and measurement of edge states [188, 189]. Moreover, it would also permit the study of domain walls and fractional charges for non-interacting fermions or hardcore bosons [65, 152, 153, 190, 191].

One of the most challenging goals in the context of ultracold atoms is to implement experimental probes revealing non-trivial topological properties of energy bands. One possible route to study this relies on the fact that the Berry curvature gives rise to an anomalous velocity which can be monitored through in-situ images of the atomic cloud [60, 61, 251]. This idea has been recently implemented in our experimental setup, where a very accurate value for the Chern number was obtained [252]. Another possibility that has been pointed out recently is that time-of-flight images could be used to reveal topological invariants [58, 59]. The protocol presented in this thesis, which can be easily applied in two dimensional systems [66], offers the possibility to directly extract the Berry phase, Berry curvature and Chern number of an energy band. Furthermore, due to the high controllability of the system, this protocol enables measurements of a topological phase transition as a function of the lattice parameters. Our protocol has recently been used to measure the  $\pi$  flux associated with a Dirac cone in a two-dimensional hexagonal lattice [186].

Further extensions of this idea allows for the measurement of non-Abelian Berry phases in Bloch bands, such as in a system with the quantum spin-Hall effect [192]. Furthermore, multiband extensions of the protocol can enable the measurement of Wilson loops [253].

In the second project, the transition from a Meissner- to a vortex-like phase was observed in a ladder-shaped optical superlattice exposed to an artificially engineered magnetic field. For this experiment, superlattice potentials combined with lattice modulation techniques were employed to realize a ladder system with an artificial magnetic field on it. The physics of this flux ladder resembles the Meissner effect in a type-II superconductor. In this case, the ladder possesses two phases: a Meissner-like phase with a maximal chiral current along the legs, and a vortex phase for which the currents along the legs form a vortex structure. To measure the transition between these two phases, we developed a projection technique that allowed us to extract the average chiral currents along the legs as a function of the ratio of transverse rung coupling  $K$  to coupling along the legs of the ladder  $J$ . The chiral current results showed evidence of the Meissner and vortex phases, and it was possible to determine the transition point between the two phases at the critical ratio  $(K/J)_c$ , in good agreement with our theoretical expectations.

The momentum distribution of the in-situ atomic cloud measured after releasing the atoms from the trap and letting them freely expand provided another experimental

method to reveal the transition between the two phases. In this case, the observable was the position of the momentum peaks which changes as a function of the ratio  $K/J$ , providing another method to determine the critical ratio  $(K/J)_c$ .

The flux ladder and the observation of an analogue of the Meissner effect, illustrate the power of ultracold atoms to mimic condensed matter systems. This work marks the first demonstration of a low-dimensional Meissner-like effect and the first observation of this effect for a bosonic lattice superfluid. Furthermore, it also demonstrates an efficient way to implement spin-orbit coupling in one-dimensional ultracold quantum gases.

In future experiments, it would be intriguing to use high resolution imaging techniques [4, 5] to spatially reveal the currents along the bonds and furthermore to measure the full current statistics [214]. Measuring the edge currents would also signal the path to explore the connection between them and the edge states of an integer quantum Hall insulator [202].

Quantum mechanical descriptions of charged particles in a magnetic field is very rich. Future works could find very prolific to explore the intricate fractal single-particle spectrum that arises in the two-dimensional limit of recent graphene experiments [254–256]. Furthermore, one could also hope to realize new many-body phenomena in the strongly interacting limit of a Mott insulator [20, 23], where the existence of chiral Mott insulators and a Spin-Meissner effect have been predicted [211, 238, 239].

In the last project presented in this thesis, an array of isolated four-sites plaquettes created by optical superlattices was used to prepare and detect minimum versions of RVB states. For this, a loading and filtering technique was developed which allowed for the preparation of plaquettes filled with four atoms in two internal states and in a Mott regime dominated by interactions. The physics of the system was then governed by the spin degrees of freedom, where next-neighbor spins interact via superexchange coupling. Within the total singlet subspace, there are two states that span the Hilbert space, which are the total singlets along the horizontal/vertical direction. The sum and the difference of these two basis states yield the  $s$ - and  $d$ -wave RVB states, respectively. By the use of lattice manipulation techniques, these two states and a resonance between them were created. The detection of the spin correlations was achieved through the use of induced singlet-triplet oscillations and a special merging and mapping technique that allowed us to determine the singlet and triplet fraction on the bonds.

The  $s$ -wave and  $d$ -wave plaquette states created here could be used to encode a minimum instance of a topologically protected qubit. When stabilized by a Hamiltonian  $H = J(\hat{X}_x + \hat{X}_y + \hat{X}_{xy})$ , which corresponds to a situation in which superexchange interaction also takes place along the diagonal bonds, these two states form a degenerate two level system which is immune to local decoherence arising, for instance, from on-site fluctuations of the external magnetic field. Such an arrangement could also be directly adapted to a setting of four coupled quantum dots to realize protected qubits

in a solid state setting [249]. Further extensions enabled by this work include the adiabatic connection of the plaquette RVB and valence bond solid states or the study of their non-equilibrium dynamics upon instantaneous coupling in quantum ladders or extended two-dimensional systems. Moreover, the plaquette tools developed here could be used as building blocks for more complex protocols leading to a variety of topologically ordered states, like Laughlin states or string net condensates [248, 250]. Finally, we note that all presented results could also be obtained using fermions instead of bosons, where the singlet valence bond is the true ground-state of a two-spin dimer. In this case, the adiabatic connection of isolated RVB states could lead to the formation of a  $d$ -wave superfluid upon doping [77–79].

# Appendix A

## Time of flight expansion and absorption imaging

### A.1 Time of flight expansion:

The main detection method for the experiments presented in this thesis is through time-of-flight expansion and subsequent absorption imaging of the atomic cloud. This method allows to reliably extract the initial momentum distribution of the atoms in the trap before they are released.

When the atoms are released from the trap, their momentum distribution is automatically projected into the free-space momentum base and it expands ballistically for some time  $t$  before being imaged [18, 257–264]. The density distribution during the expansion encodes the original momentum distribution in the trap, according to

$$\hat{n}(x) = \frac{m}{\hbar t} |w_0(\mathbf{k})|^2 \mathcal{S}(\mathbf{k}), \quad (\text{A.1})$$

where  $w_0$  is the Fourier transform of the on-site Wannier function and  $\mathbf{k} = m\mathbf{r}/(\hbar t)$ , with  $m$  the mass of the particles. The interference term is

$$\mathcal{S}(\mathbf{k}) = \sum_{r_\mu, r_\nu} e^{i\mathbf{k} \cdot (\mathbf{r}_\mu - \mathbf{r}_\nu)} \langle \hat{a}_\mu^\dagger \hat{a}_\nu \rangle. \quad (\text{A.2})$$

Here  $\hat{a}_\mu^\dagger$  is the creator operator for a particle at the lattice site  $\mathbf{r}_\mu$ . This expression shows that the time of flight density contains information on the first order correlation function  $\langle \hat{a}_\mu^\dagger \hat{a}_\nu \rangle$ . For example, in a Mott insulator state the correlations decay exponentially to zero for the off diagonal terms, and therefore the momentum distribution does not present any special feature. On the other hand, for a superfluid state the correlations are strong and a distinctive peak structure can be observed in the momentum distribution.

The Wannier term that appears in Eq. A.1 controls the width of the cloud. For a deep lattice, where the particles are strongly localized on the sites, the Wannier function is

very sharp (see Fig. 2.7) and therefore its Fourier transform is broad. In the experiment presented in chapter 6, where we measured the momentum distribution after releasing the atoms from the flux ladder, the Wannier envelope affected the position of the momentum peaks as explained in Fig. 6.19.

Equation A.1 is only valid for large expansion times, because it is obtained after a far-field approximation. The derivation of that equation is analogous to the theory of optical diffraction. Each of the lattice sites emits an atomic wave, and after some expansion time they interfere. The far field regime is obtained when the information of the location of each of the lattice sites can be neglected [265]. It can be proved that the far-field regime is accessed when the expansion time is larger than [237]

$$t_{FF} \approx \frac{m l_c R_0}{\hbar}, \quad (\text{A.3})$$

where  $l_c$  is the characteristic coherence length of the state and  $R_0$  is the size of the cloud before the expansion. When not in the far-field regime, the diffracted peaks are affected and they get broader. In typical experiments, the cloud size is about 30 lattice sites, and the lattice spacing is 400 nm. For these parameters, and a coherence length equal to the cloud size, one finds that  $t_{FF} \approx 100$  ms, which is about 5 – 10 times larger than the typical expansion times used in our experiments. Therefore, we expect that for a state with a coherence length on the order of the cloud size, the width of the peaks measured in our experiments will be dominated by the short expansion time. On the other hand, for a Mott insulator state, where the coherence length is close to a single lattice spacing, the far-field regime is reached after a very short expansion time and therefore in that regime the experiment is not limited by the finite cloud size.

## A.2 Absorption Imaging:

The experimental method used to detect the atoms is through absorption imaging [1, 266, 267]. The method consists of shining the atoms with a resonant beam of large diameter compared to the cloud size. The beam is absorbed by the atomic cloud as it passes through it, being the transmission at each point of the cloud related to the local 3D atomic density by the formula

$$I(x, y) = I_0(x, y) e^{-\int \rho(x, y, z) \sigma dz}, \quad (\text{A.4})$$

where the beam propagates along the  $z$  direction with a light intensity given by  $I_0(x, y)$ . Here  $\rho(x, y, z)$  is the atomic density and  $\sigma$  is the absorption cross section of the atoms. After the beam passes through the cloud it is redirected to a CCD camera where each pixel detects the local distribution of light intensity which is related to the integrated

atomic density at that point. With this information one can obtain an image of the integrated cloud. Further image processing is also required to take into account the non-uniform distribution of the light intensity in the beam, and also to account for an offset on each individual pixel [81, 82, 87].



## Appendix B

# Detection of population fractions on the plaquette

For the detection of the atomic populations on the left-right sites of the double wells we use a special dumping sequence that allows us to transfer the populations initially on the left and right wells of the superlattice to the first and third Bloch bands of a single long lattice. After the dumping, we apply a band mapping technique that transfers the populations on the different Bloch bands to the different Brillouin zones [28, 45, 82, 233, 268–271]. In this appendix we explain the details of the sequence, as well as its extension used to measure the population fractions on a plaquette.

### B.1 Dumping sequence:

The experimental sequence to transfer the atoms on the right well of the superlattice to the third Bloch band of a single long lattice is as follows (see Fig. B.1a). We first freeze the atoms in the lattice by ramping the long and short lattices to  $V_{lx} = 60 E_{rl}$  and  $V_x = 40 E_{rx}$  respectively in 0.2 ms, crossing the transition to the Mott insulator state. Thereafter, in 80 ms we apply a box ramp to change the phase  $\phi_x$  between the short and long lattices introducing an energy tilt that lift the energy of the right wells. During this process, the atoms on the right wells pass non-adiabatically through an avoided crossing between the groundstate of the right well ( $|R, g\rangle$ ) and the first excited level of the left well ( $|L, e\rangle$ ), and they stay in the  $|R, g\rangle$  state. Afterwards, in 0.7 ms we exponentially ramp down the short lattice to zero, with a decay constant of  $\tau = 0.3$  ms. At the end of this ramp the atoms originally on the left well are transferred to the first Bloch band of the remaining long lattice, and the ones originally on the right to the third Bloch band. During the last ramp the system pass trough an avoided crossing between the states  $|R, g\rangle$  and the fourth Bloch band, and therefore the ramp has to be slow enough

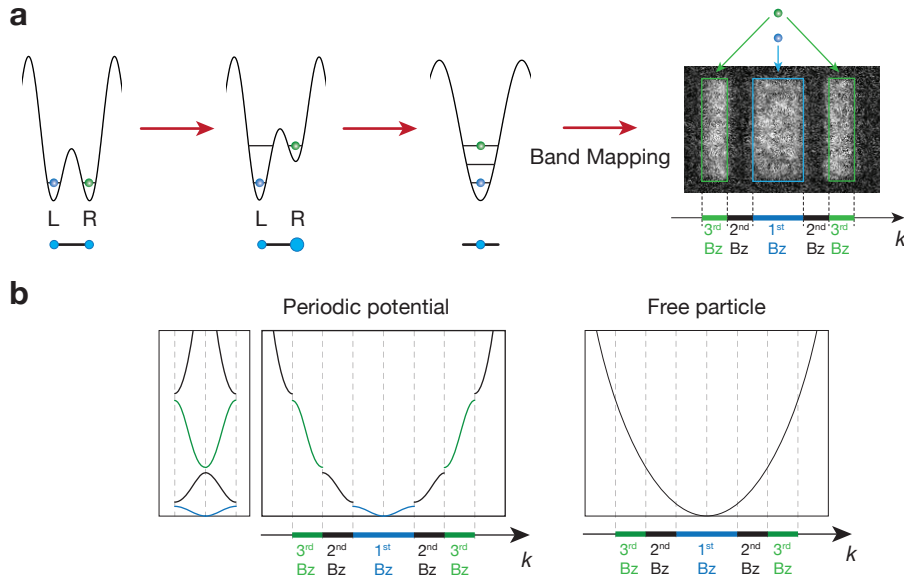


Figure B.1: Dumping and band mapping in one dimension. **(a)** The dumping technique allows to detect the atom populations on the left and right wells of the superlattice. Initially an energy tilt that put in resonance the energy of the right well with the excited energy of the left well. Then the short lattice is removed and the atoms that were initially on the left (right) well are transferred to the first (third) Bloch band of the remaining long lattice. Finally a band mapping sequence transfers the population in the first (third) band to the first (third) Brillouin zone. **(b)** The band mapping sequence consists of turning off the long lattice slow enough such that the atoms stay always in the same Bloch band, but fast enough that they do not have time to redistribute in the lattice. After the lattice has been switched off, the dispersion relation corresponds to a free particle, and the populations originally in the Bloch bands are transferred to the free momentum components as shown in the image.

to transfer the atoms to the third Bloch band and not to the fourth one.

## B.2 Band mapping sequence:

After the dumping sequence the atoms are populating the first and third Bloch bands of a single lattice potential created by the long lattice. To detect the respective atomic populations on each band and to be able to identify the initial left and right population fractions, we slowly ramp down the lattice connecting the Bloch states to the free-particle states. By slow ramp we mean slow compared to the band gap between the Bloch bands, such that the atoms stay on the same band during the ramp. On the other hand, the ramp has to be fast compared to the dynamics in the band, so that the atoms do not have time to tunnel and redistribute in the lattice. Figure B.1b illustrates how the different Bloch bands are mapped to the different free-particle momentum states. There one can

see that atoms originally in the  $i^{\text{th}}$ -Bloch band end up in the  $i^{\text{th}}$ -Brillouin zone. Figure B.1a shows an absorption image after time-of-flight expansion, where the different free-particle momentum states that are populated can be observed.

### B.3 Dumping and band mapping in two directions:

In our experiment we used an extension of the sequence to four-site plaquettes [53]. The idea is to do dumping in both directions to transfer the atoms to higher lying Bloch bands. If one denotes by  $|n_x, n_y\rangle$  the states for which the  $n_x^{\text{th}}$ - and the  $n_y^{\text{th}}$ -Bloch bands along  $x$  and  $y$  are populated respectively, then the four states involved in the dumping are:  $|1_x, 1_y\rangle$ ,  $|1_x, 3_y\rangle$ ,  $|3_x, 1_y\rangle$  and  $|3_x, 3_y\rangle$ . Figure B.2 shows the plaquettes together with the superlattice potential during the different stages of the dumping sequence. At the end, the particles originally on the sites  $A, B, C$  and  $D$  are transferred respectively to the bands  $|1_x, 1_y\rangle$ ,  $|1_x, 3_y\rangle$ ,  $|3_x, 3_y\rangle$  and  $|3_x, 1_y\rangle$ . For the band mapping we used the experimental sequence explained above, with the difference that it was done simultaneously along both directions.

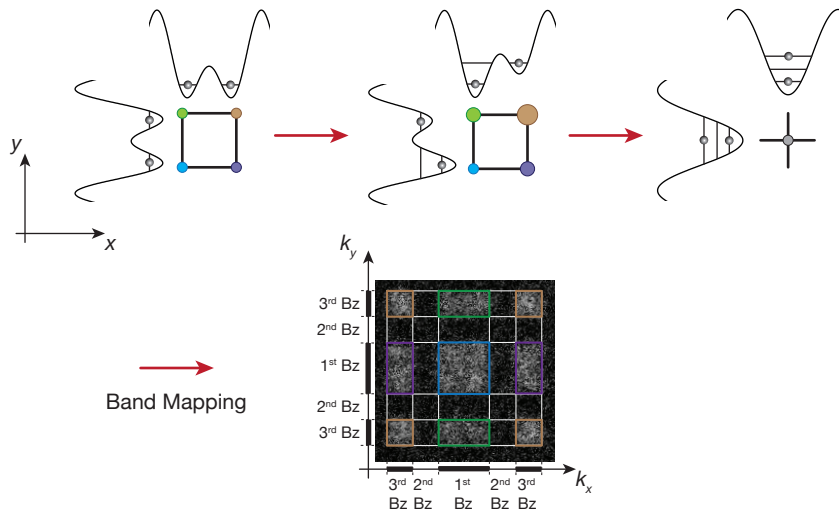


Figure B.2: Dumping and band mapping techniques in two dimensions. The dumping mechanism is similar to the one-dimensional case. In this case the atoms in the plaquette are transferred to the first and third Bloch bands along the  $x$  and  $y$  direction. Then, the particles originally in the Blue sites are transferred to the first Bloch bands along the  $x$  and  $y$  directions, the ones in the green sites to the third band along  $y$  and first along  $x$ , the ones in the violet sites to the first band along  $y$  and third along  $x$ , and the ones in the brown sites to the third band along  $y$  and  $x$ . The image shows a typical time-of-flight image after the dumping and band mapping sequences, where one can see the different populations on the different Brillouin zones.



## Appendix C

# Oscillations in double wells: calibration of the hopping terms

The experimental value of the hopping term  $J$  can be theoretically estimated if one knows the beam parameters of the lasers that create the lattice potentials, as well as the power at the atom position and the reflectivity of the retro mirror used to retroreflect the lattice beam. Instead of that, for the case of the superlattice one can also directly calibrate the tunneling terms by measuring left-right oscillations of single particles in isolated double wells. In that case, the oscillation frequency corresponds to twice the amplitude of the tunneling term.

The experimental sequence is displayed in Fig. C.1. We first loaded in 200 ms a Bose-Einstein condensate of about  $10^5$   $^{87}\text{Rb}$  atoms into a three-dimensional optical lattice created by the long lattice along  $x$ , the short lattice along  $y$  and the transverse lattice along  $z$  with the strengths  $V_{lx} = 35(1) E_{rl}$ ,  $V_y = 30(1) E_{rs}$  and  $V_z = 30(1) E_{rz}$ , respectively. During that ramp the phase  $\phi_x$  between the long and short lattices along  $x$  was ramped up to produce a large energy offset on the right wells. Thereafter, a filtering sequence was applied, which removes all the atoms from the double-occupied sites, leaving the system with either zero or one atom per lattice site [29, 76, 235, 236]. After that, the short lattice along  $x$  was increased in 20 ms to  $V_x = 30(1) E_{rs}$  to adiabatically split the sites into double well potentials. Due to the energy tilt, after this splitting only the left sites were populated. In a subsequent 20 ms ramp, the phase  $\phi_x$  is changed to zero, removing the left-right energy offset. Once in that configuration, the short lattice was quickly ramped down to  $V_x = 8.0(4) E_{rs}$  in 0.1 ms to allow for left-right oscillations. Finally, the atoms were left to evolve in that configuration during a holding time. During that time the atoms oscillate between the left and right wells, at a rate given by twice the tunneling element connecting both sites.

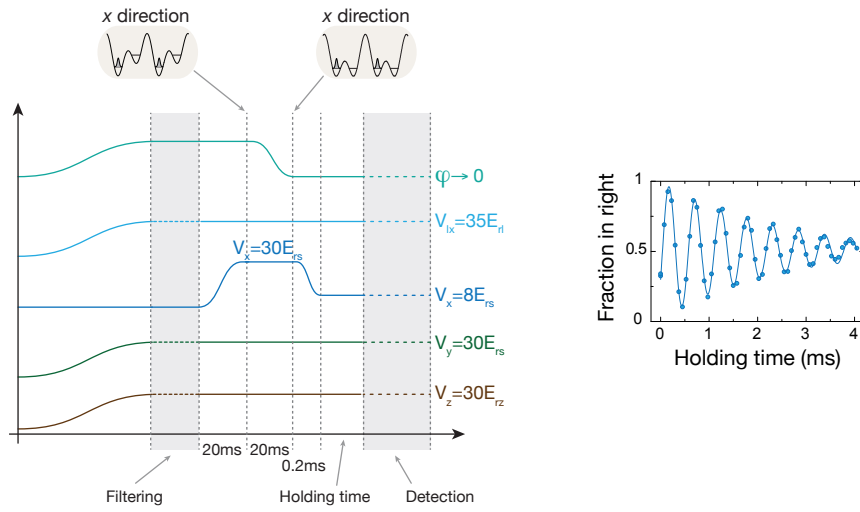


Figure C.1: Calibration of tunneling terms in double wells. The experimental sequence consists of loading the atoms on the left well of the tilted double wells and then removing the tilt and decreasing the barrier to induce left right bare tunneling. The figure on the right shows the measured atom fraction on the right double wells as a function of a holding time for the experimental parameters shown on the left sequence. The solid line is a damped sinusoidal fit to the data. The oscillation frequency of the atom population is twice the left right tunneling term  $J$ .

## Appendix D

# Eigenstates of the Rice-Mele model and the choice of the unit cell

### D.1 Boundary conditions for $\alpha_k$ and $\beta_k$ :

In this section it will be proved that for the choice of the unit cell indicated in section 3.3, the eigenstates of the Rice-Mele Hamiltonian must satisfy the relation  $\alpha_{k+G} = \alpha_k$  and  $\beta_{k+G} = -\beta_k$ .

The ansatz for the wavefunction given in Eq. 3.26 was

$$\psi_k(x) = e^{ikx} u_k(x) = \sum_n \alpha_k e^{ikx_n} w_a(x - x_n) + \beta_k e^{ik(x_n + d/2)} w_b(x - x_n - d/2),$$

from where one can rewrite the ansatz for  $u_k(x)$  as

$$u_k(x) = \sum_n \alpha_k w_a(x - x_n) + \beta_k e^{ikd/2} w_b(x - x_n - d/2). \quad (\text{D.1})$$

From the Bloch theorem it is known that  $u_{k+G}(x) = e^{-iGx} u_k(x)$ . Applying this to the expression for  $u_k(x)$  leads to

$$\begin{aligned} & \sum_n \alpha_{k+G} w_a(x - x_n) + \beta_{k+G} e^{i(k+G)d/2} w_b(x - x_n - d/2) \\ &= \sum_n \alpha_k e^{-iGx_n} w_a(x - x_n) + \beta_k e^{ikd/2 - iGx_n} w_b(x - x_n - d/2). \end{aligned} \quad (\text{D.2})$$

Finally, using that  $Gx_n = Gdn = 2\pi n$  and  $Gd/2 = \pi$ , the relations  $\alpha_{k+G} = \alpha_k$  and  $\beta_{k+G} = -\beta_k$  are obtained. These relations are a consequence of the choice of the unit cell for our system. For example, if one chooses a unit cell shifted by a distance  $a$ , then the wavefunction ansatz would be

$$\psi_k(x) = e^{ikx} u_k(x) = \sum_n \alpha_k e^{ik(x_n+a)} w_a(x - x_n - a) + \beta_k e^{ik(x_n+d/2+a)} w_b(x - x_n - d/2 - a),$$

and the eigenstates would satisfy the relations  $\alpha_{k+G} = e^{-iGa} \alpha_k$  and  $\beta_{k+G} = e^{-i\pi - iGa} \beta_k$ .

## D.2 Solutions of the Rice-Mele Hamiltonian for the choice of the unit cell indicated in section 3.3.4:

The Bloch function expansion for the unit cell indicated in Fig. 3.8 takes the form

$$\psi_k(x) = e^{ikx} u_k(x) = \sum_n \alpha_k e^{ikx_n} w_a(x - x_n) + \beta_k e^{ikx_n} w_b(x - x_n - d/2). \quad (\text{D.3})$$

By inserting this ansatz into the Schrödinger equation one arrives to the following system of equations for  $\alpha_k$  and  $\beta_k$

$$\begin{bmatrix} \Delta & -\rho_k \\ -\rho_k^* & -\Delta \end{bmatrix} \begin{pmatrix} \alpha_k \\ \beta_k \end{pmatrix} = \tilde{\varepsilon}_k \begin{pmatrix} \alpha_k \\ \beta_k \end{pmatrix}. \quad (\text{D.4})$$

where for the SSH model one has to fix  $\Delta = 0$ . In this coordinate system  $\rho(k) = J' + J e^{-ikd} = \varepsilon_k e^{i\theta_k}$ , and the  $k$ -dependent Hamiltonian is

$$\hat{H}(k) = \mathbf{B}(k) \sigma, \quad \hat{H}(k) \mathbf{u}_k = \tilde{\varepsilon}_k \mathbf{u}_k, \quad (\text{D.5})$$

with  $\mathbf{B}(k) = (\varepsilon_k \cos(\theta_k), \varepsilon_k \sin(\theta_k), \Delta)$ . Here  $\varepsilon_k$  and  $\tilde{\varepsilon}_k$  are the same as given in Eqs. 3.31 and 3.28, because the energy spectrum is gauge independent. The eigenstates  $\mathbf{u}_k$  are given by

$$\begin{aligned} \mathbf{u}_{-,k} &= \begin{pmatrix} \alpha_{-,k} \\ \beta_{-,k} \end{pmatrix} = \begin{pmatrix} \sin \frac{\gamma_k}{2} \\ \cos \frac{\gamma_k}{2} e^{-i\theta_k} \end{pmatrix}, \\ \mathbf{u}_{+,k} &= \begin{pmatrix} \alpha_{+,k} \\ \beta_{+,k} \end{pmatrix} = \begin{pmatrix} -\cos \frac{\gamma_k}{2} \\ \sin \frac{\gamma_k}{2} e^{-i\theta_k} \end{pmatrix}. \end{aligned} \quad (\text{D.6})$$

This solution has the same structure as in Eq. 3.32, but the angle  $\theta_k$  is different compared to the one given in Eq. 3.33 due to the different boundary conditions for  $\alpha_k$  and  $\beta_k$ . This condition leads to a drop of the factor 1/2 that multiplies  $k$  in the expression for the angle:

$$\theta_k = \arctan \frac{(J - J') \sin(kd)}{(J + J') \cos(kd)}. \quad (\text{D.7})$$

Thus, the angle  $\theta_k$  goes from  $-\pi$  to  $\pi$  as  $k$  travels across the Brillouin zone.

The Zak phase also depends on the choice of the unit cell as discussed in chapter 3. Using Eq. 3.20 one can see that its value is modified from  $\pm\pi/2$  to 0 and  $\pi$ , depending on the dimerization.



# Appendix E

## Theory of Bloch oscillations and the phases acquired during the evolution

### E.1 Bloch oscillations in lattices

The quantum theory of electrons in periodic potentials described by Bloch and Zener [272, 273] predicts that when electrons are placed in a periodic potential and exposed to a constant force, they perform an oscillatory movement instead of simply moving in one direction as a free particle would do. This oscillatory movement, known as Bloch oscillation, is very difficult to observe in real materials due to the high scattering rate of the electrons in the material. Ultracold atoms in optical lattices provide an ideal scenario to study this dynamics because they offer a defect-free system with a high degree of controllability in their parameters. The first experimental measurement of Bloch oscillations with ultracold atoms was carried out in the group of C. Salomon [21], and since then many other groups have observed this phenomenon. In that context, the lifetime of the Bloch oscillations is mainly limited by the atomic interactions, which lead to decoherences in the system [274].

Bloch oscillations can be intuitively explained using the band theory of solids. Consider a system initially prepared in the quasimomentum state  $q_0$  in the lowest band of a one-dimensional periodic potential with period  $d$ . When an additional weak linear potential  $F \cdot x$  is applied, the system undergoes an evolution in which on each lattice site  $x_n = d \cdot n$  the population stays constant and the phase of the wavefunction evolves according to  $e^{-i(Fdn)t/\hbar}$ . That evolution in the phases is equivalent to a linear evolution of the quasimomentum given by  $q(t) = q_0 - Ft/\hbar$ . Due to the periodicity of the Brillouin zone, i.e.  $q \in (-\pi/d, \pi/d)$ , the quasimomentum evolves periodically populating the eigenstates  $q(t)$  as illustrated in Fig. E.1. The oscillatory behavior of the quasimomentum is translated into an oscillation of the velocity of the system

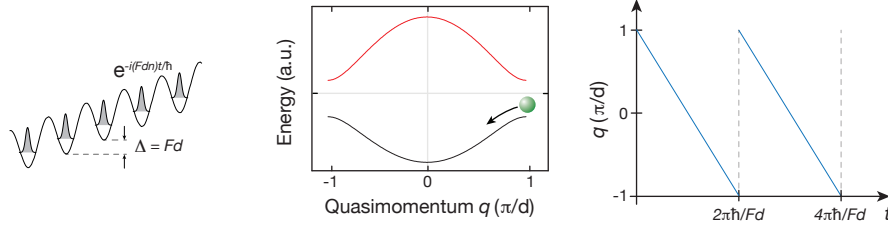


Figure E.1: Bloch oscillations in a one-dimensional lattice. A quantum system in a one-dimensional lattice exposed to a weak linear potential  $F \cdot x$  undergoes a Bloch oscillation (left, center), where the phase at each lattice site evolves as  $e^{-i(Fdn)t/\hbar}$ . Due to the linear potential, a system which is initially in the lowest band (black) and in the quasimomentum  $q_0$  ( $q_0 = \pi/d$  in the figure) evolves populating the states  $q = q_0 - F \cdot t/\hbar$ . Because of the periodicity of the Brillouin zone, the quasimomentum evolves periodically in time (right). If the strength of the linear potential is not weak, then also higher bands get populated and the dynamics becomes more complicated.

$$\mathbf{v}(t) = \frac{1}{\hbar} \frac{\partial \varepsilon_k}{\partial k} = \frac{2Jd}{\hbar} \sin(kd), \quad (\text{E.1})$$

where  $\varepsilon_k = -2J \cos(kd)$  is the energy for each quasimomentum  $k$ , with  $J$  being the hopping constant between consecutive lattice sites. Consequently, the center of mass position of the system also oscillates

$$\mathbf{r}(t) = \frac{2J}{F} \cos(kd). \quad (\text{E.2})$$

The amplitude of the oscillation is equal to  $2J/F$ , which is typically a few lattice sites.

For this explanation only the lowest band was considered, and any transition to a higher band was neglected. This approximation is valid as long as the probability of transferring atoms to a higher band is sufficiently small. This is not the case for a large linear potential, where the Landau-Zener probability of transferring atoms to the higher band is non-negligible, mainly close to the edges of the Brillouin zone where the energy gap gets smaller.

## E.2 Phase evolution during the Bloch oscillations

In the following we will derive the dynamical equations for the Bloch oscillations in the dimerized lattice, and the phase that one atom picks up as it evolves and completes one cycle will be calculated. This derivation, as well as many theoretical aspects discussed

in this project, were obtained by the theory group around E. Demler, and in particular by D. Abanin.

Consider the dimerized lattice given in Eq. 3.25 subjected to an external force, described by the Hamiltonian

$$\hat{H}_F = \hat{H}_{RM} - F \sum_n \left\{ (x_n - x_0) \hat{a}_n^\dagger \hat{a}_n + (x_n + \frac{d}{2} - x_0) \hat{b}_n^\dagger \hat{b}_n \right\},$$

with  $x_n = nd$ .

The eigenstates of  $\hat{H}_{RM}$  are Bloch waves with energies  $\pm \tilde{\epsilon}_k = \pm \sqrt{\Delta^2 + \epsilon_k^2}$ . For the analysis it is convenient to introduce the following creation operator for the quasimomentum states:

$$\hat{c}_{\pm,k}^\dagger = \frac{1}{\sqrt{N}} \sum_n \left\{ \alpha_{\pm,k} e^{ikx_n} \hat{a}_n^\dagger + \beta_{\pm,k} e^{ik(x_n + \frac{d}{2})} \hat{b}_n^\dagger \right\}, \quad (\text{E.3})$$

where  $N$  is the total number of sites in the lattice. This operator simply creates two Bloch waves, one on the even sites and one on the other on the odd sites with amplitudes  $\alpha_{\pm,k}$  and  $\beta_{\pm,k}$ , respectively. For finite  $F$  one needs to solve the Heisenberg equation of motion  $\frac{d}{dt} \hat{\Psi}^\dagger(t) = \frac{i}{\hbar} [\hat{H}_F, \hat{\Psi}^\dagger(t)]$ .

As explained above, we expect the quasimomentum to change at a constant rate, and therefore the following ansatz is used

$$\hat{\Psi}^\dagger(t) = A(t) \hat{c}_{-,k_0-vt}^\dagger + B(t) \hat{c}_{+,k_0-vt}^\dagger. \quad (\text{E.4})$$

Using

$$\begin{aligned} \frac{\partial}{\partial t} \hat{c}_{-,k_0-vt}^\dagger &= - \frac{v}{\sqrt{N}} \sum_n \left[ i\alpha_{-,k} x_n + \frac{\partial \alpha_{-,k}}{\partial k} \right] e^{ikx_n} \hat{a}_n^\dagger \Big|_{k=k_0-vt} \\ &- \frac{v}{\sqrt{N}} \sum_n \left[ i\beta_{-,k} (x_n + \frac{d}{2}) + \frac{\partial \beta_{-,k}}{\partial k} \right] e^{ik(x_n + \frac{1}{2})} \hat{b}_n^\dagger \Big|_{k=k_0-vt} \end{aligned}$$

and

$$\begin{aligned} [\hat{H}, \hat{c}_{-,q}^\dagger] &= \epsilon_{-,q} \hat{c}_{-,q}^\dagger - \frac{F}{\sqrt{N}} \sum_n \left[ \alpha_{-,q} (x_n - x_0) e^{iqx_n} \hat{a}_n^\dagger \right. \\ &\quad \left. + \beta_{-,q} (x_n + \frac{d}{2} - x_0) e^{iq(x_n + \frac{d}{2})} \hat{b}_n^\dagger \right], \end{aligned}$$

and multiplying the equation of motion on the right and left by the vacuum state  $|0\rangle$  and by  $\langle 0| c_{-,k_0-vt} = e^{-i(k_0-vt)x} \langle u_{-,k_0-vt} |$  respectively, we find that the ansatz in Eq. E.4 provides a solution of the Heisenberg equation of motion when  $v = f = F/\hbar$  and

$$\begin{aligned} -i\dot{A} &= \epsilon_{-,k_0-ft} A/\hbar + f x_0 A - \frac{fA}{i} \langle u_{-,k_0-ft} | \partial_k u_{-,k_0-ft} \rangle \\ &- \frac{fB}{i} \langle u_{-,k_0-ft} | \partial_k u_{+,k_0-ft} \rangle \end{aligned} \quad (\text{E.5})$$

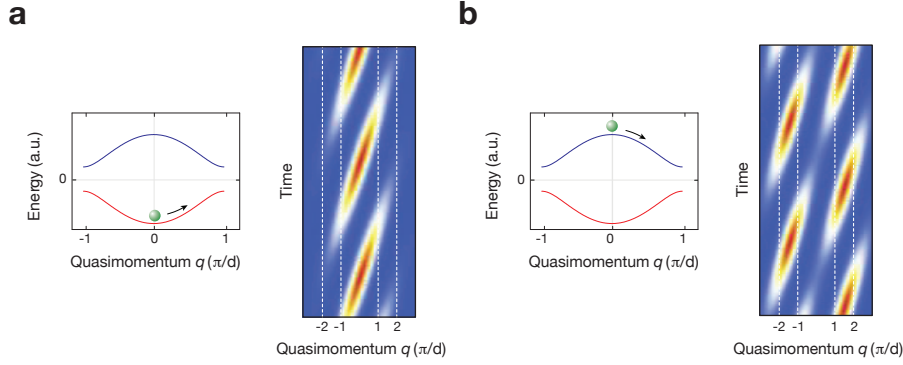


Figure E.2: Bloch oscillations in lower **(a)** and upper band **(b)**. As the particle moves along the energy band the quasimomentum evolves linearly in time. The real momentum distribution consists of peaks separated by  $\pi/d$ , where the weights of each peak depend on the band.

and a similar equation for  $B$ . The last term in Eq. E.5 describes non-adiabatic mixing of the bands, which can be neglected for a weak external force. Assuming that the atoms occupy only the lower band ( $B = 0$  and  $|A| = 1$ ) and taking  $A(t) = e^{i\varphi_{tot}(t)}$ , one arrives to:

$$\dot{\varphi}_{tot} = \varepsilon_{-,k_0-ft}/\hbar + fx_0 - \frac{f}{i} \langle u_{-,k_0-ft} | \partial_k u_{-,k_0-ft} \rangle. \quad (\text{E.6})$$

The first term in Eq. E.6 describes the dynamical phase contribution, which depends on the time that the system spends on each point of the band structure. The second term is the Zeeman phase, which is also a dynamical phase and it is due to the total contribution of the local energies  $F \cdot (x_n - x_0)$ . We call it Zeeman phase because in the experiments we use a magnetic field gradient to create a site dependent Zeeman energy which produces a force on the system (see section 4.1). The last term can be recognized from Eq. 3.17, as its integral gives the Zak phase. Integrating Eq. E.6 over a period of the Bloch oscillations gives the total phase

$$\varphi_{tot} = \varphi_{dyn} + \varphi_{Zeeman} + \varphi_{Zak}, \quad (\text{E.7})$$

where  $\varphi_{Zak}$  is defined as the Zak phase that corresponds to choosing the origin of the coordinate system at  $x = x_0$ , i.e. such that the driving force can be written as  $F(x_n + d/2 - x_0)$ .

From Eqs. 3.32, E.3 and E.4 one can calculate the corresponding momentum distribution of the state  $\hat{\Psi}^+(t) |0\rangle$  for the lowest and highest bands. From Eq. E.3 one can see that the wavefunction has two components, given by two different sublattice sites. Each of these components has momentum peaks located at  $k + \pi n/d$ , and according to

the relative phase between  $\alpha_{\pm,k}$  and  $\beta_{\pm,k}$ , those peaks interfere constructively or destructively. For the lowest band the interference yields peaks located at  $k + 2\pi n/d$ , and for the highest band at  $k + \pi/d + 2\pi n/d$ . The strength of each of those peaks is modulated by the momentum distribution of the wavefunction on each lattice site, i.e. the Wannier function, as is displayed in Fig. E.2.



# Appendix F

## Ramsey interferometry

### F.1 Ramsey interferometry

Ramsey interferometry is an interferometric method developed by Norman Ramsey to measure the transition frequency of atoms using magnetic resonances [275]. The method is nowadays used in many different contexts and for more general purposes. In this section we will focus exclusively on how the method can be used to extract a relative phase between two spin components.

Consider a two-level system with states denoted by  $|g\rangle$  and  $|e\rangle$  and energy difference  $\hbar\omega_0$ , exposed to a resonant microwave (MW) field  $V(t) = V_0 \cos(\omega_0 t - \pi/2)$  that couples the two levels (see Fig. F.1a). In the rotating frame the system is described by the Hamiltonian

$$\hat{H}_{spin} = \begin{pmatrix} 0 & iV_0/2 \\ -iV_0^*/2 & 0 \end{pmatrix}, \quad (\text{F.1})$$

where the rotated basis is  $|\uparrow\rangle = |e\rangle e^{-i\omega_0 t/2}$  and  $|\downarrow\rangle = |g\rangle e^{i\omega_0 t/2}$ . For an initial state  $|\downarrow\rangle$ , the time evolution of the system is

$$|\psi\rangle(t) = \cos(\omega t/2) |\downarrow\rangle + \sin(\omega t/2) |\uparrow\rangle, \quad (\text{F.2})$$

where  $\omega = |V_0|/\hbar$  is the Rabi frequency. A  $\pi$ -pulse is defined as a pulse of the external field for a time  $\pi/\omega$ , after which the system encounters itself in the state  $|\uparrow\rangle$ , and a  $\pi/2$ -pulse is a pulse of duration  $\pi/2\omega$ , after which the system is in the superposition state  $(|\downarrow\rangle + |\uparrow\rangle)/\sqrt{2}$ . The corresponding matrix operators are

$$\hat{R}_\pi = \begin{pmatrix} 0 & 1 \\ -1 & 0 \end{pmatrix}, \quad \hat{R}_{\pi/2} = \frac{1}{\sqrt{2}} \begin{pmatrix} 1 & 1 \\ -1 & 1 \end{pmatrix}. \quad (\text{F.3})$$

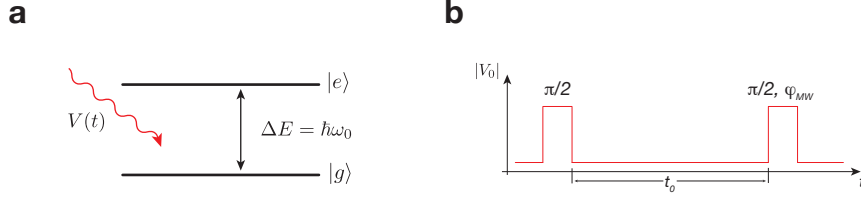


Figure F.1: Ramsey interferometry on a two-level system. **(a)** Two level system with states  $|g\rangle$  and  $|e\rangle$  and energy difference  $\hbar\omega_0$ . The MW radiation is represented by the red arrow. **(b)** Ramsey sequence consisting of two  $\pi/2$ -pulses separated the the time interval  $t_0$ . For the second pulse the phase of the MW field is changed to  $\varphi_{MW}$ .

Consider the sequence shown in Fig. F.1b, which consists of two  $\pi/2$ -pulses separated by a time interval  $t_0$ . For an initial state  $|\downarrow\rangle$ , the first pulse transforms it to  $(|\downarrow\rangle + |\uparrow\rangle)/\sqrt{2}$ . During the time  $t_0$  the MW field is off and the state stays constant (in the rotating frame). Then, when the second pulse is applied the state is transformed to  $|\uparrow\rangle$ . If for the second pulse the phase of the MW field is shifted, i.e.  $V_0 \cos(\omega_0 t - \pi/2) \rightarrow V_0 \cos(\omega_0 t - \pi/2 + \varphi_{MW})$ , then the second  $\pi/2$ -pulse transforms the state as follows

$$\begin{aligned} |\downarrow\rangle &\rightarrow \frac{e^{-i\varphi_{MW}/2}}{\sqrt{2}} (e^{i\varphi_{MW}/2} |\downarrow\rangle + e^{-i\varphi_{MW}/2} |\uparrow\rangle), \\ |\uparrow\rangle &\rightarrow \frac{e^{i\varphi_{MW}/2}}{\sqrt{2}} (-e^{i\varphi_{MW}/2} |\downarrow\rangle + e^{-i\varphi_{MW}/2} |\uparrow\rangle), \end{aligned} \quad (\text{F.4})$$

and therefore the state after the time  $t_0$  is transformed to

$$\begin{aligned} |\psi\rangle(t) &= \frac{1}{\sqrt{2}} \left[ \frac{e^{-i\varphi_{MW}/2}}{\sqrt{2}} (e^{i\varphi_{MW}/2} |\downarrow\rangle + e^{-i\varphi_{MW}/2} |\uparrow\rangle) \right. \\ &\quad \left. + \frac{e^{i\varphi_{MW}/2}}{\sqrt{2}} (-e^{i\varphi_{MW}/2} |\downarrow\rangle + e^{-i\varphi_{MW}/2} |\uparrow\rangle) \right] \\ &= -ie^{i\varphi_{MW}/2} \sin(\varphi_{MW}/2) |\downarrow\rangle + e^{-i\varphi_{MW}/2} \cos(\varphi_{MW}/2) |\uparrow\rangle. \end{aligned} \quad (\text{F.5})$$

By measuring the occupation fraction on the two levels as a function of the phase  $\varphi_{MW}$  a so-called Ramsey fringe is obtained.

Now, consider the situation in which during the time between the two MW pulses the system acquires an extra relative phase  $\varphi_0$ . In that case, the state of the system directly before the second pulse is

$$(e^{i\varphi_0/2} |\downarrow\rangle + e^{-i\varphi_0/2} |\uparrow\rangle) / \sqrt{2}. \quad (\text{F.6})$$

The extra phase could be acquired for example due to some perturbation in the system that takes place between the two pulses. In the following sections we will show that in

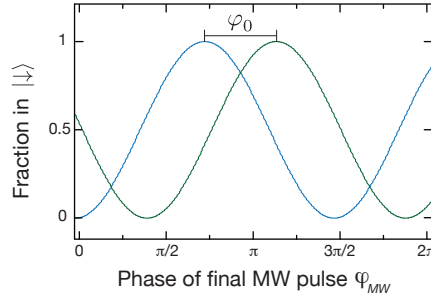


Figure F.2: Ramsey fringes. The population fraction in the state  $|\downarrow\rangle$  oscillates as a function of the MW phase  $\varphi_{MW}$ . When during the time between the two MW pulses the system is not perturbed the phase of the fringe is zero (blue curve). On the other hand, if a phase  $\varphi_0$  is acquired during that time, then the phase of the fringe is shifted by the same phase (green curve).

our experiment such a phase is the geometric phase of a Bloch band and it is picked up during the Bloch oscillations in the band.

After the second pulse, the state is transformed to

$$|\psi\rangle(t) = -ie^{i\varphi_{MW}/2}\sin((\varphi_{MW} - \varphi_0)/2)|\downarrow\rangle + e^{-i\varphi_{MW}/2}\cos((\varphi_{MW} - \varphi_0)/2)|\uparrow\rangle. \quad (\text{F.7})$$

This shows that the extra phase acquired during the evolution shifts the phase of the entire Ramsey fringe and therefore it can be easily obtained from a fit to the fringe (see Fig. F.2).



## Appendix G

# Sequence for the preparation of initial states in plaquettes

### G.1 Filtering sequences

The study presented in chapter 7 relies on the loading of plaquettes at half filling, i.e. with four atoms in total per plaquette. Despite the preparation of the atomic sample in a Mott insulator state at unit filling, defects are relatively likely in our system. In order to isolate the signal from correct configurations, a filtering sequence was performed that consists in transferring the atoms in plaquettes with incorrect fillings into different hyperfine states, which are not probed in the final atom imaging (see Fig. G.1a,b). Starting with the atoms loaded in the plaquettes in the internal state  $|F = 1, m_F = -1\rangle$ , radio frequency adiabatic passage was used to transfer all the atoms to the state  $|F = 1, m_F = 0\rangle$ . For the filtering sequence, first pairs of sites are merged along  $x$  and spin-changing collisions (SCC) are performed to convert pairs of atoms in  $|F = 1, m_F = 0\rangle$  to the Zeeman states  $|F = 1, m_F = 1\rangle$  and  $|F = 1, m_F = -1\rangle$ . A microwave pulse then transfers the remaining atoms in  $|F = 1, m_F = 0\rangle$  to the state  $|F = 2, m_F = 0\rangle$ . Then SCC are used to transfer back atom pairs in  $|F = 1, m_F = 0\rangle$ . With another microwave pulse we transfer the remaining atoms in  $|F = 1, m_F = 1\rangle$  due to finite SCC fidelity to  $|F = 2, m_F = 2\rangle$ . Then the sites along  $x$  are split. The rest of the sequence is identical to the one described in Fig. 7.6, i.e. pairs of sites along  $y$  are merged and SCC are performed. As shown in Fig. G.1, the plaquettes with one atom per site end this filtering sequence in the desired configuration. On the contrary, a hole in the initial configuration leads to the transfer of one atom to the  $F = 2$  hyperfine state, and finally to a configuration with one atom per site in  $|F = 1, m_F = 0\rangle$  before the final SCC. Therefore no atom is transferred to the state  $|F = 1, m_F = 1\rangle$  that we probe at the end of the experiment. Similar conclusions can be obtained for the configurations with additional holes or particles. In total about 10% of the atoms end the filtering sequence in  $|F = 1, m_F = 1\rangle$  (see Fig. G.1c).

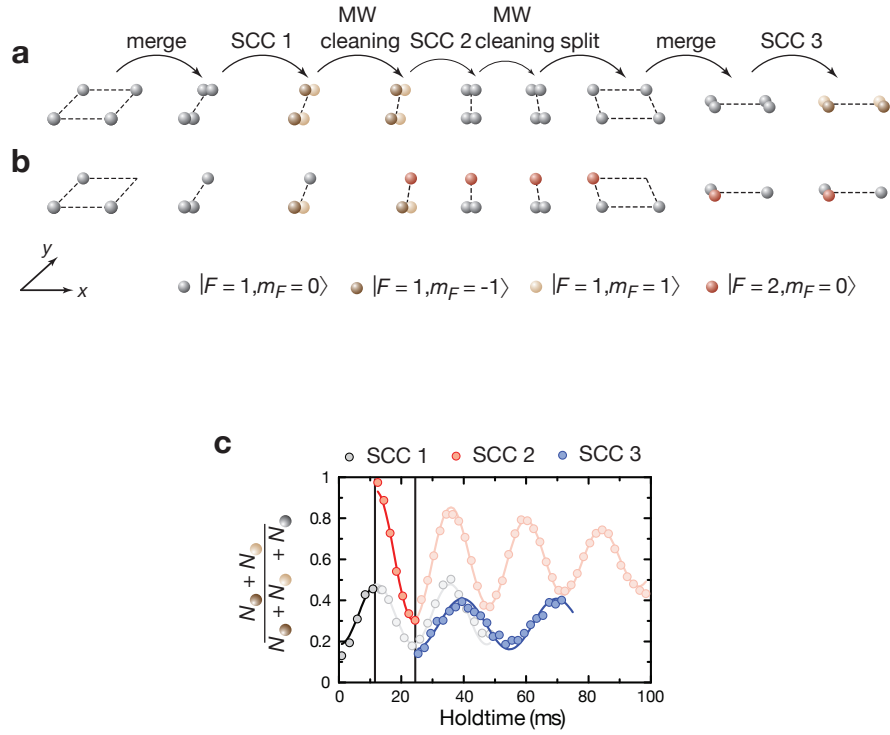


Figure G.1: Schematics of the filtering sequence for plaquettes at half filling. (a), (b) Filtering sequence applied to a plaquette initially filled with 4 atoms (a) and 3 atoms (b). In the case of 3 atoms per plaquette no atom is eventually transferred in the Zeeman state  $|F = 1, m_F = 1\rangle$  that we probe at the end of the experiment. (c) Evolution of the atom fraction in  $|F = 1, m_F = 1\rangle$  (within the  $F = 1$  manifold) during the three successive SCC used for the filtering sequence.

## Appendix H

# Singlet and triplet states: oscillations and detection

### H.1 Detection of singlet and triplet fractions

In order to measure the fraction of atoms in the singlet and triplet states a projection technique was employed, which is described here. Consider a double well potential with two particles that can have either spin  $|\uparrow\rangle$  or  $|\downarrow\rangle$ , and such that both particles can neither be in the same well nor have the same spin. The corresponding Hilbert space is spanned by the states

$$\begin{aligned} |L, \uparrow; R, \downarrow\rangle &= |\psi_L(r)_1, \uparrow_1\rangle \otimes |\psi_R(r)_2, \downarrow_2\rangle, \\ |R, \uparrow; L, \downarrow\rangle &= |\psi_R(r)_1, \uparrow_1\rangle \otimes |\psi_L(r)_2, \downarrow_2\rangle, \\ |L, \downarrow; R, \uparrow\rangle &= |\psi_L(r)_1, \downarrow_1\rangle \otimes |\psi_R(r)_2, \uparrow_2\rangle, \\ |R, \downarrow; L, \uparrow\rangle &= |\psi_R(r)_1, \downarrow_1\rangle \otimes |\psi_L(r)_2, \uparrow_2\rangle, \end{aligned} \quad (\text{H.1})$$

where the subindexes 1 and 2 label the particle number, and  $|\psi_L(r)\rangle$  and  $|\psi_R(r)\rangle$  indicate the spatial wavefunction on the left (L) and right (R) well respectively. For bosonic particles, one can only consider the states that are symmetric under particle exchange, which are given by

$$\begin{aligned} |s\rangle &= \frac{1}{2}(|\psi_L(r)_1; \psi_R(r)_2\rangle - |\psi_R(r)_1; \psi_L(r)_2\rangle) \otimes (|\uparrow_1; \downarrow_2\rangle - |\downarrow_1; \uparrow_2\rangle) \\ |t_0\rangle &= \frac{1}{2}(|\psi_L(r)_1; \psi_R(r)_2\rangle + |\psi_R(r)_1; \psi_L(r)_2\rangle) \otimes (|\uparrow_1; \downarrow_2\rangle + |\downarrow_1; \uparrow_2\rangle). \end{aligned} \quad (\text{H.2})$$

These wavefunctions are denominated singlet and triplet states, due to their spin configuration.

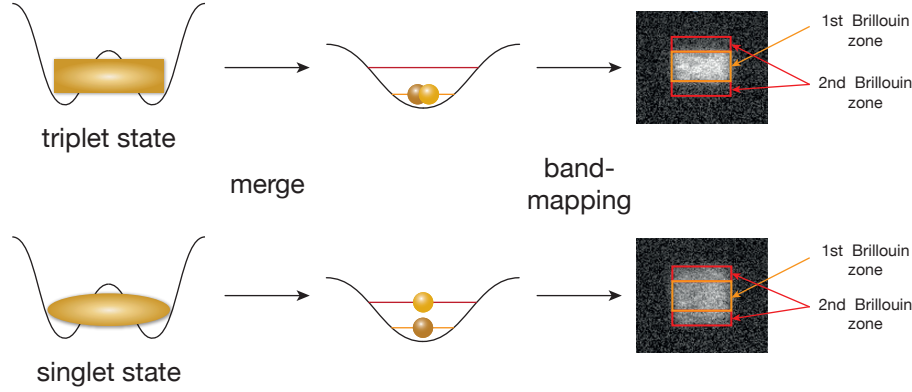


Figure H.1: Schematics of the projection method used to determine the singlet/triplet population fractions. Initially the atoms are in the double wells, where their spin is in a singlet or triplet state. Then the double wells are merged and the atoms populate the two lowest energy bands of the single wells. In the case of atoms originally in a triplet state, after the merging they end up in the lowest band. On the other hand, for atoms initially in the singlet state, half of them end up in the excited band. By using a band mapping technique (see appendix B) the population in the bands are mapped into the first and second Brillouin zone.

The projection method consists in adiabatically merging within 10 ms the sites of the double well into a single one, and extracting the atom fraction in the singlet and triplet states by measuring the populations in the two lowest bands of the single well (see Fig. H.1). The connection between these populations and the atom fractions in  $|s\rangle$  and  $|t_0\rangle$  can be seen by writing all the possible bosonic states of the single well system:

$$\begin{aligned}
 |1\rangle &= |\psi_{E0}(r)_1; \psi_{E0}(r)_2\rangle \otimes (|\uparrow_1; \downarrow_2\rangle + |\downarrow_1; \uparrow_2\rangle) / \sqrt{2}, \\
 |2\rangle &= (|\psi_{E0}(r)_1; \psi_{E1}(r)_2\rangle + |\psi_{E1}(r)_1; \psi_{E0}(r)_2\rangle) \otimes (|\uparrow_1; \downarrow_2\rangle + |\downarrow_1; \uparrow_2\rangle) / 2, \\
 |3\rangle &= (|\psi_{E0}(r)_1; \psi_{E1}(r)_2\rangle - |\psi_{E1}(r)_1; \psi_{E0}(r)_2\rangle) \otimes (|\uparrow_1; \downarrow_2\rangle - |\downarrow_1; \uparrow_2\rangle) / 2, \\
 |4\rangle &= |\psi_{E1}(r)_1; \psi_{E1}(r)_2\rangle \otimes (|\uparrow_1; \downarrow_2\rangle + |\downarrow_1; \uparrow_2\rangle) / \sqrt{2}.
 \end{aligned} \tag{H.3}$$

A full calculation of the states of the system as a function of the coupling between the two wells [75] shows that the singlet and triplet states  $|s\rangle$  and  $|t_0\rangle$  are adiabatically connected to the states  $|3\rangle$  and  $|1\rangle$ , respectively. Since  $|1\rangle$  has population only on the lowest band, when applying the band mapping technique described in appendix B one obtains that all the atoms originally in  $|t_0\rangle$  populate the first Brillouin zone. On the other hand, for the atoms originally in  $|s\rangle$ , one obtains that after the band mapping half of the atoms are mapped to the second Brillouin zone because the state  $|3\rangle$  has one atom in the lowest band and one in the excited band. As a consequence, for an initial state  $|\psi_0\rangle = \alpha |s\rangle + \beta |t_0\rangle$ , one obtains that the fraction of band excitation is equal to  $n_{exc} = |\alpha|^2 / 2$ .

In the experiment we used the method described here for a plaquette system, which consists of four sites. Let us consider a projection along the  $y$ -direction. In that case the lattice depths are chosen such that the plaquette consists of two isolated double wells along that direction, and the physics can be still described in terms of the single double-well operators. By denoting  $|s_y\rangle$  and  $|t_y\rangle$  as the singlet and triplet states along one bond in the  $y$ -direction, one can write a general state in the plaquette as

$$|\psi\rangle = (\alpha |s_y\rangle + \beta |t_y\rangle) \otimes (\alpha' |s_y\rangle + \beta' |t_y\rangle), \quad (\text{H.4})$$

where the expression on the left (right) side of  $\otimes$  corresponds to the sites  $A$  and  $D$  ( $B$  and  $C$ ). For example, the vertical singlet and triplet states on the plaquette can be written as  $|00\rangle = |s_y\rangle \otimes |s_y\rangle$  and  $|11\rangle = |t_y\rangle \otimes |t_y\rangle$ .

The fraction of band excitations along  $y$  is given by the expectation value of the operator

$$N_{exc}^y = [|s_y\rangle \langle s_y| \otimes \mathbb{I}] / 4 + [\mathbb{I} \otimes |s_y\rangle \langle s_y|] / 4. \quad (\text{H.5})$$

For the state given in Eq. H.4, the fraction of band excitation is

$$n_{exc}^y = \langle \psi | N_{exc}^y | \psi \rangle = \frac{1}{4} |\alpha|^2 (|\alpha'|^2 + |\beta'|^2) + \frac{1}{4} |\alpha'|^2 (|\alpha|^2 + |\beta|^2). \quad (\text{H.6})$$

For the particular case of the singlet subspace, where the most general state can be written as  $|\psi\rangle = a|00\rangle + b|\otimes\rangle$ , the fraction of band excitation can be written as

$$n_{exc}^y = |\langle \Psi(t) | 00 \rangle|^2 / 2 = \mathcal{C}_y / 2 = |a|^2 / 2 + |b|^2 / 4. \quad (\text{H.7})$$

A similar analysis for the case of projecting along the  $x$ -direction leads to analogous expressions.

## H.2 Singlet-triplet oscillations in isolated double wells

The most important tool to detect the state correlations used in our experiments consists of the measurement of the singlet-triplet oscillation amplitude  $A_{STO}$  in the isolated plaquettes. In this section the method used to induce the oscillations on a single double well is described, and the calculations for the oscillation amplitudes in the plaquettes are presented.

Consider the spin Hamiltonian of two particles with opposite spin in a double well exposed to an external magnetic gradient

$$\hat{H} = -J\vec{S}_L \cdot \vec{S}_R + \Delta_G / 2 (\hat{S}_L^z - \hat{S}_R^z), \quad (\text{H.8})$$

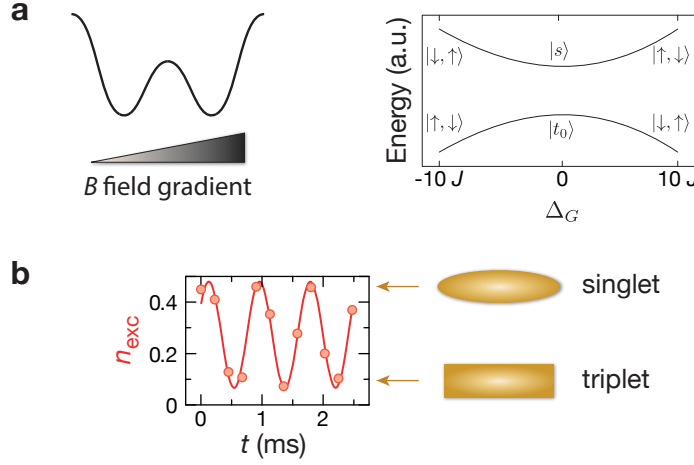


Figure H.2: Schematics for singlet-triplet oscillations in a double well. **(a)** Double well potential exposed to a magnetic field gradient. The eigenstates and eigenvectors are plotted on the right as a function of the gradient strength  $\Delta_G$ . For  $\Delta_G = 0$  the eigenstates are the singlet and triplet states  $|s\rangle$  and  $|t_0\rangle$ . For  $|\Delta_G| \gg J$  the gradient dominates the system and the eigenstates are  $|\uparrow, \downarrow\rangle$  and  $|\downarrow, \uparrow\rangle$ . **(b)** STO as a function of time, measured using the projection method described in the previous section. A band excitation fraction of one half (zero) corresponds to a singlet (triplet) state.

with  $J > 0$ . Here it is assumed that the two spin components have opposite magnetic moments and that the energy cost of moving one particle with spin  $|\uparrow\rangle$  ( $|\downarrow\rangle$ ) from the left to the right site is  $-\Delta_G$  ( $\Delta_G$ ). Given that the two atoms are in the two internal states  $|\uparrow\rangle$  and  $|\downarrow\rangle$ , the total Hilbert space is spanned by the states  $|\uparrow, \downarrow\rangle$  and  $|\downarrow, \uparrow\rangle$ . When  $\Delta_G = 0$  the eigenstates of the system are the singlet and triplet states  $|s\rangle$  and  $|t_0\rangle$ , being  $|s\rangle$  higher in energy by  $J$  (see Fig. H.2). On the other hand, in the extreme case of  $\Delta_G \gg J$ , the degeneracy between the states  $|\uparrow, \downarrow\rangle = (|L, \uparrow; R, \downarrow\rangle + |R, \downarrow; L, \uparrow\rangle)/\sqrt{2}$  and  $|\downarrow, \uparrow\rangle = (|L, \downarrow; R, \uparrow\rangle + |R, \uparrow; L, \downarrow\rangle)/\sqrt{2}$  is lifted, and they become the new eigenstates of the system, whose energy difference is  $2\Delta_G$ .

Starting from the state  $|s\rangle$  or  $|t_0\rangle$  in the spin Hamiltonian with  $\Delta_G = 0$ , one can induce singlet-triplet oscillations by suddenly switching on the gradient to  $\Delta_G \gg J$ . This process automatically projects the initial state into the Hamiltonian for which the ground states are  $|\uparrow, \downarrow\rangle$  and  $|\downarrow, \uparrow\rangle$ . Therefore, the subsequent time evolution is given by

$$|\psi\rangle(t) = (e^{-it\Delta_G/2\hbar} |\uparrow, \downarrow\rangle \pm e^{it\Delta_G/2\hbar} |\downarrow, \uparrow\rangle)/\sqrt{2}, \quad (\text{H.9})$$

which results in a singlet-triplet oscillation with frequency  $\Delta_G/\hbar$ , and where the  $\pm$  sign corresponds respectively to the initial states  $|t_0\rangle$  and  $|s\rangle$  (note that one can write  $|s\rangle = (|\uparrow, \downarrow\rangle - |\downarrow, \uparrow\rangle)/\sqrt{2}$  and  $|t_0\rangle = (|\uparrow, \downarrow\rangle + |\downarrow, \uparrow\rangle)/\sqrt{2}$ ).

STO in plaquettes are induced in the same way, either along the  $x$ - or  $y$ -direction. Let us calculate the state evolution during the STO along the  $y$ -direction and for a general

initial state

$$|\psi\rangle = a|00\rangle + b|\Xi\rangle. \quad (\text{H.10})$$

Since the gradient is along  $y$ , the state  $|\Xi\rangle$  does not evolve during the STO, and the state  $|00\rangle$  evolves according to

$$\begin{aligned} & (\cos\phi |s_y\rangle + i \sin\phi |t_y\rangle) \otimes (\cos\phi |s_y\rangle + i \sin\phi |t_y\rangle) \\ &= \cos^2\phi |s_y\rangle \otimes |s_y\rangle + i \cos\phi \sin\phi |s_y\rangle \otimes |t_y\rangle \\ &+ i \cos\phi \sin\phi |t_y\rangle \otimes |s_y\rangle - \sin^2\phi |t_y\rangle \otimes |t_y\rangle, \end{aligned} \quad (\text{H.11})$$

where  $\phi = t\Delta_G/2\hbar$ . From here one can infer that the time evolution of  $|\psi\rangle$  is

$$\begin{aligned} |\psi\rangle(t) &= a \cos^2\phi |00\rangle + b|\Xi\rangle + ai \cos\phi \sin\phi |s_y\rangle \otimes |t_y\rangle \\ &+ ai \cos\phi \sin\phi |t_y\rangle \otimes |s_y\rangle - a \sin^2\phi |\square\square\rangle. \end{aligned} \quad (\text{H.12})$$

As it was explained in the previous section, the experimental observable is the fraction of atoms in the excited band after merging the pair of double wells along one of the directions. When the merging is done along the  $y$ -direction, this observable takes the form  $N_{exc}^y = [|s_y\rangle \langle s_y| \otimes \mathbb{I}] / 4 + [\mathbb{I} \otimes |s_y\rangle \langle s_y|] / 4$ .

The four terms appearing in Eq. H.12 are orthogonal, and therefore the observable  $N_{exc}^y$  is equal to the sum of the contributions from each term. Their contributions are, respectively

$$\begin{aligned} (a^* \cos^2\phi \langle 00| + b^* \langle \Xi|) N_{exc}^y (a \cos^2\phi |00\rangle + b|\Xi\rangle) &= \frac{1}{2} |a \cos^2\phi + b/2|^2 \\ (-a^* i \cos\phi \sin\phi \langle s_y| \otimes \langle t_y|) N_{exc}^y (ai \cos\phi \sin\phi |s_y\rangle \otimes |t_y\rangle) &= a^2 \cos^2\phi \sin^2\phi / 4 \\ (-a^* i \cos\phi \sin\phi \langle t_y| \otimes \langle s_y|) N_{exc}^y (ai \cos\phi \sin\phi |t_y\rangle \otimes |s_y\rangle) &= a^2 \cos^2\phi \sin^2\phi / 4 \\ (a^* \sin^2\phi \langle \square\square|) N_{exc}^y (a \sin^2\phi |\square\square\rangle) &= 0. \end{aligned} \quad (\text{H.13})$$

By adding the four contributions the following expression results for the observable  $N_{exp}^y$ :

$$n_{exc}^y = \langle \psi(t) | N_{exp}^y | \psi(t) \rangle = \frac{1}{2} [|b/2|^2 + \cos^2\phi (|a|^2 + \text{Re}(ab^*))]. \quad (\text{H.14})$$

From this one obtains that the amplitude of the STO is  $A_{STO}^y = (|a|^2 + \text{Re}(ab^*)) / 2$ . For example, for the particular case in which  $|\psi(t=0)\rangle = \alpha |\Phi_+\rangle + \beta |\Phi_-\rangle$  the amplitude is  $A_{STO}^y = \alpha^2/3 + \alpha\beta/\sqrt{3}$ . This can be related to the value of  $n_{exp}^y$ , which was used in the experiment as a second observable during the valence bond oscillations, resulting in

$$n_{exc}^y = \frac{1}{8} + \frac{3}{4} A_{STO}^y. \quad (\text{H.15})$$



# References

- [1] W. Ketterle, D. S. Durfee, and D. M. Stamper-Kurn. *Making, probing and understanding Bose-Einstein condensates*. In S. Stringari, M. Ignuscio, and C. E. Wieman, editors, *Bose-Einstein Condensation in Atomic Gases* (1999). See pp. 1, 12, 23, 140.
- [2] G. K. Campbell, J. Mun, M. Boyd, P. Medley, A. E. Leanhardt, L. G. Marcassa, D. E. Pritchard, and W. Ketterle. *Imaging the Mott insulator shells by using atomic clock shifts*. *Science* **313**, 652–659 (2006). See p. 1.
- [3] P. T. Ernst, S. Götze, J. S. Krauser, K. Pyka, D.-S. Lühmann, D. Pfannkuche, and K. Sengstock. *Probing superfluids in optical lattices by momentum-resolved Bragg spectroscopy*. *Nat. Phys.* **6**, 56–61 (2010). See p. 1.
- [4] J. F. Sherson, C. Weitenberg, M. Endres, M. Cheneau, I. Bloch, and S. Kuhr. *Single-atom-resolved fluorescence imaging of an atomic Mott insulator*. *Nature* **467**, 68–72 (2010). See pp. 1, 116, 136, 137.
- [5] W. S. Bakr, A. Peng, M. E. Tai, R. Ma, J. Simon, J. I. Gillen, S. Fölling, L. Pollet, and M. Greiner. *Probing the superfluid-to-Mott insulator transition at the single-atom level*. *Science* **329**, 547–550 (2010). See pp. 1, 116, 136, 137.
- [6] K. B. Davis, M.-O. Mewes, M. R. Andrews, N. J. van Druten, D. S. Durfee, D. M. Kurn, and W. Ketterle. *Bose-Einstein condensation in a gas of sodium atoms*. *Phys. Rev. Lett.* **75**, 3969–3974 (1995). See pp. 1, 12, 22.
- [7] M. Anderson, J. Enscher, M. Matthews, C. E. Wieman, and E. A. Cornell. *Observation of Bose-Einstein condensation in a dilute atomic vapor*. *Science* **269**, 198–201 (1995). See pp. 1, 22.
- [8] M. R. Matthews, B. P. Anderson, P. C. Haljan, D. S. Hall, C. E. Wieman, and E. A. Cornell. *Vortices in a Bose-Einstein condensate*. *Phys. Rev. Lett.* **83**, 2498–2501 (1999). See p. 1.
- [9] K. W. Madison, F. Chevy, W. Wohlleben, and J. Dalibard. *Vortex formation in a stirred Bose-Einstein condensate*. *Phys. Rev. Lett.* **84**, 806–809 (2000). See pp. 1, 2.

- [10] J. R. Abo-Shaeer, C. Raman, J. M. Vogels, and W. Ketterle. *Observation of vortex lattices in Bose-Einstein condensates*. *Science* **292**, 476–479 (2001). See p. 1.
- [11] M. R. Andrews, C. G. Townsend, H.-J. Miesner, D. S. Durfee, D. M. Kurn, and W. Ketterle. *Observation of interference between two Bose condensates*. *Science* **275**, 637–641 (1997). See p. 1.
- [12] M. R. Andrews, D. M. Kurn, H.-J. Miesner, D. S. Durfee, C. G. Townsend, S. Inouye, and W. Ketterle. *Propagation of sound in a Bose-Einstein condensate*. *Phys. Rev. Lett.* **79**, 553–556 (1997). See p. 1.
- [13] D. M. Stamper-Kurn, A. P. Chikkatur, A. Görlitz, D. E. Pritchard, and W. Ketterle. *Excitation of phonons in a Bose-Einstein condensate by light scattering*. *Phys. Rev. Lett.* **83**, 2876–2879 (1999). See p. 1.
- [14] B. DeMarco and D. S. Jin. *Onset of Fermi degeneracy in a trapped atomic gas*. *Science* **285**, 1703–1706 (1999). See p. 1.
- [15] S. Inouye, M. R. Andrews, J. Stenger, H.-J. Miesner, D. M. Stamper-Kurn, and W. Ketterle. *Observation of Feshbach resonances in a Bose-Einstein condensate*. *Nature* **392**, 151–154 (1998). See p. 1.
- [16] C. Chin, R. Grimm, P. Julienne, and E. Tiesinga. *Feshbach resonances in ultracold gases*. *Rev. Mod. Phys.* **82**, 1225–1286 (2010). See pp. 1, 27.
- [17] W. Ketterle and M. W. Zwierlein. *Making, probing and understanding ultracold Fermi gases*. *Riv. Nuov. Cim.* **31**, 247–422 (2008). See p. 1.
- [18] I. Bloch, J. Dalibard, and W. Zwerger. *Many-body physics with ultracold gases*. *Rev. Mod. Phys.* **80**, 885–964 (2008). See pp. 1, 114, 139.
- [19] D. Jaksch, C. Bruder, J. I. Cirac, C. W. Gardiner, and P. Zoller. *Cold bosonic atoms in optical lattices*. *Phys. Rev. Lett.* **81**, 3108–3111 (1998). See pp. 2, 26.
- [20] M. P. A. Fisher, P. B. Weichman, G. Grinstein, and D. S. Fisher. *Boson localization and the superfluid-insulator transition*. *Phys. Rev. B* **40**, 546–570 (1989). See pp. 2, 26, 30, 116, 137.
- [21] M. B. Dahan, E. Peik, J. Reichel, Y. Castin, and C. Salomon. *Bloch oscillations of atoms in an optical potential*. *Phys. Rev. Lett.* **76**, 4508–4511 (1996). See pp. 2, 153.
- [22] S. R. Wilkinson, C. F. Bharucha, K. W. Madison, Q. Niu, and M. G. Raizen. *Observation of atomic Wannier-Stark ladders in an accelerating optical potential*. *Phys. Rev. Lett.* **76**, 4512–4515 (1996). See p. 2.

- [23] M. Greiner, O. Mandel, T. Esslinger, T. Hänsch, and I. Bloch. *Quantum phase transition from a superfluid to a Mott insulator in a gas of ultracold atoms*. *Nature* **415**, 39–44 (2002). See pp. 2, 116, 137.
- [24] T. Stöferle, H. Moritz, C. Schori, M. Köhl, and T. Esslinger. *Transition from a strongly interacting 1D superfluid to a Mott insulator*. *Phys. Rev. Lett.* **92**, 130403 (2004). See p. 2.
- [25] I. B. Spielman, W. D. Phillips, and J. V. Porto. *Mott-insulator transition in a two-dimensional atomic Bose gas*. *Phys. Rev. Lett.* **98**, 080404 (2007). See p. 2.
- [26] B. Paredes, A. Widera, V. Murg, O. Mandel, S. Fölling, I. Cirac, G. V. Shlyapnikov, T. W. Hänsch, and I. Bloch. *Tonks-Girardeau gas of ultracold atoms in an optical lattice*. *Nature* **429**, 277–281 (2004). See p. 2.
- [27] T. Kinoshita, T. Wenger, and D. S. Weiss. *Observation of a one-dimensional Tonks-Girardeau gas*. *Science* **305**, 1125–1128 (2004). See p. 2.
- [28] M. Köhl, H. Moritz, T. Stöferle, K. Günter, and T. Esslinger. *Fermionic atoms in a three dimensional optical lattice: observing Fermi surfaces, dynamics, and interactions*. *Phys. Rev. Lett.* **94**, 080403 (2005). See pp. 2, 143.
- [29] S. Fölling, S. Trotzky, P. Cheinet, M. Feld, R. Saers, A. Widera, T. Müller, and I. Bloch. *Direct observation of second-order atom tunneling*. *Nature* **448**, 1029–1032 (2007). See pp. 2, 94, 97, 107, 124, 127, 147.
- [30] S. Trotzky, P. Cheinet, S. Fölling, M. Feld, U. Schnorrberger, A. M. Rey, A. Polkovnikov, E. A. Demler, M. D. Lukin, and I. Bloch. *Time-resolved observation and control of superexchange interactions with ultracold atoms in optical lattices*. *Science* **319**, 295–299 (2008). See pp. 2, 121.
- [31] C. Becker, P. Soltan-Panahi, J. Kronjäger, S. Dörscher, K. Bongs, and K. Sengstock. *Ultracold quantum gases in triangular optical lattices*. *New J. Phys.* **12**, 065025 (2010). See p. 2.
- [32] L. Tarruel, D. Greif, T. Uehlinger, G. Jotzu, and T. Esslinger. *Creating, moving and merging Dirac points with a Fermi gas in a tunable honeycomb lattice*. *Nature* **483**, 302–305 (2012). See p. 2.
- [33] G.-B. Jo, J. Guzman, C. K. Thomas, P. Hosur, A. Vishwanath, and D. M. Stamper-Kurn. *Ultracold atoms in a tunable optical kagome lattice*. *Phys. Rev. Lett.* **108**, 045305 (2012). See p. 2.

- [34] V. Schweikhard, I. Coddington, P. Engels, V. P. Mogendorff, and E. A. Cornell. *Rapidly rotating Bose-Einstein condensates in and near the lowest Landau level*. Phys. Rev. Lett. **92**, 040402 (2004). See p. 2.
- [35] V. Bretin, S. Stock, Y. Seurin, and J. Dalibard. *Fast rotation of a Bose-Einstein condensate*. Phys. Rev. Lett. **92**, 050403 (2004). See p. 2.
- [36] Y.-J. Lin, R. L. Compton, K. Jiménez-García, J. V. Porto, and I. B. Spielman. *Synthetic magnetic fields for ultracold neutral atoms*. Nature **462**, 628–632 (2009). See p. 2.
- [37] J. Dalibard and F. Gerbier. *Colloquium: Artificial gauge potentials for neutral atoms*. Rev. Mod. Phys. **83**, 1523–1543 (2011). See p. 2.
- [38] M. C. Beeler, R. A. Williams, K. Jiménez-García, L. J. LeBlanc, A. R. Perry, and I. B. Spielman. *The spin Hall effect in a quantum gas*. Nature **498**, 201–204 (2013). See p. 2.
- [39] D. Jaksch and P. Zoller. *Creation of effective magnetic fields in optical lattices: the Hofstadter butterfly for cold neutral atoms*. New J. Phys. **5**, 56.1 (2003). See pp. 2, 5.
- [40] E. Mueller. *Artificial electromagnetism for neutral atoms: Escher staircase and Laughlin liquids*. Phys. Rev. A **70**, 041603 (2004). See p. 2.
- [41] F. Gerbier and J. Dalibard. *Gauge fields for ultracold atoms in optical superlattices*. New J. Phys. **12**, 033007 (2010). See pp. 2, 5.
- [42] A. R. Kolovsky. *Creating artificial magnetic fields for cold atoms by photon-assisted tunneling*. Europhys. Lett. **93**, 20003 (2011). See pp. 3, 5, 18.
- [43] A. Bermudez, T. Schätz, and D. Porras. *Synthetic gauge fields for vibrational excitations of trapped ions*. Phys. Rev. Lett. **107**, 150501 (2011). See p. 3.
- [44] J. Struck, C. Ölschläger, R. L. Targat, P. Soltan-Panahi, A. Eckardt, M. Lewenstein, P. Windpassinger, and K. Sengstock. *Quantum simulation of classical magnetism in triangular optical lattices*. Science **333**, 996–999 (2011). See p. 3.
- [45] M. Aidelsburger, M. Atala, S. Nascimbène, S. Trotzky, Y.-A. Chen, and I. Bloch. *Experimental realization of strong effective magnetic fields in an optical lattice*. Phys. Rev. Lett. **107**, 255301 (2011). See pp. 3, 72, 93, 143.
- [46] K. Jiménez-García, L. J. LeBlanc, R. A. Williams, M. C. Beeler, A. R. Perry, and I. B. Spielman. *Peierls substitution in an engineered lattice potential*. Phys. Rev. Lett. **108**, 225303 (2012). See p. 3.

- [47] M. Aidelsburger, M. Atala, M. Lohse, J. T. Barreiro, B. Paredes, and I. Bloch. *Realization of the Hofstadter Hamiltonian with ultracold atoms in optical lattices*. Phys. Rev. Lett. **111**, 185301 (2013). See pp. 3, 93.
- [48] J. Struck, M. Weinberg, C. Ölschläger, P. Windpassinger, J. Simonet, K. Sengstock, R. Hoeppe, P. Hauke, A. Eckardt, M. Lewenstein, and L. Mathey. *Engineering Ising-XY spin-models in a triangular lattice using tunable artificial gauge fields*. Nat. Phys. **9**, 738–743 (2013). See p. 3.
- [49] H. Miyake, G. A. Siviloglou, C. J. Kennedy, W. C. Burton, and W. Ketterle. *Realizing the Harper Hamiltonian with laser-assisted tunneling in optical lattices*. Phys. Rev. Lett. **111**, 185302 (2013). See p. 3.
- [50] P. W. Anderson. *The Resonating Valence Bond State in  $\text{La}_2\text{CuO}_4$  and Superconductivity*. Science **235**, 1196–1198 (1987). See pp. 3, 6, 120, 121.
- [51] M. Atala, M. Aidelsburger, J. T. Barreiro, D. Abanin, T. Kitagawa, E. Demler, and I. Bloch. *Direct measurement of the Zak phase in topological Bloch bands*. Nat. Phys. **9**, 795–800 (2013). See pp. 3, 4, 44.
- [52] M. Atala, M. Aidelsburger, M. Lohse, J. T. Barreiro, B. Paredes, and I. Bloch. *Observation of chiral currents with ultracold atoms in bosonic ladders*. Nat. Phys. **10**, 588–593 (2014). See p. 3.
- [53] S. Nascimbène, Y.-A. Chen, M. Atala, M. Aidelsburger, S. Trotzky, B. Paredes, and I. Bloch. *Experimental realization of plaquette resonating valence-bond states with ultracold atoms in optical superlattices*. Phys. Rev. Lett. **108**, 205301 (2012). See pp. 3, 97, 145.
- [54] M. V. Berry. *Quantal phase factors accompanying adiabatic changes*. Proc. Phys. Soc. A **392**, 45 (1984). See pp. 3, 32, 33.
- [55] D. J. Thouless, M. Kohmoto, M. P. Nightingale, and M. den Nijs. *Quantized Hall conductance in a two-dimensional periodic potential*. Phys. Rev. Lett. **49**, 405–408 (1982). See pp. 4, 38, 53.
- [56] M. Z. Hasan and C. L. Kane. *Colloquium: Topological insulators*. Rev. Mod. Phys. **82**, 3045–3067 (2010). See pp. 4, 38.
- [57] X.-L. Qi and S.-C. Zhang. *Topological insulators and superconductors*. Rev. Mod. Phys. **83**, 1057–1110 (2011). See pp. 4, 44.
- [58] E. Alba, X. Fernandez-Gonzalvo, J. Mur-Petit, J. K. Pachos, and J. J. Garcia-Ripoll. *Seeing topological order in time-of-flight measurements*. Phys. Rev. Lett. **107**, 235301 (2011). See pp. 4, 136.

- [59] E. Zhao, N. Bray-Ali, C. J. Williams, I. B. Spielman, and I. I. Satija. *Chern numbers hiding in time-of-flight images*. Phys. Rev. A **84**, 063629 (2011). See pp. 4, 136.
- [60] D. Xiao, M.-C. Chang, and Q. Niu. *Berry phase effects on electronic properties*. Rev. Mod. Phys. **82**, 1959–2007 (2010). See pp. 4, 5, 38, 50, 51, 52, 136.
- [61] H. M. Price and N. R. Cooper. *Mapping the Berry curvature from semiclassical dynamics in optical lattices*. Phys. Rev. A **85**, 033620 (2012). See pp. 4, 136.
- [62] J. Zak. *Berry's phase for energy bands in solids*. Phys. Rev. Lett. **62**, 2747–2750 (1989). See pp. 4, 36, 37.
- [63] P. Delplace, D. Ullmo, and G. Montambaux. *Zak phase and the existence of edge states in graphene*. Phys. Rev. B **84**, 195452 (2011). See pp. 4, 37, 46, 48.
- [64] S. Ryu and Y. Hatsugai. *Topological origin of zero-energy edge states in particle-hole symmetric systems*. Phys. Rev. Lett. **89**, 077002 (2002). See pp. 4, 37.
- [65] W. P. Su, J. R. Schrieffer, and A. J. Heeger. *Solitons in polyacetylene*. Phys. Rev. Lett. **42**, 1698–1701 (1979). See pp. 4, 37, 39, 50, 73, 136.
- [66] D. Abanin, T. Kitagawa, I. Bloch, and E. Demler. *Interferometric approach to measuring band topology in 2D optical lattices*. Phys. Rev. Lett. **110**, 165304 (2013). See pp. 5, 72, 73, 136.
- [67] A. H. C. Neto, F. Guinea, N. M. R. Peres, K. S. Novoselov, and A. K. Geim. *The electronic properties of graphene*. Rev. Mod. Phys. **81**, 109–162 (2009). See p. 5.
- [68] G. P. Mikitik and Y. V. Sharlai. *Manifestation of Berry's phase in metal physics*. Phys. Rev. Lett. **82**, 2147–2150 (1999). See p. 5.
- [69] W. Meissner and R. Ochsenfeld. *Ein neuer Effect bei Eintritt der Supraleitfähigkeit*. Naturwissenschaften **21**, 787–788 (1933). See pp. 5, 75.
- [70] J. Bardeen, L. N. Cooper, and J. R. Schrieffer. *Theory of superconductivity*. Phys. Rev. **108**, 1175–1204 (1957). See pp. 5, 6, 76.
- [71] N. Goldman, G. Juzeliunas, P. Öhberg, and I. B. Spielman. *Light-induced gauge fields for ultracold atoms*. arXiv **1308:6533** (2013). See p. 5.
- [72] P. A. Lee, N. Nagaosa, and X.-G. Wen. *Doping a Mott insulator: Physics of high-temperature superconductivity*. Rev. Mod. Phys. **78**, 17–85 (2006). See pp. 6, 120.
- [73] L. Pauling. *The nature of the chemical bond. Application of results obtained from the quantum mechanics and from a theory of paramagnetic susceptibility to the structure of molecules*. J. Am. Chem. Soc. **53**, 1367–1400 (1931). See pp. 6, 117.

- [74] P. W. Anderson. *Resonating valence bonds: A new kind of insulator?* Mater. Res. Bull. **8**, 153–160 (1973). See pp. 6, 119.
- [75] S. Trotzky, Y.-A. Chen, U. Schnorrberger, P. Cheinet, and I. Bloch. *Controlling and detecting spin correlations of ultracold atoms in optical lattices.* Phys. Rev. Lett. **105**, 265303 (2010). See pp. 6, 125, 126, 166.
- [76] A. Widera, F. Gerbier, S. Fölling, T. Gericke, O. Mandel, and I. Bloch. *Coherent collisional spin dynamics in optical lattices.* Phys. Rev. Lett. **95**, 190405 (2005). See pp. 6, 107, 124, 147.
- [77] E. Altman and A. Auerbach. *Plaquette boson-fermion model of cuprates.* Phys. Rev. B **65**, 104508 (2002). See pp. 6, 133, 138.
- [78] S. Trebst, U. Schollwöck, M. Troyer, and P. Zoller. *d-Wave resonating valence bond states of fermionic atoms in optical lattices.* Phys. Rev. Lett. **96**, 250402 (2006). See pp. 6, 133, 138.
- [79] A. M. Rey, R. Sensarma, S. Fölling, M. Greiner, E. Demler, and M. D. Lukin. *Controlled preparation and detection of d-wave superfluidity in two-dimensional optical superlattices.* Europhys. Lett. **87**, 60001 (2009). See pp. 6, 133, 138.
- [80] M. Greiner. *Magnetische Transfer von Atomen ein Weg zur einfachen Bose-Einstein-Kondensation.* Master's thesis, Ludwig Maximilians Universität München (2000). See p. 11.
- [81] M. Greiner. *Ultracold quantum gases in three dimensional optical lattice potentials.* PhD thesis, Ludwig Maximilians Universität München (2003). See pp. 11, 141.
- [82] S. Fölling. *Probing Strongly Correlated States of Ultracold Atoms in Optical Lattices.* PhD thesis, Johannes Gutenberg-Universität in Mainz (2008). See pp. 11, 17, 141, 143.
- [83] O. Mandel. *Entanglement with quantum gates in an optical lattice.* PhD thesis, Ludwig Maximilians Universität München (2005). See p. 11.
- [84] A. Widera. *Constructing Correlated Spin States with Neutral Atoms in Optical Lattices.* PhD thesis, Institut für Physik der Johannes-Gutenberg-Universität Mainz (2008). See p. 11.
- [85] A. Widera. *Controlled Cold Collisions: Towards Many-Particle Entanglement in Optical Lattices.* Master's thesis, Physikalisches Institut der Bayerischen Julius-Maximilians-Universität Würzburg (2003). See p. 11.

- [86] M. Feld. *Ultracold bosonic atoms in bichromatic optical superlattices*. Master's thesis, Institut für Physik der Johannes-Gutenberg-Universität Mainz (2007). See p. 11.
- [87] M. Aidelsburger. *Ultracold Atoms in Periodically Driven Optical Lattices*. Master's thesis, Ludwig Maximilians Universität München (2011). See pp. 11, 141.
- [88] C. S. Adams and E. Riis. *Laser cooling and trapping of neutral atoms*. *Progress in Quantum Electronics* **21**, 1–79 (1997). See p. 12.
- [89] K. E. Gibble, S. Kasapi, and S. Chu. *Improved magneto-optic trapping in a vapor cell*. *Opt. Lett.* **17**, 526–528 (1992). See p. 12.
- [90] E. L. Raab, M. Prentiss, A. Cable, S. Chu, and D. E. Pritchard. *Trapping of neutral sodium atoms with radiation pressure*. *Phys. Rev. Lett.* **59**, 2631–2634 (1987). See p. 12.
- [91] W. D. Phillips. *Laser cooling and trapping of neutral atoms*. *Rev. Mod. Phys.* **70**, 721–741 (1998). See p. 12.
- [92] H. J. Metcalf and P. van der Straten. *Laser Cooling and Trapping*. Graduate Texts in Contemporary Physics. Springer (1999). See pp. 12, 13.
- [93] C. J. Pethick and H. Smith. *Bose-Einstein condensation in dilute gases*. Cambridge University Press (2002). See pp. 12, 23.
- [94] Y.-J. Lin, A. R. Perry, R. L. Compton, I. B. Spielman, and J. V. Porto. *Rapid production of  $^{87}\text{Rb}$  Bose-Einstein condensates in a combined magnetic and optical potential*. *Phys. Rev. A* **79**, 063631 (2009). See p. 12.
- [95] T. Weber, J. Herbig, M. Mark, H.-C. Nägerl, and R. Grimm. *Bose-Einstein condensation of cesium*. *Science* **299**, 232–235 (2003). See p. 12.
- [96] M. D. Barrett, J. A. Sauer, and M. S. Chapman. *All-optical formation of an atomic Bose-Einstein condensate*. *Phys. Rev. Lett.* **87**, 010404 (2001). See p. 12.
- [97] C.-L. Hung, X. Zhang, N. Gemelke, and C. Chin. *Accelerating evaporative cooling of atoms into Bose-Einstein condensation in optical traps*. *Phys. Rev. A* **78**, 011604 (2008). See p. 12.
- [98] C. N. Cohen-Tannoudji. *Manipulating atoms with photons*. *Rev. Mod. Phys.* **70**, 707–719 (1998). See p. 13.
- [99] R. Grimm, M. Weidemüller, and Y. B. Ovchinnikov. *Optical dipole trap for neutral atoms*. *Adv. At. Mol. Opt. Phys.* **42**, 95–170 (2000). See pp. 13, 14.
- [100] J. D. Jackson. *Classical electrodynamics*. John Wiley (1962). See pp. 13, 50.

- [101] J. E. Bjorkholm, R. R. Freeman, A. Ashkin, and D. B. Pearson. *Observation of focusing of neutral atoms by dipolar forces of resonance-radiation pressure*. Phys. Rev. Lett. **41**, 1361–1364 (1978). See p. 13.
- [102] S. Chu, J. E. Bjorkholm, A. Ashkin, and A. Cable. *Experimental observation of optically trapped atoms*. Phys. Rev. Lett. **57**, 314–318 (1986). See p. 13.
- [103] D. A. Steck. *Rubidium 87 D Line Data* (2001). See p. 14.
- [104] M. Grifoni and P. Hänggi. *Driven quantum tunneling*. Phys. Rep. **304**, 229–354 (1998). See pp. 18, 73.
- [105] N. W. Aschcroft and N. D. Mermin. *Solid State Physics*. Thomson Learning, Inc. (1976). See pp. 18, 21.
- [106] C. Kittel. *Introduction to Solid State Physics*. Wiley, Philadelphia (2004). See p. 18.
- [107] G. H. Wannier. *The structure of electron excitation levels in insulating crystals*. Phys. Rev. **52**, 191–197 (1937). See p. 21.
- [108] G. H. Wannier. *Dynamics of band electrons in electric and magnetic fields*. Rev. Mod. Phys. **34**, 645–655 (1962). See pp. 21, 37, 39.
- [109] S. Kivelson. *Wannier functions in one-dimensional disordered systems: application to fractionally charged solitons*. Phys. Rev. B **26**, 4269–4277 (1982). See p. 22.
- [110] T. Uehlinger, G. Jotzu, M. Messer, D. Greif, U. Bissbort, and T. Esslinger. *Artificial graphene with tunable interactions*. Phys. Rev. Lett. **111**, 185317 (2013). See p. 22.
- [111] U. Bissbort. *Dynamical Effects and Disorder in Ultracold Bosonic Matter*. PhD thesis, Goethe Universität Frankfurt, Frankfurt (2012). See p. 22.
- [112] F. Görg. *Ultracold fermionic atoms in optical superlattices*. Master’s thesis, Technischen Universität München (2014). See p. 22.
- [113] A. Einstein. *Quantentheorie des einatomigen idealen Gases*. Sitzungsber. Preuss. Akad. Wiss., phys.-math. Klasse **23**, 1–14 (1925). See p. 22.
- [114] S. N. Bose. *Plancks Gesetz und Lichtquantenhypothese*. Z. Physik **26**, 178–181 (1924). See p. 22.
- [115] F. Dalfovo, S. Giorgini, L. P. Pitaevskii, and S. Stringari. *Theory of Bose-Einstein condensation in trapped gases*. Rev. Mod. Phys. **71**, 463–512 (1999). See p. 23.
- [116] A. J. Leggett. *Bose-Einstein condensation in atomic gases: some fundamental concepts*. Rev. Mod. Phys. **73**, 307–356 (2001). See p. 23.

- [117] O. Penrose and L. Onsager. *Bose-Einstein condensation in liquid helium*. Phys. Rev. **104**, 576–584 (1956). See p. 24.
- [118] J. Weiner, V. S. Bagnato, S. Zilio, and P. S. Julienne. *Experiments and theory in cold and ultracold collisions*. Rev. Mod. Phys. **71**, 1–85 (1999). See p. 24.
- [119] E. Merzbacher. *Quantum Mechanics*. John Wiley, 3rd edition (1998). See p. 24.
- [120] P. S. Julienne, F. H. Miles, E. Tiesinga, and C. J. Williams. *Collisional stability of double bose condensates*. Phys. Rev. Lett. **78**, 1880–1883 (1997). See p. 25.
- [121] N. Bogoliubov. *On the theory of superfluidity*. J. Phys. **11**, 23–32 (1947). See p. 25.
- [122] E. P. Gross. *Structure of a quantized vortex in boson systems*. Nuovo Cimento **20**, 454–477 (1961). See p. 26.
- [123] L. P. Pitaevskii. *Vortex lines in an imperfect Bose gas*. Sov. Phys. JETP **13**, 451 (1961). See p. 26.
- [124] D. Jaksch. *Bose-Einstein condensation and applications*. PhD thesis, Leopold-Franzens-Universität Innsbruck (1999). See p. 26.
- [125] A. Marte, T. Volz, J. Schuster, S. Dürr, G. Rempe, E. G. M. van Kempen, and B. J. Verhaar. *Feshbach resonances in Rubidium 87: Precision measurement and analysis*. Phys. Rev. Lett. **89**, 283202 (2002). See p. 27.
- [126] R. J. Glauber. *Coherent and incoherent states of the radiation field*. Phys. Rev. **131**, 2766–2788 (1963). See p. 29.
- [127] K. Sheshadri, H. R. Krishnamurthy, R. Pandit, and T. V. Ramakrishnan. *Superfluid and insulating phases in an interacting-boson model: mean-field theory and the RPA*. Europhys. Lett. **22**, 257–263 (1993). See p. 30.
- [128] D. van Oosten, P. van der Straten, and H. Stoof. *Quantum phases in an optical lattice*. Phys. Rev. A **63**, 053601 (2001). See p. 30.
- [129] B. Campogrosso-Sansone, N. V. Prokof'ev, and B. V. Svistunov. *Phase diagram and thermodynamics of the three dimensional Bose-Hubbard model*. Phys. Rev. B **75**, 134302 (2007). See p. 30.
- [130] M. Berry. *Anticipations of the geometrical phase*. Phys. Today **43**, 34–40 (1990). See p. 32.
- [131] J. Anandan. *The geometric phase*. Nature **360**, 307–313 (1992). See p. 32.

- [132] J. Moody, A. Shapere, and F. Wilczek. *Geometric phases in physics*. World Scientific (1989). See p. 32.
- [133] M. Born and V. Fock. *Beweis des Adiabatomsatzes*. *Z. Physik A* **51**, 165–180 (1928). See p. 32.
- [134] A. Messiah. *Quantum Mechanics*, volume II. North Holland, Amsterdam (1962). See p. 32.
- [135] D. J. Griffiths. *Introduction to Quantum Mechanics*. Prentice Hall (2005). See p. 32.
- [136] Y. Aharonov and D. Bohm. *Significance of electromagnetic potentials in the quantum theory*. *Phys. Rev.* **115**, 485–491 (1959). See p. 34.
- [137] R. G. Chambers. *Shift of an electron interference pattern by enclosed magnetic flux*. *Phys. Rev. Lett.* **5**, 3–7 (1960). See p. 34.
- [138] A. Tonomura, N. Osakabe, T. Matsuda, T. Kawasaki, J. Endo, S. Yano, and H. Yamada. *Evidence for Aharonov-Bohm effect with magnetic field completely shielded from electron wave*. *Phys. Rev. Lett.* **56**, 792–801 (1986). See p. 34.
- [139] G. Herzberg and H. C. Longuet-Higgins. *Intersection of potential energy surfaces in polyatomic molecules*. *Disc. Farad. Soc.* **35**, 77–82 (1963). See p. 35.
- [140] A. J. Stone. *Spin-orbit coupling and the intersection of potential energy surfaces in polyatomic molecules*. *Proc. R. Soc. Lond. A* **351**, 141–150 (1976). See p. 35.
- [141] C. A. Mead and D. G. Truhlar. *Erratum: On the determination of Born–Oppenheimer nuclear motion wave functions including complications due to conical intersections and identical nuclei*. *J. Chem. Phys.* **70**, 2284–2296 (1979). See p. 35.
- [142] T. Bitter and D. Dubbers. *Manifestation of Berry’s topological phase in neutron spin rotation*. *Phys. Rev. Lett.* **59**, 251–254 (1987). See p. 35.
- [143] R. Ticko. *Adiabatic Rotational Splittings and Berry’s Phase in Nuclear Quadrupole Resonance*. *Phys. Rev. Lett.* **58**, 2281–2284 (1987). See p. 35.
- [144] D. Suter, K. T. Mueller, and A. Pines. *Study of the Aharonov-Anandan quantum phase by NMR interferometry*. *Phys. Rev. Lett.* **60**, 1218–1223 (1988). See p. 35.
- [145] R. Y. Chiao and Y.-S. Wu. *Manifestations of Berry’s topological phase for the photon*. *Phys. Rev. Lett.* **57**, 933–936 (1986). See p. 35.
- [146] A. Tomita and R. Y. Chiao. *Observation of Berry’s topological phase by use of an optical fiber*. *Phys. Rev. Lett.* **57**, 937–940 (1986). See p. 35.

- [147] S. Pancharatnam. *Generalized theory of interference, and its applications*. Proc. Indian Acad. Sci. A. **44**, 247–262 (1956). See p. 35.
- [148] R. Nityananda. *Pancharatnam’s route to the geometric phase*. Curr. Sci. **67**, 238–244 (1994). See p. 35.
- [149] Y. Aharonov and J. Anandan. *Phase change during a cyclic quantum evolution*. Phys. Rev. Lett. **58**, 1593–1596 (1987). See p. 35.
- [150] J. Anandan and Y. Aharonov. *Geometric quantum phase and angles*. Phys. Rev. D **38**, 1863–1870 (1988). See p. 35.
- [151] B. Simon. *Holonomy, the quantum adiabatic theorem, and Berry’s phase*. Phys. Rev. Lett. **51**, 2167–2170 (1983). See p. 35.
- [152] R. Jackiw and C. Rebbi. *Solitons with fermion number 1/2*. Phys. Rev. D **13**, 3398–3409 (1976). See pp. 37, 50, 73, 136.
- [153] J. Goldstone and F. Wilczek. *Fractional quantum numbers on solitons*. Phys. Rev. Lett. **47**, 986–989 (1981). See pp. 37, 50, 73, 136.
- [154] A. J. Niemi and G. W. Semenoff. *Spectral asymmetry on an open space*. Phys. Rev. D **30**, 809–818 (1984). See p. 37.
- [155] M. J. Rice and E. J. Mele. *Elementary excitations of a linearly conjugated diatomic polymer*. Phys. Rev. Lett. **49**, 1455–1459 (1982). See pp. 37, 39, 67.
- [156] B. A. Bernevig, T. L. Hughes, and S.-C. Zhang. *Quantum spin Hall effect and topological phase transition in HgTe quantum wells*. Science **314**, 1757–1761 (2006). See pp. 38, 89.
- [157] B. A. Bernevig and T. L. Hughes. *Topological insulators and topological superconductors*. Princeton University Press (2013). See p. 38.
- [158] R. B. Laughlin. *Quantized Hall conductivity in two dimensions*. Phys. Rev. B **23**, 5632–5633 (1981). See p. 38.
- [159] R. D. King-Smith and D. Vanderbilt. *Theory of polarization of crystalline solids*. Phys. Rev. B **47**, 1651–1654 (1993). See pp. 44, 50, 51, 52.
- [160] H. Steinberg, G. Barak, A. Yacoby, L. N. Pfeiffer, K. W. West, B. I. Halperin, and K. L. Hur. *Charge fractionalization in quantum wires*. Nat. Phys. **4**, 116–119 (2008). See p. 50.

- [161] H. Inoue, A. Grivnin, N. Ofek, I. Neder, M. Heiblum, V. Umansky, and D. Mahalu. *Charge fractionalization in the integer quantum Hall effect*. Phys. Rev. Lett. **112**, 166801 (2014). See p. 50.
- [162] R. Jackiw and S.-Y. Pi. *Chiral gauge theory for graphene*. Phys. Rev. Lett. **98**, 266402 (2007). See p. 50.
- [163] R. E. Prange. *Conditions for charge fractionalization*. Phys. Rev. B **26**, 991–997 (1982). See p. 50.
- [164] C.-Y. Hou, C. Chamon, and C. Mudry. *Electron fractionalization in two-dimensional graphenelike structures*. Phys. Rev. Lett. **98**, 186809 (2007). See p. 50.
- [165] D. J. Griffiths. *Introduction to electrodynamics*. Prentice Hall (1999). See p. 50.
- [166] R. Resta. *Microscopic polarization in crystalline dielectrics: the geometric phase approach*. Rev. Mod. Phys. **66**, 899–915 (1994). See p. 50.
- [167] G. Ortiz and R. M. Martin. *Macroscopic polarization as a geometric quantum phase: many-body formulation*. Phys. Rev. B **49**, 14202–14211 (1994). See p. 50.
- [168] R. Resta and D. Vanderbilt. *Physics of ferroelectrics: a modern perspective*. Springer-Verlag, Berlin (2007). See p. 50.
- [169] R. Resta. *Electrical polarization and orbital magnetization: the modern theories*. J. Phys.: Condens. Matter **22**, 123201 (2010). See p. 50.
- [170] R. Clausius. *Die Mechanische Behandlung der electrica*. Vieweg, Berlin (1979). See p. 50.
- [171] O. F. Mossotti. *Azioni e deformazioni nei dielettrici*. Memorie di Matematica e di Fisica della Soc. It. delle Scienze Residente in Modena **24**, 49 (1850). See p. 50.
- [172] R. M. Martin. *Piezoelectricity*. Phys. Rev. B **5**, 1607–1613 (1972). See pp. 50, 52.
- [173] R. M. Martin. *Comment on calculations of electric polarization in crystals*. Phys. Rev. B **9**, 1998–1999 (1974). See pp. 50, 52.
- [174] L. L. Hirst. *The microscopic magnetization: concept and application*. Rev. Mod. Phys. **69**, 607 (1997). See p. 52.
- [175] J. W. F. Woo and R. Landauer. *Reply on "Comment on 'Piezoelectricity under hydrostatic pressure'"*. Phys. Rev. B **6**, 4876–4878 (1972). See p. 52.
- [176] R. Landauer. *Pyroelectricity and piezoelectricity are not true volume effects*. Solid State Commun. **40**, 971–974 (1981). See p. 52.

- [177] C. Kallin and B. I. Halperin. *Surface-effects charge disturbances and piezoelectricity in insulating crystals*. Phys. Rev. B **29**, 2175–2189 (1984). See p. 52.
- [178] R. Landauer. *Introduction to ferroelectric surfaces*. Ferroelectrics **73**, 41–42 (1987). See p. 52.
- [179] A. K. Tagantsev. *Electric polarization in crystals and its response to thermal and elastic perturbations*. Phase Transitions **35**, 119–203 (1991). See p. 52.
- [180] D. J. Thouless. *Quantization of particle transport*. Phys. Rev. B **27**, 6083–6087 (1983). See p. 53.
- [181] Q. Niu. *Towards a quantum pump of electric charges*. Phys. Rev. Lett. **64**, 1812–1815 (1990). See p. 53.
- [182] P. W. Brouwer. *Scattering approach to parametric pumping*. Phys. Rev. B **58**, R10135 (1998). See p. 53.
- [183] V. I. Talyanskii, J. M. Shilton, M. Pepper, C. G. Smith, C. J. B. Ford, E. H. Linfield, D. A. Ritchie, and G. A. C. Jones. *Single-electron transport in a one-dimensional channel by high-frequency surface acoustic waves*. Phys. Rev. B **56**, 15180–15184 (1997). See p. 53.
- [184] M. Switkes, C. M. Markus, K. Campman, and A. C. Gossard. *An adiabatic quantum electron pump*. Science **283**, 1905–1908 (1999). See p. 53.
- [185] F. Zhou, B. Spivak, and B. Altshuler. *Mesoscopic mechanism of adiabatic charge transport*. Phys. Rev. Lett. **82**, 608–611 (1999). See p. 53.
- [186] L. Duca, T. Li, M. Reitter, I. Bloch, M. Schleier-Smith, and U. Schneider. *An Aharonov-Bohm interferometer for determining Bloch band topology*. arXiv:1407:5635 (2014). See pp. 72, 136.
- [187] C. Weitenberg, M. Endres, J. F. Sherson, M. Cheneau, P. Schauss, T. Fukuhara, I. Bloch, and S. Kuhr. *Single-spin addressing in an atomic Mott insulator*. Nature **471**, 319–324 (2011). See p. 72.
- [188] T. Kitagawa, M. A. Broome, A. Fedrizzi, M. S. Rudner, E. Berg, I. Kassal, A. Aspuru-Guzik, E. Demler, and A. G. White. *Observation of topologically protected bound states in photonic quantum walks*. Nat. Commun. **3**, 882 (2012). See pp. 73, 136.
- [189] Y. E. Kraus, Y. Lahini, Z. Ringel, M. Verbin, and O. Zilberberg. *Topological states and adiabatic pumping in quasicrystals*. Phys. Rev. Lett. **109**, 106402 (2012). See pp. 73, 136.

- [190] J. Ruostekoski, G. V. Dunne, and J. Javanainen. *Particle number fractionalization of an atomic Fermi-Dirac gas in an optical lattice*. Phys. Rev. Lett. **88**, 180401 (2002). See pp. 73, 136.
- [191] F. Grudst, M. Höning, and M. Fleischhauer. *Topological edge states in the one-dimensional superlattice Bose-Hubbard model*. Phys. Rev. Lett. **110**, 260405 (2013). See pp. 73, 136.
- [192] C. L. Kane and E. J. Mele. *Z<sub>2</sub> topological order and the quantum spin Hall effect*. Phys. Rev. Lett. **95**, 146802 (2005). See pp. 73, 89, 136.
- [193] T. Kitagawa, E. Berg, M. Rudner, and E. Demler. *Topological characterization of periodically driven quantum systems*. Phys. Rev. B **82**, 235114 (2010). See p. 73.
- [194] N. H. Lindner, G. Refael, and V. Galitski. *Floquet topological insulator in semiconductor quantum wells*. Nat. Phys. **7**, 490–493 (2011). See p. 73.
- [195] G. E. Volovik. *The Universe in a Helium Droplet*. Oxford Univ. Press (2003). See p. 73.
- [196] H. K. Onnes. *Further experiments with liquid Helium. C. On the change of electric resistance of pure metals at very low temperatures, etc. IV-VI. The resistance of pure Mercury at Helium temperatures*. Comm. Phys. Lab. Univ. Leiden **119**, **120**, **122** (1911). See p. 75.
- [197] H. Onnes. *Investigations into the properties of substances at low temperatures, which have led, amongst other things, to the preparation of liquid Helium*. Novel Lecture (1913). See p. 76.
- [198] A. A. Abrikosov. *Type II superconductors and the vortex lattice*. Rev. Mod. Phys. **76**, 975–979 (2004). See p. 76.
- [199] A. G. Lebed. *Type-IV superconductivity: can superconductivity be more exotic than unconventional?* J. Low Temp. Phys. **142**, 173–178 (2006). See p. 76.
- [200] A. A. Abrikosov. *On the magnetic properties of superconductors of the second group*. Sov-Phys JETP **5**, 1174 (1957). See p. 76.
- [201] F. London and H. London. *The electromagnetic equations of the superconductor*. Proc. R. Soc. Lond. A **149**, 71–88 (1935). See p. 77.
- [202] D. Hügel and B. Paredes. *Chiral Ladders and the Edges of Chern Insulators*. Phys. Rev. A **89**, 023619 (2014). See pp. 78, 82, 90, 137.
- [203] E. Orignac and T. Giamarchi. *Meissner effect in a bosonic ladder*. Phys. Rev. B **64**, 144515 (2001). See p. 78.

- [204] M. Kardar. *Josephson-junction ladders and quantum fluctuations*. Phys. Rev. B **33**, 3125–3128 (1986). See p. 78.
- [205] E. Granato. *Phase transitions in Josephson-junction ladders in a magnetic field*. Phys. Rev. B **42**, 4797–4799 (1990). See p. 78.
- [206] C. Denniston and C. Tang. *Phases of Josephson junction ladders*. Phys. Rev. Lett. **75**, 3930–3933 (1995). See p. 78.
- [207] A. Tokuno and A. Georges. *Ground states of a Bose-Hubbard ladder in an artificial magnetic field: field-theoretical approach*. New J. Phys. **16**, 073005 (2014). See p. 78.
- [208] M.-C. Cha and J. Shin. *Two peaks in the momentum distribution of bosons in a weakly frustrated two-leg optical ladder*. Phys. Rev. A **83**, 055602 (2011). See p. 78.
- [209] T. Nogawa and K. Nemoto. *Nonequilibrium relaxation of a quasi-one-dimensional frustrated XY model for charge density waves in ring-shaped crystals*. Phys. Rev. B **73**, 184504 (2006). See p. 78.
- [210] S. T. Carr and B. N. Narozhny. *Spinless fermionic ladders in a magnetic field: phase diagram*. Phys. Rev. B **73**, 195114 (2006). See p. 78.
- [211] A. Petrescu and K. L. Hur. *Bosonic Mott insulator with Meissner currents*. Phys. Rev. Lett. **111**, 150601 (2013). See pp. 78, 116, 137.
- [212] G. Juzeliunas and P. Öhberg. *Creation of an effective magnetic field in ultracold atomic gases using electromagnetically induced transparency*. Opt. Spectrosc. **99**, 357–361 (2005). See p. 78.
- [213] A. Celi, P. Massignan, J. Ruseckas, N. Goldman, I. B. Spielman, G. Juzeliunas, and M. Lewenstein. *Synthetic gauge fields in synthetic dimensions*. Phys. Rev. Lett. **112**, 043001 (2014). See p. 78.
- [214] S. Kessler and F. Marquardt. *Single-site resolved measurement of the current statistics in optical lattices*. Phys. Rev. A **89**, 061601(R) (2014). See pp. 78, 100, 116, 137.
- [215] D. R. Hofstadter. *Energy levels and wave functions of Bloch electrons in rational and irrational magnetic fields*. Phys. Rev. B **14**, 2239–2249 (1976). See p. 78.
- [216] P. G. Harper. *Single band motion of conduction electrons in a uniform magnetic field*. Proc. Phys. Soc. A **68**, 874 (1955). See p. 78.
- [217] E. A. A. Silva. *Probability current in the tight-binding model*. Am. J. Phys. **60**, 753–754 (1992). See p. 82.

- [218] G. B. Hess and W. M. Fairbank. *Measurements of angular momentum in superfluid Helium*. Phys. Rev. Lett. **19**, 216–218 (1967). See p. 85.
- [219] Y. M. Kato, R. C. Myers, A. C. Gossard, and D. D. Awschalom. *Observation of the spin Hall effect in semiconductors*. Science **306**, 1910–1913 (2004). See p. 89.
- [220] M. König, S. Wiedmann, C. Brüne, A. Roth, H. Buhmann, L. W. Molenkamp, X.-L. Qi, and S.-C. Zahng. *Quantum spin Hall insulator state in HgTe quantum wells*. Science **318**, 766–770 (2007). See p. 89.
- [221] D. Hsieh, D. Qian, L. Wray, Y. Xia, Y. S. Hor, R. J. Cava, and M. Z. Hasan. *A topological Dirac insulator in a quantum spin Hall phase*. Nature **452**, 970–974 (2008). See p. 89.
- [222] A. Y. Kitaev. *Unpaired Majorana fermions in quantum wires*. Phys.-Usp. **44**, 131 (2001). See p. 89.
- [223] V. Mourik, K. Zuo, S. M. Frolov, S. R. Plissard, E. P. A. M. Bakkers, and L. P. Kouwenhoven. *Signatures of Majorana fermions in hybrid superconductor-semiconductor nanowire devices*. Science **336**, 1003–1007 (2012). See p. 89.
- [224] Y.-J. Lin, K. Jiménez-García, and I. B. Spielman. *Spin-orbit-coupled Bose-Einstein condensates*. Nature **471**, 83–86 (2011). See p. 89.
- [225] P. Wang, Z.-Q. Yu, Z. Fu, J. Miao, L. Huang, S. Chai, H. Zhai, and J. Zhang. *Spin-orbit coupled degenerate fermi gas*. Phys. Rev. Lett. **109**, 095301 (2012). See p. 89.
- [226] Y. A. Bychkov and E. I. Rashba. *Oscillatory effects and the magnetic susceptibility of carriers in inversion layers*. J. Phys. C: Solid State Phys. **17**, 6039 (1984). See p. 90.
- [227] G. Dresselhaus. *Spin-orbit coupling effects in zinc blende structures*. Phys. Rev. **100**, 580–586 (1955). See p. 90.
- [228] D. Hügel. *Chiral and topological properties of quantum ladders in artificial gauge fields*. Master's thesis, Ludwig Maximilians Universität München (2013). See pp. 90, 111, 116.
- [229] M. Aidelsburger. "In preparation". PhD thesis, Ludwig Maximilians Universität München (2015). See p. 93.
- [230] M. Aidelsburger, M. Atala, S. Nascimbène, S. Trotzky, Y.-A. Chen, and I. Bloch. *Experimental realization of strong effective magnetic fields in optical superlattice potentials*. Appl. Phys. B **113**, 1–11 (2013). See p. 93.
- [231] A. Bermudez, T. Schätz, and D. Porras. *Photon-assisted-tunneling toolbox for quantum simulations in ion traps*. New. J. Phys. **14**, 053049 (2012). See p. 95.

- [232] F. Großman and P. Hänggi. *Localization in a driven two-level dynamics*. Europhys. Lett. **18**, 571 (1992). See p. 95.
- [233] M. Greiner, I. Bloch, O. Mandel, T. Hänsch, and T. Esslinger. *Exploring phase coherence in a 2D lattice of Bose-Einstein condensates*. Phys. Rev. Lett. **87**, 160405 (2001). See pp. 97, 143.
- [234] J. Sebby-Strabley, B. L. Brown, M. Anderlini, P. J. Lee, W. D. Phillips, and J. V. Porto. *Preparing and probing atomic number states with an atom interferometer*. Phys. Rev. Lett. **98**, 200405 (2007). See p. 97.
- [235] C. J. Myatt, E. A. Burt, R. W. Ghrist, E. A. Cornell, and C. E. Wieman. *Production of two overlapping Bose-Einstein condensates by sympathetic cooling*. Phys. Rev. Lett. **78**, 586–589 (1997). See pp. 107, 147.
- [236] H. Schmaljohann, M. Erhard, J. Kronjäger, M. Kottke, S. van Staa, L. Cacciapuoti, J. J. Arlt, K. Bongs, and K. Sengstock. *Dynamics of  $F=2$  spinor Bose-Einstein condensates*. Phys. Rev. Lett. **92**, 040402 (2004). See pp. 107, 147.
- [237] F. Gerbier, S. Trotzky, S. Fölling, U. Schnorrberger, J. D. Thompson, A. Widera, I. Bloch, L. Pollet, M. Troyer, B. Campogrosso-Sansone, N. V. Prokof'ev, and B. V. Svistunov. *Expansion of a quantum gas released from an optical lattice*. Phys. Rev. Lett. **101**, 155303 (2008). See pp. 114, 140.
- [238] A. Dhar, M. Maji, T. Mishra, R. V. Pai, S. Mukerjee, and A. Paramekanti. *Bose-Hubbard model in a strong effective magnetic field: emergence of a chiral Mott insulator ground state*. Phys. Rev. A **85**, 041602 (2012). See pp. 116, 137.
- [239] M. P. Zaletel, S. A. Parameswaran, A. Rüegg, and E. Altman. *Chiral bosonic Mott insulator on the frustrated triangular lattice*. Phys. Rev. B **89**, 155142 (2014). See pp. 116, 137.
- [240] M. Endres, M. Chenau, T. Fukuhara, C. Weitenberg, P. Schauß, C. Gross, L. Mazza, M. C. Bañuls, L. Pollet, I. Bloch, and S. Kuhr. *Observation of correlated particle-hole pairs and string order in low-dimensional Mott insulators*. Science **334**, 200–203 (2011). See p. 116.
- [241] E. Hückel. *Quantentheoretische Beiträge zum Benzolproblem*. Z. Physik **70**, 204–286 (1931). See p. 117.
- [242] H. Bethe. *Zur Theorie der Metalle*. Z. Physik **71**, 205–226 (1931). See p. 119.
- [243] J. G. Bednorz and K. A. Müller. *Possible high- $T_c$  superconductivity in the Ba-La-Cu-O system*. Z. Physik B - Condensed Matter **64**, 189–193 (1986). See p. 120.

- [244] L. M. Duan, E. Demler, and M. D. Lukin. *Controlling spin exchange interactions of ultracold atoms in optical lattices*. Phys. Rev. Lett. **91**, 090402 (2003). See p. 121.
- [245] J. J. García-Ripoll and J. I. Cirac. *Spin dynamics for bosons in an optical lattice*. New J. Phys. **5**, 76 (2003). See p. 121.
- [246] A. B. Kuklov and B. V. Svistunov. *Counterflow superfluidity of two-species ultracold atoms in a commensurate optical lattice*. Phys. Rev. Lett. **90**, 100401 (2003). See p. 121.
- [247] E. Altman, W. Hofstetter, E. Demler, and M. D. Lukin. *Phase diagram of two-component bosons on an optical lattice*. New J. Phys. **5**, 113 (2003). See p. 121.
- [248] B. Paredes and I. Bloch. *Minimum instances of topological matter in an optical plaquette*. Phys. Rev. A **77**, 023603 (2008). See pp. 125, 126, 132, 138.
- [249] R. Hanson, L. P. Kouwenhoven, J. R. Petta, S. Tarucha, and L. M. K. Vandersypen. *Spins in few-electron quantum dots*. Rev. Mod. Phys. **79**, 1217–1265 (2007). See pp. 132, 138.
- [250] B. Paredes. In W. Scientific, editor, *Proceedings of the XXI International conference on Atomic Physics*, page 263 (2008). See pp. 132, 138.
- [251] A. Dauphin and N. Goldman. *Extracting the Chern number from the dynamics of a fermi gas: implementing a quantum Hall bar for cold atoms*. Phys. Rev. Lett. **111**, 135302 (2013). See p. 136.
- [252] M. Aidelsburger, M. Lohse, C. Schweizer, M. Atala, J. T. Barreiro, S. Nascimbène, N. R. Cooper, I. Bloch, and N. Goldman. *Revealing the topology of Hofstadter bands with ultracold bosonic atoms*. arXiv:1407.4205 (2014). See p. 136.
- [253] F. Grudst, D. Abanin, and E. Demler. *Measuring  $\mathbb{Z}_2$  topological invariants in optical lattices using interferometry*. Phys. Rev. A **89**, 043621 (2014). See p. 136.
- [254] C. R. Dean, L. Wang, P. Mather, C. Forsythe, F. Ghahari, Y. Gao, J. Katoch, M. Ishigami, P. Moon, M. Koshino, T. Taniguchi, K. Watanabe, K. L. Shepard, J. Hone, and P. Kim. *Hofstadter’s butterfly and the fractal quantum Hall effect in moiré superlattices*. Nature **497**, 598–602 (2013). See p. 137.
- [255] L. A. Ponomarenko, R. V. Gorbachev, G. L. Yu, C. Elias, R. Jalil, A. A. Patel, A. Mishchenko, A. S. Mayorov, C. R. Woods, J. R. Wallbank, M. Mucha-Kruczynsky, B. A. Piot, M. Potemski, I. V. Grigorieva, K. S. Novoselov, F. Guinea, V. I. Fal’ko, and A. K. Geim. *Cloning of Dirac fermions in graphene superlattices*. Nature **497**, 594–597 (2013). See p. 137.

- [256] B. Hunt, J. D. Sanchez-Yamagishi, A. F. Young, M. Yankowitz, B. J. LeRoy, K. Watanabe, T. Taniguchi, P. Moon, M. Koshino, P. Jarillo-Herrero, and R. C. Ashoori. *Massive Dirac fermions and Hofstadter butterfly in a van der Waals heterostructure*. *Science* **340**, 1427–1430 (2013). See p. 137.
- [257] F. Gerbier, A. Widera, S. Fölling, O. Mandel, T. Gericke, and I. Bloch. *Phase coherence of an atomic Mott insulator*. *Phys. Rev. Lett.* **95**, 050404 (2005). See p. 139.
- [258] R. B. Diener, Q. Zhou, H. Zhai, and T.-L. Ho. *Criterion for bosonic superfluidity in an optical lattice*. *Phys. Rev. Lett.* **98**, 180404 (2007). See p. 139.
- [259] V. A. Kashurnikov, N. V. Prokof'ev, and B. V. Svistunov. *Revealing the superfluid-Mott-insulator transition in an optical lattice*. *Phys. Rev. A* **66**, 031601 (2002). See p. 139.
- [260] Y. Kato, Q. Zhou, N. Kawashima, and N. Trivedi. *Sharp peaks in the momentum distribution of bosons in optical lattices in the normal states*. *Nat. Phys.* **4**, 617–621 (2008). See p. 139.
- [261] E. Toth and P. B. Blakie. *Thermally induced coherence in a Mott insulator of bosonic atoms*. *Phys. Rev. A* **83**, 021601 (2011). See p. 139.
- [262] S. Trotzky, L. Pollet, F. Gerbier, U. Schnorrberger, I. Bloch, N. V. Prokof'ev, B. Svistunov, and M. Troyer. *Suppression of the critical temperature for superfluidity near the Mott transition*. *Nat. Phys.* **6**, 998–1004 (2010). See p. 139.
- [263] F. Gerbier, A. Widera, S. Fölling, O. Mandel, T. Gericke, and I. Bloch. *Interference pattern and visibility of a Mott insulator*. *Phys. Rev. A* **72**, 053606 (2005). See p. 139.
- [264] P. Pedri, L. Pitaevskii, and S. Stringari. *Expansion of a coherent array of Bose-Einstein condensates*. *Phys. Rev. Lett.* **87**, 220401 (2001). See p. 139.
- [265] F. Gerbier, S. Fölling, A. Widera, and I. Bloch. *Visibility of a Bose-condensed gas released from an optical lattice at finite temperatures*. arXiv:0701:420v1 (2007). See p. 140.
- [266] B. Saleh and M. Teich. *Fundamentals of Photonics*. Wiley-Interscience (1991). See p. 140.
- [267] M. Scully and S. Zubairy. *Quantum optics*. Cambridge University Press (1997). See p. 140.
- [268] A. Kastberg, W. D. Phillips, S. L. Rolston, R. J. C. Spreeuw, and P. S. Jessen. *Adiabatic cooling of cesium to 700nK in an optical lattice*. *Phys. Rev. Lett.* **74**, 1542–1545 (1995). See p. 143.

- [269] J. H. Denschlag, J. E. Simsarian, H. Häffner, C. McKenzie, A. Browaeys, D. Cho, K. Helmerson, S. L. Rolston, and W. D. Phillips. *A Bose-Einstein condensate in an optical lattice*. J. Phys. B **35**, 3095–3110 (2002). See p. 143.
- [270] Y.-A. Chen, S. Nascimbène, M. Aidelsburger, M. Atala, S. Trotzky, and I. Bloch. *Controlling correlated tunneling and superexchange interactions with ac-driven optical lattices*. Phys. Rev. Lett. **107**, 210405 (2011). See p. 143.
- [271] T. Müller, S. Fölling, A. Widera, and I. Bloch. *State preparation and dynamics of ultracold atoms in higher lattice orbitals*. Phys. Rev. Lett. **99**, 200405 (2007). See p. 143.
- [272] F. Bloch. *Über die Quantenmechanik der Elektronen in Kristallgittern*. Z. Physik **52**, 555 (1929). See p. 153.
- [273] C. Zener. *Theory of the electrical breakdown of solids dielectrics*. Proc. R. Soc. London A **145**, 523 (1934). See p. 153.
- [274] M. Gustavsson, E. Haller, M. J. Mark, J. G. Danzl, G. Rojas-Kopeinig, and H.-C. Nägerl. *Control of interaction-induced dephasing of Bloch oscillations*. Phys. Rev. Lett. **100**, 080404 (2008). See p. 153.
- [275] N. F. Ramsey. *A molecular beam resonance method with separated oscillating fields*. Phys. Rev. **78**, 695–699 (1950). See p. 159.



# Acknowledgements

I am greatly indebted to my supervisor Immanuel Bloch, for giving me the opportunity to research in his group and for providing the appropriate environment to carry it out. During my PhD I have learnt a lot from him, not only about physics but also about how to properly present our results in conferences and papers. Furthermore, he also taught me how to prepare nice images with different programs that were very useful to illustrate our research in a practical way. I particularly would like to acknowledge his high degree of involvement in the projects and constant discussions that were very motivating and really valuable for the development of this thesis.

I would like to give a big thank to the Boson team, with who I have worked during my PhD. All the results presented in this thesis were only thanks to the great team work and to the illuminating discussions that we had together. Thank you for bringing always good mood to the lab. Especially I would like to thank:

Sylvain Nascimbène, who spent enormous amounts of time explaining me all the physics of the experiment, for his discussions during lunch time and for being not only someone of valuable knowledge but also a great person.

Yu-Ao Chen, from who I learnt all the technical aspects of the experiment. He guided me through the world of optics and taught me how to work in the lab. I would like to particularly thank him for being always good-humored.

Stefan Trotzky, for his support after I joined the group and for teaching me all the basics of cold atoms and lasers.

Julio Barreiro, with who I not only had nice discussions about physics, but also about other things like biking and skying.

Monika Aidelsburger, with who I spent most of the time in the lab. From the discussions we had together I learnt and understood a lot of physics and many of the technical aspects of the experiment, and without her help it would not have been possible to finish the projects. She was always very motivated to work and I enjoyed being her colleague. I want to thank her also for all the non-lab related

activities, like watching soccer games or grilling, and for her useful comments on my thesis.

Michael Lohse, who joined the experiment during my last year in the lab. I had not only a very nice time working with him in the lab, but I also enjoyed our biking weekends and Bagminton games. I also thank him for reading and correcting my thesis.

Christian Schweizer, who joined the lab shortly before I started writing. I enjoyed his good sense of humor and his willing to help and discuss about physics and electronics. I would also like to thank him for his feedback on my thesis and for his help in writing the german version of the abstract.

I would also like to thank the people working in the other labs: the Ytterbium team with who I shared very nice discussions during lunch, the Fermi I and Fermi II teams, that were always there to help us, and also the Single Atom, Molecules and Lithium teams, with who I shared a lot of enjoyable experiences.

An special thanks goes also to Ulrich Schneider and Simon Fölling, because of their constant help in all kind of issues, for their advices and for all the physics that they taught me.

I also would like to acknowledge Sean Hodgman and Tracy Li for proofreading the manuscript and for their help specially regarding language issues.

In general I would like to thank all the non-scientific people working in the group, who were always there supporting our research. Particularly to our secretaries Ildiko Kecskesi, Zohra Hauk, Marianne Kargl and Christina Schuldt for their help with all kind of issues and for organizing many nice activities. Also many thanks to Bodo Hecker, Anton Mayer, Oliver Mödl and Karsten Förster, without their help with all the electronics and mechanical components for the experimental apparatus it would not have been possible to carry out the experiments.

During all these years I discussed with many people, from which I learnt a notable amount of physics. Specially I would like to thank Fabian Grudst, Marin Bukov, Dmitry Abanin, Eugene Demler, Belén Paredes and Luis Foa Torres, as well as Christoph Salomon and Nigel Cooper with who I had the pleasure to discuss about physics through their half a year stay in our group.

Thanks to all my friends that where always there, some of them far but nevertheless present, for all their support and assistance. Specifically to Pablo Zangara, Christoph Lex, Diego Sulca, Mauro Schilman and Pedro Terraf.

Most specially I would like to thanks my parents Jorge and Elizabeth for their support from the distance, as well as my young sister Julieta for sharing her good mood with me and also to my other brothers and sister Kuky, Guillermo, Emiliano and Magali for their support.

Finally, I would like to thank Lea, for her unconditional support and bearing during all my time in the lab, and for helping me with so many things that there is no space here to write them out.

